Simulations of wind turbine wakes in realistic atmospheric conditions : from large eddy simulations to analytical models.

Erwan Jézéquel Jézéquel

THÈSE

En vue de l'obtention du

DOCTORAT DE L'UNIVERSITÉ DE TOULOUSE

Délivré par :

Institut National Polytechnique de Toulouse (Toulouse INP)

Discipline ou spécialité :

Océan, atmosphère, climat

Présentée et soutenue par :

M. ERWAN JÉZÉQUEL

le mercredi 19 octobre 2022

Titre :

Simulations of wind turbine wakes in realistic atmospheric conditions: from large eddy simulations to analytical models.

Ecole doctorale :

Sciences de l'Univers de l'Environnement et de l'Espace (SDU2E)

Unité de recherche :

Groupe d'étude de l'Atmosphère Météorologique (CNRM-GAME)

Directeur(s) de Thèse :

M. VALÉRY MASSON

M. FREDERIC BLONDEL

Rapporteurs :

M. JOHAN MEYERS, KATHOLIEKE UNIVERSITEIT LEUVEN

M. MAJID BASTANKHAH, UNIVERSITY OF DURHAM

MME SANDRINE AUBRUN-SANCHES, ECOLE CENTRALE NANTES

Membre(s) du jury :

M. JEAN-LUC REDELSPERGER, IFREMER PLOUZANE, Président

M. FREDERIC BLONDEL, IFPEN, Membre

M. LAURENT BEAUDET, INSA ROUEN, Membre

M. VALÉRY MASSON, METEO FRANCE TOULOUSE, Membre

Acknowledgments

The present work is the outcome of a three-year collaboration between the Centre National de Recherche Météorologiques (CNRM) and IFP Energies nouvelles (IFPEN). I would thus first like to thank both of these research structures for financing the project, but also supervising my work and granting me access to the supercomputers Beaufix and later Bélénos at Météo France.

I would also like to thank the reviewers Sandrine Aubrun-Sanches, Majid Bastankhah and Johan Meyers for spending the necessary time to read the manuscript, provide important feedbacks and confirm its quality to the university of Toulouse INP. I also thank them as well as the other members of the jury, Jean-Luc Redelsperger and Laurent Beaudet, for participating to the defence and contributing to the work through insightful questions.

This work would not be what it is without the supervision of Valéry, who helped me from the first to the last day, in particular to understand the basis of boundary-layer meteorology and to use the code Meso-NH. I would not even have had the opportunity to do this wonderful experience if Marie did not set up the project and scheduled the beginning of the work plan. She supervised the first half of this thesis, where she not only guided me in the jungle that is LES modelling but also taught me good habits and improved my self-confidence. Last but not least, Frédéric knew to support me for the second part of the Ph.D. where he helped me to work on physical analysis and analytical models, and pushed me to finish my work in time. In short, I could not have dreamt of a better supervising team.

Even though he was not officially my supervisor, I must thank my predecessor Pierre-Antoine, who developed and validated most of the actuator methods in Meso-NH, because his work was necessary to start mine, and also for his kindness and patience with me. More generally, I was lucky to find many awesome colleagues who helped me during the whole work, so thank you Quentin, Eva, Tim, Christine at CNRM and Mathieu, Pierre, Julien, Pauline, David, Olivier at IFPEN for your contributions to this work. I also must thank all the other colleagues and in particular my fellow Ph. D. students for the great atmosphere that I felt during these three years. I also got precious help from Paula Doubrawa and Eliot Quon from the National Renewable Energy Laboratory, respectively with the SWiFT benchmark and the use of the SAMWICH toolbox. Thank you also to the IT support, and the administrative staff from IFPEN, CNRM, Météo France, Toulouse INP and SDU2E without who these three years would have been very painful.

Finally, I was also well surrounded outside of work by my friends and family, whose presence was more than needed. Among them, I must thank Léonie in particular, whose love and support helped me through these years, even when she found herself locked down between me and my thesis during a global pandemic.

Abstract

Wind turbines are often clustered in wind farms where they are subject to the wakes emitted by the upstream rotors. Wind turbine wakes are regions of decreased wind velocity and increased turbulence (velocity variations), that respectively lead to a loss of production and a decreased life expectancy, in the end increasing the cost of wind power.

The wind farm layouts must thus be optimised by taking wakes into account to make the wind power more efficient. Since optimisation studies require a lot of simulations, steady analytical models have been developed to quickly provide an estimation of the velocity and turbulence in the wake of a wind turbine, and compute the effect on the downstream rotor.

Moreover, wind turbine wakes interact with the atmospheric boundary layer (ABL). Depending on the atmospheric stability, large-scale turbulent motions are created in the ABL that induce low-frequency displacements of the wake. This phenomenon, called meandering, modifies the mean wake properties but is rarely taken into account explicitly in steady analytical models. The present work aims at better understanding and modelling the interactions between wind turbine wakes and the ABL, based on high-fidelity numerical simulations.

The first part of the manuscript is dedicated to the state-of-the-art. It starts by describing the general fluid dynamic and meteorological concepts on which is based the whole work. Then, we propose a literature review of the wakes and their interactions with the ABL. We also describe the existing steady analytical models and the models for wake meandering. This part ends with a description of our high-fidelity code, Meso-NH, as well as the chosen parametrisation for the turbine.

In the second part, we focus on the high-fidelity simulations. A validation of Meso-NH against measurements and other equivalent codes of the community is performed, for three cases of atmospheric stability: neutral, stable and unstable. After a comparative study of different post-processing methods, an in-depth physical analysis of the wakes under these three conditions is proposed. We concluded that atmospheric stability mainly affects the wake meandering, and not the wake expansion which is attributed to the operating conditions.

The third part is based on this result. We separate the turbulence and velocity fields into different terms that can be associated to meandering, wake expansion, or both. These terms are compared for the different cases and a model is proposed for the preponderant ones. It results in a new steady analytical model for velocity and turbulence that independently takes into account wake expansion and meandering.

This thesis thus presents and analyses new results that enhance our understanding of the behaviour of wakes in the ABL, and proposes a new steady model that allows taking into account wake meandering.

Résumé

Les éoliennes sont souvent regroupées en parcs où elles sont sujettes aux sillages des rotors en amont. Les sillages d'éoliennes sont des régions où la vitesse du vent est réduite et la turbulence (les variations de vent) est augmentée, ce qui induit respectivement une baisse de la production et de la durée de vie du parc, résultant au final en un coût de l'électricité plus élevé.

La disposition des parcs doit donc être optimisée en prenant les sillages en compte pour rendre leur production plus efficace. Comme les études d'optimisation demandent d'étudier de nombreux cas, les modèles analytiques statiques ont été développés pour donner rapidement les caractéristiques d'un sillage, et estimer les perturbations engendrées sur les rotors qui en découlent.

De plus, les sillages d'éoliennes interagissent avec la couche limite atmosphérique (CLA). Selon la stabilité de l'atmosphère, des structures turbulentes de grande échelle sont créées dans la CLA qui induisent des déplacements à basse fréquence du sillage. Ce phénomène, appelé méandrement, modifie les propriétés moyennes du sillage, mais est rarement pris en compte explicitement dans les modèles statiques. Ce travail de thèse vise à mieux comprendre et modéliser les interactions entre les sillages et la CLA, en se basant sur des simulations haute-fidélité.

La première partie du manuscrit est dédiée à un état de l'art. On commence par décrire les principes de la météorologie, sur lesquels se base le reste de ce travail. Puis, une revue de la littérature sur les sillages et leurs interactions avec la CLA est faite. On y détaille aussi les principaux modèles de sillages, statiques et pour le méandrement. Cette partie se termine sur une description du code haute-fidélité utilisé, Meso-NH, ainsi que de la paramétrisation numérique de la turbine.

Dans la deuxième partie, nous nous focalisons sur ces simulations haute-fidélité. Meso-NH est d'abord validé par rapport à des mesures et des codes équivalents de la communauté pour trois cas de stabilité : neutre, stable et instable. Après une étude comparative de différentes méthodes de post-traitement, une analyse physique approfondie des sillages pour les trois cas est proposée. Il est conclu que la stabilité atmosphérique impacte surtout le méandrement de sillage et assez peu son expansion, qui est plutôt attribuée au fonctionnement du rotor.

La troisième partie se base sur cette conclusion. La turbulence et la vitesse du vent sont séparées en plusieurs termes qui sont associés au méandrement, à l'expansion du sillage ou aux deux. Ces termes sont comparés pour les différents cas de stabilité et un modèle est proposé pour ceux qui sont prépondérants. Il en résulte un nouveau modèle analytique statique pour la vitesse et la turbulence qui prend indépendamment en compte le méandrement et l'expansion du sillage.

Cette thèse permet donc de présenter et d'analyser de nouveaux résultats qui améliorent notre compréhension de l'interaction des sillages et de la CLA, et propose un nouveau modèle statique qui prend en compte le méandrement.

Contents

Introduction **1**

Introduction (français) **7**

I Part A - State of the art 15

1 Turbulence in the atmospheric boundary layer 17

1.1 Turbulence . . . 17
1.1.1 Definition of the velocities . . . 17
1.1.2 Origin and definition of turbulence . . . 18
1.1.3 The Reynolds decomposition . . . 19
1.1.4 Quantification of turbulence with second order moments . . . 21
1.1.5 The different scales of turbulence . . . 22
1.1.6 Spectral analysis . . . 23
1.2 The atmospheric boundary layer . . . 25
1.2.1 The Earth's atmosphere . . . 25
1.2.2 The different regimes of the ABL . . . 27
1.2.3 Characterisation of the atmospheric stability . . . 28
1.2.4 Turbulence spectra in the ABL . . . 30
1.3 System of equations . . . 32
1.3.1 Additional definitions . . . 32
1.3.2 Simplifying hypotheses . . . 33
1.3.3 The Aneslastic system . . . 34
1.3.4 The Reynolds system . . . 35
1.3.5 Equation for the TKE . . . 36
1.3.6 Turbulence modelling . . . 37

2 Wind turbines and wind turbine wakes 39
2.1 Wind turbine aerodynamics . . . 39
2.1.1 Wind turbine kinematics . . . 39
2.1.2 Working principle . . . 40
2.1.3 Performances of a wind turbine . . . 41
2.2 Wakes of wind turbines . . . 42
2.2.1 Characteristics of a wind turbine wake . . . 42
2.2.2 Structure of a wind turbine wake . . . 44
2.2.3 Influence of the ABL on the wake . . . 46
2.2.4 Spectral analysis of turbulent wakes . . . 47
2.2.5 Influence of the tower and the nacelle . . . 48
2.3 Wake meandering . . . 48
2.3.1 Origin of the phenomenon . . . 48
2.3.2 Fixed and moving frame of reference . . . 49
2.3.3 Amplitude of the wake meandering . . . 51
2.3.4 Frequency analysis of the wake meandering . . . 51
2.4 Analytical modelling in the FFOR . . . 52
2.4.1 Velocity deficit modelling . . . 53
2.4.2 Added turbulence modelling . . . 57
2.5 Wake meandering modelling . . . 58
2.5.1 Dynamic Wake Meandering . . . 58
2.5.2 Steady modelling of the wake meandering . . . 61

3 Numerical modelling 65
3.1 Large Eddy Simulation . . . 65
3.1.1 The different numerical strategies to compute turbulent flows . . . 65
3.1.2 LES formulation . . . 67
3.1.3 Implicit filtering . . . 69
3.2 Meso-NH . . . 69
3.2.1 General presentation . . . 69
3.2.2 Turbulence closure . . . 70
3.2.3 Mixing length . . . 72
3.2.4 Grid nesting . . . 73
3.3 The actuator line method (ALM) . . . 73
3.3.1 Principle . . . 73

3.3.2 Smearing . . . 74
3.3.3 Implementation in Meso-NH . . . 74

II Part B - High fidelity simulations of wind turbine wakes 79

4 Validation with the SWiFT benchmark 81
4.1 Overview of the problem . . . 81
4.1.1 Presentation of the SWiFT benchmark . . . 81
4.1.2 Methodology . . . 83
4.1.3 Turbulence build-up region . . . 84
4.1.4 Numerical setup . . . 85
4.2 The neutral case . . . 87
4.2.1 Inflow . . . 88
4.2.2 Turbine response . . . 89
4.2.3 Velocity deficit in the FFOR . . . 89
4.2.4 Wake Meandering . . . 90
4.2.5 Velocity deficit in the MFOR . . . 91
4.3 Sensitivity study on the time step and the time-splitting . . . 91
4.4 The unstable case . . . 93
4.5 The stable case . . . 97

5 Wake Tracking 101
5.1 Context . . . 101
5.1.1 Difficulties to define the wake centre . . . 101
5.1.2 Tracking methods in the literature . . . 102
5.2 Pre-processing the instantaneous velocity field . . . 104
5.2.1 Redefinition of the unperturbed velocity . . . 104
5.2.2 Moving average of the instantaneous velocity . . . 106
5.3 Modified simulations . . . 108
5.4 Results . . . 109
5.4.1 Visual analysis . . . 109
5.4.2 Time series and spectral analysis . . . 112
5.4.3 Impact on the MFOR . . . 114

6 Physical analysis of wake properties 119

6.1 Wake meandering. . . . 119
6.1.1 Amount of meandering. . . . 119
6.1.2 Self-similarity 121
6.2 Velocity deficit 123
6.2.1 Wake width 123
6.2.2 Maximum deficit 126
6.2.3 Self-similarity 127
6.3 Wake turbulence 129
6.3.1 Added TI 130
6.3.2 Self-similarity 131
6.3.3 Spectral analysis 134
6.3.4 Upstream length scale 136
6.4 Conclusions 137

III Part C - Analytical modelling 139

7 Breakdowns of the mean velocity and turbulence 141
7.1 Analytical development 141
7.2 Error induced by neglecting the cross-terms. . . . 145
7.2.1 Methodology 145
7.2.2 Numerical limitations of the approach 145
7.2.3 Velocity field 147
7.2.4 Turbulence field 148
7.3 Analysis of the terms in the turbulence breakdown 151
7.3.1 Shape and values of the terms 151
7.3.2 Physical interpretation 155

8 Proposition of a new analytical model 159
8.1 Independent modelling of the wake in the MFOR and meandering 159
8.1.1 Velocity deficit 159
8.1.2 Wake added turbulence in the MFOR 161
8.1.3 Wake meandering 164
8.1.4 Parameters of the model 165
8.2 Model for the velocity in the FFOR 166
8.3 Model for the turbulence in the FFOR 169

8.3.1 Meandering term . . . 170
8.3.2 Rotor-added turbulence term . . . 172
8.3.3 Functional analysis . . . 174
8.3.4 Results of the model for turbulence . . . 176

Conclusion **181**

Conclusion (français) **185**

IV Appendices 189

A Numerical parametrisation of the SWiFT simulations **191**
A.1 One way and two way nesting . . . 191
A.2 Effect of the tower and nacelle in Meso-NH . . . 193

B Additional figures for the wake analysis **197**

C Demonstration of Eq. 7.9 **205**

References **206**

List of Figures **218**

List of Tables **223**

List of Symbols **224**

Introduction

Context

According to the Intergovernmental Panel on Climate Change, new coal and gas field projects must be stopped to keep global warming under the 1.5°C limit [1]. More pessimistic studies even suggest that already-existing facilities should be prematurely shut down to stay below this limit [2]. Renewable energies, in particular wind turbines, are expected to play a major role in the decarbonisation of the energy system. According to the International Energy Agency (IEA), wind power capacity must be multiplied by 11 worldwide and by 25 in Europe from now to 2050 to meet our objectives on climate change [3].

In 2021, the wind energy capacity in the EU plus UK was 235 GW. It produced 437 TWh, i.e. 15% of the region's electricity consumption. The capacity is expected to grow by about 17.6 GW every year until 2030, which is not enough to meet the IEA objectives [4]. The unwillingness of society to adopt this technology faster can partially be explained by the low value of the wind farms' capacity factor. It is defined as the ratio between the installed power and the averaged power effectively produced and was on average about 25 % [5] in the EU in 2020. This relatively low value is mostly due to the inability of wind turbines to operate all the time at their rated power and is often pointed out as one of the major weaknesses of the industry. Indeed, turbines are designed for a given wind velocity corresponding to their rated power and from which is computed their capacity. However, due to the wind unsteadiness and the presence of neighbouring wind turbines or wind farms, the turbines are often working under lower wind speeds, leading to a degraded capacity factor [6]. The wind unsteadiness can hardly be addressed, but the way wind turbines hinder one another can be studied to reduce the power losses, improve the wind farms' cost of energy, and encourage industries and governments to invest in wind power.

For practical reasons such as limited available space and grid connection, wind turbines are clustered into wind farms, i.e. arrays of turbines (e.g. the Horns Rev wind farm in Fig. 1a). From an aerodynamic point of view, this clustering is problematic because the downstream turbines are affected by the wakes of the upstream turbines. Wakes are regions of low velocity and high turbulence (velocity variations), which are generated by upstream turbines that perturb and extract energy from the wind.

The power output of a turbine is related to the cube of the velocity: as a consequence, even a small decrease in velocity can have a considerable impact on the downstream turbine's energy production. As an example, measurements in the Horns Rev 1 offshore wind farm showed that the power production for turbines inside the farm can be reduced up to 60% of the first turbine's power (Fig. 1b) [8]. Note that the turbines' spacing in Horns Rev 1 is about seven turbine diameters; in other

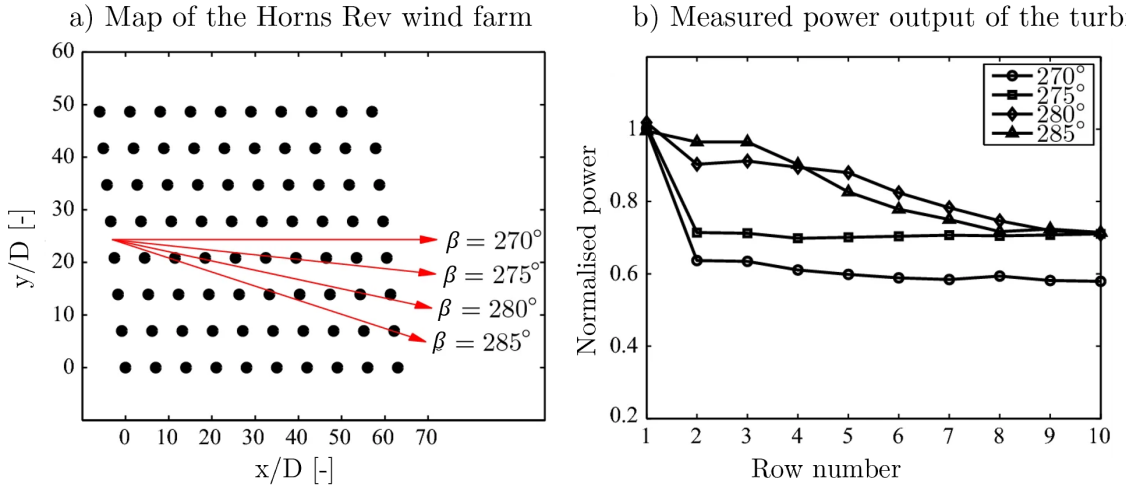

Figure 1: The Horns Rev 1 offshore wind farm. a) Map of the farm, dimensions are normalised by the turbine's diameter, b) Measured power output of the turbines in a row, depending on the wind direction. Normalisation by the power of the first turbine. Courtesy of [7].

wind farms, especially onshore, this number might be lower, leading to even stronger wake effects [9]. Moreover, the increased turbulence induces unsteady loads on the turbine's blade which can lead to fatal damage. For turbines, operating in waked conditions has thus a double negative impact: lower power output and lower life expectancy. Consequently, predicting wind turbine wakes is key to accurately estimate the annual energy production (AEP) and life expectancy of a wind farm.

Wind turbines and their wakes are located in the first hundreds of metres above the ground. This region of the atmosphere, called the atmospheric boundary layer (ABL), is characterised by strong heat transfer, gradients of wind velocity and wind directions, as well as high levels of turbulence. These characteristics, and thus the behaviour of wind turbine wakes, are fluctuating over time, driven by many parameters such as synoptic motions (e.g. anticyclone, low-pressure area...), diurnal cycle, orography, the presence of clouds, etc... Conversely, wind turbine wakes can locally modify the ABL: for instance, the swirl caused by the wind turbines moves parcels of air with different levels of temperature and humidity and can lead to the formation of clouds [10].

The ABL has historically been widely studied by meteorologists, in particular for weather predictions. More recently the wind turbine community gained interest in the subject to better understand the behaviour of turbines and their wakes in realistic conditions. For instance, it has been shown that the thermal effects in the ABL influence the wake dissipation [11], the shear near the ground modifies the turbine performances [12] and a complex terrain can significantly change the behaviour of wakes [13]. Moreover, the ABL turbulence is driven by large-scale eddies that induce unsteady displacements of the wake called wake meandering [14]. For a downstream wind turbine, these meandering motions induce an increased level of turbulence that degrades its life expectancy. This phenomenon is at the core of the present work.

Wake prediction methods

Depending on the resources at disposition and the targeted level of fidelity, there are a lot of different techniques to study wind turbine wakes, listed in Fig. 2. In fluid dynamics as in every experimental science, theoretical reasonings are considered to be valid only if they verify field measurements. Such measurements, also called *in situ* measurements or full-scale measurements if they are performed on a realistically large wind turbine, are thus considered to be the most reliable method. It requires instrumenting a real wind turbine i.e. buying one or accessing turbines at an industrial site to add measurement tools. The turbine operating conditions are usually acquired through Supervisory Control And Data Acquisition (SCADA). The upstream flowfield and ground forcings are often considered to be spatially homogeneous and are thus measured with a single meteorological mast. However, more advanced technologies such as Light Detection And Ranging (LiDAR) are needed to measure the inhomogeneous wake downstream. As a consequence, field measurements are particularly expensive and few wind turbines are instrumented around the world, ranging from full-scale [15, 16] to utility-scale [17, 18, 19].

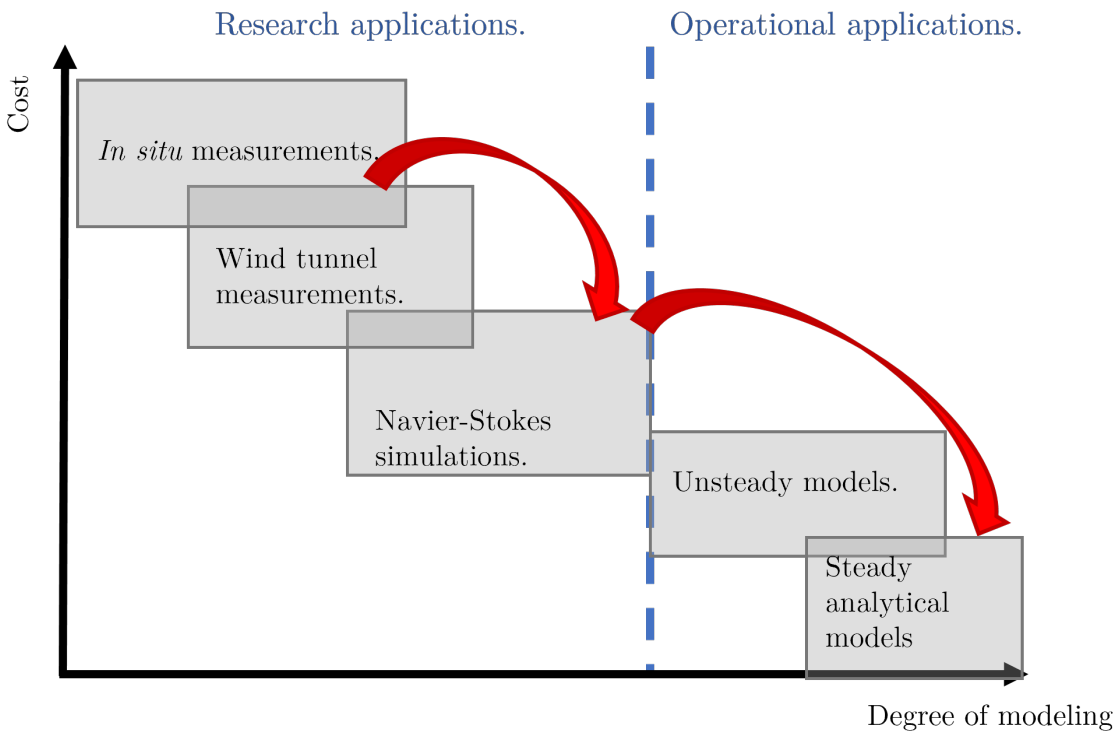

Figure 2: Reliability of different methods to assess wake effects as a function of their degree of modelling. Scales are arbitrary, red arrows indicate the process followed by the present work.

Even though they are considered to be the highest level of fidelity, full-scale experiments are limited by measurement tools. Spinning LiDARs for instance measure the instantaneous velocity point by point, so a good spatial resolution is achievable at the expense of temporal resolution and conversely. Moreover, they have a limited range and since the wake scales with the turbine diameter, they can only measure the near wake of large turbines. Alternatively, scanning LiDARs can be used on a long range, but only give data on a plane. All these methods, including SCADA data, are subject to

measurement errors. Another issue with full-scale experiments is that the user does not control the inflow conditions, making it hard to perform a sensitivity study based on field experiments.

Wind tunnel measurements are an answer to these issues. In such experiments, the turbine is modelled by a scaled rotor [20, 21] or a porous disk [22], placed in a test section. A flow similar to the ABL can be reproduced with an appropriate wind tunnel [23], and the user controls upstream conditions such as wind speed, turbulence, surface roughness [24], simplified orography terrain [25] or even thermal effects [26, 27]. Wind tunnel measurements also allow controlling the operating conditions of the turbine [28] and using measurement techniques like Particle Image Velocimetry [29] where the whole flowfield can be measured. The measured wakes in such conditions have been proven to be realistic [30] and unsteady effects such as meandering are measurable [28]. Nevertheless, generating the right length and time scales compared to the modelled rotor can be a difficult task, and these measurement campaigns still come at a high cost since wind tunnels are expensive facilities to build and run. Moreover, thermal effects play an important role in the development of wakes and few wind tunnels can model such phenomena.

The evolution of wind turbine wakes and of the ABL are driven by the laws of fluid dynamics called the Navier-Stokes equations and which know no analytical solutions yet. With the development of High-Performance Computing (HPC), this set of equations for wind turbines in the ABL has become numerically solvable, provided that some simplifications are made on the turbine modelling and the small-scale turbulence. In this work, we will focus on Large Eddy Simulations (LES) which are the most common at the moment in the wind energy community, but other high-fidelity codes exist. Even though implementing a Navier-Stokes solver is not an easy task, it is more accessible for research institutions than experimental facilities and can be based upon a long story of numerical simulations in fluid dynamics. Moreover, some models are open-source so they allow anyone with appropriate knowledge to perform their own numerical experiments provided he or she has access to sufficient computational resources.

Among the main numerical models, the Simulator fOr Wind Farm Application (SOWFA), developed by the National Renewable Energy Laboratory (NREL) in the US, is an extension of the OpenFOAM library that takes into account wind turbine wakes and ABL effects. Alternatively, researchers from the ForWind institute in Germany started from a code developed for ABL simulations called PALM [31] in which they implemented a turbine parametrisation [32]. It is this latter approach that has been chosen by IFPEN [10], but based instead on Meso-NH, the code developed by the Centre National de Recherches Météorologiques (CNRM) et le Laboratoire d'Aérologie [33]. Similarly to wind tunnel experiments, the user controls the inflow conditions, but can here very simply change the turbine or atmospheric parameters, leading to a broad diversity of studies on the interaction between wakes and the ABL. Even though numerical simulations are often used as reference results in the absence of measurements, they always include some modelling to provide a result in a reasonable amount of time. This modelling along with the intrinsic approximations of the numerical discretisation reduces the reliability of numerical methods compared to measurements. Indeed, for a given problem, different codes, or even the same code with different parametrisations can give different results [19]. Moreover, the computational cost of LES is very high: hundreds of thousand of CPU hours are needed for a given case. A study with several cases is achievable in a matter of days with a modern supercomputer, but Navier-Stokes simulations are in general not suited for industrial applications, where the assessment and optimisation of a park need thousands of cases and for which the user does not necessarily have access to supercomputers.

For some applications, the wake dynamics must be taken into account at a sufficiently low cost to be usable by industrials. For instance, rotor control allows to optimise power production, and the aero-elastic behaviour of very large wind turbines must be understood before they are built. Indeed, turbines are growing larger and larger to optimise the wind energy profitability and reduce the emitted CO_2 per produced energy [34], e.g. the HALIADE-X 14MW turbine with 107-metre long blades developed by General Electrics. New challenges arise for such elongated structures, in particular when it comes to the estimation of the blade's loading, and thus the life expectancy of the turbines. Moreover, for offshore turbines, and in particular the floating ones, the hydrodynamic phenomena are expected to take an important role in the performance of the turbine.

Unsteady multi-physics models such as DeepLinesWind^{TM}[35] or Open.FAST [36] are specially developed to deal with applications such as those listed above. To be usable in an industrial context, these codes are based on simplified models. For the aerodynamic part, a turbulent inflow can be synthetically generated and wake flow is deduced from unsteady wake models, such as the Dynamic Wake Meandering (DWM) model that is designed to model the meandering phenomenon [14]. This meandering is particularly important for the aero-elasticity of a turbine working in waked conditions since it can be successively inside and outside the wake, leading to velocity variations, and thus blade fatigue. These models are suited for industrial applications because they take into account all the physical phenomena of interest for wind turbines and their computational cost is greatly reduced compared to Navier-Stokes simulations. It is still non-negligible though, and the use of supercomputers may be needed for optimisation studies or large farm simulations.

When designing a wind farm at a specific location, all the potential wind velocities and directions must be investigated, as well as different atmospheric conditions. As a result, a large number of cases are needed, especially if the wind farm designer wants to optimise the layout: he or she thus needs a very fast and reliable tool. The computational cost of Navier-Stokes codes is too high and for some applications, even unsteady multi-physics models can be too slow. Steady-state analytical models serve this purpose: based on several analytical formulas, they can provide hundreds of results in a reasonable time on a desktop computer, making them very accessible for industrial purposes. Such models do not need unsteady inputs like unsteady models but only time-averaged atmospheric conditions and the turbine's operating conditions. Beyond their speed, these models are also particularly easy to use, even for someone with little knowledge about fluid dynamics and wakes. However, they rely on a lot of assumptions, are sensitive to the calibration data, and only a few take ABL effects into account.

This list is not complete, but the reader will understand that there is a broad diversity of methods to estimate the wake effects, each of which has its pros, cons, applications and costs. The lowest fidelity models are the ones used in industry for real-case applications but are based on insights gained from higher fidelity methods. The calibration is done from the top to the bottom of Fig. 2: engineering models are calibrated directly against measurements, or against a Navier-Stokes code, which has itself been validated against measurements.

Scope and overview of the present work

Dynamic models, in particular the DWM, have received a lot of exposure recently to model the meandering phenomena. Indeed, a better understanding of the phenomena has been identified as

one of the major questions to answer in current state-of-the-art wind energy science [37]. However, most steady-state models do not take it into account, or only as a phenomenon that on average modifies the wake expansion. Wake expansion and meandering are thus undifferentiated, leading to difficulties when building a physically-based model for turbulence. Steady models for turbulence are often empirically-based, which is, to our interpretation, due to this mixing between meandering and wake expansion.

The scope of this thesis is to better understand the interactions between atmospheric turbulence and wind turbine wakes with a particular emphasis on wake meandering. This work can be summarised by the red arrows in Fig. 2. *In situ* measurements from the literature are first reproduced with Meso-NH to validate the capacity of the code to model the interactions between wakes and ABL. Then, based on a physical analysis of LES data, the meandering is included independently to wake expansion in a wake model for velocity and turbulence that can either be used for steady-state or unsteady applications. The work is thus separated into three parts:

Part one is dedicated to the state of the art. In chapter 1, the ABL phenomena likely to interact with wind turbine wakes are described along with the main mathematical models used to model them. In chapter 2, wind turbines are quickly described, followed by a literature review on wind turbine wakes. It finishes with a review of the main steady analytical wake models and wake meandering modelling. In chapter 3 the concept of LES is introduced, followed by a description of Meso-NH and the actuator line method (ALM), which is the method used to model the turbine in the present work.

Part two focuses on high-fidelity simulations. In chapter 4, we validate the capacity of Meso-NH/ALM to simulate a realistic wake under different ABL conditions. Chapter 5 focuses on wake tracking, a post-process where the wake centre is tracked at each time step. It is a necessary step to study wake meandering. Based on the same simulations, we analyse in chapter 6 the influence of the ABL's thermal effects on the wake properties and wake meandering.

Part three presents an analytical reasoning that leads to an engineering model. In chapter 7, we demonstrate how the velocity and turbulence in the wake can be broken down into several parts that depend on the wake expansion, on meandering, or on both. This analysis highlights underlying assumptions of some literature models where several terms of the breakdown are neglected. Inspired by this breakdown, we propose an analytical model that takes meandering into account.

Introduction (français)

Contexte

D'après le Groupe d'experts Intergouvernemental sur l'Évolution du Climat (GIEC), tous les nouveaux projets d'extraction de charbon et de gaz doivent être arrêtés pour garder le réchauffement climatique sous la barre des 1.5°C [1]. Des études plus pessimistes suggèrent même qu'il faudrait fermer prématurément certaines installations pour rester sous cette limite [2]. Les acteurs de la production énergétique s'attendent à ce que les énergies renouvelables, et notamment l'éolien, jouent un rôle de premier plan dans la décarbonation du secteur de l'énergie. L'Agence Internationale de l'Énergie (IEA) estime que la puissance éolienne installée doit être multipliée par 11 mondialement et par 25 en Europe d'ici à 2050 pour atteindre nos objectifs contre le réchauffement climatique [3].

En 2021, la puissance éolienne installée dans l'UE et le Royaume-Uni était de 235 GW. Pour la même année, cela correspondait à 437 TWh c.-à-d. 15% de la consommation électrique de la région. Il est attendu que cette puissance installée augmente en moyenne de 17.6 GW chaque année jusque 2030, ce qui est insuffisant en comparaison des objectifs fixés par l'IEA [4]. La réticence de certains acteurs, industriels comme gouvernementaux, à développer plus rapidement l'éolien peut en partie être expliquée par le faible facteur de charge de l'éolien. Le facteur de charge, défini comme le rapport entre la puissance installée et la puissance moyenne effectivement produite, était en moyenne de 25% [5] dans l'UE en 2020. Cette valeur relativement faible est due au fait qu'il est impossible de faire fonctionner les éoliennes à leur puissance nominale en permanence, et est souvent soulignée comme étant une des grandes faiblesses de l'industrie. En effet, les éoliennes sont conçues pour fonctionner sur une certaine plage de vitesse de vent, où elles produiront un maximum de puissance qui définit la puissance nominale. En raison des variations de vent et de la présence d'autres éoliennes ou même d'un autre parc aux alentours, les éoliennes fonctionnent souvent en dessous de leur puissance nominale, dégradant ainsi leur facteur de charge [6]. L'instationnarité du vent étant intrinsèque à la ressource, il est difficile de résoudre ce problème. Toutefois, la manière dont les éoliennes se gênent entre elles peut être étudiée pour réduire les pertes de puissance, améliorer le coût de l'énergie éolienne et donc encourager les industriels, les pouvoirs publics et la société civile à investir dans cette technologie.

Pour des raisons pratiques telles que le faible espace disponible et le raccordement au réseau électrique, les éoliennes sont regroupées en parcs, comme par exemple le parc de Horns Rev 1, schématisé dans la Fig. 3a. Aérodynamiquement parlant, ce regroupement est problématique, car les éoliennes en aval du parc sont affectées par les sillages des éoliennes en amont. Les sillages sont des régions de faible vitesse de vent et de haut niveau de turbulence (variations de vitesse de vent) qui sont le fruit de la perturbation et de l'extraction d'énergie du vent par les éoliennes.

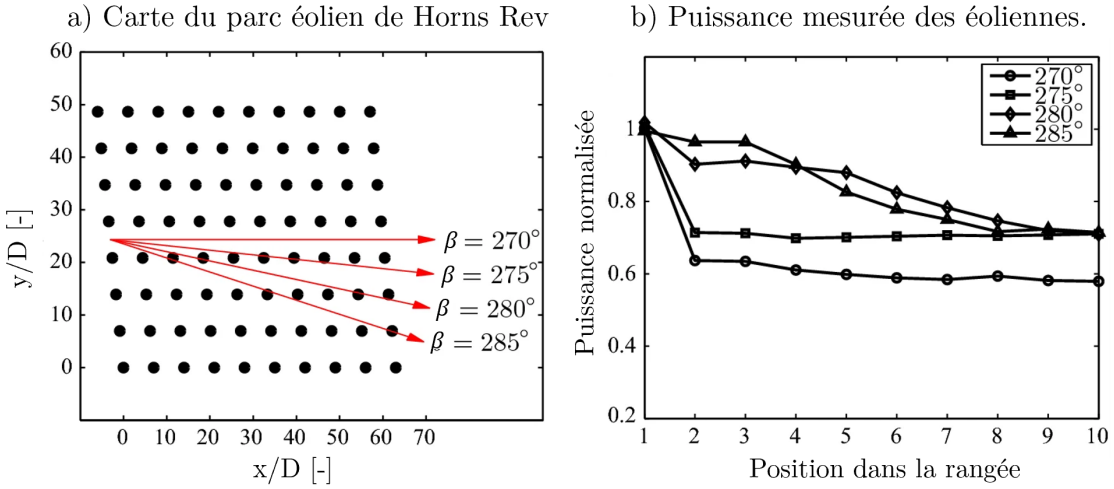

Figure 3: Le parc offshore de Horns Rev 1. a) Schéma du parc, les distances sont normalisées par le diamètre de l'éolienne, b) Puissance produite mesurée par les éoliennes au sein d'une rangée, selon la direction de vent. Normalisation par la puissance de la première éolienne. D'après [7].

La puissance produite par une éolienne est proportionnelle au cube de la vitesse de vent qu'elle subit : même une faible diminution du vent peut donc sévèrement affecter la puissance des éoliennes. Par exemple, des mesures sur le parc offshore de Horns Rev 1 ont montré que la puissance des éoliennes à l'intérieur de la ferme peut être réduite à jusque 60% de la puissance de la première éolienne de la rangée, à cause de la diminution du vent dans les sillages (Fig. 3b) [8]. On notera que l'espacement des éoliennes de Horns Rev 1 est d'environ sept diamètres ; dans d'autres parcs, en particulier onshore, ce nombre peut être bien plus bas, menant à des effets de sillages encore plus importants [9]. De plus, les niveaux élevés de turbulence dans le sillage induisent des chargements instationnaires sur les pales des éoliennes, qui peuvent mener à d'importants dommages. Pour une éolienne, fonctionner dans des conditions de sillage a donc un double impact négatif : moins de puissance produite et une espérance de vie plus faible. Prédire les sillages d'éoliennes est alors essentiel pour estimer avec précision la production annuelle d'énergie (AEP) et l'espérance de vie d'un parc éolien.

Les éoliennes et leurs sillages sont situés dans les premières centaines de mètres au-dessus du sol. Cette région de l'atmosphère, appelée couche limite atmosphérique (CLA), est caractérisée par de forts flux de chaleur, des gradients de vitesse et de direction de vent, ainsi que de hauts niveaux de turbulence. Ces caractéristiques, et donc le comportement des sillages d'éoliennes, fluctuent avec le temps, en fonction des mouvements synoptiques (par exemple les dépressions, anticyclones...), du cycle diurne, de l'orographie, de la présence de nuages, etc... À l'inverse, les sillages d'éoliennes peuvent modifier localement la CLA : par exemple, la rotation causée par les éoliennes déplace des parcelles d'air avec différents niveaux de température et d'humidité et peut ainsi mener à la formation de nuages si certaines conditions sont réunies [10].

La CLA a depuis longtemps été étudiée par les scientifiques, en particulier pour la prédiction météorologique. Plus récemment, la communauté de l'éolien s'est intéressée à ce sujet pour mieux comprendre le comportement des éoliennes et de leurs sillages dans des conditions réalistes. Par exemple, il a été montré que les effets thermiques de la CLA influencent la dissipation des sillages [11], le cisaillement vertical près du sol modifie les performances des turbines [12] et qu'un terrain

complexe peut significativement changer le comportement des sillages [13]. De plus, les tourbillons de grande échelle présents dans la CLA induisent des déplacements instationnaires des sillages appelé méandrement [14]. Pour une éolienne en aval, ces mouvements de méandrement augmentent le niveau de turbulence et réduisent sa durée de vie. Ce dernier phénomène est au cœur des présents travaux de thèse.

Méthodes de prédiction de sillage

Selon les ressources à disposition et le niveau de fidélité visé, il existe de nombreuses techniques différentes pour étudier les sillages d'éoliennes, listées sur la Fig. 4. En mécanique des fluides comme dans toute science expérimentale, les raisonnements théoriques ne sont valides que si ils vérifient les mesures de terrain. De telles mesures, dites *in situ*, ou grandeur nature si elles sont faites sur des rotors de taille réaliste, sont donc considérées comme étant les méthodes les plus fiables. Ces mesures demandent d'instrumenter une éolienne réelle, c.-à-d. en acheter une ou avoir accès à un site industriel pour ajouter des instruments de mesure. Les conditions de fonctionnement de la turbine sont relevées grâce à un système SCADA (Supervisory Control And Data Acquisition). Les conditions de vent en amont et les forçages au sol peuvent être mesurés avec un unique mât météo si ils sont considérés homogènes spatialement. Toutefois, des technologies plus avancées tels que les LiDARs (Light Detection And Ranging) sont nécessaires pour mesurer les sillages qui sont non-homogènes. Les mesures *in situ* sont donc particulièrement chères et peu de turbines sont instrumentées dans le monde, que ce soit à l'échelle 1 [15, 16] ou à l'échelle réduite [17, 18, 19].

Bien qu'elles soient considérées comme le plus haut niveau de fiabilité, les expériences *in situ* sont limitées par les instruments de mesure. Les LiDARs tournants par exemple, mesurent le champ de vent instantané point par point, et donc atteindre une bonne résolution spatiale se fera au détriment de la résolution temporelle, et inversement. De plus, ces mesures ont une portée limitée et ne peuvent ainsi que mesurer le sillage proche des grandes turbines. Il est aussi possible d'utiliser des LiDARs scannants, qui peuvent mesurer à une plus grande distance, mais ne donnent des résultats que dans un plan. Toutefois, ces outils de mesures, et en particulier les données SCADA, sont potentiellement sujettes à des erreurs de mesure. Un autre problème avec les expériences *in situ* est qu'on ne contrôle pas les conditions de vent, ce qui rend difficile de mettre en place une étude de sensibilité basée sur de telles expériences.

Les mesures en souffleries sont une réponse à ces problèmes. Dans de telles expérimentations, une maquette d'éolienne à l'échelle réduite [20, 21] ou des disques poreux [22] est placée dans une section de test où un champ de vent est imposé. Un écoulement similaire à une CLA peut être reproduit avec une soufflerie appropriée [23], et on y maîtrise les conditions en amont, telles que la vitesse de vent, la turbulence, la rugosité de surface [24], l'orographie du terrain [25] ou même des effets thermiques [26, 27]. Les mesures en souffleries permettent également de contrôler les conditions d'opération des éoliennes [28] et d'utiliser des méthodes de mesures telles que la vélocimétrie par image de particules [29] où tout l'écoulement peut être mesuré. Il a été prouvé que de telles expériences permettent une représentation réaliste des sillages [30] et que les effets instationnaires comme le méandrement peuvent être mesurés [28]. Toutefois, générer des échelles temporelles et spatiales correctes comparées à la maquette d'éolienne utilisée peut se révéler difficile et les mesures en soufflerie nécessitent un budget conséquent car les souffleries sont coûteuses à construire et à utiliser. De plus, les effets thermiques jouent un rôle important dans le développement des sillages, et peu d'installations sont,

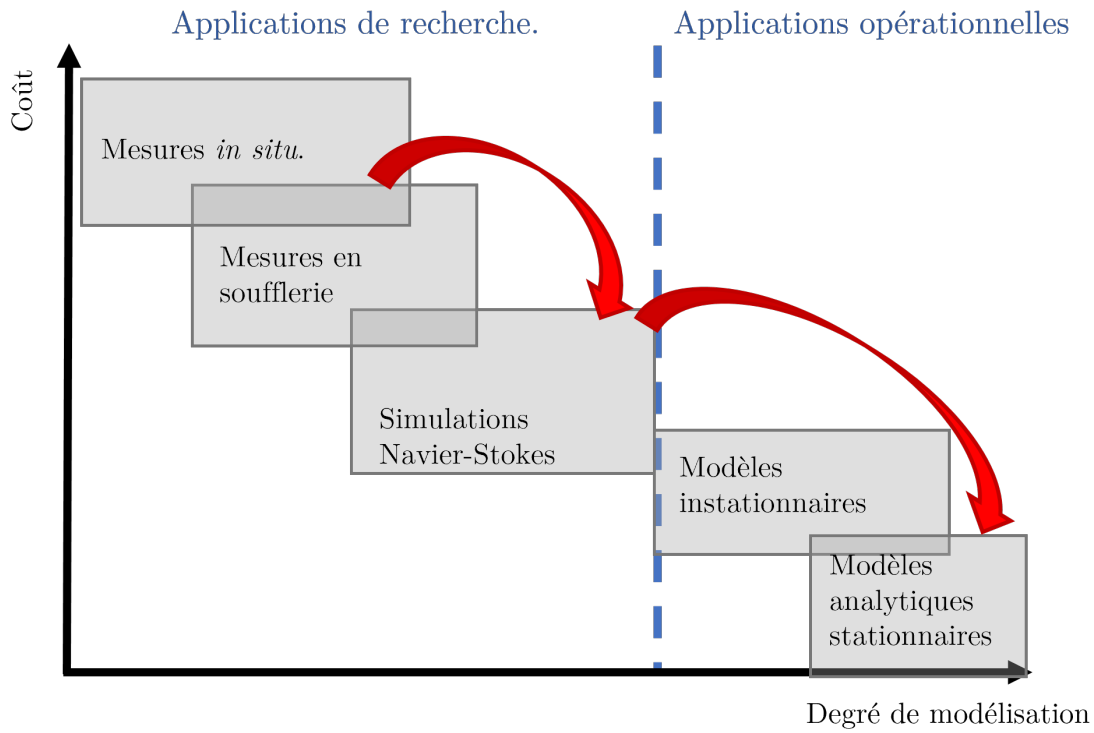

Figure 4: Coût de différentes méthodes existant pour estimer les sillages d'éoliennes, en fonction de leur degré de modélisation. Les échelles sont arbitraires, et les flèches rouges indiquent le cheminement effectué dans ce travail.

à ce jour, capables de les prendre en compte.

Les sillages d'éoliennes et la CLA évoluent en fonction des lois de la dynamique des fluides, aussi appelées équations de Navier-Stokes, et qui ne connaissent pas de solution analytique à l'heure actuelle. Avec le développement du calcul haute performance (HPC), il est devenu possible de résoudre numériquement ce système d'équations pour les éoliennes dans la CLA, en faisant certaines hypothèses sur la modélisation de la turbine et sur la turbulence de petite échelle. Dans ce travail, nous nous focalisons sur les Simulations des Grands Échelles (LES) qui sont les plus populaires à l'heure actuelle sur le sujet, bien que d'autres méthodes existent. Implémenter un solveur de Navier-Stokes n'est pas une tâche aisée, mais peut se révéler plus accessible pour beaucoup d'organismes de recherche que de mettre en place une installation de mesure, d'autant qu'on peut se baser sur une longue histoire de simulation numérique en mécanique des fluides. De plus, certains modèles sont open-source, et permettent donc à quiconque ayant les connaissances appropriées de mettre en place sa propre expérience numérique, tant qu'elle ou il a accès aux moyens de calcul adéquats.

Parmi les principaux modèles numériques, le 'Simulator fOr Wind Farm Application' (SOWFA), développé par le laboratoire national des énergies renouvelables (NREL) aux USA, est une extension de la librairie OpenFOAM qui prend en compte les sillages d'éolienne et les effets de CLA. Les chercheurs de l'institut ForWind en Allemagne ont eux choisi de partir d'un code développé pour des simulations de CLA appelé PALM [31] et d'y implémenter une paramétrisation pour modéliser les turbines [32]. C'est cette dernière approche qui a été choisie à l'IFPEN [10], en partant à la place

du code Meso-NH, développé par le Centre National de Recherches Météorologiques et le laboratoire d'Aérologie [33]. Comme pour les expériences en soufflerie, les conditions en amont de l'éolienne sont contrôlées, mais peuvent ici être modifiées simplement. Bien que les simulations numériques soient souvent utilisées comme résultats de référence en absence de données expérimentales, elles nécessitent toujours une dose de modélisation et d'approximation pour donner un résultat dans un temps raisonnable. Il en résulte que leur fiabilité est souvent considérée comme étant plus faible que celle des mesures. En effet, pour un problème donné, différents codes de calculs, ou deux paramétrisations différentes d'un même code peuvent donner des résultats significativement différents [19]. De plus, le coût de calcul est considérable : il faut des centaines de milliers d'heures CPU pour calculer un cas. Une étude de sensibilité peut donc être menée à bien en quelques jours avec un supercalculateur moderne, mais les simulations basées sur les équations de Navier-Stokes ne sont en général pas adaptées aux applications industrielles, où l'estimation et l'optimisation des performances d'un parc éolien nécessitent des centaines voir des milliers de cas et pour lesquelles l'utilisateur n'a de toute façon pas forcément accès à un supercalculateur.

Pour certaines applications, il est important de prendre en compte la dynamique des sillages tout en gardant un coût de calcul suffisamment bas pour pouvoir être utilisé par des industriels. Parmi ces applications, le contrôle des éoliennes permet d'optimiser la production et le chargement des pales, et le comportement aéro-élastique des très grands rotors doit être prévu avant qu'ils ne soient construits. En effet, les turbiniers prévoient de plus grands rotors d'années en année afin d'améliorer la rentabilité de l'énergie éolienne, mais aussi de réduire la quantité de CO_2 émis rapportée à l'énergie produite [34]: par exemple, l' HALIADE-14 MW développée par General Electrics avec ses pales de 107 mètres de long. L'aéro-élasticité de telles structures allongées, essentielle pour estimer et améliorer les durées de vie des pales, est encore un phénomène méconnu, et doit être étudié de manière instationnaire. Un autre exemple peut être trouvé du côté des turbines offshores, en particulier des projets d'éolien flottant, où on s'attend à ce que les phénomènes hydrodynamiques jouent un rôle important.

Les modèles instationnaires multiphysiques tels que DeepLinesWind^{TM}[35] ou Open.FAST [36] sont spécialement conçus pour répondre à ce type de besoin. Afin d'être utilisables dans un contexte industriel, ces codes de calculs se basent sur des modèles simplifiés. Typiquement, pour la partie aérodynamique, un vent amont turbulent peut être généré synthétiquement, et le sillage sera déduit par un modèle instationnaire, comme par exemple le modèle de Méandrement Dynamique de Sillage (DWM), qui a été spécifiquement développé pour modéliser le phénomène de méandrement [14]. Ce phénomène est particulièrement important pour les calculs aéro-élastiques d'une éolienne fonctionnant dans un sillage car il induit que cette éolienne peut successivement être à l'intérieur et à l'extérieur du sillage, ce qui amène des fluctuations de vitesse, et donc une fatigue des pales. Ces modèles sont appropriés pour des applications industrielles, car ils prennent en compte tous les phénomènes physiques d'intérêt pour une éolienne et leur coût de calcul est considérablement réduit par rapport à une simulation des équations de Navier-Stokes. Ce coût n'est toutefois pas négligeable, et l'utilisation de supercalculateurs peut se révéler nécessaire pour des études d'optimisation ou pour de grands parcs.

Pour concevoir un parc éolien à une localisation spécifique, toutes les vitesses et directions de vent potentielles doivent être étudiées, ainsi que différentes conditions atmosphériques. Un grand nombre de cas doit donc être étudié, en particulier si on cherche à optimiser l'agencement des éoliennes entre elles dans le parc pour diminuer les effets de sillage. Le coût de calcul des codes Navier-Stokes est bien trop élevé pour de telles applications, et même les codes multiphysiques instationnaires

peuvent se révéler trop lents. Les modèles analytiques statiques répondent à ce besoin : basés sur quelques formulations analytiques, ils peuvent produire des centaines de résultats dans un temps raisonnable, même avec un ordinateur de bureau, ce qui les rend très accessibles pour une utilisation industrielle. Ces modèles ne nécessitent pas d'entrée instationnaire et se basent plutôt sur des données atmosphériques moyennées dans le temps et sur le point de fonctionnement des turbines. Au-delà de leur rapidité, ces modèles sont aussi particulièrement faciles à utiliser, même pour quelqu'un dont la mécanique des fluides et les sillages n'est pas le cœur de métier. Toutefois, ils sont basés sur de nombreuses hypothèses, sont sensibles aux données de calibrations, et encore peu d'entre eux prennent en compte les effets de la CLA.

Cette liste n'est pas complète, mais on comprendra qu'il existe une grande diversité de méthodes pour estimer les effets de sillage, chacune ayant ses propres avantages, inconvénients, applications et coûts. Les modèles basse-fidélité sont utilisés dans l'industrie pour des applications en cas réel, mais sont basés sur des résultats obtenus avec des modèles de recherche, de plus haute fidélité mais également beaucoup plus coûteux. La calibration des différents modèles se fait donc de haut en bas dans la Fig. 4: les modèles d'ingénierie sont calibrés directement sur des résultats de mesures ou de codes haute-fidélité type Navier-Stokes, qui ont eux-mêmes été validés avec des mesures expérimentales.

Objectifs et résumé de la thèse

Les modèles dynamiques, en particulier le DWM, ont reçu beaucoup d'attention dans la communauté scientifique pour modéliser le phénomène du méandrement. En effet, une meilleure compréhension de ce phénomène a été identifiée comme un des verrous majeurs à étudier dans l'état de l'art actuel de l'aérodynamique de l'éolien [37]. Toutefois, la plupart des modèles statiques ne le prennent pas en compte, ou bien seulement comme un phénomène qui en moyenne augmente l'expansion du sillage. Cette démarche mélange l'expansion du sillage et le méandrement, ce qui rend le développement d'un modèle basé sur la physique plus difficile. Notre interprétation est que si la plupart des modèles de turbulence ajoutée dans le sillage sont empiriques, c'est à cause de cette non-différentiation entre les deux phénomènes.

L'objectif de cette thèse est de mieux comprendre les interactions entre la turbulence atmosphérique et les sillages d'éolienne avec une attention particulière portée au phénomène de méandrement. Ce travail peut se résumer par les flèches rouges dans la Fig. 4. Des mesures *in situ* de la littérature sont d'abord reproduites avec notre code LES Meso-NH pour valider sa capacité à modéliser les interactions CLA/sillages. En se basant sur une analyse physique des résultats LES, le méandrement est ensuite inclut indépendamment de l'expansion du sillage dans un modèle analytique pour la vitesse et la turbulence, qui peut être utilisé en stationnaire ou en instationnaire. Le travail présenté ici est donc séparé en trois parties :

La première partie est dédiée à l'état de l'art. Dans le chapitre 1, les phénomènes de la CLA susceptibles d'interagir avec les sillages d'éoliennes sont présentés, ainsi que les principaux modèles mathématiques pour les représenter. Dans le chapitre 2, les éoliennes sont rapidement décrites, puis une revue de la littérature sur les sillages d'éoliennes est présentée. Ce chapitre finit par une description des principaux modèles analytiques de sillage puis de ceux traitant du méandrement. Le

chapitre 3 commence en présentant les méthodes LESs. Ensuite, notre code LES Meso-NH est décrit, ainsi que de la méthode de ligne actuatrice (ALM), qui est utilisée pour représenter l'éolienne dans le code LES.

La deuxième partie se focalise sur les simulations haute-fidélité. Dans le chapitre 4, nous validons les capacités du couplage Meso-NH/ALM pour simuler un sillage réaliste dans différentes conditions atmosphériques. Le chapitre 5 se concentre sur le suivi de sillage, une étape de post-traitement où le centre de sillage est suivi à chaque pas de temps. C'est une étape nécessaire pour étudier le méandrement. En se basant sur les mêmes simulations, nous analysons dans le chapitre 6 l'influence des effets thermiques de la CLA sur les propriétés du sillage et sur le méandrement.

La troisième partie présente un raisonnement analytique qui mène à un modèle d'ingénierie. Dans le chapitre 7, nous démontrons que la vitesse de vent et la turbulence dans le sillage peuvent être décomposées en plusieurs termes qui dépendent de l'expansion de sillage, du méandrement, ou des deux. Cette analyse montre des hypothèses sous-jacentes à certains modèles de la littérature où plusieurs termes de la décomposition sont implicitement négligés. À l'aide de cette décomposition, nous proposons un modèle analytique pour la vitesse et la turbulence qui prend explicitement le méandrement en compte.

Part I

Part A - State of the art

Chapter 1

Turbulence in the atmospheric boundary layer

In this first chapter, we describe the atmospheric phenomena that are likely to modify the operating conditions and wakes of wind turbines. The general concept of turbulence in fluid dynamics is first introduced. The atmospheric boundary layer in which turbines are embedded is then detailed, with a focus on atmospheric stability and its consequences on the turbulence in this region of the atmosphere. Finally, the set of equations used in this work to study the atmosphere and its turbulence is written down and explained.

1.1 Turbulence

The mean wind alone is not sufficient to study the wake of a wind turbine, for two main reasons. First, the flow upstream of the turbine and in the wake is said to be turbulent: in this state, the variations of the wind velocity (called turbulence) induce changes of the mean state and must thus not be neglected. Secondly, turbulence leads to unsteady loadings on the wind turbine blades that reduce their lifespan, in particular if the turbine is working in waked conditions. For both reasons, it is essential to take turbulence into account when studying wind turbine wakes.

1.1.1 Definition of the velocities

For wind turbine aerodynamics, the most important variable is the wind speed, which will be referred to as "velocity" and written $\overrightarrow{U}$ in the present work. It is a vector in three dimensions whose norm is denoted U and its components U_x, U_y and U_z for the streamwise, lateral and vertical directions. When it is possible, the Cartesian coordinate system $(\overrightarrow{x}, \overrightarrow{y}, \overrightarrow{z})$ is aligned in order to have $\overrightarrow{x}$ colinear with the main wind direction.

The wind direction (measured in degrees) is written:

$$\beta = 270 - \tan^{-1}(U_y/U_x) \tag{1.1}$$

This definition allows yielding $\beta = 270°$ for a wind perfectly aligned with $\overrightarrow{x}$, as if it came from the west. Since this direction can vary over time and height, we also use U_H to define the horizontal wind component:

$$U_H = \sqrt{U_x^2 + U_y^2} \tag{1.2}$$

Finally, the concepts of shear and veer are used a lot in this work. Shear is a vertical gradient of horizontal velocity ($\partial U_H / \partial z$) and veer is a vertical gradient of wind direction ($\partial \beta / \partial z$).

1.1.2 Origin and definition of turbulence

Turbulence is everywhere in our daily life, from the smoke of a cigarette to the water in the rapids of a river. It refers to the state of the flow where a chaotic behaviour with seemingly random patterns appears. In the 16th century, Leonardo Da Vinci observed this phenomenon on a water cascade: "*Observe the motion of the surface of the water, which resembles that of hair, which has two motions, one is caused by the weight of the hair, the other by the direction of the curls. Thus, the water has eddying motions, one part of which is due to the principal current, the other to random and reverse motion*". He compares the turbulent flow to curled hair and introduces the decomposition of a turbulent velocity in a mean motion, due to the weight of the air and a turbulent motion, due to the curl of the air. The Reynolds decomposition, described in Sect. 1.1.3 and which is at the core of modern turbulence modelling, is based on a similar concept.

Turbulent motions only happen in certain conditions: if the mean motion is low or the viscosity of the fluid is high, only regular patterns are observed. This has been proven by the British physicist O. Reynolds in 1883 with his famous experiment: in a channel is flowing some fluid, for instance liquid water, and a pipe injects coloured ink which acts as a tracer (see Fig. 1.1). He observed that for a low flow rate, the ink keeps a regular pattern but if the flow rate is increased, this pattern becomes chaotic. Similar results arise when the diameter of the tube increases or the viscosity of the fluid decreases.

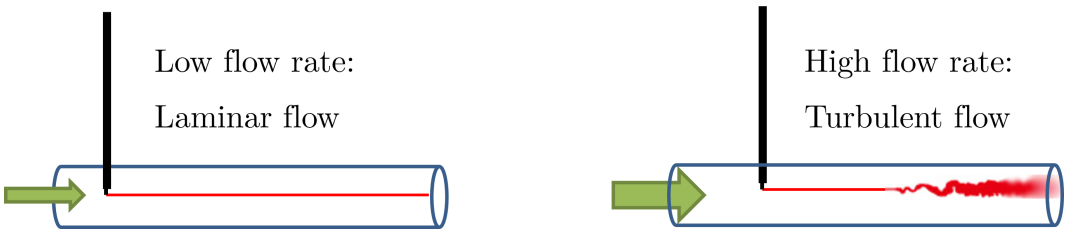

Figure 1.1: The Reynolds' experiment.

As a consequence, he introduced a dimensionless number, the Reynolds number:

$$Re = \frac{UL_c}{\nu} \tag{1.3}$$

where L_c is a characteristic length e.g. the channel diameter and ν is the kinematic viscosity of the fluid. Depending on the chosen length and velocity scales, the limit above which the flow transforms from laminar to turbulent is around $Re \approx 3000$. The frontier is not a sharp limit, but in the case

of the atmosphere, the Reynolds number is about 10^9 and above: in this work, only turbulent flows are studied.

The Reynolds experiment highlights the phenomenon of mechanically-created turbulence. Turbulent motions can also be created by heat, even if the flow velocity, and thus the Reynolds number, is low. An everyday life example is the smoke of a cigarette: after a few centimetres, the smoke will have the same shape as the turbulent flow in the Reynolds experiment even though the velocity is low. Turbulence can thus be generated either mechanically or thermally and is characterised by the following properties [38]:

- Three dimensional.
- Time dependent.
- Rotational.
- Random, chaotic.
- Enhances dissipation and diffusion.
- Intermittent in both space and time.
- Includes a large range of time and length scales.

The word 'random' must not be misunderstood. The trajectory of a fluid particle is always a deterministic phenomenon because it follows the deterministic equations of Navier-Stokes. However, at high Reynolds numbers, this system is said to be chaotic: its result is strongly dependent on the fluid properties as well as initial and boundary conditions. These conditions are never perfectly known: there are always at least infinitesimal variations of velocity, temperature, surface characteristics and so on. In the common language, chaotic behaviour is sometimes referred to as the butterfly effect: small perturbations such as the motions of a butterfly can lead to tremendous consequences such as a storm.

This is comparable to the toss of a coin: if one could perfectly know the force and angular momentum given by the thumb, the properties of the air and the surface properties of the coin and the table, flipping a coin would be an entirely deterministic process. Since no one can do that, the event {Coin is tail} is considered to be a random variable. Likewise, in a turbulent flow, the event $\{U = 10 \pm 1 \text{ m s}^{-1}\}$ is a deterministic event which we consider to be random because of our incapacity of knowing perfectly the state of the world.

1.1.3 The Reynolds decomposition

In fluid dynamics, the separation between the mean and the fluctuating values introduced by Leonardo Da Vinci is performed with the Reynolds decomposition. It can be applied to any variable ϕ (velocity, temperature, pressure...):

$$\phi = \overline{\phi} + \phi'. \qquad (1.4)$$

$$\overline{\phi(x,t)} = \frac{1}{N}\sum_{k=1}^{N}\phi_k(x,t) \qquad (1.5)$$

where the overline defines an ensemble average of N independent measures of ϕ, which supposedly depends on both time and space (Eq. 1.5) and the prime denotes the fluctuating motions. For any variables ϕ, ψ and s and constant K, the Reynolds decomposition verifies:

$$\overline{\phi'} = 0 \qquad \overline{\overline{\phi}} = \overline{\phi} \qquad \overline{K\phi} = K\overline{\phi}$$
$$\overline{\phi + \psi} = \overline{\phi} + \overline{\psi} \qquad \overline{\phi\psi} = \overline{\phi} \cdot \overline{\psi} + \overline{\phi'\psi'} \qquad \frac{\overline{\partial \phi}}{\partial s} = \frac{\partial \overline{\phi}}{\partial s}$$

The definition of the Reynolds average with an ensemble average is however complicated to use. In practice, it is assumed that the system is ergodic i.e. that the average behaviour of the system can be deduced from the trajectory of a typical point. Therefore, the ensemble average can be substituted with a time average. It is a strong assumption but it allows applying the Reynolds averaging and the subsequent turbulence theory with relatively simple samples such as a probe in a flowfield that measures a given time-dependent variable. As an illustration, Fig. 1.2a shows a typical turbulent velocity signal extracted from Meso-NH over 1800 seconds. The black lines in Figs. 1.2b and 1.2c are the mean and the fluctuating parts of this signal.

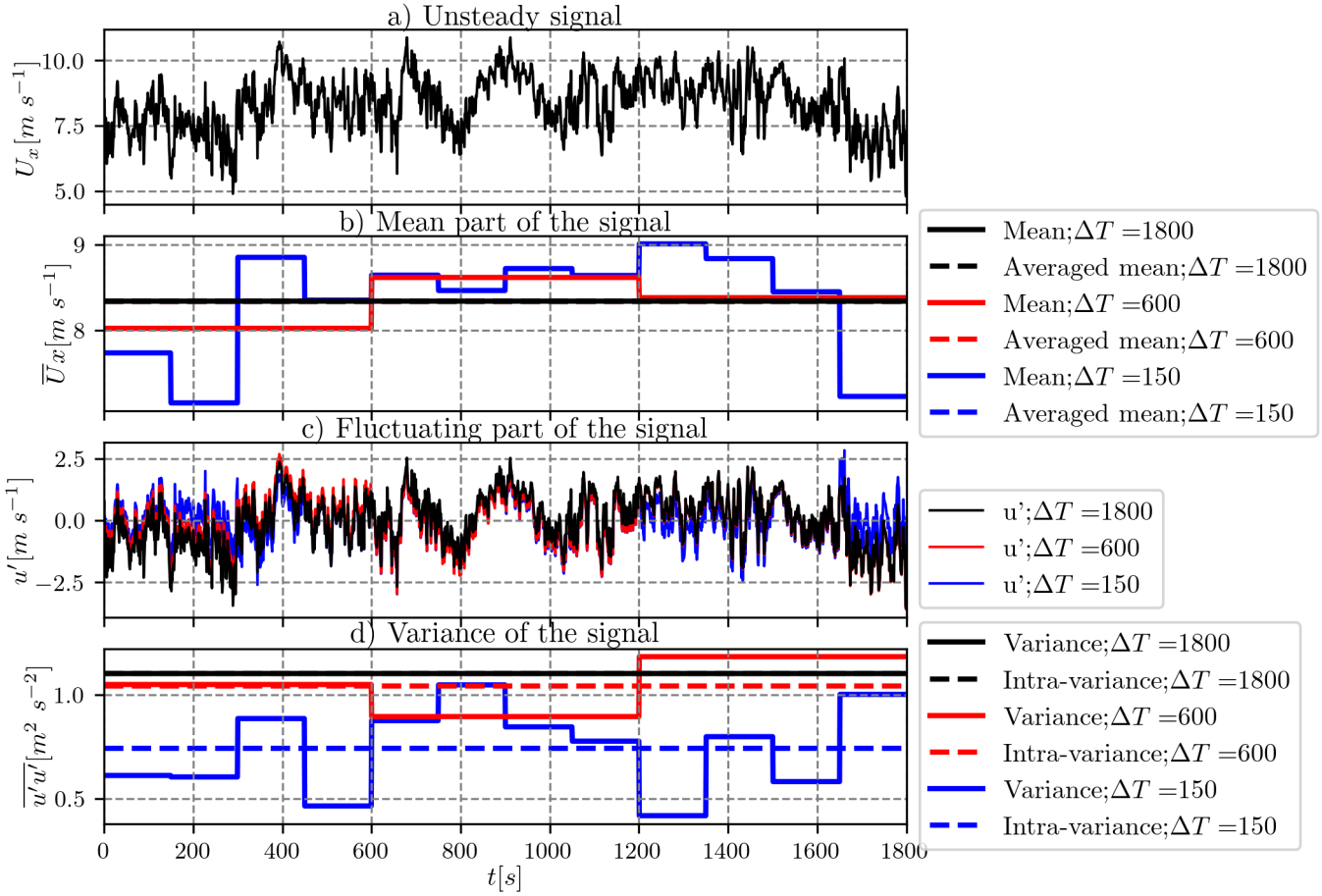

Figure 1.2: Reynolds decomposition applied to a time-dependent velocity signal, for different averaging periods.

When it comes to the norm of the velocity vector $\overline{U}$, it is common to compute the norm after applying the Reynolds averaging to each component:

$$\overline{U} = \sqrt{\overline{U}_x^2 + \overline{U}_y^2 + \overline{U}_z^2}. \tag{1.6}$$

1.1.4 Quantification of turbulence with second order moments

Turbulent kinetic energy

The turbulence is characterised by the varying part of the velocity field U'. However, it is not practical to study a raw time series, so the amount of turbulence is often measured with the turbulent kinetic energy (TKE), noted k and defined as:

$$k(x,y,z) = \frac{1}{2}\left(\overline{U_x'^2}(x,y,z) + \overline{U_y'^2}(x,y,z) + \overline{U_z'^2}(x,y,z)\right) \tag{1.7}$$

where $\overline{U_x'^2}$ is the variance of U_x with the Reynolds decomposition notation. In this work, the notations $u' = U_x'$, $v' = U_y'$ and $w' = U_z'$ are used for conciseness. The components of the TKE are also written $k_x = \overline{u'^2}$, $k_y = \overline{v'^2}$ and $k_z = \overline{w'^2}$.

Turbulence intensity

The unit of k is $m^2\ s^{-2}$, and it scales with the square of the mean velocity. In wind energy science, it is common to use the non-dimensional form of TKE, called turbulence intensity and abbreviated TI. In the streamwise direction, it gives:

$$I_x(x,y,z) = \frac{\sqrt{k_x}(x,y,z)}{\overline{U}} \tag{1.8}$$

Similarly, the lateral (I_y) and vertical (I_z) TI can be defined from k_y and k_z as well as a total TI I, from the TKE k. The scaling velocity $\overline{U}$ can be taken as a reference value (in wind energy, the velocity upstream the turbine at hub height $\overline{U}_h$ is a common choice) to simply scale the TKE without modifying the shape of the field. The scaling velocity can also be computed locally i.e. at the same position as k: therefore, it quantifies at a given location the amount of variations compared to the mean value. It can be compared to a noise-to-signal ratio used in signal processing, even though turbulence is not a noise. If this local scaling is used, the TI will be noted I^l and called 'local TI'.

The TKE cannot perfectly describe the fluctuating part of a turbulent field since a given TKE value can lead to an infinite number of different time series. Higher-order statistics such as skewness or kurtosis can help refine the description of U' but are not used in this work. A more advanced approach called spectral analysis is presented in Sect. 1.1.6.

Other turbulent fluxes

The variances k_x, k_y and k_z are particular cases of second-order mixed moments that are called turbulent fluxes and that take the form: $\overline{\phi'\psi'}$ with $\phi', \psi' \in \{u', v', w', \theta_v', q_T'\}$ (see Sect. 1.3 for the

definition of θ_v and q_T). These can be viewed as covariances between the different thermodynamic variables, or the variances if $\phi = \psi$.

We also define the friction velocity u_* to give a scale of the shear at the ground. It is used to scale the velocity profile near the ground (cf Eq. 1.24). Subscript $|_s$ denotes a value taken near the ground.

$$u_*^2 = \sqrt{\overline{u'w'}|_s^2 + \overline{v'w'}|_s^2} \tag{1.9}$$

1.1.5 The different scales of turbulence

As explained above, the ergodicity of the flow is assumed to substitute the ensemble averaging with a time averaging in the Reynolds decomposition. This simplifies a lot the computation of mean and fluctuating parts of the variables, but by doing so, one must be careful with the data sampling. If a signal is sampled at frequency f_s over a time-period ΔT, it will be blind to variations occurring at $f > f_s$ and $f < 1/\Delta T$. In fluid dynamics, intercomparisons are often used, between numerical codes, wind tunnel data or field measurements but due to different practices, these datasets might not be sampled similarly, leading to differences.

This is illustrated in Fig. 1.2: for a given unsteady signal sampled at $f_s = 1$ Hz (Fig. 1.2a), the mean value can be either directly computed over the 1800 seconds (black continuous line in Fig. 1.2b), or the segment can be decomposed into a number of sub-segments, for instance of $\Delta T = 600$ s in red continuous lines and $\Delta T = 150$ s in blue continuous lines. Computing the ensemble average of the mean value over all the segments leads to the same value, whatever the number of segments (dashed lines in Fig. 1.2b are all superimposed). The decomposition into sub-segments has no impact on the mean value.

In Fig. 1.2c, the fluctuating part of the velocity segments is plotted for each approach. The average of the plotted lines is always 0 over each sub-segment. Since there are more sub-segments for the blue line, it includes fewer large-scale modifications than the black curve. The largest differences arise when there are large differences between the mean values, for instance between $t = 1650$ s and $t = 1800$ s. The variances can then be computed on each segment, and are plotted in continuous lines in Fig. 1.2d. The ensemble average of the variances over all the segments (dashed lines) is dependent on ΔT, and leads to significant differences between the blue and black cases.

This mean of the variances over different segments is called the intra-variance and relates to the small-scale variations. To reconstitute the total variance of a large segment from many small segments, one needs to also take into account the inter-variance which is the variance of the segments' means i.e. the large-scale variations. The total variance writes [39]:

$$\overline{\phi'^2} = \frac{1}{N} \sum_{i=1}^{M} n_i \left(\overline{\phi_i'^2} + \left(\overline{\phi_i} - \overline{\phi} \right)^2 \right). \tag{1.10}$$

where M is the number of segments with n_i samples each (total of N samples). The first term of the sum is the intra-variance and the second term is the inter-variance. Studying only the intra-variance can make sense depending on the study, but one must be aware that large-scale variations are missing. To compare two datasets, it is thus essential to be sure that the sampling frequency and time of acquisition are identical.

Clouds are natural depictions of turbulence and can be used to illustrate these different scales of turbulence. The cumulus of Fig. 1.3 seems to be composed of many curled and independent parts, three of which have been highlighted in colours. If we zoom for instance on the orange structure, we could again define some new, smaller structures, and we could again zoom on one, differentiate many other structures and so on. These structures also called 'eddies', can be seen on measurements done by a probe and would give a result similar to Fig. 1.2a. Measuring the whole cloud at once would give a variance similar to the black curve in Fig. 1.2d, measuring independently the largest eddies would be similar to the red curve and measuring all the small eddies one by one would result in something similar to the blue line.

Figure 1.3: A cumulus highlighting the different structures of turbulence. Photographer: Dimitri Svetsikas.

As eddies get smaller and smaller, the effect of viscosity becomes more and more important. When they reach their smallest possible scale, called the Kolmogorov or dissipation scale η, eddies dissipate into heat due to viscosity. If Λ is the scale of the largest eddy (called integral scale) and Re_Λ the associated Reynolds number, the largest and smallest scales are related by: $\Lambda/\eta \sim Re_\Lambda^{3/4}$. Due to the large Reynolds number at stake, the difference between the largest and smallest eddies in the atmosphere is large as well.

1.1.6 Spectral analysis

An eddy's size can be characterised by its wavelength λ and by its frequency $f = \overline{U_x}/\lambda$. A convenient tool to study all these scales of turbulence is the cross power spectral density $S_{\phi\psi}(f)$, which is the Fourier transform of the temporal cross-correlation $R_{\phi\psi}(\tau)$, itself defined for any couple of signals $(\phi(t), \psi(t))$ as a function of the lag τ:

$$R_{\phi\psi}(\tau) = \int_0^\infty \phi'(t)\psi'(t-\tau)dt. \tag{1.11}$$

If $\psi = \phi$ we will simply call it power spectral density (PSD) or spectrum. The Taylor hypothesis considers that the turbulence is 'frozen' and allows relating the spectrum in frequency to a spectrum in wavenumber $\Phi = f/\overline{U_x}$. The spectrum of the signal at wavenumber Φ (or frequency f) indicates the energy carried by the eddies of size $2\pi/\Phi$. Consequently, the integral of the spectrum over all wavelengths is equal to the total TKE and the TKE of a signal sampled at an infinite wavenumber over a distance $2\pi/\Phi_0$ will be:

$$k_{\Phi>\Phi_0} = \int_{\Phi_0}^{\infty} S_{uu}(\Phi) d\Phi \tag{1.12}$$

In absence of thermal effects, the longitudinal velocity spectrum near the ground can be decomposed into several regions, theoretically developed and then validated from *in situ* data [40]. At the highest frequencies, the spectrum is written:

$$S_{uu}(f) = C_1 U^{2/3} \epsilon_D^{2/3} f^{-5/3} \tag{1.13}$$

where C_1 is a constant and ϵ_D is the dissipation rate of turbulence (that will be defined in Eq. 1.42). This range is known as the Richardson-Kolmogorov cascade or inertial range. In this region, the turbulence is supposedly isotropic ($S_{uu} = S_{vv} = S_{ww}$) and the largest eddies feed on the smaller ones, which are themselves feeding smaller eddies and so on until the Kolmogorov length scale is reached, where dissipation of eddies by friction becomes predominant [41]. This turbulence cascade is thus valid between the Kolmogorov length scale $\eta = (\nu^3/\epsilon_D)^{1/4}$ and the integral length scale Λ, defined as the length of the largest horizontal eddy. The value of Λ can be defined analytically, or by integrating the autocorrelation of the velocity variation (see the next paragraph).

Length scales larger than Λ (i.e. wavenumbers below k_Λ), are referred to in the literature as the 'energy-containing range'. The following relation is verified [40]:

$$S_{uu}(f) \propto u_*^2 \tag{1.14}$$

Note that Eq. 1.14 implies that there is no dependency of S_{uu} on f in the energy-containing range. Near the ground, a transition region can be defined between the inertial range and the energy-containing range where [40, 42]:

$$S_{uu}(f) \propto u_*^2 f^{-1} \tag{1.15}$$

For the vertical variance, the spectrum can be separated into two regions. In the inertial range, the turbulence has been supposed to be isotropic, leading to $S_{ww} = S_{uu}$. For lower wavenumbers, the following relation is proposed in the literature [40]:

$$S_{ww} = C_\lambda u_*^2 z/\overline{U_x} \tag{1.16}$$

Note that this latter relation predicts a vertical velocity spectrum independent of the frequency. One should keep in mind that these laws have been derived for canonical isotropic turbulence with no external forcings. For instance, the region inertial range is based on free-decaying turbulence and isotropic turbulence assumptions. On one hand, the energy is only transferred from the large scales

to the smaller scales (forward scatter). If this assumption is assumed to be globally accurate, there are pieces of evidence of the existence of local backscattering of turbulence, i.e. transfer of energy from the small scales to the large scales. On the other hand, the presence of the ground suppresses the isotropic turbulence assumption.

Spatial correlation and eddy size

Another method to determine the size of the eddies in the flow is to compute the spatial correlation which is similarly defined as in Eq. 1.11, but with a spatial displacement instead of temporal lag. The displacement is defined in two dimensions and can be related to the temporal lag through the frozen turbulence hypothesis $\tau_x = \tau/\overline{U}_x$ and $\tau_y = \tau/\overline{U}_y$. The 2D correlation function writes:

$$\rho_{\phi\psi}(\tau_x, \tau_y) = \frac{R\phi\psi(\tau_x, \tau_y)}{\sqrt{R\phi\phi(0,0)R\psi\psi(0,0)}} \tag{1.17}$$

The largest eddies of the flow, also called integral length scale Λ_{u_i,x_j}, is the length scale of fluctuations of the u_i velocity component in the x_j direction:

$$\Lambda_{u_i,x} = \int_0^{\tau_0} \rho_{ii}(\tau_x, 0) d\tau_x \tag{1.18}$$

$$\Lambda_{u_i,y} = \int_0^{\tau_0} \rho_{ii}(0, \tau_y) d\tau_y \tag{1.19}$$

Where τ_0 is the first zero-crossing value of the correlation function. The streamwise eddies take the shape of elongated streaks: $\Lambda_{u_i,x} >> \Lambda_{u_i,y}$ [43]. With the Taylor's frozen hypothesis, the integral time scale can be retrieved: $\mathcal{T}_{x_j} = \Lambda_{u_i,x_j}\overline{U}_i$.

Conversely, Λ_{u_i,x_j} can be computed from the integral time scale and the frozen turbulence hypothesis:

$$\Lambda_{u_i,x_j} = \frac{\mathcal{T}_{x_j}}{U_i} = \frac{1}{U_i}\int_0^{\tau_0} \rho_{ii}(\tau) d\tau \tag{1.20}$$

Note that the spanwise integral length scale $\Lambda_{u_i,y}$ is not defined if $\overline{U}_y = 0$ as it is often the case when the coordinate x is aligned with the main wind direction. This highlights a limit of the frozen turbulence hypothesis.

1.2 The atmospheric boundary layer

In the precedent section, the general concept of turbulence has been introduced. Depending on the state of the atmosphere, the nature of the mean flow and of the turbulence changes and the turbine's operating conditions with them. The present section focuses on the atmospheric phenomena that are likely to modify a wind turbine's operating condition and wake.

1.2.1 The Earth's atmosphere

The atmosphere is the gaseous layer that surrounds a celestial body such as the Earth, Mars or Venus. In the case of the Earth, its thickness varies between 350 and 800 km. Compared to the

Earth's radius of about 6000 km, it is a thin layer around the planet, especially when acknowledging that 99% of the atmosphere's mass lies below 30 km, due to the decrease of density with height. The Earth's atmosphere is decomposed into layers, characterised by their temperature profile (see Fig. 1.4)[44]:

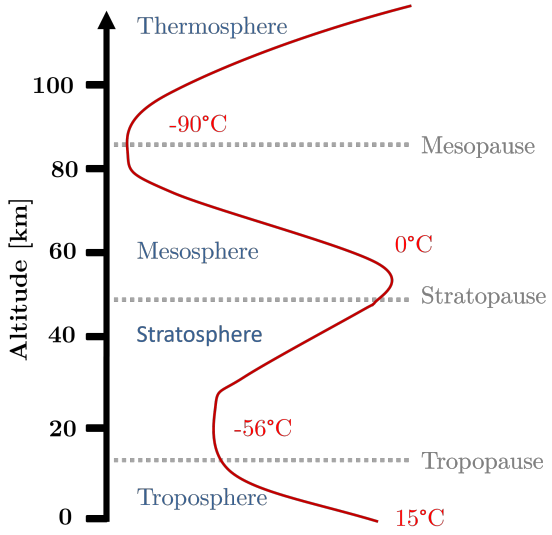

Figure 1.4: The different layers of the terrestrial atmosphere, replotted from [44].

- **The thermosphere** is the top layer of the atmosphere. There, the temperature increases up to 2500 °C but it would not feel warm for a human or a classical thermometer because temperature as we know it is ill-defined due to the very low density. At around 600 km, the thermosphere gradually becomes the exosphere, where the last Earth's particles are no longer retained by gravitational forces. The International Space Station orbits around the Earth in the thermosphere at 400 km. At 100 km lays the Karman line, which is a legal boundary between Earth's atmosphere and outer space. Most of the polar lights arise at the bottom of the thermosphere.

- **The mesosphere** is the third highest layer. It extends from around 50 km to around 85 km and the temperature decreases with height. It is the layer where meteors self-destroy.

- **The stratosphere** lays below the mesosphere and down to a few kilometres. This layer absorbs the ultraviolet radiation emitted by the sun which leads to an increase in temperature with height.

- **The troposphere** is the closest to the ground, where the temperature decreases regularly with height. Its thickness depends on the latitude and meteorological situation: between 6 km at the poles and 18 km at the equator. Consequently, it comprises all the Earth orography (Everest mount is 8849 m high) and most of the atmospheric phenomena. The work herein is restrained to this layer.

The atmospheric boundary layer (ABL) is the region of the troposphere directly in contact with the ground. There is a weak analogy between the ABL and the usual boundary layer definition

in fluid mechanics as the region directly in contact with the ground, where the velocity goes from 0 m s^{-1} at the surface to the free-stream value at the top of the boundary layer. The boundary layer height is often defined as the height where 99 % of the free-stream velocity is reached.

Contrarily to a classic boundary layer, neither the temperature nor the velocity in the atmosphere reaches a constant state with height, as shown in Fig. 1.4. Instead of a threshold that would never be reached, the ABL is thus defined as the region of the troposphere *which is directly influenced by the presence of the earth's surface, and which responds to surface forcings with a time scale of about an hour or less* [45]. These forcings can be friction at the ground, heat exchange (radiation, convection), evaporation, etc...

Potential temperature

As the altitude increases, the pressure decreases as well as the temperature. To take this dependency into account and have consistent profiles of temperature over hundreds of metres, boundary layer meteorologists use the potential temperature θ instead of the absolute temperature T:

$$\theta = \frac{T}{\Pi} \qquad \Pi = \left(P/P_{1b}\right)^{R_d/C_{pd}} \qquad R_d/C_{pd} = 0.286 \tag{1.21}$$

where Π is the Exner function, derived from the pressure P and $P_{1b} = 1$ bar, R_d is the gas constant for dry air and C_{pd} the specific heat of the air for dry air.

1.2.2 The different regimes of the ABL

The ABL thickness, or depth, z_i is fluctuating with time and space, ranging from hundreds of meters to a few kilometres. The region of the troposphere above the ABL is called the free atmosphere. The diurnal cycle can be observed in measurements of velocity or temperature in the ABL but not so clearly in the free atmosphere. Even though the whole troposphere reacts to ground forcings, it does so with a slower time response hence the ABL definition given in Sect. 1.2.1. Depending on both the diurnal cycle and synoptic forcing (i.e. of scales larger than 1000 km as low-pressure areas and anticyclones), the ABL can take two main forms:

- When the bottom of the ABL is hotter than the top, the ABL becomes a convective boundary layer (CBL) . This typically occurs during the day: the sun heats the ground which itself conducts the heat to the first layers of air. Due to this heating, the parcels of air are dilated and progressively elevate since low-density fluid goes up and high-density fluid goes down. It leads to large vertical motions that are called thermals. Typically, the plume of a chimney in a CBL will be looping up and down due to these vertical motions (see Fig. 1.5a). The thermals rise higher and higher during the day, leading to fairly large values of z_i. This regime is characterised by a large amount of turbulence which is mostly thermally created. Since turbulence enhances mixing, it results in a near-constant velocity magnitude, direction and temperature in the middle of the CBL (see Fig. 1.6a) hence called the mixed layer. The velocity magnitude in the mixed layer is below the geostrophic wind, (i.e. the velocity in the free atmosphere). On the top of the CBL, a region of strong gradients called the entrainment zone or inversion zone delimits the ABL from the free atmosphere.

(a) Vertical motions of the plume of a chimney typical of CBL. Photographer: Elīna Arāja, free licence of Pexels.com.

(b) The SBL traps the pollution emitted by a chimney in the Arve valley. Photographer: L. Cousin.

Figure 1.5: Visualisations of different ABL states

- On the opposite, when the bottom of the ABL is colder than the top, the ABL is called the stable boundary layer (SBL) . This typically happens during the night when the Earth's surface is cooling down through infrared radiation. In this configuration, any air parcel that moves vertically will tend to return to its initial position. This stratification prevents any mixing: for instance, pollutants are trapped close to the ground as in Fig. 1.5b. In this case, z_i is lower than in CBL case. The SBL is a region of low turbulence and strong veer and shear (see Fig. 1.6b), resulting sometimes in a velocity magnitude higher than the geostrophic wind on the top of the layer. This phenomenon is called a low-level jet. The SBL does not fully replace the mixed layer in one night: a residual layer stands on top of the CBL, which is characterised by a near-neutral temperature profile and a velocity that goes back to the geostrophic value.

Due to the relatively large heat capacity of water, the diurnal variations over the ocean are less pronounced than above the ground. Most changes in ABL depth above the ocean are due to synoptic mesoscale processes and this depth is kept around $z_i = 1$ km.

In any conditions, the region at the bottom of the ABL is called Surface Layer (SL), and is defined as the region where turbulent fluxes and stresses vary by less than 10% [45]. In the surface layer, the velocity and temperature profiles can be approximated by canonical expressions (see Sect. 1.2.3). The surface layer height is often around 10% of the ABL height.

1.2.3 Characterisation of the atmospheric stability

In the preceding definitions, stability refers to the potential temperature gradient in the ABL, sometimes called lapse rate. If θ increases with height, the conditions are said to be stable, unstable if it decreases with height and neutral if it is invariant. This definition is not always satisfying however: in the CBL for instance, the temperature profile is constant with height because of turbulent mixing, even though the ABL is unstable. The local lapse rate alone does not indicate the nature of the ABL. From the turbulent flux of temperature at the ground, which is however harder to measure, a non-local definition of stability can be set up:

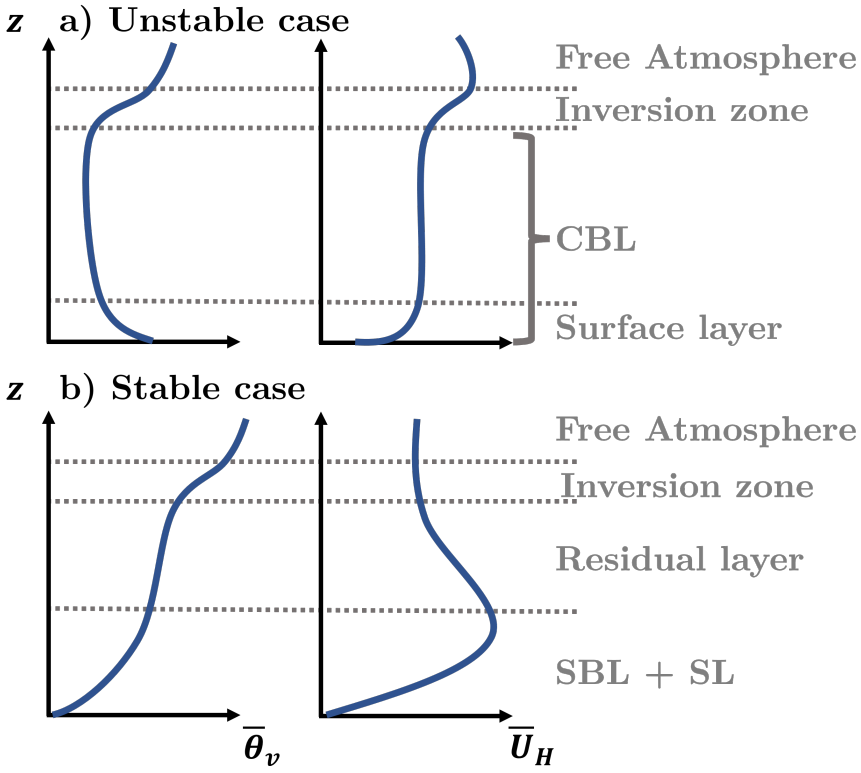

Figure 1.6: Typical profiles of mean virtual potential temperature θ_v and mean horizontal velocity for **a)** a CBL and **b)** a SBL. Inspired from [45].

- If $\overline{w'\theta'}|_s > 0$, the ABL is unstable.
- If $\overline{w'\theta'}|_s < 0$, the ABL is stable.

The vertical turbulent heat flux $\overline{w'\theta'}$ is never exactly equal to zero, however in some cases, the heat-generated turbulence is negligible compared to the friction-generated turbulence and the atmosphere is said to be neutral. In reality, it is a transitory case and the atmosphere never stays exactly neutral.

These are the static definitions of stability: they do not take shear into account. In some statically stable cases, the atmosphere can become unstable due to Kelvin-Helmholtz's instabilities and is then called dynamically unstable. Conversely, a statically unstable atmosphere will always be dynamically unstable.

Static stability can be characterised with the Monin-Obukhov length defined in Eq. 1.22, where $\kappa = 0.4$ is the Kolmogorov constant and g is the gravity constant. A physical interpretation of this length scale is that it is proportional to the height at which buoyant effects start to overcome the mechanical production of turbulence due to shear at the ground. If $L_{MO} > 0$, the atmosphere is statically stable and as $L_{MO} \to 0^+$, the region of damped turbulence approaches the ground. If $L_{MO} < 0$, it is unstable: buoyant effects overcome mechanical effects in the whole air column. In a neutral ABL, $L_{MO} \to \infty$ because buoyant effects never overcome shear effects. More often, the stability parameter, defined in Eq. 1.23, is used.

$$L_{MO} = -\frac{\overline{\theta} u_*^3}{\kappa g (\overline{w'\theta'})_s} \qquad (1.22) \qquad\qquad \zeta = z/L_{MO} \qquad (1.23)$$

The Monin-Obukhov similarity theory

In the SL, the velocity profile has a behaviour similar to the one of a classical boundary layer flow. Indeed, velocity must go from 0 m s^{-1} at the ground interface (no-slip condition) to its free flow value, or more exactly in our case to the ABL profile described in Fig. 1.6. This transition is achieved within a few metres, which results in a large shear. In this region, the so-called Monin-Obukhov similarity theory can lead to an expression of the velocity profile as a logarithmic function of the altitude z:

$$\overline{U}_H(z) = \frac{u_*}{\kappa} \ln\left(\frac{z}{z_0}\right) \qquad (1.24)$$

where the roughness length z_0 is a measure of the ground irregularity. The Monin Obukhov similarity theory extends this definition for the cases of convective and stable SL. Field experiments gave a relationship between wind shear and the stability coefficient [46], which once integrated led to:

$$\overline{U}_H(z) = \frac{u_*}{\kappa}\left[\ln\left(\frac{z}{z_0}\right) + \psi_M(\zeta)\right] \qquad (1.25)$$

with ψ_M a function of the stability coefficient and whose expression depends on the stability regime:

$$\psi_M = \begin{cases} 4.7\zeta & \text{if } \zeta > 0 \text{ (unstable)} \\ -2\ln\left[\frac{(1+x_M)}{2}\right] - \ln\left[\frac{(1+x_M^2)}{2}\right] + 2\tan^{-1}(x_M) - \frac{\pi}{2} & \text{if } \zeta < 0 \text{ (stable).} \end{cases} \qquad (1.26)$$

Where $x_M = [1-(15\zeta)]^{1/4}$ in the second equation. In both cases, the limit $\zeta \to 0$ takes the expression back to the neutral case i.e. Eq. 1.24. The impact of u_*, z_0 and L_{MO} on the theoretical logarithmic velocity profile is schemed in both linear (Fig. 1.7a) and semi-logarithmic (Fig. 1.7b) scales. The relationship between wind shear and stability coefficients that are used to deduce Eqs. 1.26 is issued from measurements on flat terrains: it typically fails when applied to complex terrain, ground with vegetation or strongly stable ABLs. [47].

1.2.4 Turbulence spectra in the ABL

Very large turbulent structures

The spectral behaviour of turbulence presented in Sect. 1.1.6 is for a canonical spectrum of turbulence. In the case of the ABL turbulence, one may need to define the variations at very high wavenumbers. Indeed, beyond the energy-containing range, the mesoscale quasi-2D motions lead to a region where the spectral energy decreases as frequency increases. This region is not considered as 'boundary layer turbulence' and has been less studied in the literature, but theory and measurements suggest a spectrum of the form [42]:

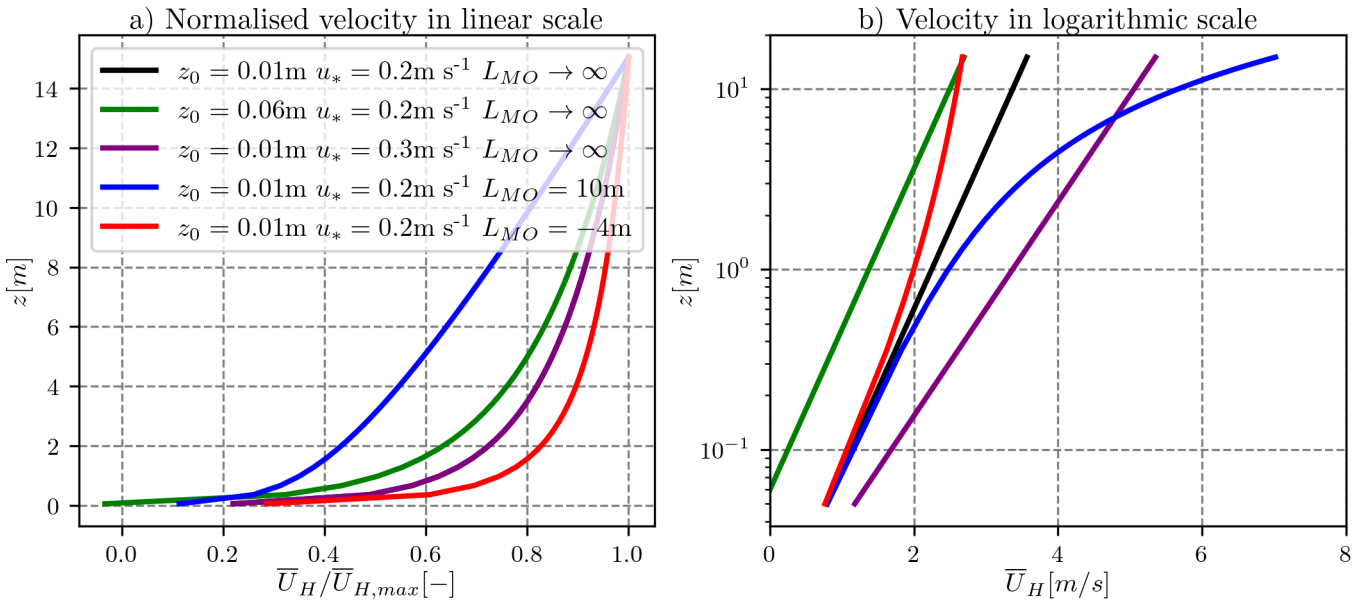

Figure 1.7: The impact of the different parameters on the theoretical velocity profile in the SL.

$$S_{uu}(f) = C_{a1} f^{-5/3} + C_{a2} f^{-3} \tag{1.27}$$

It is separated from the energy-containing range by a 'spectral gap' i.e. a region of low energy levels [48, 49]. Measurements show that this gap decreases as the height increases, reaching a plateau at about 80 metres and that in the inertial range, the turbulence level decreases with increasing height [42].

Impact of stability

Moreover, the spectral characteristics developed in Sect. 1.1.6 are for mechanically-generated turbulence, i.e. a neutral ABL. In unstable conditions, the different regions presented for the neutral ABL case do not change fundamentally. In the inertial range, there is still a collapse of the three velocity components' spectra to the same $-5/3$ slope. Most of the differences are seen in the energy-containing range, especially for the vertical component: when the stability parameter ζ increases, the level of energy in the low-frequency region increases. This was already measured by the pioneering work of Kaimal [50] and leads to larger values of Λ.

In a stably stratified ABL, a new anisotropic region appears inside the inertial range, called the buoyant subrange. Early studies [51] suggested a dependency of $k^{-11/5}$ in this region. A more recent work [47] based on new length scales (Ozmidov, buoyancy and vertical length scales) has shown that a more complex behaviour can be expected from the stably stratified turbulence spectra. This is not detailed herein because it is out of the scope of this thesis and because the behaviour of this new region is not perfectly known yet. One must retain that in a stably stratified boundary layer, the turbulence becomes anisotropic, the inertial subrange is modified and the relation between S_{uu} and f becomes dependent on stability. Moreover, the low-frequency region of the spectra is damped, leading to smaller values of Λ.

Simplified model

To estimate the nature of the loading experienced by a wind turbine when no measure is available, a generic form of the ABL spectrum called the Kaimal model [50] has been adopted in the IEC 61400-1 [52], which is a reference standard for many wind energy studies:

$$\frac{fS_{ii}(f)}{\overline{u_i'^2}} = \frac{4fL_i/U_h}{(1+6fL_i/U_h)^{5/3}} \tag{1.28}$$

where i is the velocity component index and $L_i = K_i \Lambda_{u_i,x}$ is the corresponding integral scale parameter, and K_i is a constant. U_h is the mean velocity at the height of the wind turbine's hub. If these parameters are not known, the standard also proposes generic values for them.

1.3 System of equations

In this section, the Boussinesq system is presented. It is a set of equations that are commonly used to describe the dynamics of the ABL, and that will be numerically solved in our high-fidelity code. These equations are a modified form of the incompressible Navier-Stokes equations, with additional equations for temperature and moisture. Most of this section is extracted from [45], and the reader can refer to this book for a more comprehensive description.

1.3.1 Additional definitions

Humidity variables

The total specific humidity of the air, written q_T, is the mass of water in all phases per unit of moist air. It is not used in this thesis but is introduced here since it takes an important place in Meso-NH (even though it can be deactivated).

When humidity is taken into account in the equations, the potential temperature is replaced by the virtual potential temperature which corresponds to the temperature a mass of dry air must reach to obtain the same density as the same mass of wet air. For unsaturated air, i.e. in clear sky conditions, it writes:

$$\theta_v = \theta\,(1 + 0.61 r_m)\,. \tag{1.29}$$

where r_m is the water mixing ratio: the mass of water divided by the mass of dry air in for given air parcel.

Reference state

We will refer in the following parts to a 'reference state' which corresponds to an atmosphere with no wind ($\overrightarrow{U} = \overrightarrow{0}$), adiabatic (no heat transfer outside of the domain), barotrope (density solely depends on the pressure), stationary ($\partial/\partial t = 0$), dry ($q_T = 0$), and in hydrostatic equilibrium

($\partial P/\partial z = -\rho g$). Any variable ϕ can then be defined as the sum of a profile in this state of reference and a variation from this profile $\phi(x, y, z, t) = \phi_r(z) + \phi^v(x, y, z, t)$.

Einstein notation

To improve the clarity of the equations, the Einstein notation will be used. Indice i stands for the i-th component of the velocity vector, whereas the repetition of the other indices stands for a summation. Hence for any field ϕ, a divergence is written $\partial\phi_j/\partial x_j$, and a gradient $\partial\phi/\partial x_i$. δ_{ij} is the Kronecker symbol: it equals 1 if $i = j$ and 0 if not. Finally, the i-th component of a vectorial product is written with the Levi-Civita ϵ_{ijk} symbol: $\overrightarrow{\phi} \wedge \overrightarrow{\psi} = \epsilon_{ijk}\phi_j\psi_k$.

Miscellaneous

The vector of the Earth rotation is written $\overrightarrow{\Omega_E}$, and its magnitude is $\Omega_E = 2\pi$ rad/24 hours $\approx 7.27 \cdot 10^{-4}$ s^{-1}.

The gravitational acceleration is written $\overrightarrow{g}$ and its magnitude is taken as $g = 9.81$ m s^{-2}.

1.3.2 Simplifying hypotheses

Reference frame

The terrestrial frame of reference is not Galilean because of Earth's rotation: the centripetal and Coriolis forces should in theory be taken into account. However, in the scope of this thesis, we will only consider relatively small domains compared to the radius of the Earth: several kilometres in every direction at most. As a consequence, the reference frame can be considered Galilean, a Cartesian coordinate system can be used, the centripetal force is included in the gravitational acceleration $\overrightarrow{g}$ and the Earth's curvature is neglected. This last assumption allows simplifying the Coriolis force by introducing $F_c = 2\Omega_E \sin(\phi_l)$ where ϕ_l is the latitude:

$$\overrightarrow{F}_{Coriolis} = -2\overrightarrow{\Omega_E} \wedge \overrightarrow{U} \rightarrow \overrightarrow{F}_{Coriolis} = F_c \overrightarrow{U} \wedge \overrightarrow{z}. \tag{1.30}$$

Ideal gas law

The systems of equations developed in this chapter use the ideal gas law to relate the pressure to the density and the absolute temperature:

$$P = \rho R_d T \tag{1.31}$$

Incompressible flow

Compressibility is related to the likeliness of fluids to experience variations in their density. Any fluid, and particularly any gas, is compressible: in a closed environment, a variation of pressure induces

a variation of density (e.g. in a bike pump). However, when the fluid is incompressibly flowing, a local change of pressure results in a movement of the fluid and the density remains constant. In the case of a flowing gas like the wind in the ABL, it is usual to consider it to be incompressible if the velocity does not exceed 30% of the sound velocity (Mach number above 0.3) which is about 110 m s^{-1} for air in atmospheric conditions and if no temperature changes are involved: incompressibility is thus a property of the flow and not of the fluid. The condition on velocity is always fulfilled in normal atmospheric conditions (although modern wind turbines may approach this limit [53]), but not the one on temperature.

The anelastic approximation

The condition of incompressibility is too constraining for atmospheric flows because variations in temperatures induce variations in density. However, solving numerically the fully compressible Navier-Stokes equations is computationally expensive because it requires a very small time step and is thus reserved for large Mach numbers or large gradients of temperature. In the atmosphere, the temperature variations are limited, leading to limited density variations. The anelastic approach is used to model this particular case of compressibility: a constant density profile $\rho_r(z)$ is used in the continuity and momentum equations. To take into account the effects of temperature variations on the flow, a 'buoyancy term' is introduced, which modifies the gravity term:

$$\overrightarrow{g} \rightarrow \overrightarrow{g}\left[1 - \frac{\theta^v}{\theta_r}\right] = -\overrightarrow{g}\frac{\theta^v}{\theta_r} - \frac{\overrightarrow{\text{grad}}P_r}{\rho_r} \tag{1.32}$$

The second equality is obtained from the ideal gas law and from the fact that the reference profile is hydrostatic.

Geostrophic equilibrium

At the synoptic scale (scales of thousands of km and several days), the Coriolis force and the pressure gradient are the two predominant forces and are thus at equilibrium. With all the precedent approximations, it results in a geostrophic wind $\overrightarrow{U_g} = (U_{gx}, U_{gy}, 0)$ that verifies:

$$U_{gx} = -\frac{1}{\rho_r F_c}\frac{\partial P}{\partial y} \qquad \text{and} \qquad U_{gy} = -\frac{1}{\rho_r F_c}\frac{\partial P}{\partial x} \tag{1.33}$$

The geostrophic equilibrium is valid only at the synoptic scale, however, we assume that the wind in the ABL converges toward the geostrophic wind in the free atmosphere. In the Meso-NH simulations, the geostrophic wind is imposed by the user and forces the system.

1.3.3 The Aneslastic system

Applying these approximations on the mass conservation (also called continuity equation), the momentum conservation for a Newtonian fluid (Navier-Stokes equation), the conservation of heat and the conservation of moisture leads respectively to equations 1.34, 1.35 ,1.36 and 1.37: it is called the

anelastic system [54]. Even though the reference state was considered to be hydrostatic, the system at time t may not be so. We, therefore, present the non-hydrostatic version of the anelastic system where no simplification is done between the gravity and pressure terms.

$$\frac{\partial \rho_r U_j}{\partial x_j} = 0 \tag{1.34}$$

$$\frac{\partial \rho_r U_i}{\partial t} + U_j \frac{\partial \rho_r U_i}{\partial x_j} = \rho_r g \frac{\theta_v^v}{\theta_{v,r}} \delta_{i3} - \frac{\partial P^v}{\partial x_i} + \rho_r F_c \epsilon_{ij3}(U_j - U_{g,j}) + \nu \frac{\partial^2 \rho_r U_i}{\partial x_j^2} + S_{m,i} \tag{1.35}$$

$$\frac{\partial \rho_r \theta_v}{\partial t} + U_j \frac{\partial \rho_r \theta_v}{\partial x_j} = S_\theta + \nu_\theta \frac{\partial^2 \rho_r \theta_v}{\partial x_j^2} \tag{1.36}$$

$$\frac{\partial \rho_r q_T}{\partial t} + U_j \frac{\partial \rho_r q_T}{\partial x_j} = S_q + \nu_q \frac{\partial^2 \rho_r q_T}{\partial x_j^2} \tag{1.37}$$

where ν is the kinematic viscosity of the air, ν_θ is the thermal diffusivity of air, and ν_q is the molecular diffusivity for water vapour in the air. S_θ and S_q are respectively the temperature and the moisture source terms. S_m is the source of momentum due to external forces on the system. This is how we can model the interactions between wind turbines and the atmosphere: introducing source terms in the momentum equation will lead to changes in the evolution of U but also of θ_v and q_T since all the equations of the anelastic system are coupled.

From left to right, the different terms of the momentum equation (Eq. 1.35) are called: unsteady term, advection term, buoyant term, pressure gradient term, Coriolis term, diffusion term and body force term.

At this point, there are six unknowns (three components of U, P, θ_v and q_T) and six equations, but the smoothness and existence of a solution for this system have not been proven yet. The equations can although be numerically solved, as will be explained in Sect. 3.1.

1.3.4 The Reynolds system

No analytical solution is yet known for the Navier-Stokes equations, and thus for the anelastic system. One can argue though that for most aerodynamic computations there is no need to know the exact pattern of every eddy of the flow: the knowledge of the mean variables and a global measure of the turbulence should be enough. The evolution of the mean variables can be obtained from the anelastic system by applying the Reynolds decomposition (Eq. 1.4) to the six unknowns. The averaging operator $X \rightarrow \overline{X}$ is then applied to every equation to yield the Reynolds averaged system [45]:

$$\frac{\partial \rho_r \overline{U_j}}{\partial x_j} = 0 \tag{1.38}$$

$$\frac{\partial \rho_r \overline{U_i}}{\partial t} + \overline{U_j}\frac{\partial \rho_r \overline{U_i}}{\partial x_j} = \rho_r g \frac{\overline{\theta_v^v}}{\theta_{v,r}}\delta_{i3} - \frac{\partial \overline{P^v}}{\partial x_i} + \rho_r F_c \epsilon_{ij3}(\overline{U_j} - U_{g,j}) + \nu \frac{\partial^2 \rho_r \overline{U_i}}{\partial x_j^2} + \overline{S_{m,i}} - \frac{\partial \rho_r \overline{u_i' u_j'}}{\partial x_j} \tag{1.39}$$

$$\frac{\partial \rho_r \overline{\theta_v}}{\partial t} + \overline{U_j}\frac{\partial \rho_r \overline{\theta_v}}{\partial x_j} = S_\theta + \nu_\theta \frac{\partial^2 \rho_r \overline{\theta_v}}{\partial x_j^2} - \frac{\partial \rho_r \overline{\theta_v' u_j'}}{\partial x_j} \tag{1.40}$$

$$\frac{\partial \rho_r \overline{q_T}}{\partial t} + \overline{U_j}\frac{\partial \rho_r \overline{q_T}}{\partial x_j} = S_q + \nu_q \frac{\partial^2 \rho_r \overline{q_T}}{\partial x_j^2} - \frac{\partial \rho_r \overline{q_T' u_j'}}{\partial x_j} \tag{1.41}$$

Since $\overline{\phi'} = 0$, all turbulent parts of the variables are simplified, except the non-linear advection term which results in the sum of a mean advection and of the divergence of a turbulent flux (last term of every equation). The existence of these turbulent fluxes proves that the turbulence, i.e. small-scale behaviour, cannot be neglected, even when predicting the mean flow only. Dimensional analysis shows that the Reynolds number can be viewed as the ratio between the advection and diffusion term. Consequently, at low Reynolds numbers the advection, from which the turbulence terms arise, becomes negligible compared to the diffusion term. This validates the observations of the Reynolds experiment (see Sect. 1.1.2) that turbulence appears only for high Reynolds number flows.

1.3.5 Equation for the TKE

The state of the atmosphere (neutral, unstable, stable) can be characterised by the source of turbulence. This is achieved by first developing the TKE equation and analysing the different terms:

$$\begin{aligned}\frac{\partial k}{\partial t} + \underbrace{\frac{1}{\rho_r}\overline{U_k}\frac{\partial \rho_r k}{\partial x_k}}_{\text{Mean transport}} = & \underbrace{-\frac{1}{\rho_r}\frac{\partial \rho_r \overline{k u_k'}}{\partial x_k}}_{\text{Turbulent transport}} \underbrace{-\frac{1}{\rho_r}\overline{u_k'\frac{\partial P^{v'}}{\partial x_k}}}_{\text{Pressure correlation}} \underbrace{-\overline{u_i' u_k'}\frac{\partial \overline{U_i}}{\partial x_k}}_{\text{SP}} \underbrace{+\frac{g}{\theta_{v,r}}\overline{w'\theta_v'}}_{\text{BP}} \\ & + \underbrace{\nu\frac{\partial^2 k}{\partial x_k^2}}_{\text{Molecular diffusion}} \underbrace{-2\nu\overline{\left(\frac{\partial u_i'}{\partial x_k}\right)^2}}_{\text{Viscous diffusion } (\epsilon_D)} .\end{aligned} \tag{1.42}$$

The shear production (SP>0) appears in high-velocity gradient regions, typically near the ground or at the interface between two atmospheric layers with different wind velocities. The buoyant production (BP) grows in magnitude with stability or unstability. SP is always a source term but BP can be either a source or sink term.

Depending on the value of BP and SP, different regimes of turbulence exist: when the dissipation of turbulence by stability is greater than the production by shear, the turbulence disappears. When it is slightly lower, there is a regime of stratified turbulence characteristic of the SBL. When SP is much greater in magnitude than BP, the regime is called 'forced convection' i.e. the mechanically-produced turbulence mainly drives the physics and the ABL is statically neutral. Conversely, when

there is almost no shear compared to the temperature flux, the regime is called 'free convection' (one can think of the cigarette example). The middle ground between forced and free convection is characteristic of the CBL, where both shear and buoyancy are a source of turbulence.

1.3.6 Turbulence modelling

There are still 6 equations but there are now 15 additional unknowns due to the turbulent fluxes. It can be proved that the Reynolds stress is a symmetric tensor [45] hence reducing this number to 12 additional unknowns. If the proof of existence has not been proven yet for the anelastic system, it is known for sure that a system of 6 equations and 18 unknowns cannot be solved. It is possible to find evolution equations for the turbulent fluxes, but this leads to the appearance of third-order terms, and a never-ending problem. If one wants to compute the mean variable of a turbulent flow, the first step is to close the equations, i.e. relate the turbulent fluxes to already existing variables or known parameters of the anelastic system. Turbulence modelling is a very dense field and the description provided herein is concise, the point is just to introduce some concepts that will be used afterwards.

K-Theory

One possible source of turbulence is the presence of gradients. The idea of the K-theory is to relate any turbulent flux to a gradient of a mean quantity:

$$\overline{u_i'\phi'} = -K_\phi \frac{\partial \overline{\phi}}{\partial x_i} \tag{1.43}$$

Where K_ϕ can be a constant or a parameter depending on mean quantities. If the turbulence is considered isotropic, $K_u = K_v = K_w = \nu_t$ where ν_t is also called 'eddy viscosity' because this parametrisation acts similarly to the viscosity term. A lot of parametrisations of K_ϕ and relationships between K_u, K_θ and K_q can be found in the literature [45]. K_ϕ should follow the constraints:

- $K_\phi = 0$ when there is no turbulence, in particular at the ground.
- K_ϕ increases with TKE, and varies with static stability.
- K_ϕ is non-negative.

The latter constraint corresponds to the fact that a flux should move down-gradient e.g. heat flux moves from hot to cold. However in the atmosphere, counter-gradient flows can arise, for instance, large eddies in thermals may transport air parcels regardless of the local gradient. The K-theory may thus fail at modelling the CBL.

Mixing length formulation

The mixing length formulation is one of the most used versions of the K-theory. By assuming that the surrounding mean quantities vary linearly, the eddy viscosity is modelled as:

$$\nu_t = l_m^2 \left| \frac{\partial U}{\partial z} \right| \tag{1.44}$$

where l_m is called the mixing length and corresponds to the typical size of eddies. It has been introduced by Prandtl who proposed the value of $l_m = \kappa z$ in 1925 but in almost one century a large number of other parametrisations have been proposed (a review is made in [54]). Even though some of these models try to take stratification into account, the assumption of linear evolution of the mean variables only holds for small eddies. As a consequence, the mixing length theory can be considered as a 'small-eddy theory' and thus does not work for cases with large eddies, such as CBL.

One-and-a-half-order closure

The K-gradient with mixing length is sometimes called one-order closure because it retains as prognostic equations only the zero-order variables (mean velocities, mean temperature and mean humidity), and diagnostic equations are found for second-order moments (e.g. Eq. 1.43). A second-order closure would aim at writing the 12 diagnostic equations for these second-order momentum terms and find diagnostic equations for the third-order moments (e.g. $\overline{u_i' u_j' u_k'}$). The large number of equations makes it slow to resolve numerically and the large number of unknowns makes it sensible to the calibration.

A middle ground between these is the one-and-a-half-order closure. The principle is to develop only one or several prognostic equations for the prediction of second-order momentum (for instance, the TKE i.e. Eq. 1.42). These new equations will lead to new unknowns of third order but they will also give a prognostic measure of the turbulence, instead of estimation through a parametrisation. This type of closure is chosen in the Meso-NH formulation and is detailed in Sect. 3.2.

Conclusion of the chapter

In this chapter, we described the ABL, with a particular focus on turbulence and stability. The anelastic and Reynolds systems of equations that drive the turbulent flow in the ABL have been introduced. However, they know no analytic solutions and thus need to be solved numerically: this will be detailed in Ch. 3. The next chapter is focused on wind turbine and their wakes and will re-use the concepts defined above to describe the wake behaviour in the ABL.

Chapter 2

Wind turbines and wind turbine wakes

This second chapter is dedicated to the description of wind turbine wakes. The first section details how a wind turbine works. It is an essential foreword to understand wind turbine wakes, which are described in the second section. The third section is dedicated to the unsteady behaviour of wind turbines called wake meandering. Numerically solving the Boussinesq system (as will be detailed in the next chapter) is too computationally expensive to estimate the impact of wakes on the production or life expectancy of a farm. To do so, the industry uses analytical models, which are described in the fourth section. Finally, models for wake meandering are described in the fifth section.

2.1 Wind turbine aerodynamics

2.1.1 Wind turbine kinematics

Along with the Cartesian coordinate system $(\overrightarrow{x}, \overrightarrow{y}, \overrightarrow{z})$ used to describe the atmosphere, let us define a cylindrical coordinate system $(\overrightarrow{x}, \overrightarrow{r}, \overrightarrow{\varphi})$ centred at the middle of the rotor, where $\overrightarrow{x}$ coincides between both coordinate systems. A classical Horizontal Axis Wind Turbine (HAWT) can be decomposed in five parts, illustrated in Fig. 2.1a:

- The tower of the wind turbine. Onshore, it is fixed on the ground, but in the case of floating offshore wind turbines (FOWT), it can move with the marine swell.
- The nacelle of the wind turbine, which contains the gearbox and generator. It can rotate around the vertical axis $\overrightarrow{z}$ to maintain the turbine aligned with the wind. If it is not aligned, the misalignment angle is called yaw.
- The hub is rotating around the nacelle (along the axis $\overrightarrow{x}$ if it is aligned with the mean wind direction) at rotational speed Ω. This is the main movement of the turbine, which is used to produce power.
- The blade can move around the radial direction of the wind turbine axis. This pitch angle γ allows controlling and optimising the power production.

- Finally each blade is defined by 2D sections, called airfoils. Each airfoil has a different length, called chord (larger near the root than near the tip) and orientation called twist. It can be visualised in Fig. 2.1b.
- Note that other degrees of freedom exist in the kinematics of the turbine, such as the tilt of the nacelle. However, it is not used in this work and is therefore not described herein.

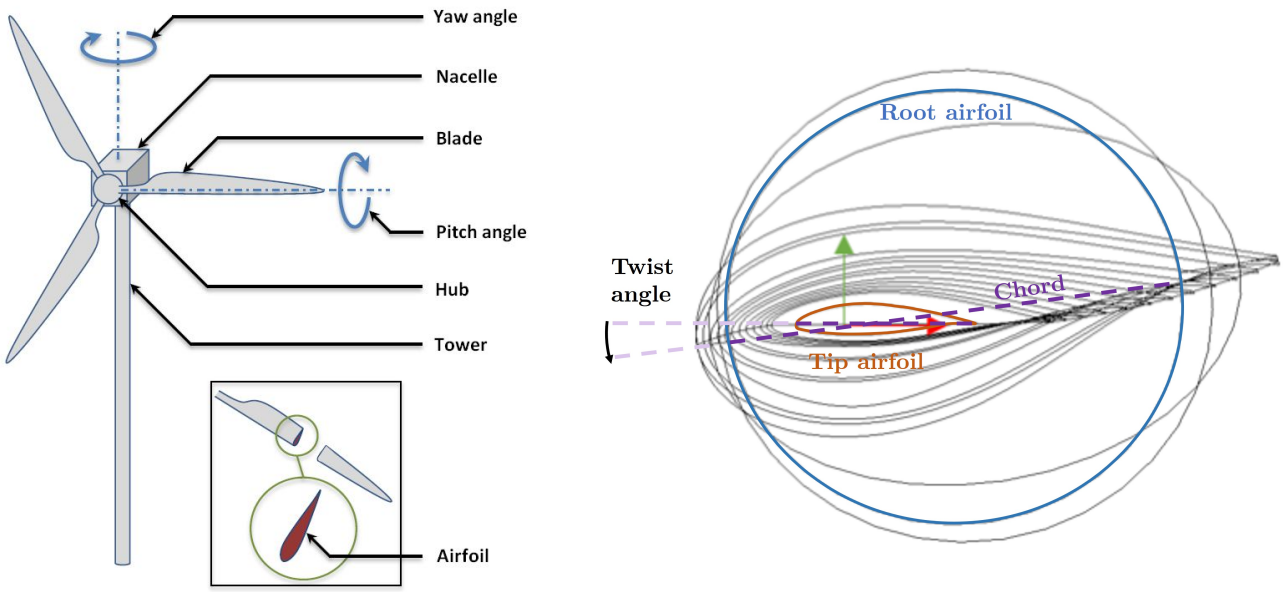

(a) The different parts of a HAWT, courtesy of [10].

(b) The different airfoils along the blade, adapted from [55].

Figure 2.1: Composition of a wind turbine.

2.1.2 Working principle

Wind turbines harvest wind energy through the force induced by the wind on the blades. As described in Sect. 2.1.1, the blades can be decomposed into airfoils, similarly to propellers or aircraft wings. Each airfoil has a particular shape, which leads to a given pair of infinitesimal lift and drag δL and δD, acting on the airfoil in the perpendicular and the collinear directions of the incoming wind respectively (see Fig. 2.2). These forces are usually computed under their non-dimensional form C_L and C_D which are dependent on the angle of attack α i.e. the misalignment of the airfoil's chord with the incoming wind. In the case of a wind turbine blade, the rotation of the blade must be taken into account to define this incoming wind, so a relative wind $\overrightarrow{U_{rel}}$ is used:

$$\overrightarrow{U_{rel}} = \left(U_\varphi - \Omega r; U_x\right) \tag{2.1}$$

where U_φ and U_x are the tangential and axial components of the incoming velocity field, and Ω is the rotational velocity of the wind turbine hub. Integrating δL and δD over the entire blades leads to the

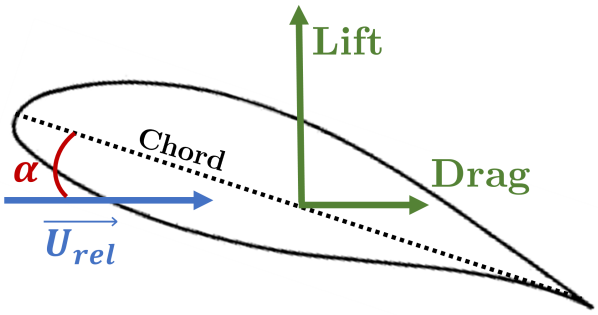

Figure 2.2: Schematic of the lift and drag forces acting on an airfoil.

force induced by the blades on the surrounding wind. It is decomposed into normal and tangential forces F_N and F_T respectively to the blade axis (i.e. along $\overrightarrow{x}$ and $\overrightarrow{\varphi}$ if $\gamma = 0$). The torque is the moment of the whole rotor: multiplied by the rotational velocity Ω, it gives the mechanical power extracted by the turbine. The thrust is the force acting against the wind, i.e. it is slowing down the wind and induces a wake behind the turbine.

2.1.3 Performances of a wind turbine

We introduce here some concepts extracted from the 1D-theory [56] which are essential for the understanding of wind turbine wakes. Let us consider an undisturbed wind of velocity U_∞ and density ρ in which is placed a turbine of diameter D, thus sweeping an area of $A_r = \pi(D/2)^2$. If the velocity of the wind just behind the rotor is written U_1, the axial induction factor a is defined by Eq. 2.2. It quantifies how the turbine is slowing down the wind passing through its blades. For $a = 0$, the wind turbine has no effect on the surrounding wind and for $a = 1$, the wind turbine is totally stopping the wind. The tip speed ratio λ_T (abbreviated TSR) is the ratio between the velocity of the tip of the blade and the incoming wind velocity. It is widely used as a non-dimensional form of the rotor speed (Eq. 2.3).

$$a = \frac{U_\infty - U_1}{U_\infty} \qquad (2.2) \qquad\qquad \lambda_T = \frac{\Omega D/2}{U_\infty}. \qquad (2.3)$$

We write $\mathcal{P}$ the mechanical power generated by the wind turbine and T the total thrust of this turbine, but the non-dimensional forms ($C_\mathcal{P}$, C_T) are often preferred (Eqs. 2.4 and 2.5). From Eq. 2.4, one can deduce the maximum power that can be extracted by a wind turbine, known as the Betz limit: $C_\mathcal{P}^M \simeq 0.593$ for $a = 1/3$. In other words, the optimum machine should slow down the wind to 67% of its free-stream value.

It should be noted that $C_\mathcal{P}$ and C_T depend on the inflow velocity and the TSR. If an idealised rotor is considered (axisymmetric, infinite number of blades and neglected azimuthal velocity), then $C_\mathcal{P}$ and C_T are increasing functions of λ_T, asymptotically reaching 0.593 and 0.9 at around $\lambda_T \approx 10$

$$C_{\mathcal{P}} = \frac{\mathcal{P}}{\frac{1}{2}\rho A_r U_\infty^3} = 4a(1-a)^2 \qquad (2.4) \qquad C_T = \frac{T}{\frac{1}{2}\rho A_r U_\infty^2} = 4a(1-a). \qquad (2.5)$$

[57]. This increase of the power coefficient with the TSR has since been confirmed by experimental measurements [28, 29, 58] at least up to $\lambda_T = 4$. For larger TSR values, the $C_{\mathcal{P}}$ of real turbines may decrease.

The stability of the ABL also plays a role: it has been observed that for a given velocity at hub height, a turbine working in non-waked conditions can lead to a smaller value of $C_{\mathcal{P}}$ and C_T in unstable conditions compared to neutral or stable conditions [59, 60]. Similar behaviour happens for a lower value of z_0 [59]: an explanation could thus be that the choice of the velocity at hub height for U_∞ might not be appropriate for a large turbine in a shear flow and that a correction for shear should be applied in Eqs. 2.4 and 2.5.

2.2 Wakes of wind turbines

An equivalent of the Betz limit can be derived for a clustered wind farm: one can write the power density of wind as [37]:

$$PD = 2a(1-a)^2 \rho U_\infty^3 (\pi/2)\mathcal{D}^{-2} \qquad (2.6)$$

where $\mathcal{D}$ is the distance between two turbines made dimensionless with D. If one assumes that all the turbines are working at the Betz limit, that the inflow velocity is 10 m s^{-1} and that the turbine spacing is approximately $x/D = 3$, this leads to a power density of 30 MW km^{-2}. This ideal, maximum power density has to be compared to the actual one measured in real parks which is on average 3 MW km^{-2} [37]. This gap is due to the fact that the wind is not always at 10m s^{-1} and that turbines are not working all the time at the Betz limit, in particular due to the intermittency of the wind. Another cause is the wake effect, which induces a non-negligible velocity decrease in the wake of the turbines at $\mathcal{D} = 3$. The intermittency of the wind cannot be directly tackled since it is intrinsic to the resource, so this thesis focuses on the wake phenomenon, which is introduced in the present section.

2.2.1 Characteristics of a wind turbine wake

A wind turbine affects the flow upstream (induction region) and downstream (wake region). This thesis focuses on the wake effects. As schemed in Fig. 2.3, there are two main phenomena of interest in the wake:

- When it is rotating, a turbine induces a thrust force on the surrounding flow which slows the air down. As a consequence, the wake is a region of low velocity (in blue in Fig. 2.3), and this velocity deficit can be interpreted as the consequence of energy extraction from the flow by the wind turbine. The velocity deficit δU and its normalised form ΔU are defined as:

$$\delta U(x,y,z,t) = U_0(x,y,z,t) - U(x,y,z,t) \qquad \Delta U(x,y,z,t) = \frac{\delta U(x,y,z,t)}{U_0(x,y,z,t)} \tag{2.7}$$

where U_0 is the unperturbed velocity and U is the velocity in the wake. In most of the cases, U_0 is defined as the time- and lateral-averaged velocity profile upstream of the turbine $U_\infty = \overline{U}(x_\infty, z)$. Unless specified otherwise, this definition will be used, with $x_\infty = -2.5D$, but for some specific applications, another definition might be used in this work. The deficit of the time-averaged velocity, i.e. $\Delta\overline{U} = (\overline{U}_0 - \overline{U})/\overline{U}_0$ is more commonly used than its instantaneous counterpart.

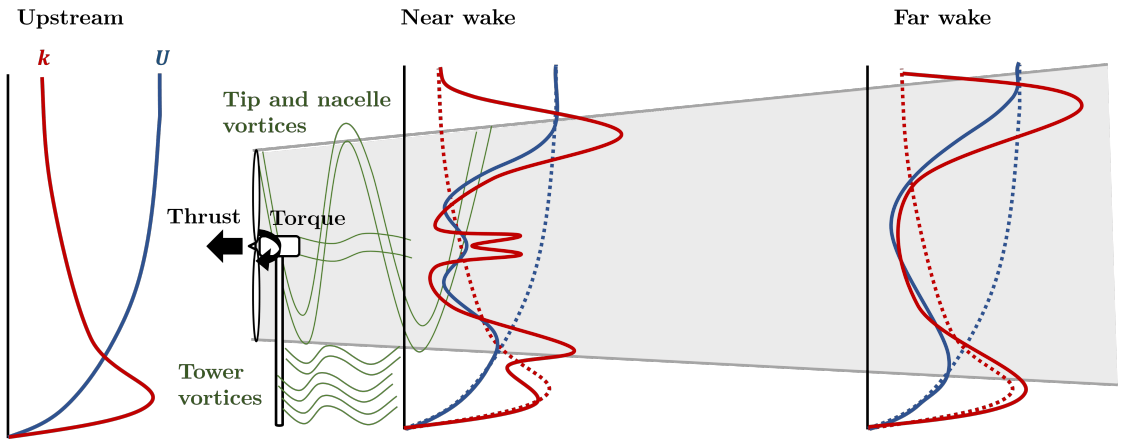

Figure 2.3: Schematic of the mean wake structure. Typical vertical profiles of velocity and turbulence are plotted in blue and red respectively.

- The wake is also a region of increased turbulence caused by blade-induced vortices, the wake-generated shear (due to the velocity deficit) and the wake meandering (a phenomenon described in Section 2.3) [61]. This enhanced turbulence is plotted in red in Fig. 2.3. Due to background atmospheric shear, the wake-generated shear is stronger on the top of the wake than on the bottom, leading to a maximum of TI near the top tip, at $z = z_h + D/2$ [62]. This interaction between wake-added shear and atmospheric shear must not be neglected or it leads to erroneous values for wake-added turbulence [63]. Similarly to the velocity deficit, the concept of added turbulence (Eq. 2.8) can be introduced to quantify the difference between the turbulence in the inflow and in the wake:

$$\Delta k(x,y,z) = k(x,y,z) - k_0(x,y,z) \tag{2.8}$$

where, k_0 is the unperturbed turbulence, and similarly to the velocity, is usually taken as the laterally averaged turbulence profile at the position x_∞ upstream of the turbine and then noted k_∞. It is common to use Eq. 2.8 under its non-dimensional form, i.e. define an added turbulence intensity. In the literature, the normalisation is not universal though: in some works, the global normalisation of the TI is used (Eq. 2.9) whereas the local TI (Eq. 2.10) is preferred in other works.

$$\Delta I = \sqrt{I(x,y,z)^2 - I_0(x,y,z)^2} \Leftrightarrow \frac{\sqrt{\Delta k}}{U_0} = \sqrt{\frac{k}{U_0^2} - \frac{k_0}{U_0^2}} \tag{2.9}$$

$$\Delta I^l = \sqrt{I^l(x,y,z)^2 - I_0^l(x,y,z)^2} = \sqrt{\frac{k}{U^2} - \frac{k_0}{U_0^2}} \tag{2.10}$$

The advantage of the global added TI definition is that it is equivalent to the added turbulence (Eq. 2.8), and if U_0 is taken as a single point (for instance, U_h), it simply acts as a scaling without modifications of the shape of the field Δk. For some cases, however, it can make more sense to work with the local turbulence intensity, in particular when it comes to defining an upstream TI for a turbine operating in waked conditions. This local added turbulence is not consistent with Eq. 2.8 since the right-hand side is not under the same denominator. Note that nothing prevents the wake turbulence to be locally lower than the upstream value, leading to undefined values of ΔI. Consequently, we will use the following formula that allows negative values:

$$\Delta I = \frac{|I - I_0|}{I - I_0} \cdot \frac{\sqrt{|I^2 - I_0^2|}}{U_0} \tag{2.11}$$

and similarly for ΔI^l. Even though it is not used here, it has been shown that the thrust velocity $U_T = T/\pi A_r$, where T is the thrust of the emitting turbine, is a pertinent variable to normalise the velocity deficit and added turbulence in the wake [64] since it makes the wake independent on the operating conditions.

Depending on parameters such as atmospheric stability, ambient TI, or surface roughness [65], the flow returns to its inflow state after a given recovery distance (up to $20D$ at low inflow TI [66]). This wake recovery is dependent on atmospheric conditions, in particular TI at hub height and thrust coefficient of the wake-emitting turbine.

In wind farms, wind turbines are influenced by the wakes of the upstream wind turbines. It is thus of primary importance to take into account the wake effects on downstream wind turbines to predict accurately their power output, blade loads and fatigue, which are modified in wake conditions by the momentum decrease and turbulence increase.

2.2.2 Structure of a wind turbine wake

In the literature, the wind turbine wake is usually divided into two main regions, schemed in Fig. 2.3 [7]: the near wake, starting from the turbine down to about $5D$ and then the far wake downstream. Other regions, such as the induction region upstream of the turbine [7], the expansion or very near wake region [67, 68], the transition region [67] and the decay region [68] can be defined as well but are not used herein.

Near wake

Behind the wind turbine, the pressure and velocity both suddenly drop. There is a discontinuity between the slow motions inside the wake and the fast flowfield outside, separated by the tip vortices. These vortices come from the pressure difference between the leading and the trailing edges at the tip of the blade. There also exist root and hub vortices that appear in the centre of the wake, but which are less detailed here.

The tip vortices gradually dissipate, mainly because of vortex pairing: when two vortices touch, they pair and destroy one another. The dissipation of the tip vortices happens faster when the TSR is increased because vortices are closer and thus will pair and self-destroy more easily [29]. These tip vortices can be interpreted as a cylindrical shear layer, which expands as the wake moves downstream because of turbulent diffusion. This shear layer shields the wake and prevents it from dissipation [69]. When the tip vortices dissipate and the shear layer edge reaches the wake axis the wake can dissipate faster, marking the end of the near wake.

As a consequence of the angular momentum conservation, the near wake is also a region of swirl, i.e. a rotation of the wake in the direction opposite to the blade's rotation. The swirl vanishes gradually, until approximately $3D$ to $5D$ downstream depending on the inflow and operating conditions [58, 70, 71].

In the near wake, the flow is dependent on the detailed characteristics of the turbine (e.g. airfoils and twist distribution, tower and nacelle shape) [67] but is Reynolds invariant [72]. The very near wake ($x < 1D$) is characterised by four peaks of turbulence: two strong peaks near the wake edge due to the tip vortices and two smaller peaks near the wake centre for the root vortices [72]. As the root vortices dissipate and only the tip vortices remain, this turbulence distribution becomes rapidly bimodal with a maximum at the top tip [73].

Far wake

Contrary to the near wake, the far wake depends only weakly on the turbine itself [7], and more on generic parameters such as thrust coefficient, TSR [29, 58], ambient turbulence [62, 74] and atmospheric stability (see Sect. 2.2.3). In the present work, the far wake is defined as the region where the velocity deficit is self-similar [75, 76, 77], analogously to the bluff body wake case [41]:

$$\Delta U(r,z) = C(x)F\left(\frac{r}{\sigma(x)}\right) \tag{2.12}$$

where $C(x)$ is the maximum velocity at the downstream distance x (located at the centerline), r is the distance from the centerline of the wake and $\sigma(x)$ is the characteristic size of the wake at streamwise position x [77]. Many studies have shown that a Gaussian function is well suited for the self-similar function F (see Sect. 2.4.1) [20, 77, 78, 79, 80]. As the wake moves downstream, it expands: $\sigma(x)$ increases and $C(x)$ decreases, until the ambient velocity is reached. The turbulence intensity in the far wake has a bimodal shape, with maxima around the tips of the blades [72, 79, 81, 82], i.e. the regions of high shear.

2.2.3 Influence of the ABL on the wake

These canonical wake characteristics tend to be modified under the action of the ABL. It is a trending research topic and the whole point of this thesis is to investigate these interactions. The main driver of these interactions is the atmospheric stability: as the stability increases, the TI decreases and thus the wake length increases [11, 59, 60] because turbulence is the main cause of wake dissipation. Wakes in a SBL have thus potentially a stronger impact on the downstream wind turbines. This is illustrated in Fig. 2.4. However, the effect of atmospheric stability cannot be reduced to a TI modification: with a constant TI at hub height, the wake recovery is still dependent on stability [83], a phenomenon attributed to the modification of the turbulent scales by the stratification.

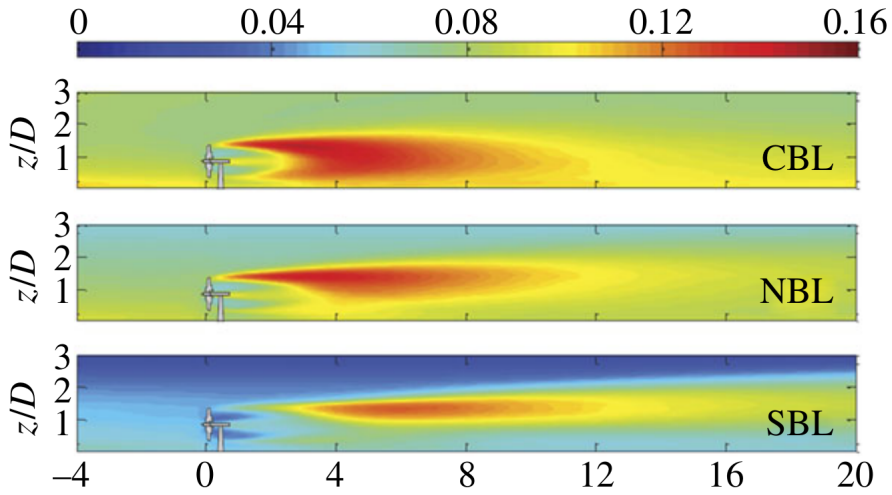

Figure 2.4: Isocontours of turbulence intensity simulated with LES in the two-dimensional plane normal to the ground and cutting through the rotor centre under a convective (CBL), neutral (NBL) and stable (SBL) atmospheric boundary layer condition. Copied from [7].

Usually, the turbine's rotor is embedded in the SL, where the wind follows the logarithmic law, inducing a non-negligible velocity gradient between the bottom and the top of the wake. Consequently, the velocity deficit at the bottom tip is smaller than that at the top tip, invalidating the self-similarity assumption in the vertical direction [66, 67]. This non-symmetric velocity deficit induces a non-symmetric turbulence profile in the wake. Either the maximum of turbulence is seen at the top tip and minimum of turbulence at the bottom tip [24, 84], or there are two maxima, one at the top tip and the other at the bottom tip, with the top one being stronger than the second one [64]. Depending on the upstream turbulence profile, the turbulence at the bottom of the wake can be smaller than the inflow conditions (implying $\Delta k < 0$) [20]. The peaks of added turbulence near the wake edge and at the top tip are less pronounced in the case of a CBL and more pronounced in SBL [85], due to the higher level of shear in the second case.

Another indirect consequence of stability is the veer. Typically in the SBL the atmosphere experiences a strong veer, i.e. a gradient of wind direction with height. This phenomenon can also arise in a CBL due to non-uniform terrain effects. If the veer is sufficiently strong, it can modify the shape of the wake as in Fig. 2.5 [11, 86, 87, 88].

The roughness length z_0 also affects the wake behaviour: as it increases, the wake expansion increases

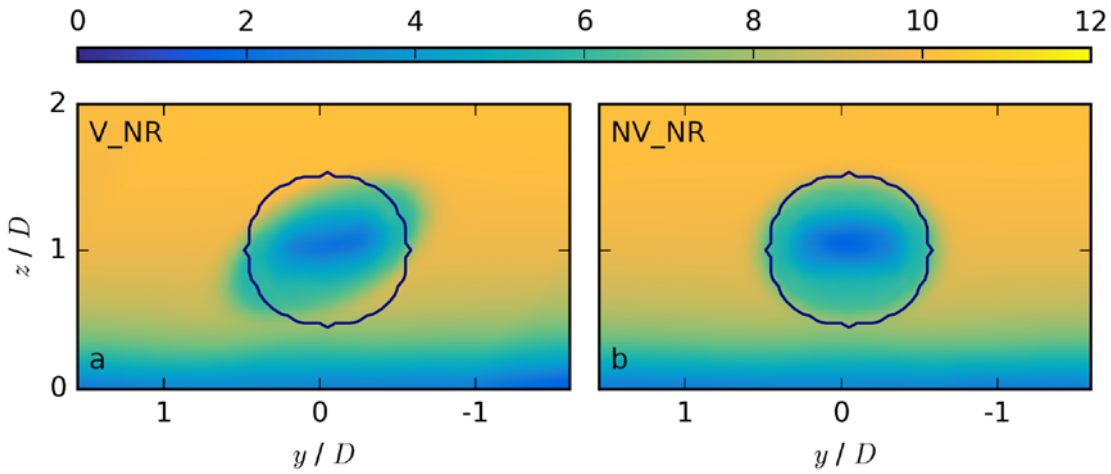

Figure 2.5: Isocontours of wind velocity five diameters downstream the wake: left figure with veer, right figure without veer. Copied from [86].

[24], due to an increase of TI. This leads to a faster dissipation of the wake as a consequence of momentum conservation. The presence of the ground also induces a shear layer, which affects the wake evolution [63]. Complex terrain must also be taken into account when simulating a wind farm flow. It has been also observed that in stable conditions, the wake tends to follow the orography (e.g. a small slope) compared to neutral or unstable conditions [60]. This can indirectly affect power production for onshore turbines: for instance, a wind farm in complex terrain can overproduce in a SBL and underproduce in a CBL, whereas the opposite is expected since wakes dissipate faster in a CBL [13]. Other phenomena may occur in specific conditions, for instance, the apparition of gravity waves [89] or the impact of low-level jet on the blade loading [90].

It should be kept in mind that an increase of turbulence (due to an increase of z_0 or a decrease of z/L_{MO} for instance) leads to a higher fatigue level for a turbine operating in waked conditions: the enhanced wake dissipation does not compensate for the inherent higher turbulence level [59]. Power production however is increased in such cases. The CBL developing over rough terrain can contain eddies similar to a wind turbine far wake, leading to similar effects such as large lift drop or dynamic stall on a portion of a turbine [59].

2.2.4 Spectral analysis of turbulent wakes

Similarly to the unperturbed ABL, the study of the instantaneous velocity in the wake allows a better understanding of the nature of the phenomena taking place in this particular region. For a wind turbine, the turbine characteristic frequency f_T is defined as:

$$f_T = \frac{\Omega}{2\pi} \tag{2.13}$$

where Ω is the rotational velocity of the rotor. At top tip height $z = z_h + D/2$, peaks in the vertical velocity spectrum can be observed at this frequency, which is related to the tip vortices [20, 59, 68]. This signature cannot be seen in the middle of the wake and is hardly visible at the bottom tip height

$z = z_h - D/2$, probably due to the proximity of the ground [58].

When considering the streamwise velocity component, it is observed that the spectrum in the wake has less energy attributed to the large-scale eddies and more energy corresponding to the small-scale eddies [24, 91, 92]. Thus, the turbine can be considered as an active filter, with a cut-off frequency around $0.1f_T$ [24, 68, 91, 93, 94]. It is also observed that the large eddies are especially damped between the hub height and the ground and that the small eddies are increased especially near the top tip. At higher frequencies, the turbulence in the wake follows the $-5/3$ cascade and is fairly isotropic [18].

It has also been measured that at low frequencies, the torque spectrum is coupled with the $-5/3$ turbulence cascade but is not at higher frequency [58]. The precise cut-off frequency could not be determined but it was always comprised between f_T and $2f_T$.

2.2.5 Influence of the tower and the nacelle

The wake is mostly due to the thrust applied by the turbine's blades to the incoming flow. In many numerical models, only the blades are thus represented. Real turbines are however also composed of a nacelle and a tower. These elements can affect the flow field to a lesser extent than the blades, but may still be relevant. The nacelle adds a drag force in the middle of the wake. Failing to represent this drag in numerical simulations leads to a near-zero velocity deficit at hub height, which is not a physical reality [95]. In the near wake, it also induces added turbulence due to the nacelle vortices. The tower induces drag and acts like a cylindrical bluff body that creates vortex shedding, whose spectral signature is found in the low-frequency part of the near wake turbulence spectrum [96].

Laminar numerical simulations have shown that the presence of the tower and nacelle leads to a faster breakdown of the tip vortices, hence leading to faster wake recovery. This is attributed to the von Karman vortices shed by the tower, which break the cylindrical shear layer developed by the blades. Moreover, both the tower and nacelle generate modes that increase the amount of mean kinetic energy brought to the wake [69].

2.3 Wake meandering

2.3.1 Origin of the phenomenon

In atmospheric conditions,*"random unsteady oscillations of the entire wake with respect to the time-averaged wake centreline"* are observed [7]. Due to this phenomenon, called wake meandering, a downstream turbine can be successively inside wake (Fig. 2.6a), and outside (Fig. 2.6b) the wake, even though the mean wind direction has not changed. This intermittent loading reduces the lifespan of the downstream turbine, and the displacements change the mean wake properties, which is why wake meandering is an important subject to tackle. To study the intermittent behaviour of the flowfield, it is common to normalise the frequency f as the Strouhal number here defined as:

$$St = \frac{fD}{U_h} \tag{2.14}$$

where D is the turbine diameter and U_h is the velocity at hub height. Note that $St(f_T) = \lambda_T/\pi$. The source of wake meandering is not yet totally identified but it seems to be a combination of a self-induction phenomenon in the near wake and the atmospheric turbulence in the far wake [73, 93, 97]. Wind tunnel measurements have highlighted the existence of wake meandering in the near wake oscillating at a constant Strouhal number, associated with the helical tip vortex [98]. The wake meandering is also driven by atmospheric turbulence, in particular changes in instantaneous wind direction [61]. Consequently, it should not be periodic like in the case of vortex shedding alone, especially since atmosphere-induced meandering is expected to be stronger than the vortex-induced one.

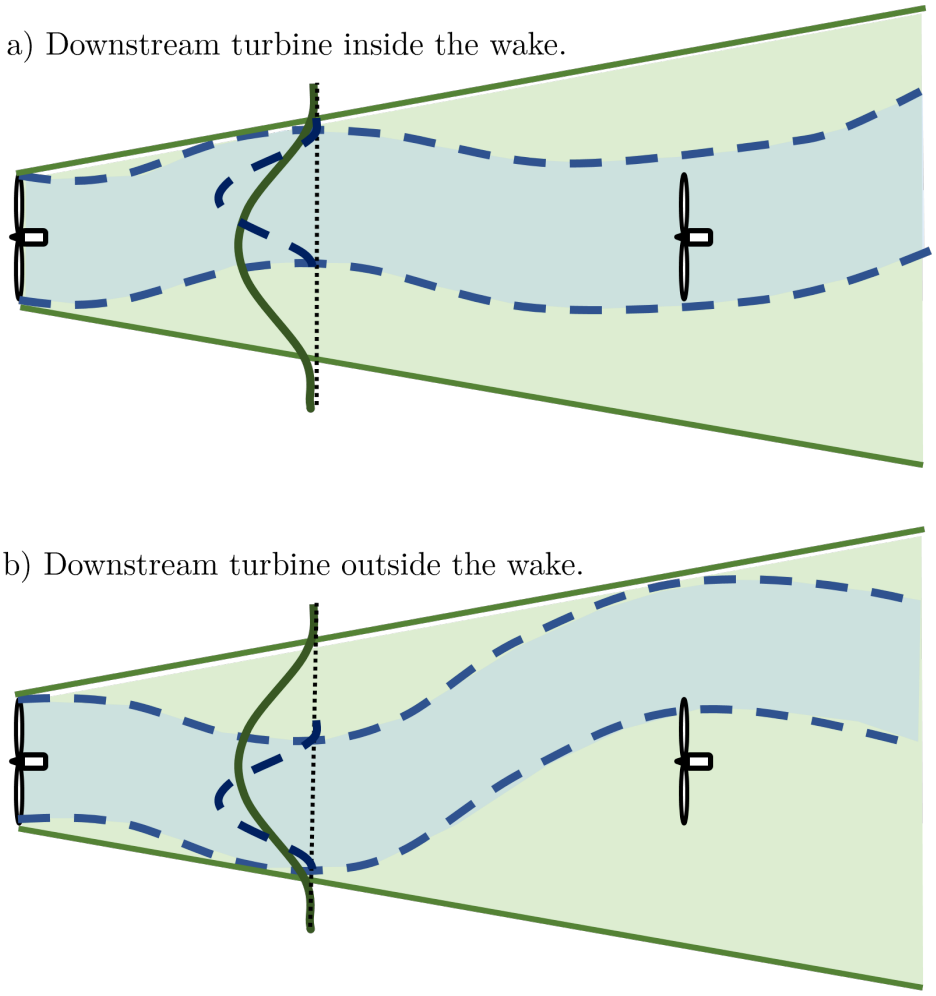

Figure 2.6: Schematic of wake meandering and the frames of reference at two time steps. In the blue and dashed line: instantaneous wake at two time steps and velocity profile in the moving frame of reference (MFOR); in the green and continuous: mean wake and velocity profile in the fixed frame of reference (FFOR).

2.3.2 Fixed and moving frame of reference

When the velocity field of a meandering wake is averaged in time, the velocity deficit is 'spread': the maximum deficit will be lower and the wake width higher than for the same wake without meandering.

This first method of computing statistics is said to be in the fixed frame of reference (FFOR, green in Fig. 2.6). It is the frame of reference of the ground and could also be called an Eulerian frame of reference because the observer is at a fixed position and simply computes the mean velocity deficit or TKE at a given position (x,y,z). This procedure is straightforward but the wake expansion and meandering are not differentiated. As was shown in the preceding sections, those phenomena have different sources: small-scale turbulence and operating conditions for the wake expansion and large-scale eddies of the ABL for the meandering. To better understand and model the behaviour of a meandering wake, it is important to decouple these phenomena.

This decoupling can be achieved with the use of the moving frame of reference (MFOR), which is linked to the wake centre. It could be called a 'semi-Lagrangian' frame of reference because the observer is following the wake in the y and z directions. The principle is to centre every snapshot of the time-dependent data (measurements or simulation) around the centre of the wake. That way, the meandering motions are filtered out and a non-meandering wake is obtained. Due to the spreading caused by the meandering, the mean velocity deficit in the FFOR (continuous green profiles in Fig 2.6) is weaker and wider compared to the mean velocity deficit in the MFOR (dashed and blue profiles in Fig 2.6). Conversely, the turbulence (not shown on the scheme) is stronger in the FFOR compared to the MFOR [18]. The instantaneous streamwise velocity can be changed from one frame to another according to the relation:

$$U_{MF}(x, y, z, t) = U_{FF}(x, y + y_c(x, t), z + z_c(x, t), t) \tag{2.15}$$

where subscripts MF and FF denote the velocity fields in the MFOR and FFOR respectively, $y_c(x,t)$ and $z_c(x,t)$ are the time series of the wake centre at the downstream position x. To illustrate these two averaging approaches, let us consider a Gaussian wake of maximum velocity deficit 0.6 at three snapshots t_0, t_1 and t_2. At time t_0, the wake is centred around $y = 0$. At t_1 and t_2, the wake keeps the same characteristics but an arbitrary meandering motion is set so the Gaussian functions are centred around $y = -D$ and $y = +D$ respectively (Fig. 2.7a). Averaging these three snapshots in the FFOR (blue curve in Fig. 2.7b) results in a Gaussian shape of maximum velocity deficit around 0.35 but a wider wake, whereas averaging them in the MFOR (green curve in Fig. 2.7b) leads to the same Gaussian shape as the instantaneous profiles.

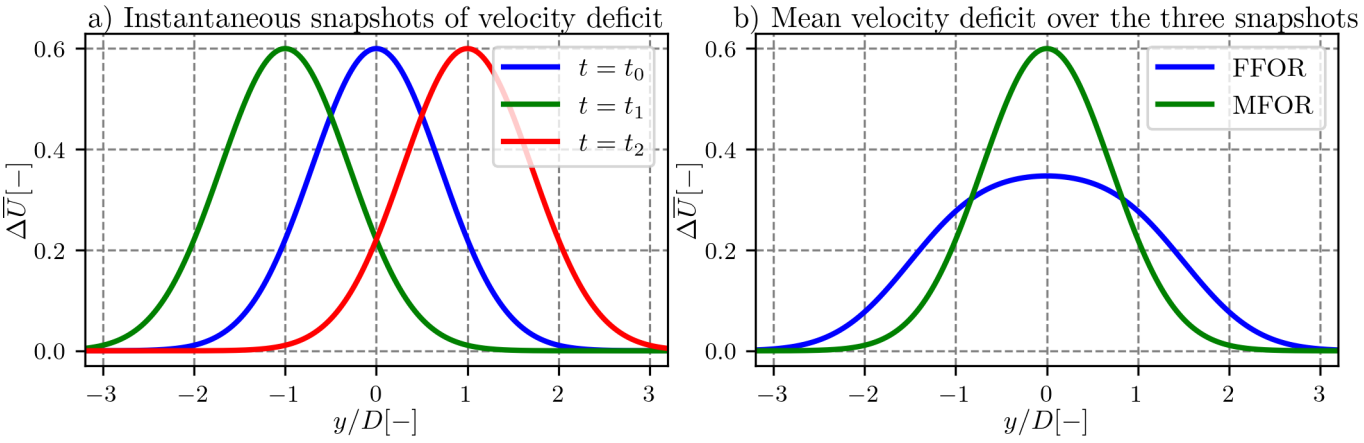

Figure 2.7: The effect of averaging on the wake's velocity deficit in the FFOR and the MFOR.

According to Kaimal's work, the normalised velocity spectra for any stratified ABL collapses into a single curve at high frequencies [50]. Since the argument of the split of scales says that only the large scales contribute to the dissipation of the wake in the MFOR, one should expect that the wake dissipation in the MFOR is not a function of stability. This has been confirmed by full-scale and numerical studies [60, 85], under the condition that the TI remains constant. For a turbine high above the ground, the wake velocity deficit in the MFOR has been observed to be axisymmetric [99], indicating that the asymmetry observed in the FFOR is mainly due to meandering. This matter of the dependency of the MFOR on stability is one of the objectives of this Ph. D. thesis, and is developed in Ch. 6.

2.3.3 Amplitude of the wake meandering

In this thesis, we quantify the wake meandering with the root-mean-square of the wake centre displacement. For the lateral wake meandering it is written as in Eq. 2.16 and the amount of vertical wake meandering σ_{fz} is similarly defined from z_c.

$$\sigma_{fy} = \sqrt{\overline{y_c'^2}} \tag{2.16}$$

It has been observed in the literature that the vertical amplitude of the wake meandering is smaller than the horizontal one. Experimental measurements at a 1:400 scale in a wind tunnel imitating a neutrally stratified flow have shown a rate of $\sigma_{fy}/\sigma_{fz} = \{1.28; 1.32\}$ for $a = \{0.12; 0.19\}$ [23]. Since the length scales involved in the latter case are subsequently smaller, the difference between horizontal and vertical wake meandering in atmospheric flow is attributed to the presence of the ground that blocks the largest eddies. The dependency of σ_f with x is often found to be linear, with possibly a break of slope at a given distance [11, 29, 60, 64].

The amount of meandering is dependent on whatever can change large-scale turbulence: inflow TI [100], hub height [99], and more importantly, atmospheric stability [11, 60, 80, 83, 100]. For instance, despite having equal turbulence levels, simulations of wind turbines in a NBL and a CBL have shown an increase of the meandering between 10 and 50% [94]. Vertical meandering has a greater increase than horizontal meandering. This last observation has also been observed on full-scale field measurements, with a ratio σ_{fy}/σ_{fz} going from 3.5 to 2.14 from stable to unstable cases, even though $I_{\infty,y}/I_{\infty,x} \approx 1.5$ in every cases [85]. Conversely, the turbine's operating conditions (C_T, λ_T) have less or even no impact on σ_f [29, 64].

In wind farms, numerical simulations indicate that the meandering is weaker in the middle rows than on the border rows [21]. This is attributed to the neighbouring rows of turbines that "block" the largest eddies.

2.3.4 Frequency analysis of the wake meandering

Only the largest eddies of the atmosphere contribute to the wake meandering, whereas the smaller eddies only affect wake expansion and dissipation. The cut-off wavelength separating these small-scale and large-scale eddies is discussed in the literature between a value of $2D$ [14, 18, 101] and $3D$ [102]. The scaling of the cut-off frequency with D has been proven by the fact that wakes of larger rotors are less subject to meandering [99]

When it is subject to an ideally perturbed flow, the wake oscillates with the same frequency as the inflow at different distances downstream of the rotor. Harmonics of this frequency develop only after some distance downstream [73].

In real cases, the dominant frequencies of wake meandering can be deduced from a low-frequency peak in the turbulence spectra of the wake [24, 58, 72, 91, 94] or simply the PSD of the wake centre's position [93]. In a NBL, these studies gave results in the range of $St = 0.25$ to $St = 0.3$, i.e. a frequency range spanning from $U/4D$ to about $U/3D$. For a CBL, the frequency peak is broader and centred around $St = 0.1$ [94].

In an experimental study with very low turbulence, it has been shown that the wake can be separated into four regions with different behaviour of the meandering [98]. It showed that the wake flow oscillates in the y and z direction at a frequency f_T. This study has however been done in a water channel where the turbulence intensity is very low. Such regions may not be found in ABL simulations because all these frequency components are overwhelmed by the wake meandering due to large-scale motions. Early wind tunnel measurements have also shown a dependency of the meandering frequency on the TSR and the thrust coefficient [28], but those may also be erased by the meandering signature in realistic ABLs.

2.4 Analytical modelling in the FFOR

Analytical models, whether it is for velocity deficit or added turbulence, are very fast to use: usually, they consist of one or a couple of formulas to compute, or a simple set of equations to solve. Most of the time, they are based on theoretical considerations and calibrated with reference data: high-fidelity simulations, wind tunnel measurements or full-scale data, when available. As shown in Fig. 2.8, the wind turbine's operating conditions are deduced from the atmospheric conditions, and allow computing the wake properties, which are used as the inflow conditions for the next turbine, and so on for the whole wind farm. In this section, the focus is on wake models that do not take meandering into account, or only implicitly through calibration: they are thus entirely computed in the FFOR and cannot differentiate the effect of meandering from the effect of wake expansion. Only the main models of the literature are presented in this section. For a broader overview and comparisons, the reader can refer to the reviews of the literature [7, 74, 103, 104].

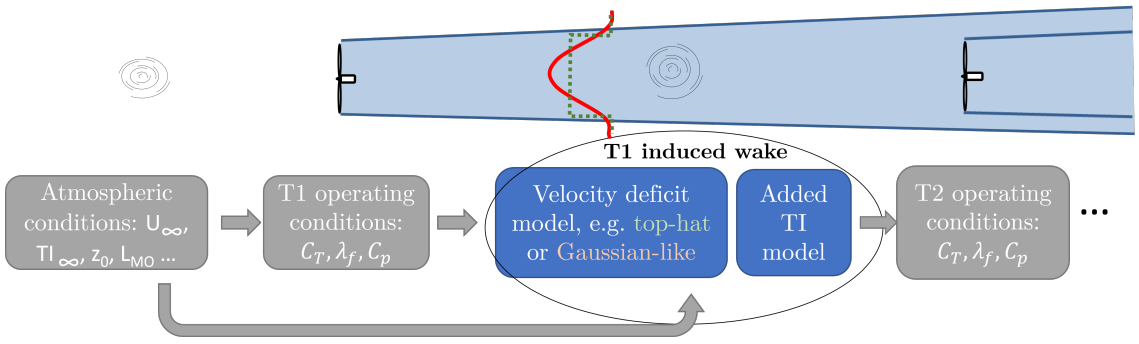

Figure 2.8: Working principle of analytical wake modelling.

Unless specified otherwise, the models presented here are built for the far wake, where the wake properties are more generic and easier to model. An analytical expression of the near wake length

(x_N) can be written as a function of N_b, λ_T, C_T, I_x and $\overline{u}_c$, respectively the number of blades, tip speed ratio, thrust coefficient, streamwise turbulence intensity and the mean convective velocity of the tip vortices normalised by the incoming flow speed [105]:

$$\frac{x_N}{D} = -0.5\Big[\Big(\frac{16\overline{u}_c^3}{N_b\lambda_T C_T}\Big)\ln(0.3I_x) + 5.5\ln(I_x)\Big]. \tag{2.17}$$

2.4.1 Velocity deficit modelling

Jensen model

The model developed by Jensen [75] and improved by Katic [106] has set the basis of analytical wake modelling. This model is based on the assumption that the wake grows linearly and that the wake deficit has a 'top-hat' distribution: the velocity in the wake is constant with the radial distance (green profile in Fig. 2.8) i.e. $F(y,z) = 1$ in Eq. 2.12. Initially, Jensen derived Eq. 2.18 using the axial induction factor a, but it is more convenient to write it as a function of the thrust coefficient (Eq. 2.19) since it is usually the variable available in an industrial framework. The parameter α_J (the wake growth rate) is driving the wake expansion and must be tuned. A value of $\alpha_J = 0.1$ is proposed in the original paper. The far wake has a Gaussian-like profile and such a top-hat model for the wake overestimates the velocity deficit at the boundary of the wake and underestimates it at the centreline. However, for wind farm power output computations, these are expected to compensate and give relatively accurate results when averaged on the downstream rotor area.

$$U(x) = U_\infty\Big[1 - 2a\Big(\frac{1}{1+2\alpha_J x/D}\Big)\Big]^2 \tag{2.18}$$

$$\Delta U(x) = \frac{1-\sqrt{1-C_T}}{(1+2\alpha_J x/D)^2} \tag{2.19}$$

Due to its low cost, accuracy and simplicity, the Jensen model is still very popular in the industry. It performs sometimes as well as recent models which take into account more physical parameters. More recent works improved the model by adding a dependency of α_J on turbulence and atmospheric stability, resulting in good estimations of the Sexbierum wind farm AEP but it was observed that the model is not suited to study the wake characteristics in detail [107, 108]

Frandsen model

Frandsen developed a model for wind farms [76] which can also be applied for a single wake turbine. Similarly to the Jensen model, he used the self-similarity hypothesis with a top-hat distribution. The difference is that both the mass and the momentum conservation equations are enforced to write his model. The wake diameter at distance x is introduced, with $D_w(x)/D = \sqrt{\beta_w + \alpha_F x/D}$. The variable β_w is the wake width just behind the turbine, and the new wake expansion coefficient is estimated as $\alpha_F \simeq 10\alpha_J$. The Frandsen model can be written:

$$\frac{\Delta U(x)}{U_\infty} = 0.5\left(1 - \sqrt{\frac{2C_T}{\beta_w + \alpha_F x/D}}\right) \tag{2.20}$$

$$\beta_w = \frac{1+\sqrt{1-C_T}}{2\sqrt{1-C_T}}. \tag{2.21}$$

The Gaussian model

In the model of Bastankhah and Porté-Agel (in the following abbreviated BP14) it is considered that the velocity deficit has a Gaussian shape (red profile in Fig. 2.8) [77]. Pressure and viscous terms are neglected in the momentum equation and a Gaussian shape of velocity deficit is assumed. This approach is much more consistent with the physics than applying a correction to a top-hat model as proposed by Jensen. Like the previous ones, the model's equation is written as a function of the thrust coefficient, as well as the hub height z_h and a new expansion parameter k^*, which is the only variable needed to tune in the model, making it very practicable. The velocity deficit is found to be:

$$\Delta U(x) = \left(1 - \sqrt{1 - \frac{C_T}{8(k^* x/D + \epsilon)^2}}\right) \exp\left[- \frac{1}{2(k^* x/D + \epsilon)^2} \left(\left(\frac{z - z_h}{D}\right)^2 + \left(\frac{y}{D}\right)^2 \right) \right] \tag{2.22}$$

One can recognise the self-similarity equation (Eq. 2.12) with F a Gaussian function of standard deviation σ and:

$$C(x) = 1 - \sqrt{1 - \frac{C_T}{8(\sigma/D)^2}} \tag{2.23}$$

$$\sigma/D = k^* x/D + \epsilon \tag{2.24}$$

where $C(x)$ is the maximum wake deficit and σ is the wake width. The wake width at the beginning of the wake is estimated to be $\epsilon = 0.2\sqrt{\beta_w}$ where β_w is defined in Eq. 2.21. This model assumes that the wake grows linearly with the downstream distance ($\sigma \sim x$), despite the theory of bluff bodies predicting $\sigma \sim x^{1/3}$ [41]. This choice is made in regard to experimental results [77] and is explained by the high turbulence intensity in the incoming turbulent boundary layer. These experiments and LES for five different cases led to the conclusion that k^* depends on the surface roughness z_0, and its value must be chosen wisely as a function of the shear of the ambient flow. For instance, based on LES, the following calibration is proposed for $0.065 < I_x < 0.15$ [109]:

$$k^* = 0.3837 I_x + 0.003678 \tag{2.25}$$

where I_x is either the streamwise inflow turbulence or the streamwise wake turbulence if the turbine is working in waked conditions, and is then estimated with a turbulence wake model (see Sect. 2.4.2). This calibration allowed us to correctly estimate the power production of the Horns Rev wind farm, compared to field measurements. Note that it is not the only calibration possible, as wind tunnel measurements and LES led to [15]:

$$k^* = 0.35 I_x \tag{2.26}$$

Instead of such empirical scaling, k^* can be computed by adapting the Taylor theory for pollutants to wind turbine wakes [110]. It led to the conclusion that the growth rate scales differently depending on the region: in the near wake, $\sigma \sim x$ whereas in the far wake, $\sigma \sim x^{1/2}$.

Non axisymmetric wake

The Xie and Archer [66] model (XA14) aims at modelling the ground effect on the wake. The authors argue that the self-similarity and axisymmetry hypotheses are questionable in the presence of ground, where a strong shear takes place. They used a LES code to simulate the wake generated by a single wind turbine in a neutral ABL and deduced that the self-similarity hypothesis is not verified in the vertical direction. They proposed the following modification of BP14 model (Eq. 2.22) :

$$\Delta U(x) = \left(1 - \sqrt{1 - \frac{C_T}{8(k_y^* x/D + \epsilon)(k_z^* x/D + \epsilon)}}\right) \exp\left[- \frac{y^2}{2(k_y^* x/D + \epsilon)^2 D^2} - \frac{(z - z_h)^2}{2(k_z^* x/D + \epsilon)^2 D^2}\right] \tag{2.27}$$

where two wake widths σ_y and σ_z are thus defined for the lateral and vertical directions:

$$C(x) = 1 - \sqrt{1 - \frac{C_T}{8\sigma_y \sigma_z / D^2}} \tag{2.28}$$

and k_y^* and k_z^* are the new wake expansion coefficients that can be calibrated independently to model non-axisymmetric wakes.

Near wake modelling

In the near wake, the velocity deficit does not have a Gaussian shape, but rather a top hat or bimodal shape, depending on the studies. Most of the analytical models are not built for the near wake because it is shown to be turbine-dependent, however, turbines may operate in the near wake of upstream turbines, typically in closely spaced wind farms and when the inflow turbulence is low. A simple approach is to apply a correction term to the centreline deficit $C(x)$ in the BP14 model [111]. Additionally, two models are proposed in the literature to achieve a more complex and realistic shape: the double- and super-Gaussian models. They are plotted in Fig. 2.9 along the Gaussian function (in black), with $\sigma/D = 0.3$ and $C_T = 0.6$.

Double Gaussian shape Based on measurements, Keane et al. [78] proposed to follow the same reasoning as the BP14 model but by considering a double-Gaussian instead of the Gaussian shape. It leads to:

$$U = U_\infty \left[1 - c_- C(x) F(r, \sigma(x))\right] \tag{2.29}$$

$$F(r, \sigma(x)) = \frac{1}{2}\left[e^{D_+} + e^{D_-}\right] \tag{2.30}$$

where c_- is a constant of the model and $D_\pm(r)$ represent the two Gaussian functions, centred at $r \pm r_0$ where r_0 is calibrated analytically. The expression of $C(x)$ is quite more complex than for the BP14 model, full details can be found in the original article. Similarly to the BP14 model, a linear wake expansion can be chosen [112]. The resulting shape function takes a bimodal shape with two Gaussian functions, progressively evolves into a top hat function and finally into a Gaussian function.

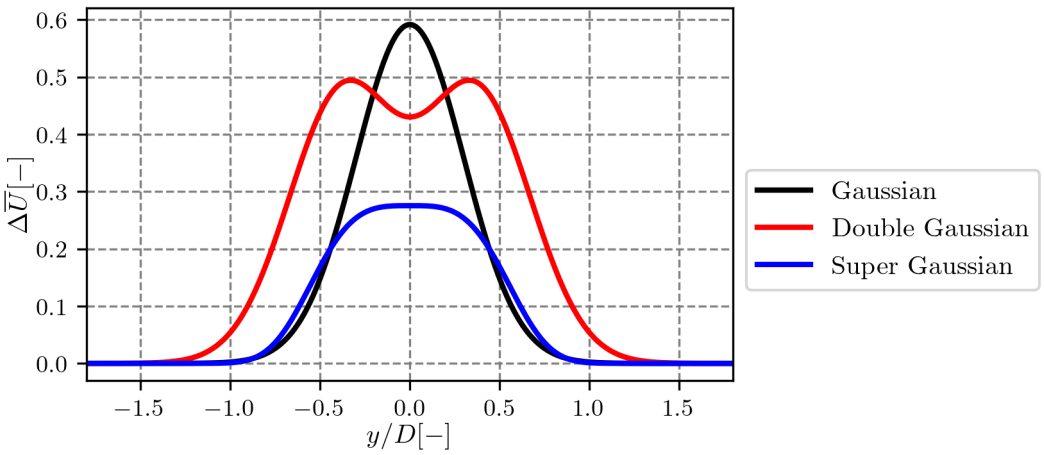

Figure 2.9: Near wake velocity deficit modelling.

This function is plotted in red in Fig. 2.9 for $c_- = 0.4$ and $r_0 = 0.75D/2$. The main drawback of this model is that one needs to tune two new parameters c_- and r_0 besides the k^* of BP14.

Super-Gaussian shape Alternatively, a generalisation of the Gaussian function called super-Gaussian can be used to smoothly transition from a top hat function in the near wake to a Gaussian function in the far wake [113]. It is based on self-similarity (Eq. 2.12) with:

$$F = \exp\left(\frac{-(r/D)^{n_s}}{2(\sigma/D)^2}\right) \tag{2.31}$$

where n_s is the super-Gaussian order and needs to be calibrated. At $n_s = 2$, it leads to a normal Gaussian function and evolves to a top hat function as $n_s \to \infty$. Similarly to the BP14 model, mass and momentum conservation are enforced to determine the corresponding maximum velocity deficit [114]

$$C(x) = 2^{2/n_s - 1} - \sqrt{2^{4/n_s - 2} - \frac{n_s C_T}{16\Gamma(2/n_s) \cdot (\sigma(x)/D)^{4/n_s}}} \tag{2.32}$$

where Γ is the gamma function. This model is simpler than the double-Gaussian, and performs well against measurements but cannot retrieve the bimodal shape in the very near wake [114]. The super-Gaussian model is plotted in blue in Fig. 2.9 for $n_s = 3.5$.

Impact of the ABL

To take ABL stability into account in the BP14, it is possible to find expressions for the initial wake width ϵ and the wake growth k^* as a function of surface roughness z_0 and the Monin-Obukhov length L_{MO} [115]. Moreover, the lateral turbulence intensities (I_y, I_z) which result from the Coriolis forces are used instead of the streamwise turbulence intensity (I_x). This model yields very good results against LES in neutral and unstable atmospheric conditions but some discrepancies appear for stable conditions. One of the major drawbacks of the model is its complexity with three new parameters

to tune. Moreover, the Monin-Obukhov length can be tricky to estimate during the design phase of a wind farm.

The skewness of the wake induced by the veer, in particular in SABL can also be modelled by modifying the BP14 model with a coefficient that depends on the veer upstream of the turbine [116].

2.4.2 Added turbulence modelling

In the IEC standard [52], turbines are classified as a function of the turbulent intensity they experience. To know the regime of a wind turbine operating in waked conditions, it is thus very important to be able to compute the turbulent intensity in the wake. Early models focused on the prediction of the maximal value of the added turbulence $\Delta I^M = \max(\Delta I)$ (see Eq. 2.9). The IEC 61400-1 [52] standard focuses on practicability: it uses the Frandsen [117] model which solely depends on the upstream velocity and downstream distance:

$$\Delta I_m = \frac{0.9}{1.5 + 0.3\sqrt{U_h/u_{n1}}\frac{x}{D}}. \tag{2.33}$$

where u_{n1} is a constant equal to 1 m s^{-1}. This model neither depends on the atmospheric conditions nor the operating conditions of the turbine. To take them into account, a model can be written as a function of the turbulent intensity and the induction factor [118]:

$$\Delta I^M = 0.73 a^{0.8325} I_\infty^{-0.0325} \left(\frac{x}{D}\right)^{-0.32}. \tag{2.34}$$

More recently, a modification of the empirical Hassan model [119] was proposed by Xie and Archer [66] (Eq. 2.35). It depends on the near wake x_N defined in Eq. 2.17. This model gives good results, but the near-wake length dependency degrades its robustness because x_N is itself defined by an analytical model (Eq. 2.17), inducing more uncertainty.

$$\Delta I^M = 5.7 C_T^{0.5} I_\infty^{0.68} \left(\frac{x}{x_N}\right)^{-0.96}. \tag{2.35}$$

Even though they depend roughly on the same parameters, the coefficients of Eqs. 2.34 and 2.35 radically differ. In particular the first is decreasing with the inflow TI whereas the second is increasing. The dependency on x is debated in the literature, with wind tunnel measurements predicting dependency of $x^{-0.5}$ over a smooth surface and $x^{-0.6}$ over a rough surface [24]. Ishihara and Qian [111] also developed a model for the maximum added turbulence, with a correction for the near wake, written in brackets:

$$\Delta I^M = \frac{1}{2.3 C_T + I_\infty^{0.1}\frac{x}{D} + \left[0.7 C_T^{-3.2} I_\infty^{-0.45}\left(1 + \frac{x}{D}\right)^{-2}\right]}. \tag{2.36}$$

To take into account the spatial distribution of the TI, the same authors proposed a double-Gaussian function distribution that collapses in a Gaussian function in the far wake, with a correction term to include the effect of the ground.

It must be acknowledged that contrary to the velocity deficit models that are based on assumptions of self-similarity and mass/momentum conservation, the aforementioned added turbulence models are empirical relations. The main drawback of such relations is that the empirical fit tends to be case-sensitive and the models may need to be recalibrated, with possibly many parameters to tweak. To cope with this, a physically-based model for the three turbulent components is proposed in [92]:

$$\frac{\overline{u_i' u_i'}}{U_\infty^2} = \frac{\overline{u_i' u_i'}_\infty}{U_\infty^2} + K_i K_K C(x) F_i(r) \tag{2.37}$$

where i is the velocity component index, K_i and K_K are constants that must be calibrated, $C(x)$ is the (maximum) centreline velocity deficit and F_i is a shape function. The authors proposed a double-Gaussian shape for $\overline{u'u'}$ and a Gaussian shape for $\overline{v'v'}$ and $\overline{w'w'}$, all formulated to take their maximum values at the top tip. The total TKE and TI can then be retrieved by summing the three components.

2.5 Wake meandering modelling

2.5.1 Dynamic Wake Meandering

The models presented above have two main drawbacks: they are steady and are directly calibrated in the FFOR, making them difficult to calibrate because of meandering. If one is interested in the time variations of the wake such as the wake meandering effect or the effect of the swell for FOWT, a time-dependent model must be used. Modelling the unsteady effects is particularly useful for multiphysics models (in particular for aero-elasticity) such as FAST.Farm [120] HAWC2 [121] or DeepLines Wind^{TM}.

The Dynamic Wake Meandering (DWM), detailed herein aims at modelling the unsteady effects of wake meandering at a low cost. The approach, schemed in Fig. 2.10 for the horizontal direction, is to consider the wake as a passive tracer, whose displacements downstream are driven by changes of wind direction due to eddies of large size in the ABL [14]. The atmospheric turbulent field surrounding the wake can be generated by a cost-efficient method such as a Mann box [122]. The split of scales introduced in Sect. 2.3.4 is used to separate the large and the small eddies. The large eddies drive the wake's meandering motions whereas the small eddies affect the turbulent evolution in the wake. The DWM methodology is built on two main steps [123]: first, the wake velocity and turbulence fields are computed by a steady model, and then the resulting field is separated into small sections, or releases, which are displaced by the large eddies of the turbulent field.

Modelling in the MFOR

The wake velocity and TI profiles are computed in the MFOR, plotted in blue in Fig. 2.10, which has a cylindrical coordinate system. This primary step does not take wake meandering into account and thus the wake is supposed to be steady: inspired by the Ainslie model [62, 124], the steady-state, axisymmetric thin shear layer equations are solved for u (axial velocity) and v (radial velocity) [125]:

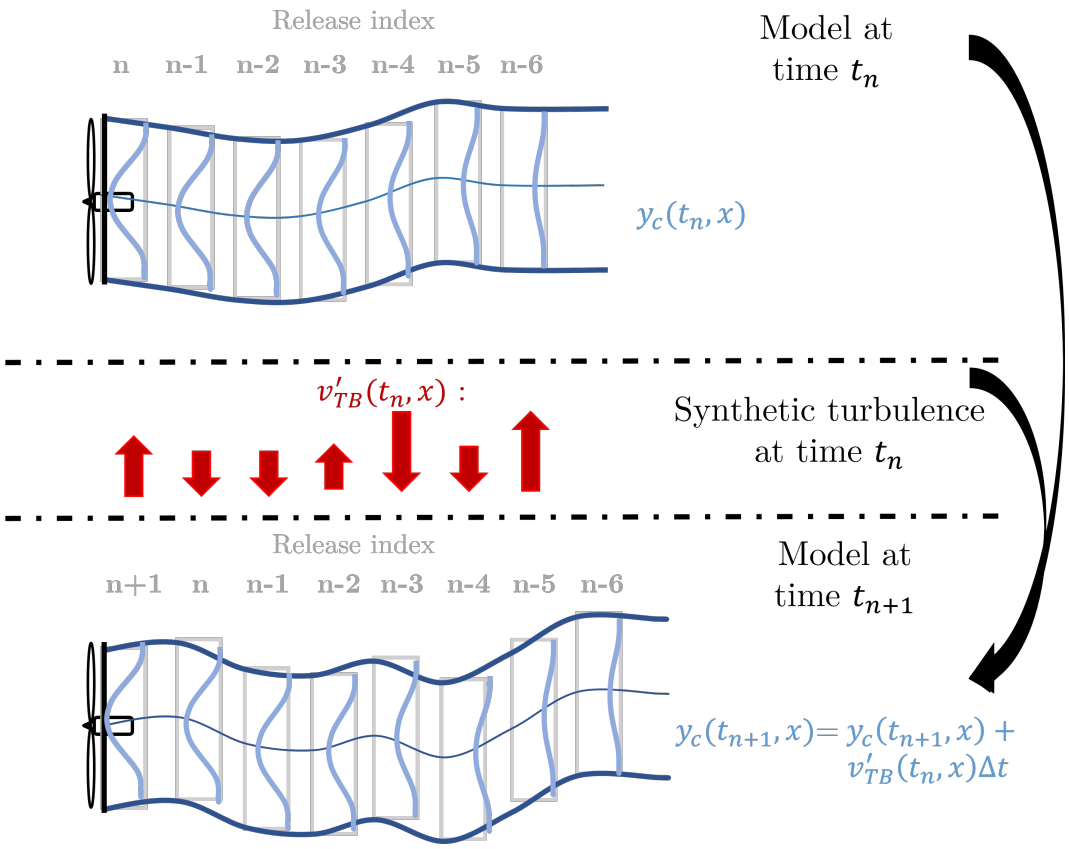

Figure 2.10: The dynamic wake meandering model: example for the lateral (y) direction.

$$\frac{1}{r}\frac{\partial r v}{\partial r} + \frac{\partial u}{\partial x} = 0 \tag{2.38}$$

$$u\frac{\partial u}{\partial x} + v\frac{\partial u}{\partial r} = -\frac{\nu_T}{r}\frac{\partial}{\partial r}\left(r\frac{\partial U}{\partial r}\right) \tag{2.39}$$

The eddy-viscosity ν_T takes into account both the ambient turbulence and the wake contribution due to velocity gradients. It is based on a mixing length formulation [126]:

$$\frac{\nu_T}{U_\infty D/2} = F_1 k_1 I_\infty + F_2 k_2 l_m^2 \left|\frac{\partial u}{\partial r}\right| \left(\frac{1}{U_\infty D/2}\right) \tag{2.40}$$

where F_1, F_2 are filter functions and k_1, k_2 are model coefficients. The mixing length l_m is assumed to be equal to half the width of the wake. Instead of the ambient TI, an alternative formulation that depends on the atmospheric length scale can be used to take the ABL stability into account [63]. The boundary conditions of this set of equations are located directly after the studied wind turbine and are determined by the velocity distribution upstream of the wind turbine and the induction factor.

The added turbulence in the MFOR can be estimated by scaling the inflow turbulence field with a radially dependent factor $k_{mt}(r)$ [125]:

$$k_{mt}(r) = k_{m1}\left|1 - \Delta U_{MF}(r)\right| + k_{m2}\left|\frac{\partial \Delta U_{MF}(r)}{\partial r}\right| \tag{2.41}$$

where k_{m1} and k_{m2} are calibration constants and ΔU_{MF} is deduced from the system of equations formed by Eqs. 2.38, 2.39 and 2.40. Equation 2.41 leads to an axisymmetric added turbulence in the wake but can be modified to take atmospheric shear into account [127].

Meandering

At the end of this first step, the velocity and TI profiles are known at every (x, r) location of the MFOR. In a second step, the effect of wake meandering is taken into account: the wake is divided into releases (grey boxes in Fig. 2.10) which are regularly emitted and advected downstream at a velocity lower than the ambient velocity. At every time step, the velocity variations of the turbulent box v'_{TB} and w'_{TB} and mean streamwise velocity U_{TB} are computed for each release based on its position (red arrows in Fig. 2.10). According to the split of scales, the small-scale fluctuations are filtered out so only the eddies of size larger than a given eddy size λ_M are taken into account. Every release is finally displaced depending on the large-scale turbulent field [14]:

$$dx_c = U_{TB}dt \tag{2.42}$$
$$dy_c = v'_{TB;\lambda>\lambda_M}dt \tag{2.43}$$
$$dz_c = w'_{TB;\lambda>\lambda_M}dt \tag{2.44}$$

where (x_c, y_c, z_c) is the position of the wake centre. The velocity and TI profiles are then transposed into the FFOR (green part of Fig. 2.10) which is in a Cartesian coordinate system. The cut-off frequency f_M corresponding to wavelength λ_M, above which the fluctuations are considered to affect the wake dissipation and under which it affects the meandering, was initially estimated as [61, 97]:

$$f_M = \frac{U}{2D} \Leftrightarrow \lambda_M = 2D. \tag{2.45}$$

This is based on the physical argument that if an eddy is larger than twice the diameter of the turbine, it will move the whole wake. Other studies have shown that this cut-off frequency may be progressive, starting from $4D$ to $2D$ [23, 102]. It can also be argued that this cut-off frequency should be scaled on the wake diameter D_w instead of the turbine diameter, however the latter is less handy to use. Finally, this cut-off frequency can be computed with an iterative method, based on the auto-correlations of the lateral and vertical velocities [128].

Result in the FFOR

Applying Eqs. 2.42, 2.43 and 2.44 to determine the instantaneous wake trajectory and resolving the system of Eqs. 2.38, 2.39 and 2.40 at each of these downstream positions leads to the instantaneous wake velocity field subject to meandering. Similarly, the wake-added turbulence at the position defined by the wake centre can be superposed on the stochastic turbulence field generated by the turbulent box. This will result in an unsteady velocity field that can be used as such or from which the average and the variance give respectively the mean velocity and turbulence in the wake.

2.5.2 Steady modelling of the wake meandering

The DWM allows getting the instantaneous behaviour of a wind turbine wake, but for some applications, the instantaneous value is not necessary and it is sufficient to directly compute the mean velocity and TKE in the wake. It can be argued that the models presented in Sect. 2.4 give good results despite meandering because they take implicitly into account the wake meandering [129]. However, doing so leads to a blend of wake expansion and meandering, which are different phenomena with different sources. The models presented below allow decoupling the effect of wake meandering from the wake expansion.

The first model that aimed to correct for the effect of meandering was introduced to correct discrepancies observed between the Ainslie model (not described here, but similar to Eqs. 2.38 and 2.39) and full-scale wind turbine wake measurements for non-stable cases. The centreline deficit is corrected with a simple equation [62]:

$$C_{FF} = \frac{C(x)}{\sqrt{1 + A(x)C(x)[1 - 0.5C(x)]}} \tag{2.46}$$

which can be reverted as:

$$C(x) = \frac{A(x) + \sqrt{A^2(x) + 2A(x) + 4/C_{FF}^2(x)}}{A(x) + 2/C_{FF}^2(x)} \tag{2.47}$$

where $\sigma_{\beta_\infty}^2 = \overline{\beta_\infty'^2}$ is the variance of the upstream wind direction. In both equations, A is defined as :

$$A(x) = \frac{16\sigma_\beta^2 x^2}{C_T} \tag{2.48}$$

This development is based on three hypotheses [130]:

- In the MFOR, the velocity deficit in the wake has a Gaussian shape: $F(r) = \exp\left[-K_a(r/D_w)^2\right]$ where K_a is measured in a wind tunnel as $K_a = 3.56$.
- The wake meandering follows a Gaussian distribution of variance σ_f^2 :

  $f_c(r) = \frac{1}{\sqrt{2\pi}\sigma_f} \exp\left[-(r/2\sigma_f)^2\right]$.
- The variance of the wake meandering can be written $\sigma_f^2 = x^2\overline{\sigma_\beta^2}$.

Another method starts from the DWM model. It conserves the MFOR modelling but the unsteady field is not computed. Since the velocity is assumed to be steady in the MFOR, the wake centre time series resulting from Eqs. 2.42, 2.43 and 2.44 can be permuted with no effect on the mean result in the FFOR. The mean velocity field in the FFOR can thus be found with a 2D convolution product, noted $**$:

$$\overline{U_{FF,dwm}}(y,z) = \int\int U_{MF,dwm}(y-y_c, z-z_c)\, f_c(y_c,z_c) dy_c dz_c = U_{MF,dwm}(y,z) ** f_c(y,z) \quad (2.49)$$

where f_c is the probability density function (PDF) of the wake centre position, normalised such as $\int\int f_c(y_c,z_c)\ dy_c dz_c = 1$. Similarly, the turbulence in the MFOR modelled by Eq. 2.41 can be transposed in the FFOR [63, 127]:

$$k_{a,dwm}(y,z) = \int\int k_{MF,dwm}(y-y_c, z-z_c)\, f_c(y_c,z_c) dy_c dz_c = k_{MF,dwm}(y,z) ** f_c(y,z) \quad (2.50)$$

where $k_{a,dwm}$ will be called hereafter 'rotor added turbulence'. However, it does not represent the total amount of turbulence in the FFOR and must be combined with the turbulence generated by meandering. Indeed, due to the displacements of the wake, a fixed point downstream will successively be under low velocity (when it is inside the wake) and high velocity (when it is outside the wake). These fluctuations induce turbulence; which is modelled in the DWM as [63, 127]:

$$k_{m,dwm}(y,z) = \int\int \left(U_{MF,dwm}(y-y_c, z-z_c) - \overline{U_{FF,dwm}}(y,z)\right)^2 f_c(y_c,z_c) dy_c dz_c \quad (2.51)$$

where $k_{m,dwm}$ is the meandering added turbulence. Both k_a and k_m can be transposed into the corresponding rotor added and meandering turbulence intensities through normalisation by $\overline{U}$. The total turbulence intensity in the wake can simply be found by:

$$I = \sqrt{I_a^2 + I_m^2} \quad (2.52)$$

A more recent model, hereafter denoted BS19, starts from the model of Bastankhah and Porté-Agel (Eq. 2.22) and adds that the wake centreline should follow a Gaussian distribution [129]. Averaged in time, the velocity deficit writes:

$$\overline{\Delta U}(x,y,z) = C(x)\left(\left[1+\left(\frac{\sigma_{fy}}{\sigma_y}\right)^2\right]\left[1+\left(\frac{\sigma_{fz}}{\sigma_z}\right)^2\right]\right)^{-1/2} exp\left[-\frac{(y-y_{oc})^2}{2\sigma_y^2+2\sigma_{fy}^2} - \frac{(z-z_{oc})^2}{2\sigma_z^2+2\sigma_{fz}^2}\right] \quad (2.53)$$

where C, σ_y, σ_z are dependent on the operating conditions. These three parameters were deduced in the original publication using linearised simulation. The position of the wake centre y_{oc} and z_{oc} have to be defined by the user. Finally, the variances of the meandering σ_{fy} and σ_{fz} are deduced by the author by extending the particle dispersion theory to the wake meandering effect (Eq.2.54). It is a function of some unknown convection velocity U_c, the integral time-scales $\mathcal{T}_{v,w}$ and the standard deviations of the lateral and vertical velocities fluctuations $\sigma_{v,w}$. As suggested by ABL theory [45], these values are taken to $\sigma_v = \sigma_w = 2.5u_*$ and $\Lambda_z = 0.5\Lambda_y = \kappa z/(2\sigma_v)$.

$$\sigma_{fy,fz}^2(x/U_c) = 2\sigma_{v,w}^2 \mathcal{T}_{y,z}^2 \left[\frac{x}{U_c/\mathcal{T}_{y,z}} + e^{-x/(U_c\mathcal{T}_{y,z})} - 1\right] \quad (2.54)$$

This model predicts that $\sigma_f \propto x$ in the near wake and $\sigma_f \propto \sqrt{x}$ in the far wake. The linear slope has been widely verified in the literature (see Sect. 2.3.3) and the square root limit could explain the slope break downstream in some results. If one assumes that meandering is the main driver of the total mean wake expansion in the FFOR, this result is following the finding that wake expansion is a linear function of x [110].

Conclusion of the chapter

In this chapter, we described the state of the scientific knowledge on wind turbine wakes and their interactions with the ABL. A review of the main wind turbine's wake models has also been done. On one hand, a lot of models have been developed over the past years to deal with the velocity deficit. These models are often derived from physical arguments (conservation of mass and/or momentum) with some parameters to fit. As a result, there are now reliable models to compute the annual energy production (AEP). On the other hand, the analytical models for added turbulence intensity are less numerous and mostly based on empirical approaches. They are thus less reliable and give very different results from one model to another [131], making the estimation of blade loading more uncertain than AEP. This Ph. D. thesis aims at better modelling the wakes of wind turbines, in particular for the added turbulence and the interaction with the ABL stratification. The next chapter presents the high-fidelity numerical methods that will be used to better understand the wake behaviour and the phenomena at stake.

Chapter 3

Numerical modelling

Even though it can be considered of lower fidelity than field measurements, numerical methods are popular for their lower cost and because they provide data in the whole studied domain whereas *in situ* measurements provide data only at the positions of the probes. Moreover, the inflow conditions are controlled and can be easily changed, allowing to better isolate the effect of a given parameter of the ABL on wakes. To study a wind farm embedded in the ABL, the highest-fidelity models achievable with modern supercomputers are Large Eddy Simulations (LES) with an actuator method (ALM). In this chapter, we will introduce the concept of LES, then describe Meso-NH, the LES code used in this Ph. D. thesis which is based on the ABL equations described in Ch. 1 and finally detail the actuator line method used to model the effects of the wind turbine on the surrounding flow.

3.1 Large Eddy Simulation

3.1.1 The different numerical strategies to compute turbulent flows

Even though no analytical solution has yet been found for the Navier-Stokes equations nor for the Boussinesq system, it is possible to solve approximate forms of these equations numerically. The principle is to spatially discretise the domain of interest into a given number of cells. Each prognostic variable (U_i, θ, P...) has a fixed value for each cell at time t. The Taylor series allow writing every derivative of the equations presented in Sect. 1.3.3 as a function of the value in the neighbouring cells (for spatial derivative) or at the preceding time steps (for temporal derivative). At the time $t + \Delta t$ (i.e. the next time step), the value of all the prognostic variables in each cell is deduced from this discretisation of the Boussinesq system. This approach allows resolving equations without analytical solution but leads to unavoidable approximation: Taylor series being infinite sums, the discretisation must be stopped at a given order. For instance, a 4th-order discretisation scheme means that the solution is a $O(\Delta^4)$ of the Taylor series where Δ is the mesh size or time step.

Since the variables are constant over a given cell, the smallest eddies that can be resolved will be of the order of magnitude of the mesh size. Resolving directly the Navier-Stokes equations (i.e. direct numerical simulations or DNS) requires resolving every eddy at stake. The ratio between the smallest and the largest eddies varies with $Re^{3/4}$, so the number of cells required for a DNS is proportional to this number in the three spatial directions i.e. $Re^{9/4}$. Moreover, the Courant-Friedrich-Levy

(CFL) criterion imposes to reduce the time step proportionally to the mesh size to prevent a fluid particle to cross more than one cell per time step, leading the total computational cost of DNS to be proportional to Re^3. As a consequence, it is limited to low Reynolds number flows and restrained domain in time and space. With today's supercomputers, resolving the atmosphere in DNS is not feasible and will not be for decades, even according to the optimistic Moore's law.

An alternative is to perform Reynolds Averaged Navier Stokes (RANS) simulation. The principle is to use the Reynolds system (Sect. 1.3.4) to only solve the mean flow (in the Reynolds averaged definition). For most aerodynamic applications, the mean flow information is enough, but the problem that arises with this approach is finding an accurate and reliable turbulence modelling approach because all the turbulence is modelled and not resolved. This is usually done with models presented in Sect. 1.3.6, but is dependent on the calibration of these turbulence models.

In the middle ground between DNS (all the turbulence is resolved) and RANS (all the turbulence is modelled) are the large eddy simulations (LES) where most of the turbulence is resolved. The idea is that small-scale turbulence is often considered to have a universal behaviour and can thus be more easily modelled than large-scale motions. The approach of LES is to apply a low-pass filter to the equations. Only the eddies bigger (lower wavenumber and frequency) than a given length are solved in the equations: this is the resolved, or filtered, part of the equations. The eddies filtered out cannot be neglected, and their effect on the resolved part is modelled in the equations through a subgrid term. Likewise, we speak about subgrid stress, subgrid kinetic energy, etc... when it comes to the unresolved, but modelled, part of these quantities. It is abbreviated SGS for subgrid scale.

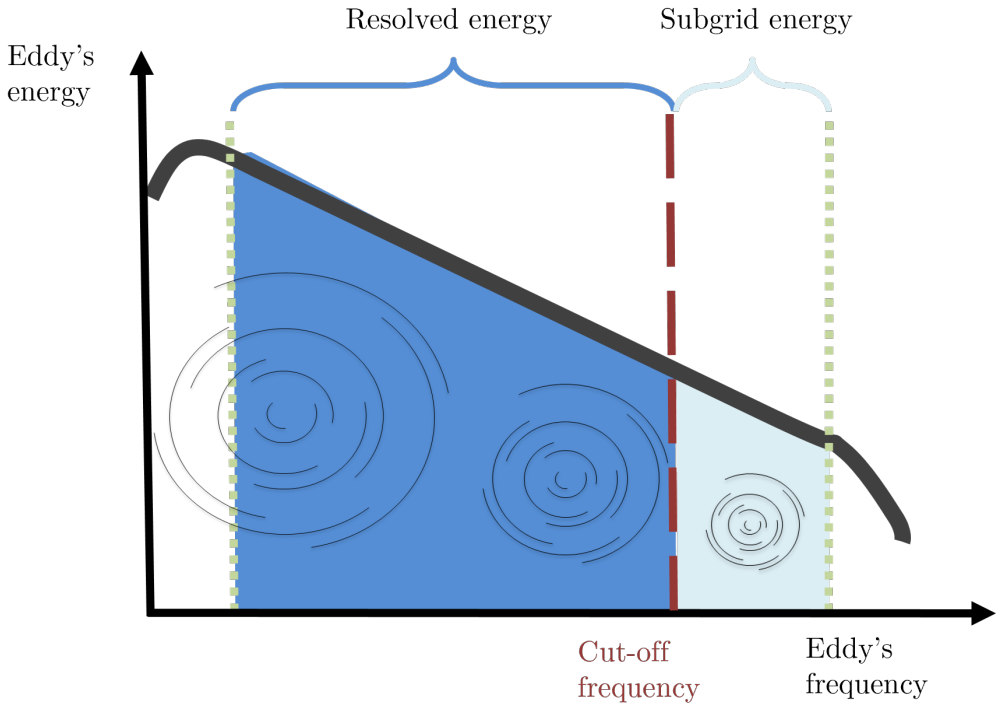

Figure 3.1: Separation of the turbulence spectrum in resolved and subgrid parts.

This separation between resolved and subgrid parts is illustrated on the Kolmogorov-Richardson cascade (see Sect. 1.1.6) in Fig. 3.1. A usual measure for a LES to be 'well-resolved' is that the

resolved TKE is at least 80% of the total TKE. If more than 20 % of the turbulence is subgrid, the impact of subgrid modelling induces too much uncertainty and the results of the simulation can hardly be trusted.

3.1.2 LES formulation

The low-pass filter G (for instance a gaussian filter [41]) characterised by a cut-off width Δ_G is applied in the equations according to Eq. 3.1 [132]. Every variable can then be separated into filtered and subgrid parts $\phi = \widetilde{\phi} + \phi"$. Many filters can be used, at the condition that it commutes with space and time derivatives. However in general, $\widetilde{\phi"} \neq 0$.

$$\widetilde{\phi}(\overrightarrow{x}, t) = \int G(\overrightarrow{r}, \overrightarrow{x}, \Delta_G)\phi(\overrightarrow{x} - \overrightarrow{r}, t)d\overrightarrow{r} \tag{3.1}$$

Applying this filter to the Boussinesq system leads to the filtered Navier-Stokes equations. This system of equations is similar to the Reynolds system presented in Sect. 1.3.4, except that the turbulent fluxes are replaced by the tensors τ_{ij}, $\tau_{\theta j}$ and τ_{qj} (Eq. 3.12). Similarly to the Reynolds system, these terms are potentially new unknowns and must be parametrised to close the equations.

$$\frac{\partial \rho_r \widetilde{U_j}}{\partial x_j} = 0 \tag{3.2}$$

$$\frac{\partial \rho_r \widetilde{U_i}}{\partial t} + \widetilde{U_j}\frac{\partial \rho_r \widetilde{U_i}}{\partial x_j} = \rho_r g \frac{\widetilde{\theta_v^v}}{\theta_{v,r}}\delta_{i3} - \frac{\partial \widetilde{P^v}}{\partial x_i} + \rho_r F_c \epsilon_{ij3}(\widetilde{U_j} - U_{g,j}) + \nu \frac{\partial^2 \rho_r \widetilde{U_i}}{\partial x_j^2} + \widetilde{S_{m,i}} - \frac{\partial \rho_r \tau_{ij}}{\partial x_j} \tag{3.3}$$

$$\frac{\partial \rho_r \widetilde{\theta_v}}{\partial t} + \widetilde{U_j}\frac{\partial \rho_r \widetilde{\theta_v}}{\partial x_j} = S_\theta + \nu_\theta \frac{\partial^2 \rho_r \widetilde{\theta_v}}{\partial x_j^2} - \frac{\partial \rho_r \tau_{\theta j}}{\partial x_j} \tag{3.4}$$

$$\frac{\partial \rho_r \widetilde{q_T}}{\partial t} + \widetilde{U_j}\frac{\partial \rho_r \widetilde{q_T}}{\partial x_j} = S_q + \nu_q \frac{\partial^2 \rho_r \widetilde{q_T}}{\partial x_j^2} - \frac{\partial \rho_r \tau_{qj}}{\partial x_j} \tag{3.5}$$

Let's consider the turbulent tensor $\tau_{\phi j}$ where ϕ is either u_i, θ_v or q_T. This can be developed into:

$$\tau_{\phi j} = \widetilde{\phi u_j} - \widetilde{\phi}\widetilde{u_j} \tag{3.6}$$

$$= \widetilde{(\widetilde{\phi} + \phi")(\widetilde{u_j} + u_j")} - \widetilde{(\widetilde{\phi} + \phi")}\widetilde{(\widetilde{u_j} + u_j")} \tag{3.7}$$

$$= \left[\widetilde{\widetilde{\phi}\widetilde{u_j}} - \widetilde{\widetilde{\phi}}\widetilde{\widetilde{u_j}}\right] + \left[\widetilde{\widetilde{\phi} u_j"} + \widetilde{\phi" \widetilde{u_j}} - \widetilde{\widetilde{\phi}}\widetilde{u_j"} - \widetilde{\phi"}\widetilde{\widetilde{u_j}}\right] + \left[\widetilde{\phi" u_j"} - \widetilde{\phi"}\widetilde{u_j"}\right] \tag{3.8}$$

We can thus write $\tau_{\phi j} = L_\phi + C_\phi + R_\phi$ where L_ϕ (Leonard stress), C_ϕ (crossed stress) and R_ϕ (Reynolds SGS stress) are respectively the terms in the first, second and third brackets. Each of these terms can be modelled separately but in practice, it is very common to model the whole subgrid stress with a unique formula, similar to the K-theory:

$$\tau_{ij}^{a} = -K_m\Big(\frac{\partial\widetilde{u_i}}{\partial x_j} + \frac{\partial\widetilde{u_j}}{\partial x_i}\Big) \tag{3.9}$$

$$\tau_{\theta j} = -K_\theta \frac{\partial\widetilde{\theta_v}}{\partial x_j} \tag{3.10}$$

$$\tau_{qj} = -K_q \frac{\partial\widetilde{q_T}}{\partial x_j} \tag{3.11}$$

Where τ_{ij}^{a} is the anisotropic subgrid stress tensor, which is a modification of τ_{ij} to have a tensor of trace equal to 0 (k_{sgs} is the subgrid TKE):

$$\tau_{ij}^{a} = \widetilde{u_i"u_j"} - \widetilde{u_i"}\widetilde{u_j"} - \frac{2}{3}\delta_{ij}k_{sgs} \tag{3.12}$$

$$k_{sgs} = \frac{1}{2}(\widetilde{u_i u_i} - \widetilde{u_i}\widetilde{u_i}) \tag{3.13}$$

And where the K_m, K_θ and K_q can be modelled for instance with the Smagorinsky model [133] which gives for the momentum:

$$K_m = (c_s\Delta)^2\sqrt{2\mathcal{S}_{ij}\mathcal{S}_{ij}} \tag{3.14}$$

where Δ is the mesh size, c_s is a constant and $\mathcal{S}_{ij}$ is the strain-rate tensor:

$$\mathcal{S}_{ij} = \frac{1}{2}\Big(\frac{\partial\widetilde{u_i}}{\partial x_j} + \frac{\partial\widetilde{u_j}}{\partial x_i}\Big). \tag{3.15}$$

This model is only diffusive (because K_m is always positive) and assumes isotropic turbulence. It thus cannot take into account backscattering arising near the walls or the anisotropy that exists in stable conditions. This type of formulation is still popular among the LES community even if more complex models have been developed e.g. [134].

Remarks on the notations

At this point, Eq. 3.14 combined with Eq. 3.3 is not very different from Eq. 1.39 with a K-formulation. Many LES parametrisations are inspired by RANS parametrisations. The main difference at the end is that a filtered field $\widetilde{\phi}$ remains an unsteady random variable from which we can still extract a mean and turbulent motion. Moreover, every second-order momentum has a resolved and subgrid part: both must be taken into account to represent the actual amount of said variable.

In the following parts and especially in the results, the first-order variables such as $\widetilde{U}$, $\widetilde{\theta}$ or $\widetilde{P}$ will be assumed equal to the 'real' values and thus written without the tilde (because anyway the subgrid components of these quantities cannot be computed). An overbar or a prime will denote respectively the time-averaged and the varying parts of this filtered variable. Except specified otherwise, the value of the second-order variables in this work (such as $\overline{\theta' w'}$ or k) are reduced to their resolved values. Even though the subgrid part should theoretically be taken into account, this choice was initially made to match the SWiFT requirements and was kept for the other part of this work since the same data were re-used.

3.1.3 Implicit filtering

Applying the low-pass filter defined by Eq. 3.1 on every field can be an expensive operation, in particular because for a filter of width Δ_G to work properly, it needs to be applied on a spatial resolution $\Delta < \Delta_G$. Indeed, the discretising operation acts already as a low-pass filter, since a field can only have a constant value over a cell. An alternative approach of LES is to not use any explicit filter G but only the implicit filtering of the discretisation. It allows using all the computational power to take Δ as low as possible and also substantially simplifies the method. This approach is the most commonly used nowadays, and in particular in Meso-NH. We thus replace the Reynolds operator with the filtering operator $\widetilde{.}$ in all the equations of Ch. 1.

This comes however with disadvantages that must be kept in mind. A numerical artefact is used for filtering whereas turbulence modelling is based on a physical approach: numerics and modelling become coupled. Theoretically, one should develop a new SGS model every time a new discretisation method is used, which is not the case in practice. Moreover, some methods such as grid convergence become obsolete because changing the grid changes the physics at stake. At best one can expect that the LES solution converges to the DNS solution as $\Delta \to 0$. Finally, the implicit filter due to discretisation and numerics is unknown, and no reverse filter exists as it can be the case for explicit filters.

"Implicit LES filtering" must not be confused with "implicit LES" which is a particular branch of LES where the mesh size is taken as low as possible and no SGS model is used [135]. This approach is also called rough DNS and is not treated in this thesis.

3.2 Meso-NH

3.2.1 General presentation

Meso-NH (MESOscale Non Hydrostatic) is an open-source research code for ABL simulations developed by the Centre National de Recherches Météorologique and the Laboratoire d'Aérologie. The first version of the model is presented in [136], and recent updates are shown in [33]. It can deal with scales ranging from synoptic (hundreds of kilometres) to micro-scale (around a meter). In this work, version 5-4-3 is used, with user modifications, in particular for the ALM implementation that has only been introduced in the main release from V5-5-0. The mesh generator can take into account the orography of complex terrains, and several physical schemes allow the modelling of phenomena such as clouds and precipitation. Moreover, it can be coupled with chemical or surface schemes, leading to a broad variety of capabilities ranging from cyclones to urban heat island predictions [33]. The code is parallelised to run on supercomputers. Meso-NH solves the anelastic, non-hydrostatic, filtered system formed by Eqs 3.2, 3.3, 3.4 and 3.5. In this thesis, only dry air is considered: the moisture equation (Eq. 3.5) is neglected and $\theta_v = \theta$.

The equations are solved on an Arakawa grid: the velocity variables are positioned on the frontier of each cell whereas the other variables (temperature, subgrid TKE...) take place at the centre of the cells. Meso-NH allows taking into account the Earth's curvature, but in this work, only the Cartesian frame is used, where the curvature of the Earth is neglected and the latitude and longitude are kept constant. For the wind advection, we use in this work a centred scheme of fourth-order (CEN4TH)

for the spatial integration and Runge-Kunta fourth-order scheme (RKC4) for the time integration. In Meso-NH, this combination of schemes gives the finest effective resolution, of the order of $4\Delta x$ [33], i.e. the largest resolved turbulent structures will be at best four times the mesh size. Other combinations with schemes of lower order can be used, for instance for a fast computation or if a domain with steep gradients is needed, but lead to coarser effective resolution and are thus not used herein.

For theoretical studies, Meso-NH is often used in its "idealised" mode, described in the following lines. Horizontally-constant profiles of velocity, temperature and moisture are imposed on the whole domain as the initial conditions. Then, a perturbation field is set, either on the vertical component of the velocity or the temperature field. This perturbation leads to the creation of turbulent eddies much faster than if it had to naturally develop. Moreover, the equations of Meso-NH are modified to model the horizontal synoptic pressure gradient, which cannot be naturally taken into account in too small domains. To do so, the geostrophic wind velocity U_g is imposed by the user, and the forcing is incorporated in the momentum equation (Eq. 1.35). Alternatively, Meso-NH can be used in its "real" mode where all these steps are replaced with a coupling with meteorological fields extracted from large-scale forecasting models or reanalysis data.

3.2.2 Turbulence closure

Meso-NH is built to work on both mesoscale and LES resolutions. Consequently, turbulence modelling is the same for any resolution; only the formulation of the mixing length differs. A one-and-a-half closure is chosen (see Sect. 1.3.6) with a prognostic equation for k_{sgs} [137]. Starting from Eq. 1.42 with the filter operator instead of the Reynolds average, the molecular diffusion term is neglected because meteorological models are often too coarse to resolve the viscous sublayer, and the turbulent transport and pressure correlation terms are modelled as [138]:

$$\rho_r \widetilde{k_{sgs} u_k''} + \widetilde{u_k'' P^{v''}} = -C_{TT} \rho_r l_m k_{sgs}^{1/2} \frac{\partial k_{sgs}}{\partial x_j} \tag{3.16}$$

where C_{TT} is a constant. The subgrid TKE is the turbulence of length scale smaller than the mesh size. It can be obtained by combining Eqs. 1.12 and 1.13 for $\Phi_\Delta = 2\pi/\Delta$. The viscous dissipation is then deduced:

$$k_{sgs} = \int_{\Phi_\Delta}^{\infty} K_1 \epsilon_D^{2/3} \Phi^{-5/3} d\Phi = -\frac{3}{2} K_1 \epsilon_D^{2/3} \Phi_\Delta^{-2/3} \quad \Rightarrow \quad \epsilon_D = C_\epsilon \frac{k_{sgs}^{3/2}}{\Delta} \tag{3.17}$$

where C_ϵ is a constant. Note however that this parametrisation is only viable in the inertial subrange. It will not work in mesoscale simulations where the grid size is much larger than the largest eddy of the inertial range or in the case of a stably stratified flow or a flow too close to the ground where the Richardson-Kolmogorov cascade is not verified (see last paragraph of Sect. 1.2.3). Δ is thus replaced by the mixing length l_m which will be equal to the grid size in the case of LES in a convective or neutral case but will be modified in mesoscale simulations or for a stable LES case. As a result, the subgrid TKE equation is written in Meso-NH:

$$\frac{\partial k_{sgs}}{\partial t} = -\frac{1}{\rho_r}\frac{\partial}{\partial x_j}(\rho_r k_{sgs}\widetilde{U_j}) - \widetilde{u_i"u_j"}\frac{\partial \widetilde{U_i}}{\partial x_j} + \frac{g\widetilde{w"\theta_v"}}{\theta_{v,r}} + \frac{1}{\rho_r}\frac{\partial}{\partial x_j}\Big(C_{2m}\rho_r l_m k_{sgs}^{1/2}\frac{\partial k_{sgs}}{\partial x_j}\Big) - C_\epsilon\frac{k_{sgs}^{3/2}}{l_m} \quad (3.18)$$

There are still turbulent fluxes that need to be modelled to close the equations. To formulate this closure, the full equation of every second-order momentum had been developed. Then, several assumptions were made on these fluxes to simplify them as [137] :

$$\widetilde{u_i"u_j"} = \frac{2}{3}\delta_{ij}k_{sgs} - \frac{4}{15}\frac{l_m}{C_m}k_{sgs}^{1/2}\Big(\frac{\partial \widetilde{u_i}}{\partial x_j} + \frac{\partial \widetilde{u_j}}{\partial x_i} - \frac{2}{3}\delta_{ij}\frac{\partial \widetilde{u_k}}{x_k}\Big) \quad (3.19)$$

$$\widetilde{u_i"\theta"} = -\frac{2}{3}\frac{l_m}{C_{p\theta}}k_{sgs}^{1/2}\frac{\partial\widetilde{\theta}}{\partial x_i}\phi_i \quad (3.20)$$

$$\widetilde{u_i"q_T"} = -\frac{2}{3}\frac{l_m}{C_{pq}}k_{sgs}^{1/2}\frac{\partial\widetilde{q_T}}{\partial x_i}\psi_i \quad (3.21)$$

where $C_{p\theta}$, C_{pq}, C_m are constants. Similar expressions can be derived for $\widetilde{\theta"^2}$, $\widetilde{q_T"^2}$ and $\widetilde{\theta"q_T"}$ but these fluxes are only used in subgrid condensation schemes which are not in the scope of this work. ϕ_i and ψ_i are stability functions. These functions are unity for horizontal directions ($\phi_1 = \phi_2 = \psi_1 = \psi_2 = 1$). In the vertical direction, these functions cast the buoyancy effects into the fluxes and are written:

$$\phi_3 = 1 - \frac{(1 + A_1R_{q1}\big(2A_2R_{\theta q}^2 + A_1R_{\theta 3}^2\big)R_{\theta_1}^{-1} + A_1A_2(R_{\theta 3}^2 - R_{q3}^2)}{1 + (A_1 + A_2)(R_{\theta 1} + R_{q1}) + A_1\big[A_2(R_{\theta 1}^2 + R_{q1}^2) + A_1R_{\theta 1}R_{q1}\big]} \quad (3.22)$$

$$\psi_3 = 1 - \frac{(1 + A_1R_{\theta 1})\big(2A_2R_{\theta q}^2 + A_1R_{q3}^2\big)R_{q_1}^{-1} + A_1A_2(R_{q3}^2 - R_{\theta 3}^2)}{1 + (A_1 + A_2)(R_{\theta 1} + R_{q1}) + A_1\big[A_2(R_{\theta 1}^2 + R_{q1}^2) + A_1R_{\theta 1}R_{q1}\big]} \quad (3.23)$$

where $A_1 = \frac{2}{3}\frac{1}{C_{p\theta}C_{\epsilon\theta}}$, $A_2 = \frac{2}{3}\frac{1}{C_{p\theta}C_{q\theta}}$ and R are the dimensionless numbers of Redelsperger:

$$R_{\theta 1} = \frac{g}{\theta_{v,r}}\frac{l_m^2}{k_{sgs}}E_\theta\frac{\partial\widetilde{\theta}}{\partial z} \quad (3.24)$$

$$R_{q1} = \frac{g}{\theta_{v,r}}\frac{l_m^2}{k_{sgs}}E_q\frac{\partial\widetilde{q}}{\partial z} \quad (3.25)$$

$$R_{\theta 3} = \frac{g}{\theta_{v,r}}\frac{l_m^2}{k_{sgs}}E_\theta\sqrt{\Big(\frac{\partial\widetilde{\theta}}{\partial x_k}\frac{\partial\widetilde{\theta}}{\partial x_k}\Big)} \quad (3.26)$$

$$R_{q3} = \frac{g}{\theta_{v,r}}\frac{l_m^2}{k_{sgs}}E_q\sqrt{\Big(\frac{\partial\widetilde{q_T}}{\partial x_k}\frac{\partial\widetilde{q_T}}{\partial x_k}\Big)} \quad (3.27)$$

$$R_{\theta q} = \Big(\frac{g}{\theta_{v,r}}\frac{l_m^2}{k_{sgs}}\Big)^2E_\theta\frac{\partial\widetilde{\theta}}{\partial x_k}E_q\frac{\partial\widetilde{q}}{\partial x_k} \quad (3.28)$$

where $E_\theta = \dfrac{\widetilde{\theta_v}}{\theta}$ and $E_q = 0.61\widetilde{\theta}$ also to take into account the effect of moisture in the equations. In the version of Meso-NH used in the present work (V5.4.3), the different constants are set to the values given in Table 3.1.

C_ϵ	C_{2m}	C_m	$C_{p\theta}$	C_{pq}	$C_{\epsilon\theta}$	$C_{q\theta}$
0.85	0.2	4	4	4	1.2	2.4

Table 3.1: Values of the constants of the MNH subgrid parametrisation.

3.2.3 Mixing length

The last step is to parametrise the mixing length l_m which appears in the subgrid fluxes parametrisation and subgrid TKE energy. It will be assumed that it has the same expression in every term it appears. In the case of Reynolds averaging it was interpreted as the size of the largest eddies feeding the Kolmogorov-Richardson cascade. In the LES framework, it could be called a 'subgrid mixing length' because it corresponds to the largest subgrid eddy of the cascade [137]. A first approximation could be to simply write it as the mean size of the cells:

$$l_m = \left(\Delta_x \Delta_y \Delta_z\right)^{1/3} \tag{3.29}$$

However, this relies on the hypothesis that the grid size is inside the inertial region, which would not be the case in three situations: in a very stable ABL, if Meso-NH is used in "mesoscale" mode, and near the ground. Three approaches are used in Meso-NH to cope with these issues:

- To account for the reduction of the mixing length in a stably stratified ABL, a correction to Eq. 3.29 is introduced [138]. In the following, it will be called the Deardorff mixing length or simply DEAR:

$$l_m = \min\left(\left(\Delta_x \Delta_y \Delta_z\right)^{1/3}, 0.76\left(\frac{k_{sgs}}{N_{BV}^2}\right)^{1/2}\right) \tag{3.30}$$

  where $N_{BV} = \sqrt{\dfrac{g}{\theta_r}\dfrac{\partial \theta_r}{\partial z}}$ is the Brunt-Väisälä frequency.

- When Meso-NH is working in its mesoscale mode, the mesh size is much larger than the size of the largest eddies of the Kolmogorov-Richardson cascade. Another mixing length $l_{m,RM17}$ is introduced which is related to the distance an air parcel can travel upward and backwards, confined by stratification and ground [139].

- To use the DEAR model, one needs to assume that the cells of the mesh are almost isotropic [140]. However, it might not be the case, particularly close to the ground where it is common to refine the vertical mesh. In these strongly stretched cells, it is possible to use an adaptive mixing length (abbreviated HM21):

$$l_m = \min\left(\frac{1}{2}\sqrt{\Delta X \Delta Y}, l_{m,RM17}\right). \tag{3.31}$$

With this mixing length, the turbulence spectrum is similar to the one obtained with the DEAR mixing length, and it gives a satisfying total TKE profile.

- Finally, to improve the mixing length near the ground, a correction can be applied to the mixing length l_m and the dissipation length l_m/C_ϵ [141]. This leads to a better match with the canonical logarithmic profile. If the HM21 mixing length is used, this correction is only applied to the $l_{m,RM17}$ part.

3.2.4 Grid nesting

The grid nesting technique [142] allows resolving a limited region of the computational domain (for instance, the wind turbine's wake region) with a higher spatial resolution. The idea is to compute in parallel two computational domains: a large one with a relatively coarse mesh (CM) and a smaller one with a finer mesh (FM). In Meso-NH, the grid nesting is only available in the horizontal direction i.e. the vertical mesh for CM and FM is the same. The mesh size ratio must be an integer lower or equal to five, and a different time step can be applied to both models (to fulfil the CFL condition in all models).

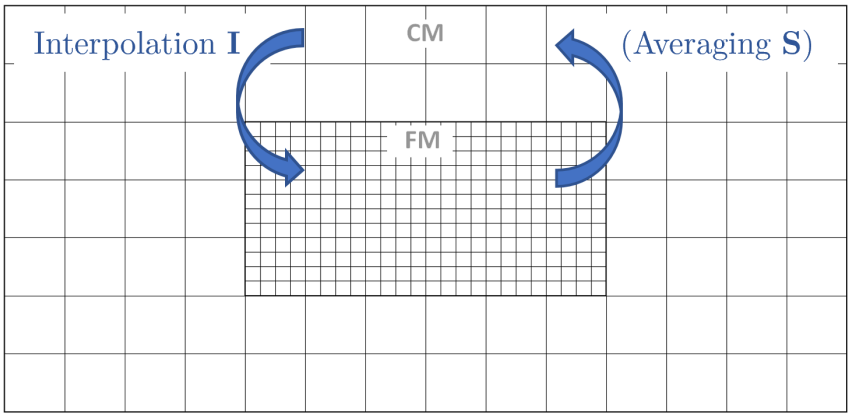

Figure 3.2: Grid nesting principle in Meso-NH

Figure 3.2 describes the two modes of grid nesting. In the 'one-way grid nesting' (abbreviated 1WAY), the FM boundaries are derived through interpolation of the CM flowfield (operation **I**). If the 'two-way grid nesting' (abbreviated 2WAY) is used, the FM also affects the CM model through a relaxation procedure (operation **S**).

3.3 The actuator line method (ALM)

3.3.1 Principle

In the ALM, the wind turbine blades are modelled by lines of body forces, i.e. momentum source terms $S_{m,i}$ added to the momentum equation (Eq. 1.35). Blade element theory [143] quickly presented in Sect. 2.1.2 and tabulation in airfoil data of each blade allow computing the values of the body

forces [144]. The infinitesimal force $\overrightarrow{F(r)_{2D}}$ associated with an airfoil that encounters a relative velocity of norm U_{rel} (Eq. 2.1) is given by:

$$\overrightarrow{F(r)_{2D}} = \frac{1}{2}\rho c_a ||\overrightarrow{U_{rel}}^2|| (C_L(\alpha, Re)\overrightarrow{e_L} + C_D(\alpha, Re)\overrightarrow{e_D}) \tag{3.32}$$

where $c_a$is the chord of the airfoil, C_D and C_L are the drag and lift coefficients associated with the studied airfoil, associated with the unitary vectors $\overrightarrow{e_L}$ and $\overrightarrow{e_D}$. These coefficients are usually in the form of tabulated data as a function of the local angle of attack α and possibly the Reynolds number. These data either come from 2D numerical simulations of the airfoil geometry or wind tunnel measurements. The local angle of attack is deduced from $\alpha = \Psi - \gamma_l$ where $\gamma_l(r)$ is the local pitch angle (sum of the pitch of the blade and the twist) and $\Psi = \tan^{-1}(U_x/(\Omega r - U_\varphi))$ is the angle between the relative velocity and the rotor plane (U_φ and U_x are defined in Eq. 2.1). The source term $S_{m,i}$ to add to the momentum equation is then deduced by multiplying F_{2D} with the size of the body force, i.e. the length of the blade divided by the number of body forces.

3.3.2 Smearing

In order to ensure numerical stability, the body forces are smeared to the neighbouring cells. The most common method used in the wind energy community is the convolution with a 3D Gaussian kernel [144] :

$$S_m = \delta b F_{2D} * * * \eta_\epsilon \tag{3.33}$$

$$\eta_\epsilon = \frac{1}{\epsilon_k^3 \pi^{3/2}} \exp\left[-(d/\epsilon_k)^2\right] \tag{3.34}$$

where δb is the size of the body force element, $* * *$ is a 3D convolution product, ϵ_k is the kernel size and d is the distance between the element and the cell where the force is computed. To enforce numerical stability, a value of $\epsilon = 2\Delta$ (where Δ is the grid resolution) is recommended [145].

Due to this smearing, there is not a sharp edge at the tip of the blade, which leads to overestimated efforts at this location. The most straightforward approach to correct this issue has been to use the Glauert correction [143] even though it was originally meant to artificially add the effect of a finite number of blades in actuator disk methods. It writes:

$$C_G = \frac{2}{\pi}\cos^{-1}\left[\exp\left(-\frac{N_b(D/2 - r)}{2r\sin(\Psi)}\right)\right] \tag{3.35}$$

The correction is then used as a factor to C_L and C_D in Eq. 3.32. An alternative is to use a kernel size that is based on the chord instead of the mesh size, but enforcing $\epsilon_k \geq 2\Delta$ for numerical stability [146].

3.3.3 Implementation in Meso-NH

The ALM has been implemented in Meso-NH to study the interactions between the ABL and wind turbines [10, 147]. Instead of computing directly the relative velocity, it has been preferred to build one coordinate system for each part of the turbine described in Sect. 2.1.1 plus one 'global' which

corresponds to the Meso-NH domain. They are called R_G, R_T, R_N, R_H, R_{B_i} and $R_{E_{i,j}}$ respectively for the global, tower, nacelle, hub, blade i and element j of the blade i. The transfer matrices between each coordinate system are computed at every time step. Once these matrices are known, the computation of relative velocities is easier:

$$\overrightarrow{U_{rel}^{ij}}|_{R_{E_{ij}}} = M_{R_{E_{ij}} \longrightarrow R_{G_{ij}}} \cdot \overrightarrow{U^{ij}}|_{R_{G_{ij}}} - \overrightarrow{U_{trans}^{ij}}|_{R_{E_{ij}}} \tag{3.36}$$

$$\alpha = \tan^{-1}\left(\frac{\overrightarrow{U_{rel}^{ij}}|_{R_{E_{ij}}} . \vec{x}}{\overrightarrow{U_{rel}^{ij}}|_{R_{E_{ij}}} . \vec{y}}\right) \tag{3.37}$$

where $\overrightarrow{U_{trans}^{ij}}|_{R_{E_{ij}}}$ is the translation velocity, equal to $\vec{0}$ if the tower is not moving. The infinitesimal lift and drag forces can be computed with:

$$\delta L = \frac{1}{2} C_L \rho c_a U_{rel}^2 dr \tag{3.38}$$

$$\delta D = \frac{1}{2} C_D \rho c_a U_{rel}^2 dr. \tag{3.39}$$

C_L and C_D are deduced from a cubic spline interpolation of tabulated data of the different airfoils composing the blades. These forces must be rotated by an angle of α and put in the global frame (multiplication by $M_{R_{G_{ij}} \longrightarrow R_{E_{ij}}}$). The resulting body forces to insert into the Meso-NH momentum equation is finally computed by applying the smearing in Eq. 3.33. For practical reasons however, the Gaussian kernel is not used, but the body forces are smeared linearly to the neighbouring cells [10].

Similarly to the blades, the forces induced by the tower and nacelle can be taken into account. During this Ph. D we implemented in Meso-NH a drag force that corresponds to the drag of a cylinder (the wind is coming from the side for the tower and from the top for the nacelle), with $C'_{\text{nacelle}} = 4$ and $C'_{\text{tower}} = 0.68$, according to [148]:

$$F_{\text{nacelle}} = -\rho \frac{1}{2} C'_{\text{nacelle}} U^2_{\text{nacelle}} \frac{\pi}{4} D^2_{\text{nacelle}} \tag{3.40}$$

$$F_{\text{tower}} = -\rho \frac{1}{2} C'_{\text{tower}} U^2_{\text{tower}} D_{\text{tower}} z_h \tag{3.41}$$

Time step requirement and time-splitting

The main drawback of the ALM is that it implies a strong requirement on the time step value: the blade tip must not cross more than one cell per time step [149]. This criterion, written $\Delta t_{CFL-ALM}$, is usually more constraining than the time step requirement of the LES code which imposes that a flow particle does not cross more than one cell at each time step, written $\Delta t_{CFL-MNH}$. As shown in Eq. 3.42, they are approximately related through the tip speed ratio λ_T, which is most of the time higher than one. As a consequence, the time step in the whole Meso-NH domain must be reduced because of the actuator line leading to a needlessly small time step for most of the simulation domain, and thus an increased simulation cost.

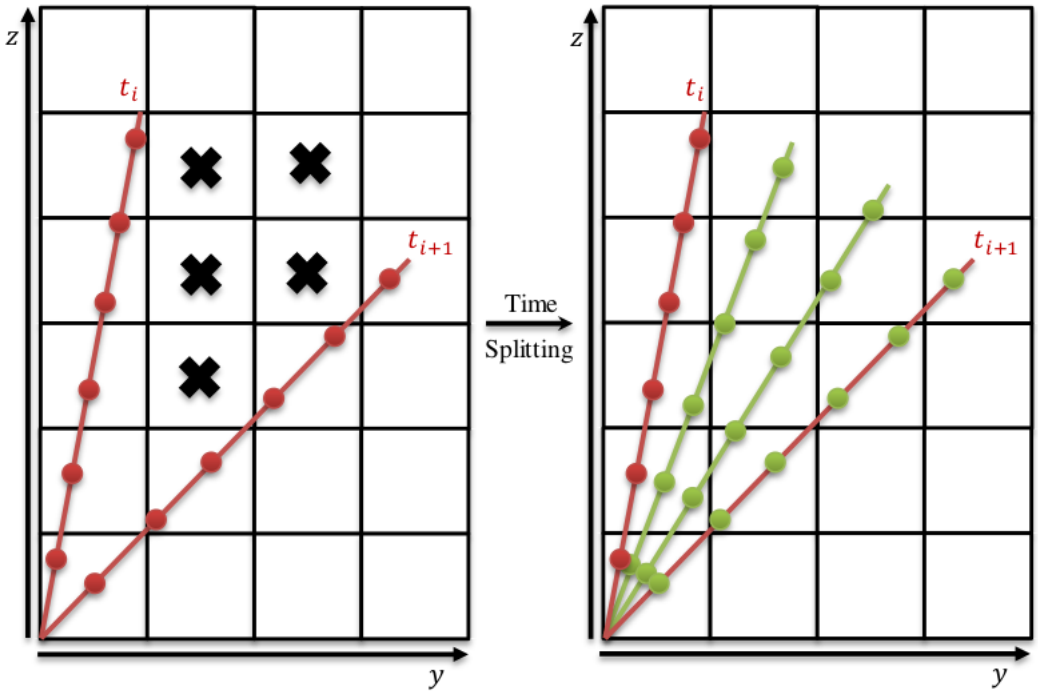

Figure 3.3: Schematic of the time splitting principle. Courtesy of [10]

$$\Delta t_{CFL-ALM} \approx \frac{\Delta x_i}{\Omega D/2} = \frac{U}{\Omega D/2}\frac{\Delta x_i}{U} = \frac{1}{\lambda_T}\Delta t_{CFL-MNH} \tag{3.42}$$

To cope with this major issue, a 'time-splitting' method has been introduced in Meso-NH, which results in something similar to the Actuator Sector Method presented in [150]. The principle is to keep $\Delta t = \Delta t_{CFL-MNH}$ for the whole simulation. When it predicts that the blade will cross n per time step cells with $n > 1$, n sub-iterations of the ALM are called at different locations, as shown in Fig. 3.3.

Validation situation at the beginning of the present Ph. D.

The ALM in Meso-NH and the time splitting method have been validated against wind tunnel measurements of the MEXICO case [10]. For up to nine sub-iterations, both normal and tangential efforts gave similar results to the simulation fulfilling the usual ALM criterion, as displayed in Fig. 3.4. The wakes (not shown here) gave good results as well for less than five sub-iterations of the time-splitting method. Whether with or without the time splitting, this ALM implementation seems to slightly overestimate the tangential efforts of the blades. This issue is attributed to the smearing technique, which needs to be adapted.

The MEXICO case is however quite simplified compared to an actual wind turbine case: it is based on measurements in a wind tunnel with a constant inflow, and the turbine is relatively small. Further validation must thus be performed, for a more realistic inflow with sheer, veer and all the other physical phenomena likely to occur in the ABL.

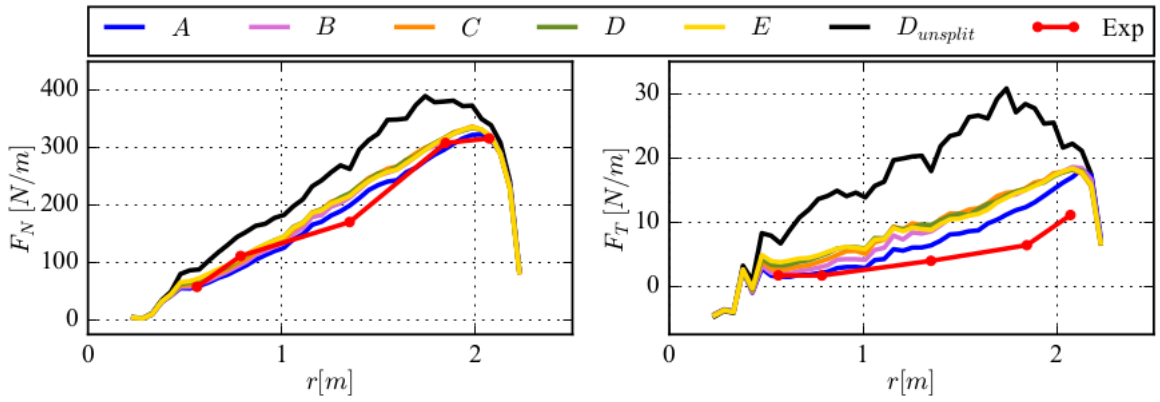

Figure 3.4: Comparison of the normal and tangential efforts per unit length along the blade, evaluated in Meso-NH against the Mexico experiments (red). Case A is with $\Delta t = \Delta t_{CFL-ALM}$ without time splitting, cases B to E are with time-splitting with respectively 3, 5, 7 and 9 sub-iteration and the simulation in black is with $\Delta t = \Delta t_{CFL-MNH}$ without time splitting. Courtesy of [10].

Conclusion of the chapter

In this chapter, we introduced the high-fidelity numerical method called large eddy simulations and the Meso-NH code that numerically solves the Boussinesq system with LES. The ALM, a body force method used to model the effects of wind turbines on the atmosphere, was also described. At this point, sufficient theoretical concepts have been introduced in this thesis to simulate the atmosphere's dynamics. However, the ALM implementation in Meso-NH lacks validation of the wake properties under a realistic ABL. In the next chapter, the interaction between the ABL and wind turbine wakes in Meso-NH is validated against an international benchmark for different atmospheric conditions. The results will be used in further chapters to analyse the interaction between ABL and wakes and propose an analytical model.

Part II

Part B - High fidelity simulations of wind turbine wakes

Chapter 4

Validation with the SWiFT benchmark

At the beginning of this Ph. D, the ALM in Meso-NH was validated for two cases: on one hand, the loads and the wake were validated against the MEXICO (Model Experiments in Controlled Conditions) experimental results that were performed in a wind tunnel. On the other hand, the formation of clouds due to wakes within an offshore wind farm has been successfully reproduced [147, 151]. The former is based on reduced-scale measurements without turbulence whereas the latter is mostly qualitative. The present chapter aims at completing this validation with a comparison of the wake computed by Meso-NH/ALM with an international benchmark for different cases of stability. Comparing our results with the literature is a necessary step before using them for a physical analysis (Chs. 6 and 7 in particular). First, the benchmark is introduced. Then the methodology is described and finally we present results for the three cases of stability of the benchmark: near neutral, strongly stable and weakly unstable. Additionally, the neutral case is used for a sensitivity study on the time step size and on the time-splitting method. The main results of this chapter have been published and presented at the Journées de l'hydrodynamique 2020 and WAKE 2021 conferences [152].

4.1 Overview of the problem

4.1.1 Presentation of the SWiFT benchmark

SWiFT (Scaled Wind Farm Technology) is a facility funded by the United States Department of Energy, operated by Sandia National Laboratories as well as National Renewable Energy Laboratory (NREL), and hosted at Texas Tech University's National Wind Institute Research Center in Lubbock, Texas. The SWiFT site is located in the U.S. Great Plains and is therefore assumed to be exempt from complex, terrain-induced flow patterns. In the absence of weather phenomena, the atmospheric conditions at the SWiFT site approximate canonical diurnal cycles: the characteristics of wakes can be measured without the influence of complex terrain and weather [153].

The NREL has organised an international exercise of code intercomparison based on this facility, called hereafter 'SWiFT benchmark'. It compares different types of codes (steady-state analytical models, DWM-type models, RANS and LES) from different institutions around the world: NREL, DTU (Danmarks Tekniske Universitet), IFPEN, and ForWind [80]. This benchmark aimed at assessing the capability of the different codes to reproduce the wake of a single wind turbine in an

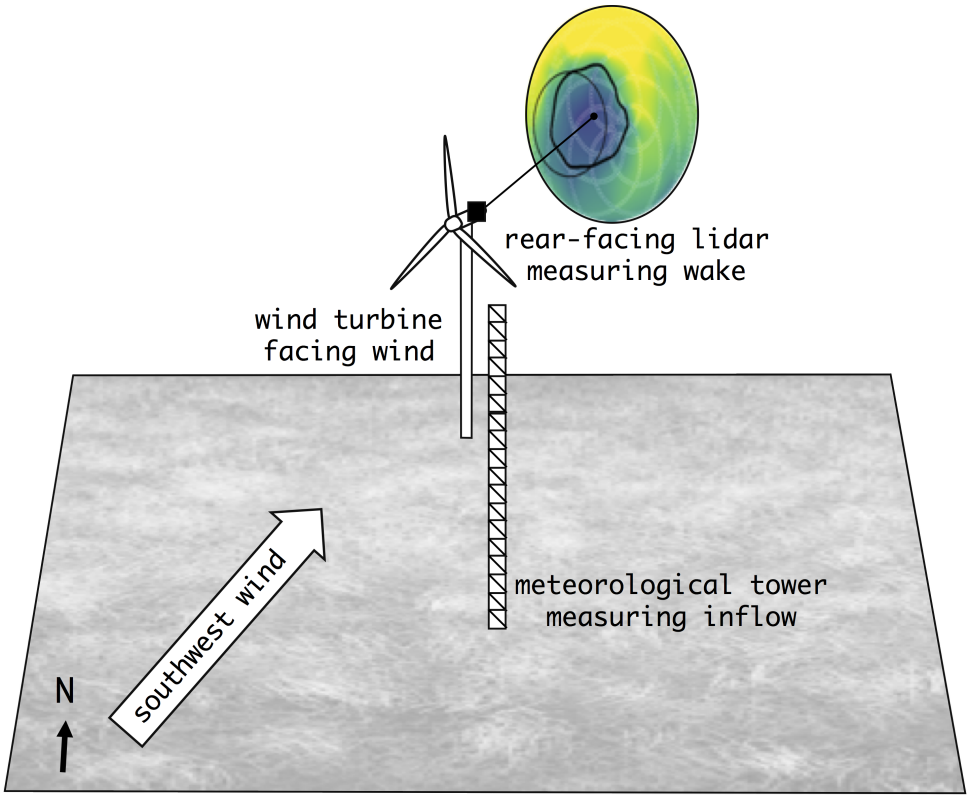

Figure 4.1: Schematic of the SWiFT facility used for this benchmark. From https://wakebench-swift.readthedocs.io/en/latest/measurements.html.

atmospheric inflow. The turbine is a classical 3-bladed HAWT of diameter $D = 27$ m and hub height $z_h = 32.1$ m. A LiDAR mounted on the nacelle measures the wake at different locations downstream, and a meteorological mast measures the inflow conditions. The lidar sampling period was set to about 30–42 s for the neutral and stable cases, where the measurements focused on the spatial evolution of the mean wake. It was set to about 2 s in the unstable case in order to compute the dynamic behaviour such as wake meandering, but was restrained at one distance downstream: $x = 3D$ [19]. A scheme of the experimental facility is displayed in Fig. 4.1.

Variable	Notation	Height	Neutral	Unstable	Stable
Hub height velocity	$\overline{U}_{H,h,\infty}$	32.1 m	8.7 m s^{-1}	6.7m s^{-1}	4.8m s^{-1}
Hub height TI	I	32.1 m	10.7 %	12.6 %	3.4 %
Roughness length range	z_0	-	$0.005 - 0.05$ m	$0.005 - 0.05$ m	$0.005 - 0.05$ m
Friction velocity	u_*	10 m	0.45 m s^{-1}	0.33m s^{-1}	0.08m s^{-1}
Stability parameter	ζ	10 m	0.004	-0.089	1.151
Kinematic vertical heat flux	$\overline{w'\theta'}$	10 m	-0.002 K m s^{-1}	0.023K m s^{-1}	-0.005 K m s^{-1}

Table 4.1: Inflow conditions measured with the meteorological mast.

4.1.2 Methodology

The SWiFT benchmark is decomposed into three steps:

- First, it is necessary to reproduce with fidelity the inflow conditions, which are listed in Table 4.1. The measurements are performed with the meteorological mast, approximately positioned $2.5D$ (65 m) upstream. In the simulations, it corresponds to the time- and lateral-averaged values in a plane 65 m upstream of the turbine. In the original publication [80], five criteria are examined to validate the inflow: mean horizontal wind speed profile, mean wind direction, turbulent kinetic energy and spectra of the u' and v' quantities. To have comparable outputs, modellers were asked to provide the 10-minutes series of u, v and w at a frequency of 1 Hz. Consequently, the TKE profile does not take into account the subgrid quantities and only the contribution of eddies of frequency comprised between 1.67×10^{-3} Hz (= 1/10 min) and 1 Hz (see Sect. 1.1.5). Likewise, spectra can only be computed in this range.

- Then, the wind turbine response is evaluated. Four variables were used in the original publication: the output thrust coefficient, power, torque and rotational speed. In this work, the rotational speed is fixed to the value corresponding to the output of the controller for the benchmark's velocity at hub height and is not changed during the simulation. Consequently, only the mean thrust coefficient $\overline{C}_T$ and the mean power of the generator $\overline{\mathcal{P}}_{gen}$ are studied. Note that no thrust measurements were available on the turbine and thus $\overline{C}_T$ is only compared against other numerical models.

- Finally, the velocity deficit in the wake is computed using the horizontal velocity in the inflow plane at hub height $\overline{U}_{H,\infty}$ as a reference velocity U_0 (Eq. 2.7). The results are plotted as a function of the spanwise (y) variable. The amount of meandering σ_f is also computed in both directions and compared between the LES codes. The only experimental data available for this variable is for the unstable case at $x/D = 3$.

Reaching the inflow conditions of the benchmark with Meso-NH is, however, not an easy task: the user cannot prescribe directly a given profile of wind speed or TKE. Instead, the geostrophic wind, initial conditions and ground forcing ($\overline{w'\theta'}$, z_0) must be tweaked to reach the desired inflow profile and values at hub height. The second main difficulty arising in this case is the wide range of scales involved. On one hand, a domain large enough must be used to take into account the largest scales of the atmospheric boundary layer. For the neutral and convective cases, domains must be several kilometres long and wide (for the stable case, large scales are damped, resulting in a domain smaller by an order of magnitude). On the other hand, best practices for the use of the ALM [145] advise using a mesh fine enough to have at least 30 mesh points per blade. For the SWiFT turbine, this condition is fulfilled with a resolution of 0.5 m. Meshing directly such a large domain with such fine resolution would result in a mesh size of $O(10^9)$, which would be unreasonably expensive to simulate.

To address these difficulties, a methodology, which is similar for the three cases of the benchmark, has been established and is schemed in Fig. 4.2. First, a domain of large dimensions and large mesh size ('father' domain D_1) is run for a couple of hours to let the turbulence establish in the whole domain: this is referred to as the D_1 spin-up in the following. The forcing parameters in Meso-NH were iteratively tuned to match as closely as possible the inflow conditions given in Table 4.1. Then, nestings (three for the neutral and convective cases and only one for the stable case) are performed

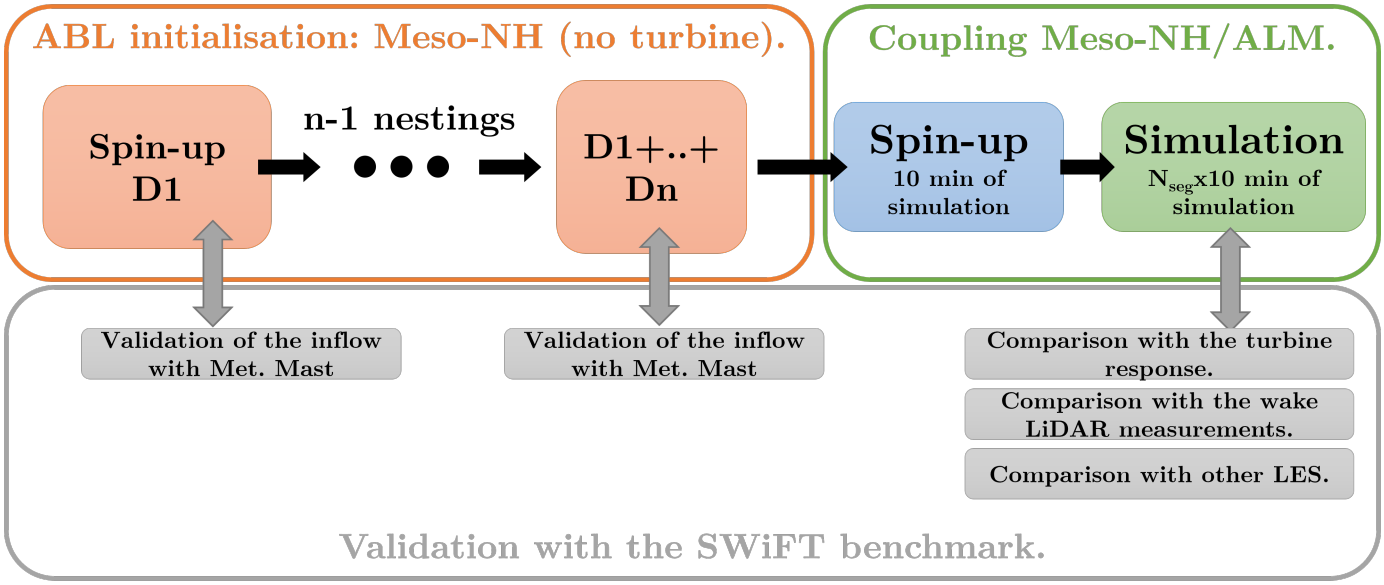

Figure 4.2: Flowchart of the methodology of the presented work.

to resolve the small scales in a restricted domain, and the turbine is finally placed in the smallest domain. After each nesting, 10 minutes of dynamics are simulated to evaluate the turbulence build-up region (see Sect. 4.1.3). After another validation with the inflow *in situ* data in the last domain, the ALM is activated in Meso-NH. This methodology comes with one main drawback: when nesting from a coarse to a fine mesh, the vertical profiles of wind velocity and directions slightly change: several iterations are thus needed to have the right flowfield in the most refined region.

When the ALM is activated, a spin-up of ten minutes is first simulated to let the wake establish and then the main run is launched. A given number of 10-minutes segments, noted N_{seg}, are simulated and the ensemble average of these segments is computed before comparing to the benchmark data i.e. *in situ* measurements and other LES codes. This averaging period of 10 minutes has been chosen in the benchmark and reused for the Meso-NH data to have similar outputs (see Sect. 1.1.5) but this choice has limitations as will be shown in the unstable case.

4.1.3 Turbulence build-up region

When nesting a domain D_i from a domain D_{i-1}, there is a region near the inlet in D_i where the turbulent structures are still of the size of the D_{i-1} mesh and progressively scale down to the size of the D_i mesh. To have a resolution corresponding to the actual mesh size (around $4\Delta X$ for the numerical schemed used herein), one needs to be outside of this turbulence build-up region. Thus, the domain D_{i+1}, or the turbine in the most refined region, must be placed downstream of the build-up region. This region can be seen with the naked eye (Fig. 4.3a), however, we propose a more quantitative approach: once the streamwise velocity PSD S_{uu} does no longer vary with x and that a neat cut-off frequency is seen, we consider to be outside of the build-up region.

This is illustrated for the neutral case between D_1 and D_2 in Fig. 4.3b. Near the inlet boundary of the domain (blue curve), the flow has not a clear cut-off at the frequency $f \simeq 0.55$ Hz corresponding to the domain's spatial resolution of 4 m. From Fig. 4.3b, one can see that the cut-off frequency

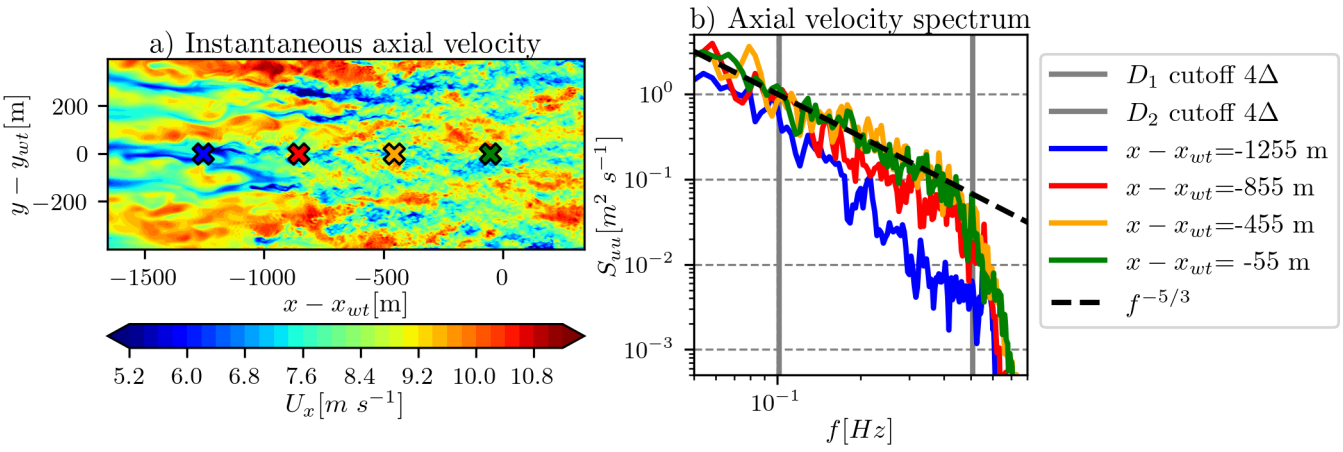

Figure 4.3: a) Instantaneous axial velocity at hub height in domain D_2. b) Velocity spectra at four positions downstream. The frequency corresponding to the resolution of the domain is drawn in grey.

of domain D_1 ($f \simeq 0.1$ Hz) has still an important influence on the flowfield at this location. This influence reduces progressively with the distance from the inlet, and the two last probes (orange and green) measure a similar spectrum with a neat cut-off frequency and follow correctly the canonical slope of the Kolmogorov cascade (dashed black line) for $f \leq 0.55$ Hz. It is thus decided to set the next nested domain D_3 at least after the green probe. This methodology is then applied to the domains D_3 and D_4 to have a correct turbulence cascade 65 m upstream of the wind turbine. The turbulence build-up region for D_3 and D_4 is smaller than for D_2. It can be attributed to the already smaller mesh in D_3 compared to D_2 or to the fact that the refinement ratio is smaller.

4.1.4 Numerical setup

The three Meso-NH simulations have a similar numerical setup, which is summed up here. Numerical parameters are listed in Tables 4.2, 4.3 and 4.4, for the neutral, unstable and stable cases. Meso-NH is used in the idealised mode: the flowfield is initialised with a constant-velocity profile equal to the geostrophic wind, and a constant temperature profile is also set, up to the arbitrarily defined ABL height, which is capped by an inversion region. To establish turbulence, a perturbation of the velocity field (for the neutral case) or temperature field (for the stable and unstable cases) is set at $t = 0$ and the simulation runs with only D_1. No orography nor surface scheme is used: the fluxes at the ground are directly imposed.

The size of the horizontal mesh depends on the domain D_i but the vertical mesh is the same for every domain. This is a limitation of Meso-NH which leads to flat cells near the ground and to a needlessly large number of vertical mesh points in the father domain. Near the ground, ΔZ is set to the targeted mesh in the last domain, so the cells around the turbine and in the wake are isotropic. Above the rotor-swept region, the vertical mesh is gradually stretched to reach $\Delta Z = 40$ m. Between the capping inversion and the top of the numerical domain, a buffer zone is set to absorb wave reflections from the top boundary condition.

Since cyclic boundary conditions are used for D_1, we must ensure that no turbulent structures expand from the inlet to the outlet. The domain dimensions L_X and L_Y are thus chosen for D_1 to be larger

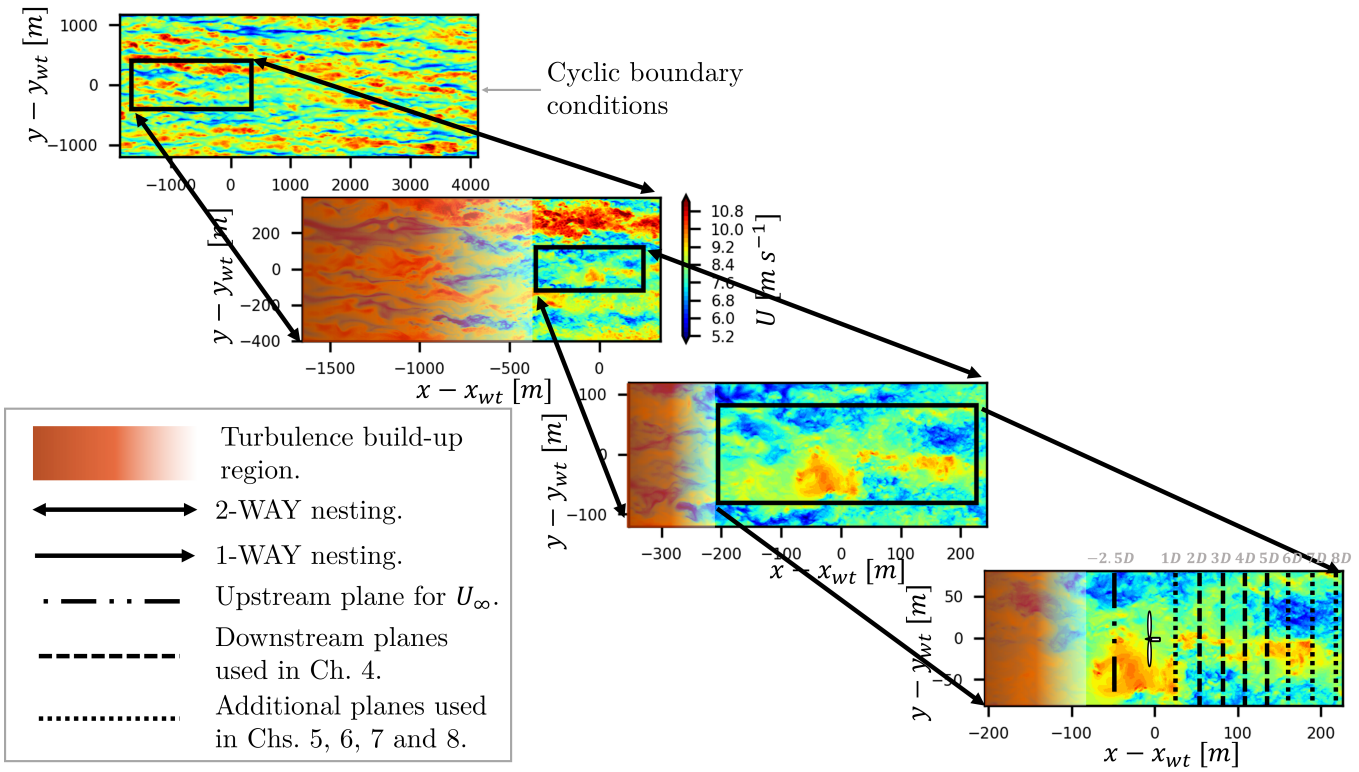

Figure 4.4: Illustration of the successive nestings in the neutral simulation.

than the largest eddies of the flow, typically a couple of times the ABL height. In nested domains (D_2, D_3 and D_4), boundary conditions are interpolated from D_{i-1} and the domain size is only constrained by the turbulence build-up region described in Sect. 4.1.3. The nested domains and their turbulence build-up regions are schematised in Fig. 4.4. The 2WAY nesting is used, except for the last domain which is nested with the 1WAY mode. It allows the largest domains to be blind to the wind turbine and prevent the wake to be recycled by the boundary conditions of D_1. However, one can argue that the 2WAY nesting could be used: except for the stable case, the father domain may be sufficiently large to have the wake fully dissipated before reaching the boundary conditions. The differences between 1WAY and 2WAY for the last nesting have been investigated and only small differences are found as long as the results are taken far from the outflow conditions (see Sect. A.1 in appendices). For the SWiFT study, the 1WAY nesting is thus chosen.

The time step in every domain is driven by the CFL condition, except for the last domain, where it is equal to the time needed for the tip of the blades to cross one cell ($\Delta t_{CFL-ALM}$, see Sect. 3.3.3). The impact of the time step and of the time splitting method is investigated in Sect. 4.3. The mixing length is chosen to reach the best velocity profile near the ground and numerical diffusion is set so no spurious numerical waves appear in the flowfield. The temporal and spatial schemes, RKC4 and CEN4TH respectively, are chosen to reach the best spatial resolution for a given cell size.

The rotational velocity of the wind turbine Ω is set constant in the whole simulation. It is interpolated in the controller table of the turbine to find the value corresponding to U_∞. A similar method is applied to set the pitch angle. Note that some other models of the benchmark use a "true" controller which modifies the turbine rotational speed depending on the unsteady inflow conditions, but this

has not been implemented yet in Meso-NH. The Glauert correction for tip loss is used [147] (Eq. 3.35). The momentum sources are not computed directly with the value of the velocity in the given cell, but instead, an interpolation with the eight neighbouring cells is performed. A linear function is used to smear the resulting body forces in the Meso-NH field. A simple implementation of the nacelle and the tower has been used (Eqs. 3.40 and 3.41) even though it is not clear whether these elements were included in the other LES codes of the benchmark. The effects of this last implementation on the wake flow field are detailed in Sect. A.2 of the appendices. The nacelle and tower body forces could be improved by imposing source terms in more than one point or using more advanced techniques than simple drag elements. Nevertheless, the implementation fulfils its main purpose, i.e. preventing a too strong velocity acceleration where there is no ALM body force.

4.2 The neutral case

This section presents the results of the Meso-NH simulation in the neutral case, compared to the SWiFT benchmark. The most important data of the benchmark for the validation of Meso-NH are the experimental data (in black) and the LES codes (in red): EllipSys-3D, SOWFA (two different simulations, denoted SOWFA and SOWFA-2), NaluWind and PALM. For both, the ensemble mean value is plotted in a continuous line and the range between minimum and maximum values is in a shaded area. The benchmark's results as well as a description of each code and the experimental method can be found in the original publication [80].

Meso-NH parameters					Turbine parameters	
Parameter	D_1	D_2	D_3	D_4	Ω [rad s^{-1}]	4.560
ΔZ [m]	0.5				Pitch angle γ [°]	-0.75
ΔX=ΔY [m]	20	4	1	0.5	Glauert correction	Yes
L_X [m]	6400	2000	600	432	Wind interpolation	Yes
L_Y [m]	2400	800	240	162	N_{seg}	8
Δt [s]	0.2	0.1	0.05	0.008		
Number of cells [10^6]	6.6	18.4	26.5	51.5		
Mixing length	DEAR					
Numerical Diffusion [s]	600	120	30	15		
ABL height [m]	1000					
D1 spin-up time [hr]	30					

Table 4.2: Numerical parameters of the different domains in the neutral case.

The post-processing of the results is reproduced in Meso-NH as it has been done for the other codes of the SWiFT benchmark: in the domain D_4, the velocity field at five planes (respectively dashed-dotted and dashed lines in Fig. 4.4) is extracted from the simulation, at a frequency of 1 Hz during 10 min. Figures 4.5, 4.6 and 4.8 are post-processed from these fields.

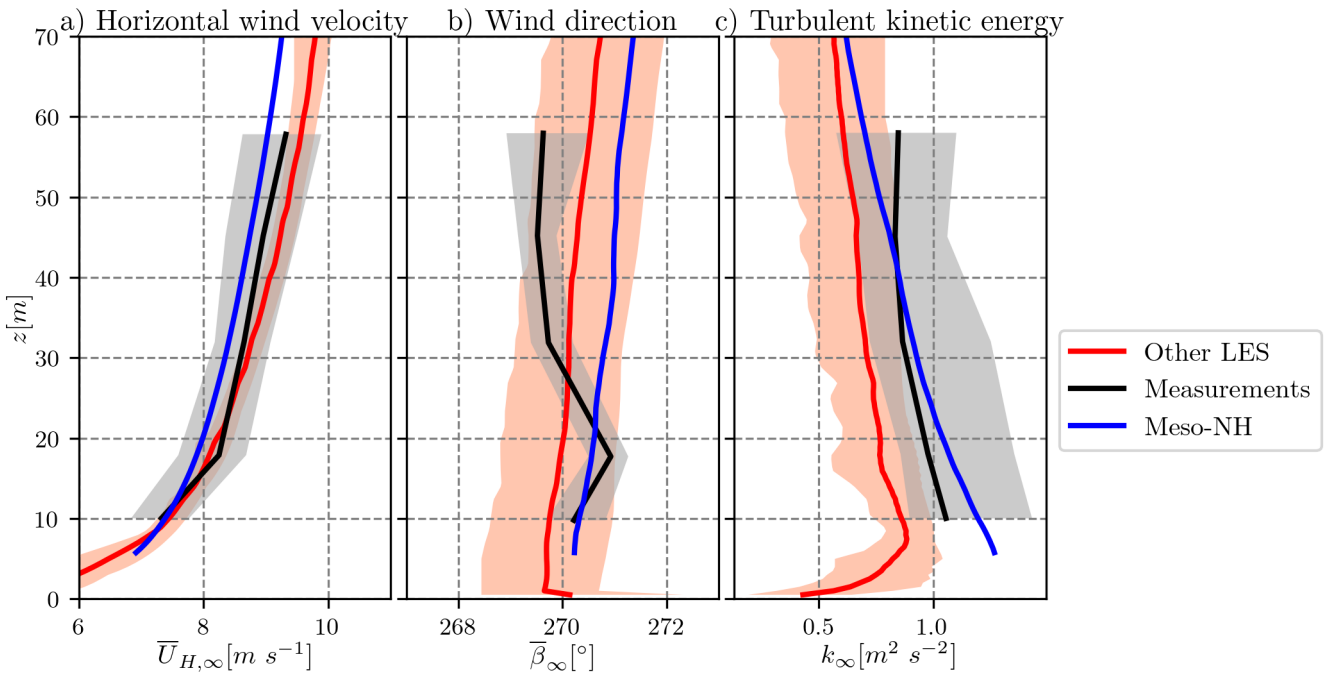

Figure 4.5: Neutral benchmark: mean inflow (65 m upstream the wind turbine), Y-averaged.

4.2.1 Inflow

The mean inflow wind gives overall satisfying results: the horizontal wind magnitude (Fig. 4.5a) is in the range of the experimental data, and slightly lower than the other LES codes. For the wind direction, there is a small yaw at hub height, of less than 1°, (Fig. 4.5b). As observed in the original publication, the meteorological mast did not measure a veer in the direction of the Ekman spiral, contrarily to Meso-NH and the other LES codes.

Compared to other LES codes, Meso-NH overestimates the TKE (Fig. 4.5c), but the predicted value is similar to the experimental measurements. The streamwise (Fig. 4.6a) and spanwise (Fig. 4.6b) velocity spectra are also satisfying for Meso-NH, which can be attributed to the special care taken to the turbulence during the different nesting steps.

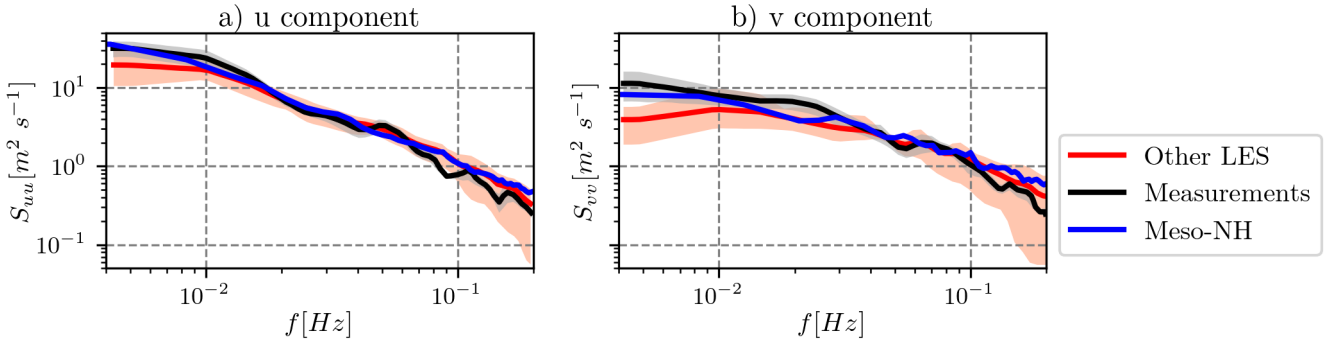

Figure 4.6: Neutral benchmark: velocity spectra (65 m upstream the wind turbine).

4.2.2 Turbine response

As detailed above, the ALM in Meso-NH is rotating at a fixed value, so it would be redundant to look at both the power and the torque outputs. Consequently, only the thrust coefficient $\overline{C}_T$ and the generator's power output $\overline{\mathcal{P}}_{gen}$ are shown here. Results are plotted respectively in Fig. 4.7a and Fig. 4.7b: the mean value corresponds to the magnitude of the colour bar, and the standard deviation is represented by the black line on each bar. The measured power on the turbine is reported as the dashed line in Fig. 4.7b. It is known that Meso-NH overestimates the tangential efforts [147] which explains the overestimation of $\overline{\mathcal{P}}_{gen}$. The thrust coefficient gives more satisfying results even though it is difficult to conclude in absence of measurements.

The two main sources of error could be the projection of the effort in Meso-NH (here, linear smearing) and the constant rotational velocity used. In parallel to the presented work, the smearing has been improved in Meso-NH, leading to a better estimation of the tangential force. This improvement is fairly new and could not be used in the present work but may improve our results. In the future, the implementation of a controller for the wind turbines in Meso-NH will allow the rotational velocity of the hub to fluctuate during the simulation and might also improve the results.

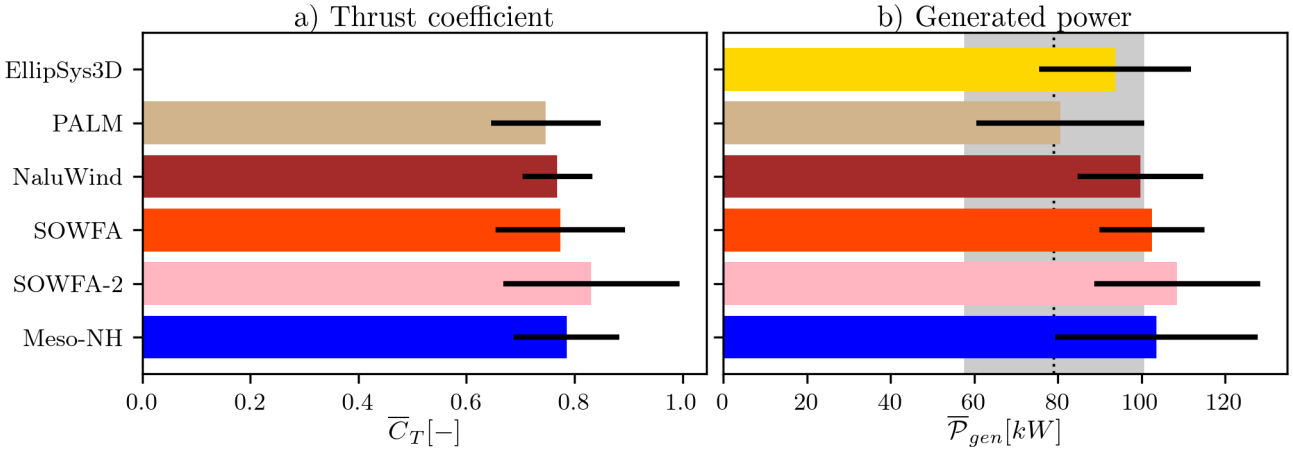

Figure 4.7: Neutral benchmark: mean turbine response. Measurements are plotted in a black dotted line.

4.2.3 Velocity deficit in the FFOR

The spanwise distribution in the FFOR of the mean velocity deficit behind the wind turbine is plotted in Fig. 4.8 in blue, against the distribution of the LiDAR measurement (black) and the other LES codes (red). It is important to note that the LES codes of the benchmark were, on average, underestimating the wake strength as well as the wake recovery compared to field measurements [80]. Meso-NH simulations show a wake recovery similar to the measurements and a wake deficit at $2D$ similar to the other solvers.

The wake recovery can be linked to the ambient turbulence, which is consistent here since Meso-NH shows values closer to the inflow TKE measurements than the average of the other LES (Fig. 4.5c). Likewise, since the thrust coefficient in Meso-NH is similar to the other codes, it is expected that the near wakes are similar as well. To conclude, the wake in Meso-NH shows satisfying results, and

slight differences with other LES codes and measurements can be explained by differences observed in the efforts and the inflow conditions.

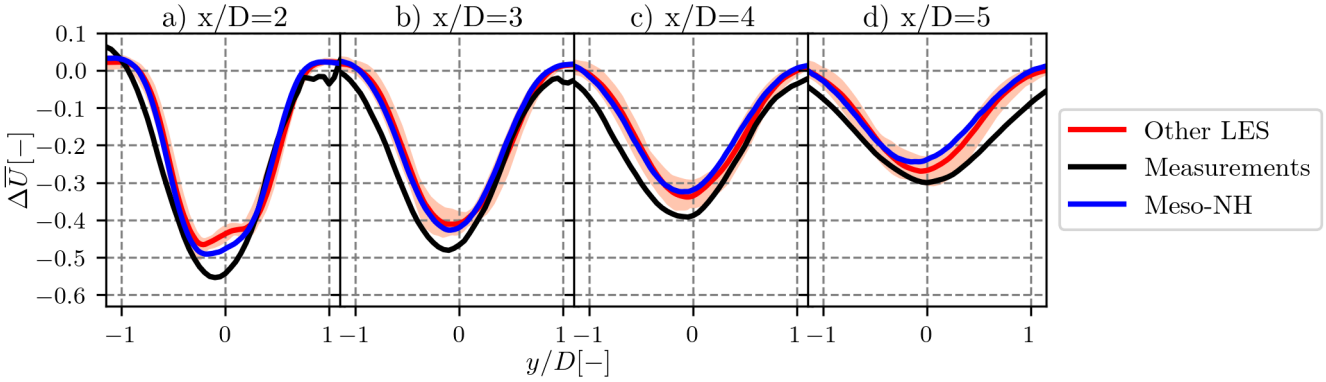

Figure 4.8: Neutral benchmark: mean velocity deficit in the wake at hub height.

4.2.4 Wake Meandering

To evaluate wake meandering, the wake centres at $2D$, $3D$, $4D$ and $5D$ downstream the turbine are detected at each time step by fitting a 2-D Gaussian function on the planar data. To do so, the open-source SAMWICH (Simulated And Measured Wake Identification and CHaracterization) python toolbox has been used [154]. The false positives that are detected by this method are filtered out with an *ad hoc* filter, where values too far from the rotor centre are discarded. An additional median filtering is applied to dampen other further variations. This methodology is the same as the one used in the benchmark [80] to compare data that had the same post-processing, but it will be shown in Ch. 5 that it is not optimal.

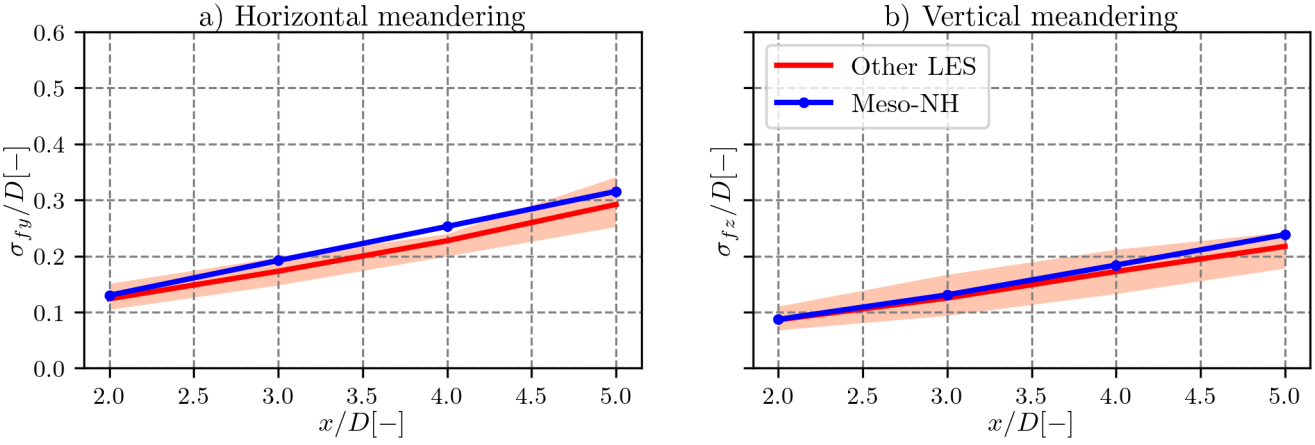

Figure 4.9: Neutral benchmark: wake meandering in the y and z directions.

The standard deviations of the wake centres σ_{fy} and σ_{fy} are computed and plotted as a function of the downstream distance in Fig. 4.9. No *in situ* data was available for this quantity in the neutral benchmark. Compared to the other LES results, Meso-NH gives a slightly larger horizontal wake meandering but is around the mean of the codes for the vertical meandering. It is complicated to

conclude whether the differences come from an overprediction of the meandering, better accounting of large-scale turbulence or errors in the tracking algorithm.

4.2.5 Velocity deficit in the MFOR

Finally, it is important to validate the wake in the MFOR i.e. the wake decoupled from the effect of meandering. Indeed this will be used further for the construction of the analytical model. Similarly to the FFOR it is plotted in Fig. 4.10 for the four studied positions downstream. The results in the MFOR are even better than those in the FFOR, indicating that the small discrepancies observed in Fig. 4.8 are actually due to the rather strong wake meandering predicted by Meso-NH, itself correlated to the higher upstream TKE, in particular at low frequencies (see Figs 4.5c and 4.6). One can also note that the shape in the near wake is less similar to a Gaussian function. This is imputed to the modelling of the nacelle which is improvable, and this flaw is increased in the MFOR because the meandering (that was spreading the velocity deficit at the wake centre) has been removed. The results are thus overall satisfying in the neutral case.

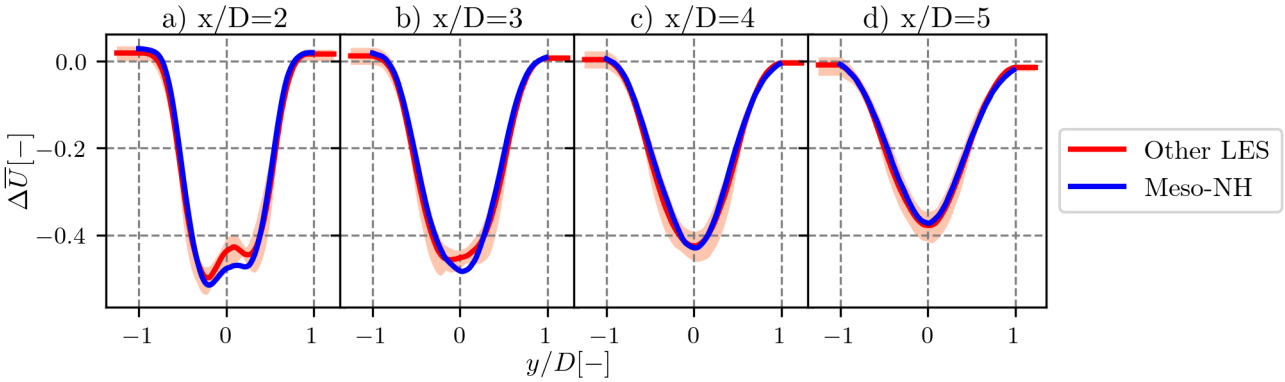

Figure 4.10: Neutral benchmark: mean velocity deficit in the MFOR.

4.3 Sensitivity study on the time step and the time-splitting

The time-splitting technique allows using the time step imposed by the CFL of Meso-NH $\Delta t_{CFL-MNH}$ instead of the one imposed by the ALM $\Delta t_{CFL-ALM}$, resulting in a faster simulation. This method is based on the assumption that the wind is frozen during the ALM substeps, which is the case for a uniform inflow as in the first time-splitting validation [147] but not for a turbulent inflow as herein. The present section is dedicated to a complementary validation with the SWiFT neutral case (where the inflow is turbulent), along with a sensitivity study on the impact of the time step, leading to a total of four simulations. In the first one (purple), $\Delta t = \Delta t_{CFL-MNH} = 25$ ms is set: with the rotational speed of the rotor and the resolution reported in Table 4.2, the blade tip crosses three cells per time step. To cope with that, the time-splitting is activated, with three sub-iterations per Meso-NH iterations. The second simulation (blue) is the same as presented in Sect. 4.2, where $\Delta t = \Delta t_{CFL-ALM} \approx 8.3$ ms without time-splitting. In a third simulation (green), the time step is lowered to the value of $\Delta t \approx 6.3$ ms. Finally, a fourth simulation (pale blue) is computed with $\Delta t \approx 4.2$ ms, corresponding to a hub rotation of one degree of azimuth per time step.

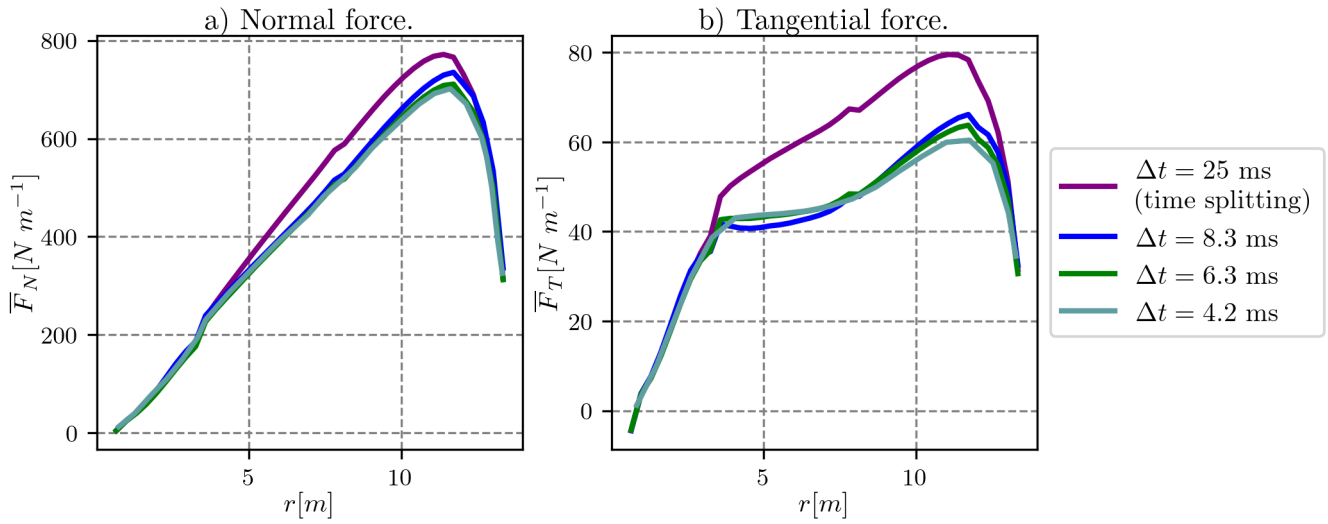

Figure 4.11: Time step sensitivity: mean tangential and normal forces on the blades.

The resulting efforts for these four simulations are plotted in Fig. 4.11. Even though there are no reference data for the blades' efforts, one can observe that both the normal (a) and tangential (b) forces are overestimated with the time-splitting method. The validation of the time-splitting in the MEXICO experiments did not show such differences, at least not for three sub-iterations. The results showed Fig. 4.11 indicate that the efforts are converged when a blade's tip crosses a cell in about three time steps (green curve) and that the time-splitting leads to an overestimation of these efforts.

Vertical profiles at the middle of the wake (at $y = y_{wt}$) are plotted in Figs. 4.12 and 4.13 for the velocity deficit and TKE, respectively. One can see that even though the velocity deficit is overestimated in the near wake for the time-splitting simulation, all simulations collapse in the far wake. However, the overestimation of TKE by the time-splitting simulation does not disappear at five diameters downstream of the wind turbine (Fig. 4.13). This phenomenon was not observed for the actuator sector [150], which is a version of the actuator line very similar to the time-splitting.

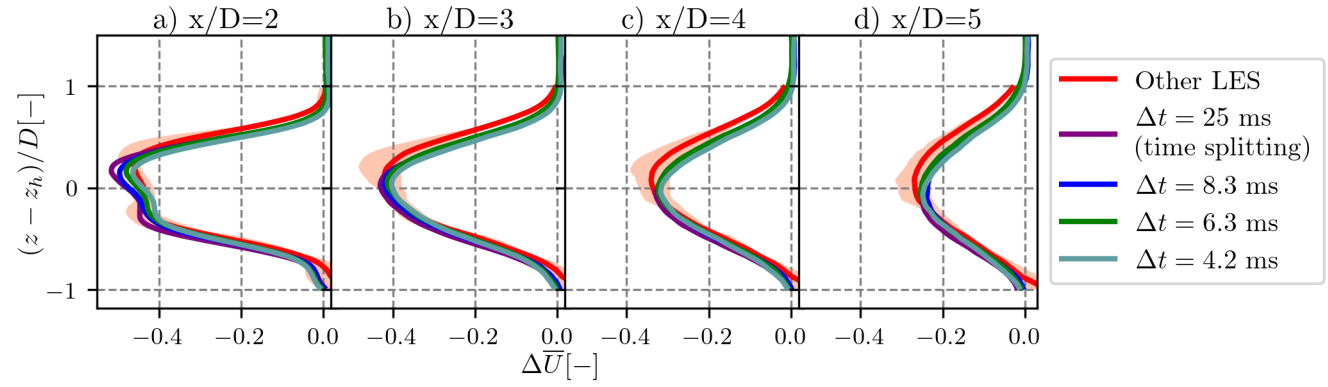

Figure 4.12: Time step sensitivity: vertical profiles of mean velocity deficit in the wake at $y = y_{wt}$.

Reducing the time step below the usual $\Delta t_{CFL-ALM}$ (green and pale blue curves) value does not change significantly the results in the wake. The integrated efforts are however sensibly changed, leading to $\overline{C}_T = 0.74$ in both cases (the blue case corresponds to $\overline{C}_T = 0.79$) and $\overline{\mathcal{P}}_{gen} = \{100, 98\}$

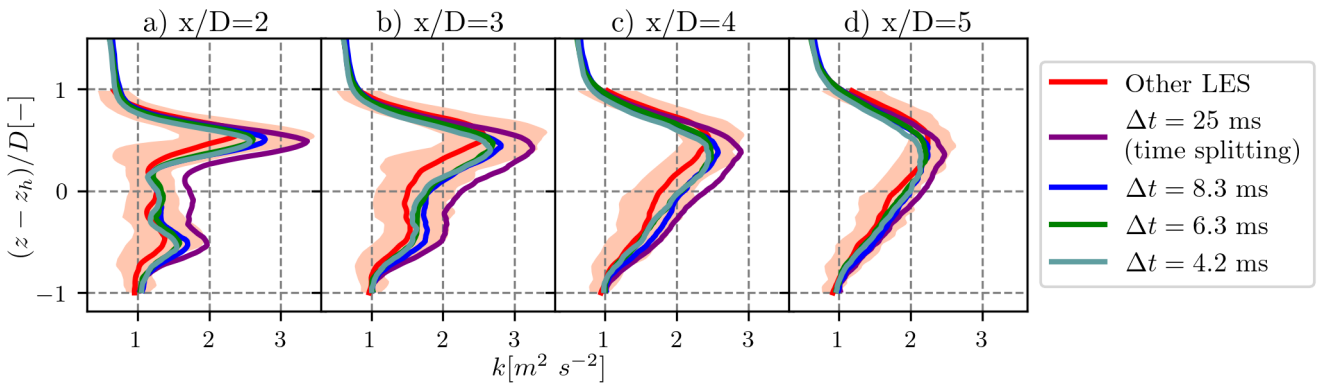

Figure 4.13: Time step sensitivity: vertical profiles of mean TKE in the wake at $y = y_{wt}$.

kW for the green and pale blue cases (the blue case corresponds to $\overline{\mathcal{P}}_{gen} = 104$ kW).

To conclude, one should be cautious when using time-splitting. Indeed, discrepancies are observed in the efforts of the blades and in the velocity deficit in the near wake, but more importantly, the TKE is overestimated in the whole wake. As a consequence, the time-splitting cannot be used as it is in version V5-4-3 for the calibration of added turbulence models, but is sufficient for first-order estimations of variables in the far wake, as it was done for the Horns Rev photo case [147]. This sensitivity study also proves that lowering the time step below $\Delta t_{CFL-ALM}$ does not drastically change the results of the simulation, even for the TKE, and it thus appears more cost-effective to use $\Delta t = \Delta t_{CFL-ALM}$. For all the following simulations, the criterion $\Delta t = \Delta t_{CFL-ALM}$ will thus be used.

4.4 The unstable case

Meso-NH parameters					Turbine parameters	
Parameter	D_1	D_2	D_3	D_4	Ω [rad s^{-1}]	3.890
ΔZ [m]	0.5				Pitch angle γ [°]	-0.75
ΔX=ΔY [m]	20	4	1	0.5	Glauert correction	Yes
L_X [m]	12000	3200	1000	450	Wind interpolation	Yes
L_Y [m]	6000	1600	500	225	N_{seg}	2
Δt [s]	0.1	0.1	0.05	0.01		
Number of cells [10^6]	46.1	81.9	128.0	103.7		
Mixing length	HM21					
Numerical Diffusion [s]	1800	1800	1800	1800		
ABL height [m]	1000					
D1 spin-up time [hr]	4					

Table 4.3: Numerical parameters of the different domains in the unstable case.

Despite an overall similar methodology, there are some differences between the setups in the unstable and neutral cases due to the different physical phenomena at stake. On the one hand, the convective motions in the unstable case allow a better development of the turbulence in the simulated ABL,

which is why a smaller D_1 spin-up time is needed. On the other hand, the maximum eddy size is larger in the CBL than in the neutral ABL and thus a large domain size for D_1 is needed. Moreover, the nested domains are larger than for the neutral case as well because the spectral study has shown larger turbulence build-up regions for the unstable case. As a result, the unstable benchmark is computationally more expensive than the neutral one (see Table 4.3).

One difficulty of the unstable case is that the mean wind direction varies from one segment of 10 minutes to another: it is not possible to compute 80 consecutive minutes of dynamics with the same 10-minutes averaged wind direction as in the neutral case. Only four consecutive segments with small variations of $\overline{\beta}$ could be found. It highlights the issue of the choice of 10-minutes averaging for the CBL, where the maximum time scale might be higher than that. This has also probably been observed in the measurements, which are actually an average of six non-consecutive segments of 10 minutes. The HM21 mixing length has been chosen because it gives better results than the Deardorff mixing length for a free convection case [140], even though this case is far from free convection. The list of numerical parameters can be found in Table. 4.3.

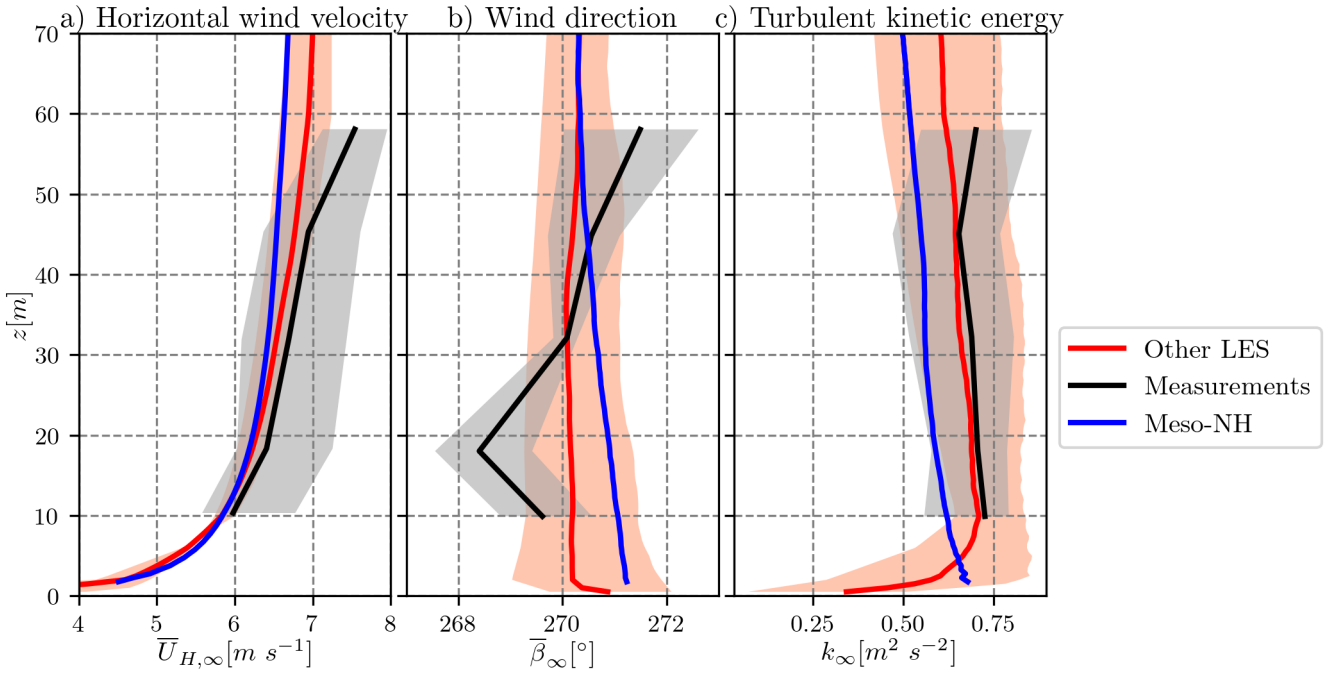

Figure 4.14: Unstable benchmark: mean inflow (65 m upstream the wind turbine), Y-averaged.

Between the ground and hub height, the mean velocity magnitude (Fig. 4.14a) is very similar between Meso-NH and the other LES or the measurements. However, our simulation shows a lower shear that leads to a slightly underestimated velocity at the top tip. This low shear indicates a more strongly unstable ABL in Meso-NH compared to the other LES and measurements, but ζ has not been computed here since no data from the other LES were available. The veer (Fig. 4.14b) is very weak in all LES and similarly to the neutral case, our simulations lead to negligible yaw, around 1° at hub height.

The TKE (Fig. 4.14c) is underestimated at the inlet and is at the edge of the lowest values of both LES and measurements. This underestimation is found as well on the velocity spectra (Figs. 4.15a and 4.15b): the Meso-NH turbulence is larger in the low frequency and lower in the high frequency,

indicating that the integral length scale is larger in Meso-NH than in the other LES or measurements despite a smaller total TKE. The slope of the spectra is however satisfying, indicating that the Kolmogorov-Richardson cascade is respected. The aforementioned issue of varying $\overline{\beta}$ between the different segments can be seen in Fig. 4.15b: the Meso-NH PSD becomes higher than the other datasets in the low-frequency region, indicating more large-scale variations.

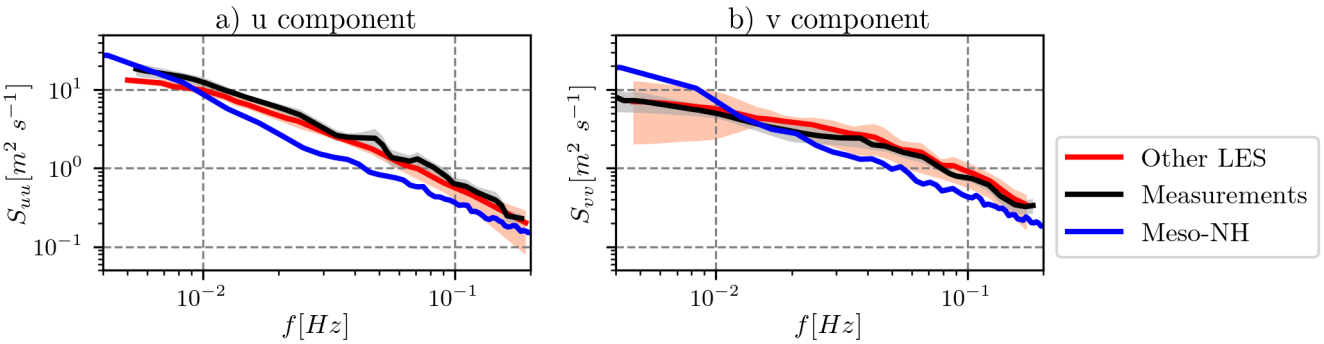

Figure 4.15: Inflow u and v spectra for the unstable benchmark

For the thrust coefficient (Fig. 4.16a), there is a large dispersion between the two available LES codes and Meso-NH is in the middle. If one assumes that the turbine is working at $a = 1/3$ to maximise the power according to the Betz limit, the corresponding C_T is around 0.89 (Eqs. 2.4 and 2.5). Considering that it is not an idealised rotor and that turbulence degrades the optimal point, Meso-NH might here predict the most realistic value, but it is difficult to conclude in absence of measurements. Due to the overestimation of tangential efforts, the generator power in Meso-NH (Fig. 4.16a) is higher than for PALM and the measurements, but one can note that this overestimation is lower than in the neutral case and is here similar to EllipSys3D and SOWFA.

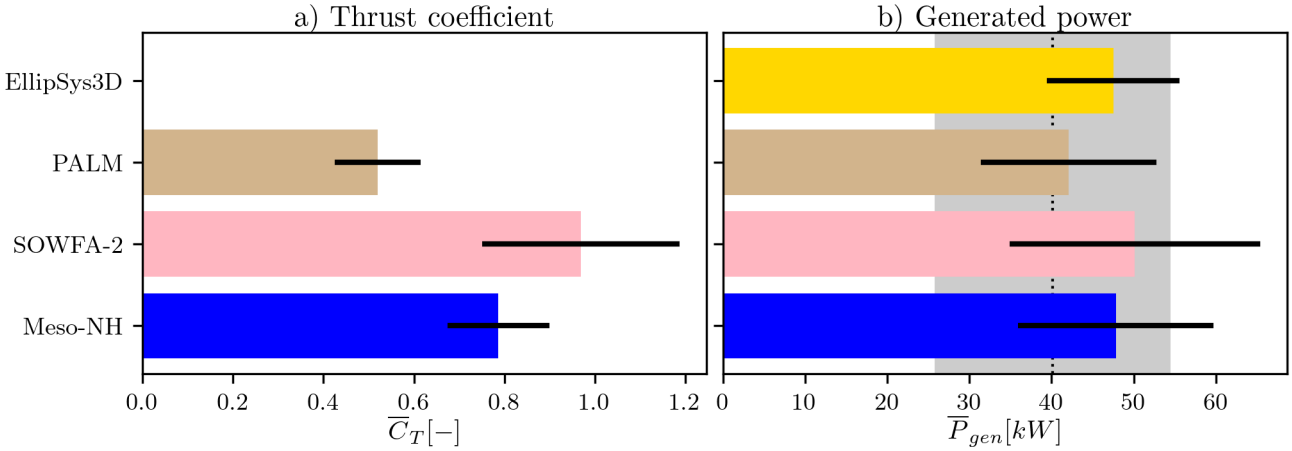

Figure 4.16: Unstable benchmark: mean turbine response. Measurements are plotted in a black dotted line.

The wake behind the wind turbine is plotted in Fig. 4.17, but only measurement data for $x/D = 3$ were available for this benchmark. Overall the Meso-NH simulation gives a result similar to the measurements for both the maximum velocity deficit and the wake width (Fig. 4.17b). These results are in the FFOR: the wake meandering increases the wake dissipation; since Meso-NH predicts more meandering (see next paragraph), it is not surprising that it leads to a faster-dissipating wake.

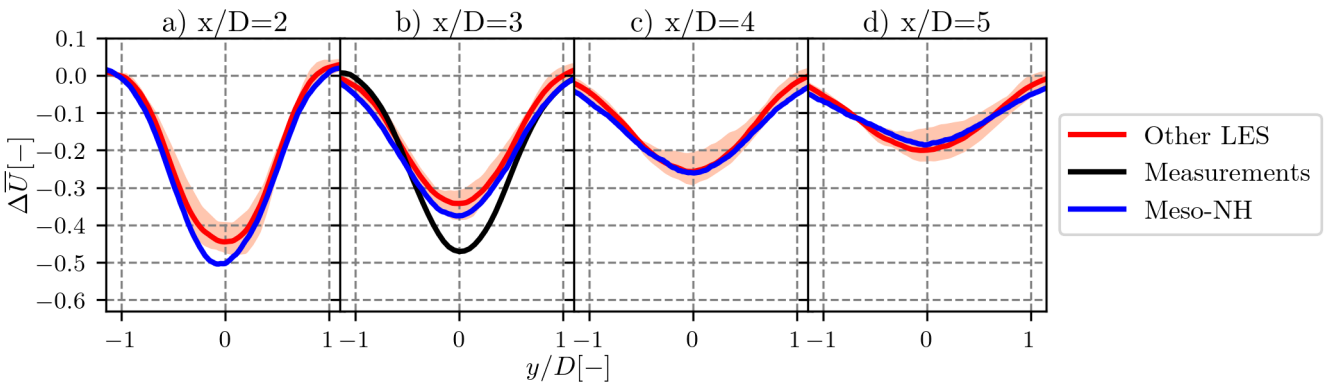

Figure 4.17: Unstable benchmark: mean velocity in the FFOR deficit in the wake at hub height.

The amount of meandering is plotted in Fig. 4.18: for every distance downstream, the horizontal meandering is stronger in Meso-NH than in the other codes and the vertical one is comparable to the other codes. The stronger horizontal meandering can be explained with the lateral velocity spectrum in (Fig. 4.15b): Meso-NH has more variations at low frequencies, which are those responsible for wake meandering. Moreover one must note that the 10-minutes averaged wind direction is not always aligned with the turbine in Meso-NH: only the overall 40-minute averaged wind is aligned with the turbine. In other words, the turbulence at frequencies even lower than those represented in Fig. 4.15 might be more energetic in Meso-NH compared to other codes.

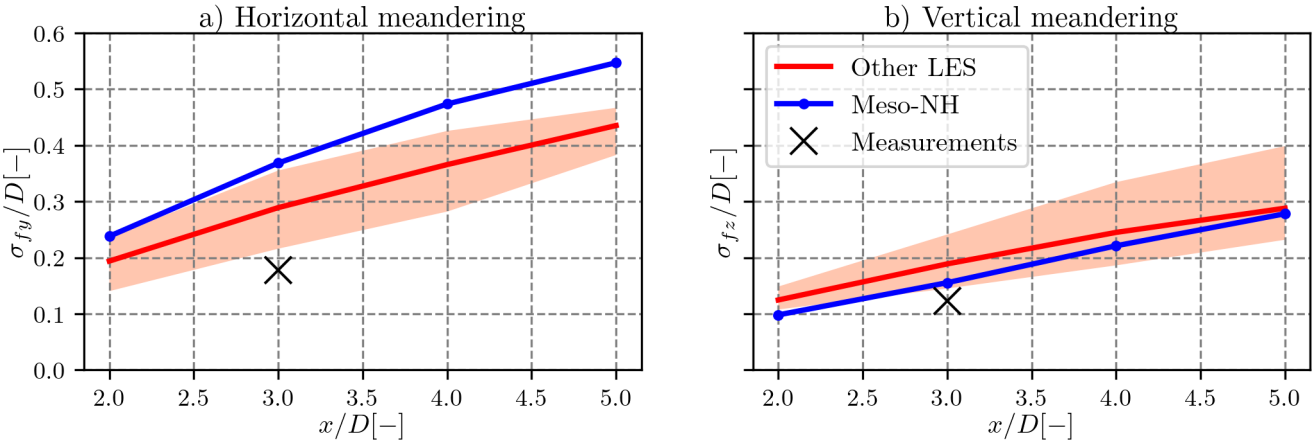

Figure 4.18: Unstable benchmark: wake meandering in the y and z directions.

Similarly to the neutral case, the velocity deficit profiles in the MFOR are plotted in Fig. 4.19. Contrarily to the FFOR, the velocity deficit does not dissipate much faster in Meso-NH compared to the other codes, because the effect of wake meandering has been filtered out. One can note that the near-wake velocity deficit is stronger in Meso-NH, even though the mean thrust coefficient is not the strongest among the LES. The results in the MFOR are however similar to the measurements at $x/D = 3$ and show overall similar values to the other codes.

To conclude, this unstable case was an opportunity to validate Meso-NH for a convective case but also to validate its ability to estimate the wake meandering. It performed quite well compared to both *in-situ* measurements and three other LES codes of the community: we can conclude that it

can be used as a reference tool for the study of the wake in the CBL and the wake meandering.

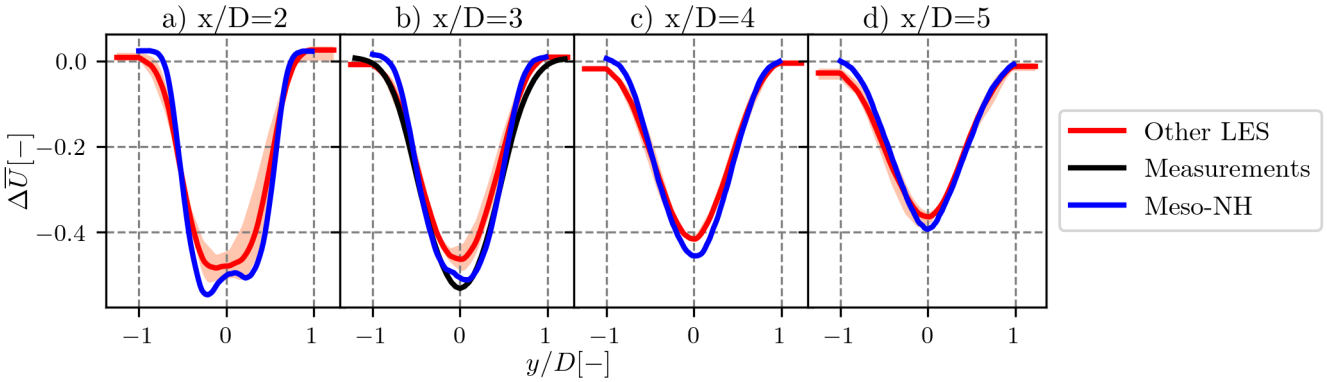

Figure 4.19: Unstable benchmark: mean velocity deficit in the MFOR in the wake at hub height.

4.5 The stable case

Meso-NH parameters			Turbine parameters	
Parameter	D_1	D_2	Ω [rad s^{-1}]	2.788
ΔZ [m]	0.4		Pitch angle γ [°]	-0.75
ΔX=ΔY [m]	1.2	0.4	Glauert correction	Yes
L_X [m]	540	360	Wind interpolation	Yes
L_Y [m]	300	150	N_{seg}	1
Δt [s]	0.012	0.009		
Number of cells [10^6]	35.0	104.9		
Mixing length	HM21			
Numerical Diffusion [s]	1800	1800		
ABL height [m]	200			
D1 spin-up time [hr]	4			

Table 4.4: Numerical parameters of the different domains in the stable case.

For a LES to be valid, it is often assumed that the share of the subgrid TKE k_{sgs} should be lower than 20% of the total TKE [41]: it ensures that the simulation is not too dependent on the SGS model. For the unstable and neutral cases, this was not a problem: near the ground, the domain D_1 is resolving the TKE at this order of magnitude and the share of TKE is decreasing at each nesting, leading to $\overline{k}_{sgs}/\overline{k}_{tot} << 0.2$ in D_4. However, in the stably stratified ABL the turbulence is damped, in particular at the low frequencies, resulting in small amounts of $\overline{k}_{tot}$. Therefore, a very stably stratified ABL as the one in the SWiFT benchmark must be modelled with a very fine mesh to resolve a correct amount of turbulence, even in D_1. On the bright side, since the large-scale turbulence is damped out, there is no need to compute a very large domain in D_1: the largest eddies are no longer of the order of magnitude of the ABL depth, which is fairly reduced in SBL. Another issue is that the benchmark provides only some values near the ground ($z = 10$ m) and at hub height ($z = 32$ m), but no other information such as the boundary layer depth, presence of a low-level jet,

geostrophic wind or the history of heat flux were given. They could have been useful to know more about the boundary layer and to set the Meso-NH simulation up.

A different meshing strategy has thus been used for the simulation of the stable benchmark with only two nested domains: the first one at 1.2 m of resolution and the second one going down to 0.4 m of resolution. Despite this fine resolution of D_1, a stability parameter of $\zeta = 1.151$ at $z = 10$ m could not be reached. An even finer mesh could have been used, but it would have been too computationally expensive.

Only the second simulation of SOWFA participated in the stable benchmark, which is why no red range appears in the corresponding figures. Our comparisons will be limited to this simulation, along with the measurements when they are available.

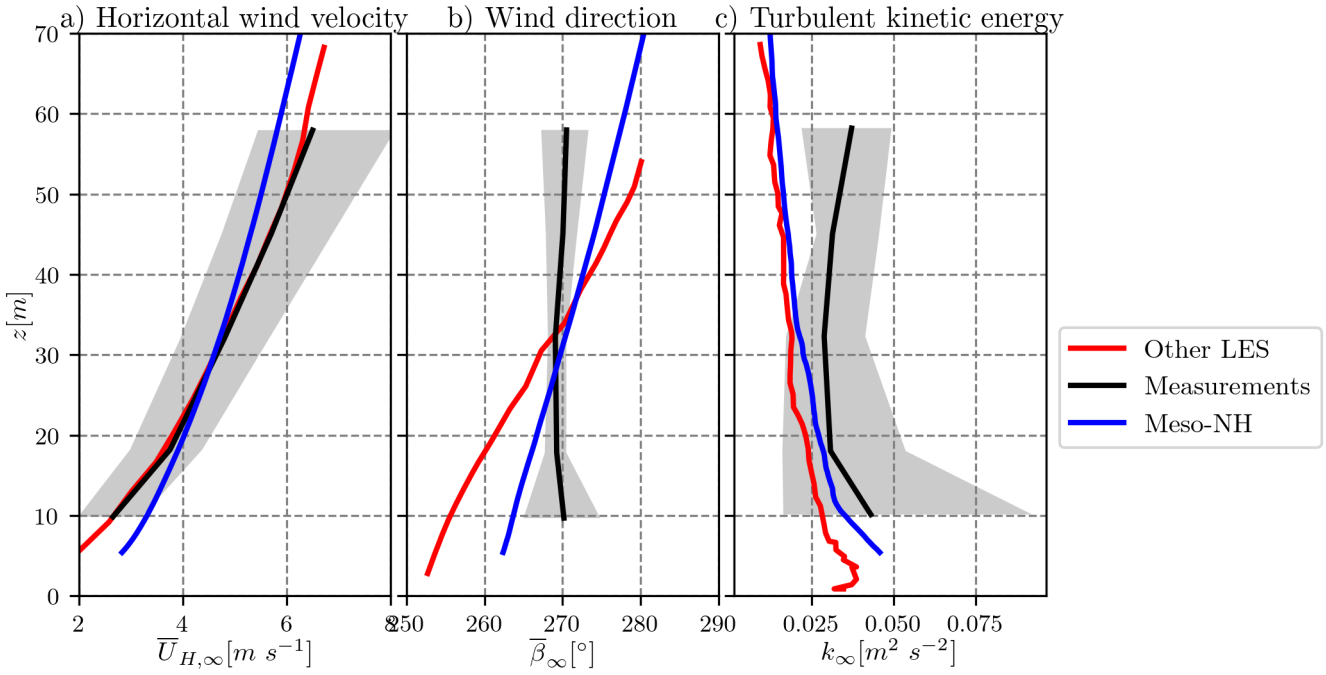

Figure 4.20: Stable benchmark: mean inflow (65 m upstream the wind turbine), Y-averaged.

The horizontal velocity profile of Meso-NH (Fig. 4.20a) is of a good order of magnitude but the shear is largely lower than the measurements or SOWFA, which shows a slope closer to the one measured in the benchmark. Similarly, the veer is lower than for SOWFA (Fig. 4.20b): those two elements indicate a less-stable ABL simulated by Meso-NH. Conversely, the TKE is underestimated with Meso-NH (Fig. 4.20c), but to a lesser extent than the SOWFA simulation. No better inflow could be achieved because increasing the stability would have resulted in a higher shear and veer but into an even lower TKE, so the present inflow was the best compromise found.

Conversely to the unstable case, the thrust coefficient is slightly larger in Meso-NH compared to SOWFA (Fig. 4.21a). However, one can note that for the three cases of stability, the value of $\overline{C}_T$ in Meso-NH is close to 0.8 i.e. close to the optimal point of an idealised turbine whereas SOWFA shows much more dispersion among the cases. Similarly to the other cases, both Meso-NH and SOWFA overestimate the generator power compared to the measurements (Fig. 4.21b).

The wake in Meso-NH behaves similarly to the one in SOWFA from $x = 2D$ to $x = 5D$, with a

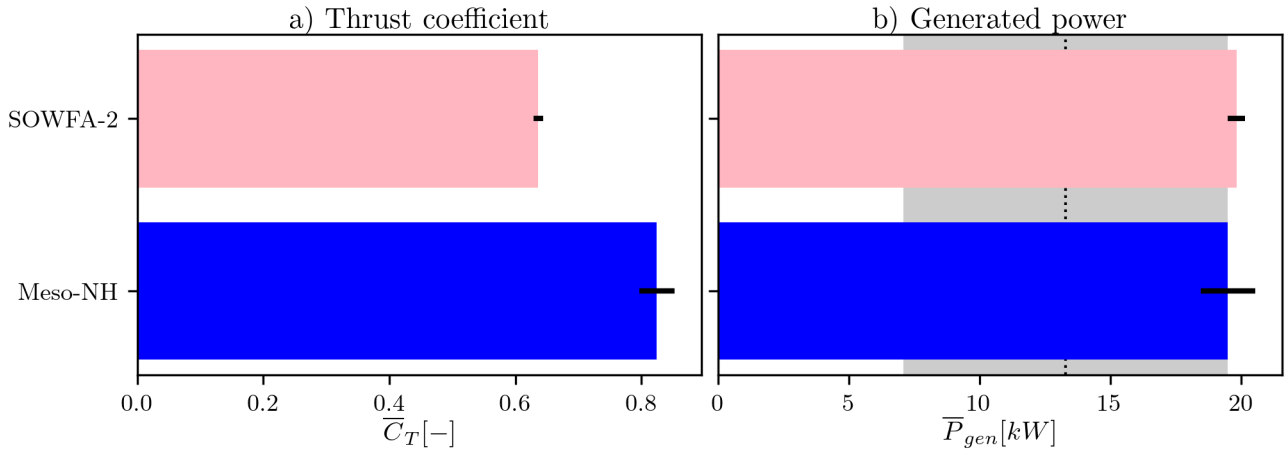

Figure 4.21: Stable benchmark: mean turbine response. Measurements are plotted in a black dotted line.

slightly narrower wake width at $x/D = 5$. Even though the ABL is strongly stratified, it is surprising that the measurements are so similar at three diameters of interval (from Fig. 4.22a to 4.22d), and especially since the TKE levels are similar to the three simulations presented herein. It is important to note that due to the strong veer upwind of the turbine, the velocity profiles such as those plotted in Fig. 4.21 hardly restitute the real wake shape, which is very skewed. This is why the velocity profiles are not quite like a Gaussian profile, in particular in Meso-NH. The meandering computed with Meso-NH is very low: it barely reaches $\sigma_{fy}/D = 0.1$ at $x/D = 5$ and no reference data was available. Consequently, the mean velocity deficit in the MFOR is very similar to that in the FFOR. These two variables are thus not plotted in this section.

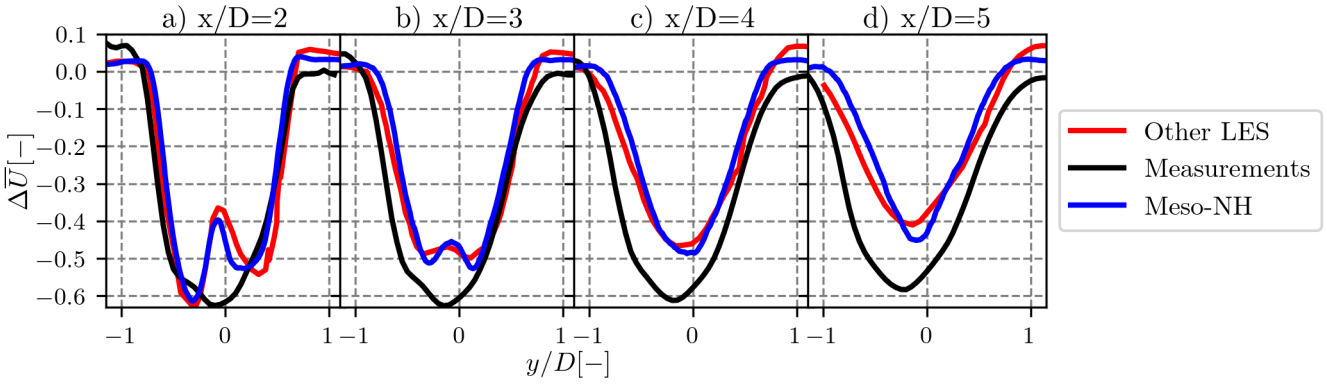

Figure 4.22: Stable benchmark: mean velocity deficit in the wake at hub height.

A possible explanation for the discrepancies between the LES codes and the measurements is the lack of veer in the latter. Indeed, in a canonical SBL, there is a strong veer due to the Coriolis force. This phenomenon was modelled in LES but not measured. It could be due, for instance, to a baroclinic atmosphere (whereas the barotropic one is presumed in LES codes), i.e., not constant geostrophic wind. Correcting the veer in the simulations would modify the velocity deficit [155] and could match better the experimental results. Indeed, the veer does not dissipate the wake but it skews it more and more as it travels downstream, thus modifying the velocity deficit profiles.

To conclude, the results of Meso-NH are similar to those of the SOWFA code, but not really to the measurements. Since SOWFA is a reference in the domain and that some doubts have been pointed out in the measurements; we consider that our SBL case is validated. Not shown here because there was no reference data but the wake meandering was also smaller than the neutral and convective case. The very strong stability that was measured in the Great Plains could not be exactly reproduced, but the inflow in terms of velocity magnitude, direction and TKE of the *in situ* measurements could approximately be reproduced. A simulation with an even finer mesh could be launched to try reaching $\zeta = 1.151$ and see if the simulated wake dissipates at the same rate as the measurements. This could not be done here because of the required computational power and needed time, but also since we expected it to decrease the TKE to even lower levels and thus our results would hardly compare to those of the benchmark. It highlights the limitations of Meso-NH (as of any LES code) in the very stable ABL: when stability increases, the mesh needs to be refined, leading to an increased computational cost. In this case, we managed to approach the inflow measurements (even though our stability parameter ζ is largely lower) but if the turbine was larger (for instance the DTU 10MW), we should have had a longer computational domain to reach $x/D = 5$ with the same mesh and the computational cost would have certainly been too expensive.

Conclusion of the chapter

The SWiFT benchmark is a complementary validation of the first implementation of the ALM in Meso-NH. The three cases of stability have been successfully reproduced and compared with other LES codes as well as *in situ* measurements. Overall good results are produced with Meso-NH even though the stable case is at the edge of the capacity of the code. Most of the differences between our code and the others or the measurements in the wake can be explained by differences in the inflow conditions. This benchmark was also the occasion to test the time-splitting technique in a turbulent ABL, which led to overestimated efforts. Now that the code is considered to be validated, it will be used as a reference for the calibration of new analytical wake models. Some improvements can still be brought to the code, for instance adding a Gaussian smearing of the forces, a controller or a better implementation of the tower and nacelle.

Chapter 5

Wake Tracking

Defining the instantaneous position of the wake centre (hereafter called 'wake tracking') is essential to compute the amount of wake meandering σ_f and the velocity deficit and added turbulence in the MFOR. This chapter aims at defining the best tracking method and improving it with additional pre-processing techniques. Even though in Ch. 4 the fitting of a 2D-Gaussian function is used to be consistent with the other results of the SWiFT benchmark, it will be shown that it is not the best tracking method and that it leads to significant discrepancies in the far-wake.

This chapter starts with a short description of various wake tracking algorithms that can be found in the literature. We also propose two methods of pre-processing to improve the dataset before applying the tracking algorithm. Four algorithms are then compared with different pre-processing to find the best practices that will be followed for the rest of the work. This comparison is performed on the neutral case because it is the largest dataset at our disposal (80 min i.e. 4800 frames), and most of the results are presented at 8 diameters downstream, where there is the highest amount of meandering and also where the wake tracking is the most likely to fail. The main results presented herein have been published and presented at the TORQUE 2022 conference [156].

5.1 Context

5.1.1 Difficulties to define the wake centre

Defining the wake centre is rather easy for an averaged wake because it is usually a smooth distribution. In the case of an instantaneous wake immersed in a turbulent flowfield, this can be much more complicated. Besides the displacement from the largest eddies as predicted by the DWM model, smaller eddies from the ABL can also skew, elongate or even split the wake. As a consequence, the wake loses its consistency as it travels downstream and becomes less and less distinguishable from the atmospheric turbulence.

Figure 5.1 highlights four examples of instantaneous velocity planes, taken 8 diameters downstream of the turbine, where the wake centre is hard to define. In Fig. 5.1a, the wake is split into several small wakes, inducing several possible definitions of the wake centre. In Fig. 5.1b, a low-velocity eddy appears around $y/D = 2$ which can be mistaken by the algorithms with the actual wake, positioned around $y/D = 0$. In Fig. 5.1c, the wake is almost dissipated, and although it is distinguishable by

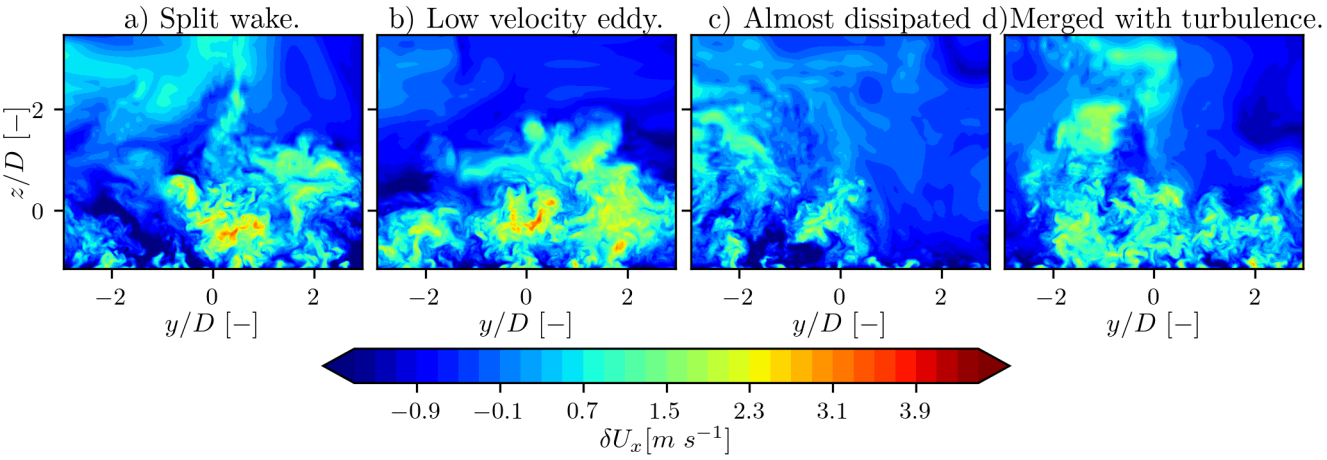

Figure 5.1: Snapshots of instantaneous velocity in the wake on the neutral case at 8 diameters downstream. a) split wake case; b) presence of a low-velocity eddy similar to a turbine wake; c) wake almost dissipated; d) merging of the wake and near-ground turbulence.

a human observer, it may fail to fulfil definitions of wake based on velocity, momentum or power deficit. In Fig. 5.1d the wake is undistinguishable from the turbulence generated at the ground, and neither a human observer nor an algorithm can define properly a wake centre.

These situations will lead to failures of the algorithms, which, if not detected and removed from the dataset, will add spurious fluctuations in the wake centre position. It is more likely to happen as the wake travel downstream since the velocity deficit is weaker and turbulence has more time to affect the wake. Note that the interpretation of these velocity planes given above is arbitrary and is solely used here for the reader to understand some sources of error in wake tracking.

The wake centre could be manually detected by the user, but it would be a fastidious task and from a scientific point of view, it is more interesting to have a mathematical criterion to define the wake centre instead of a qualitative approach. This manual detection will be used as a reference tool in this work but one must keep in mind that it relies on visual and qualitative estimation, and is thus hardly reproducible by another analyst. That is why it is completed by a physical analysis.

5.1.2 Tracking methods in the literature

Many methods have been developed in the literature to define the wake centre:

- The most intuitive way to define the wake outline is to base it on a threshold, for instance 95% of the freestream velocity or 20-50% of the velocity deficit [22, 23]. For an instantaneous wake embedded in a turbulent boundary layer like those plotted in Fig. 5.1, this method is likely to fail due to the many outlines fulfilling such conditions.
- The centroïd of a given field, e.g. velocity, velocity deficit or momentum, can be used to define

the wake centre [21]. These methods are however not considered to be robust in the presence of low-velocity eddies, like in the ABL, that will attract the centroïd toward them [157].

- The most commonly used method in the literature [11, 18, 80, 101, 94, 85, 83, 158, 88] for its easy implementation, low computational cost and simplicity to implement is to fit a 2D skewed Gaussian function (Eq. 5.1) on the normalised instantaneous velocity deficit ΔU.

$$\mathcal{F}(y, z, \mathcal{A}, y_0, z_0, \sigma_y, \sigma_z, \omega_f) = \mathcal{A} \exp\left[-c_1(y-y_0)^2 - 2c_2(y-y_0)(z-z_0) - c_3(z-z_0)^2\right] \tag{5.1}$$

with $c_1 = \left(\frac{\cos^2\omega_f}{2\sigma_y^2} + \frac{\sin^2\omega_f}{2\sigma_z^2}\right)$, $c_2 = \left(-\frac{\sin^2\omega_f}{4\sigma_y^2} + \frac{\sin^2\omega_f}{4\sigma_z^2}\right)$ and $c_3 = \left(\frac{\sin^2\omega_f}{2\sigma_y^2} + \frac{\cos^2\omega_f}{2\sigma_z^2}\right)$.
The optimisation is run on the six parameters $\{\mathcal{A}, y_0, z_0, \sigma_y, \sigma_z, \omega_f\}$ at each time step and position downstream. These parameters are respectively the Gaussian deficit amplitude, the coordinates of the wake centre, the Gaussian widths and the rotation angle. The wake centre position $y_c(x,t), z_c(x,t)$ is deduced from the results of parameters y_0, z_0. This approach is based on a Gaussian shape hypothesis that is verified for the averaged velocity field but not for the instantaneous one (e.g. Figure 5.1). An alternative is to use a univariate Gaussian function (i.e. Eq. 5.1 with $\sigma_y = \sigma_z$ and $\omega_f = 0$). The number of parameters is reduced from six to four so this method is faster but it fails when the wake is skewed (e.g. in presence of turbulent eddies, yaw or veer) [159].

- Since the main wake effect is the decrease of available power for a given downstream turbine, a practical definition (as opposed to physically-based ones) of the wake centre is the position that 'feels' the less power. In this other algorithm, denoted MinPower, the wake centre is defined as the region with the lowest available power [159], i.e. an optimisation algorithm is applied at every time step to find the minimum of the function:

$$\mathcal{F}(y_c, z_c) = \int\int_{S_T} U^3(y - y_c, z - z_c) dy dz \tag{5.2}$$

where S_T is a disk of the size of the rotor-swept area.

- It is possible to define the wake outline as a velocity deficit δU isocontour, which value is not *a priori* fixed. Instead, one can impose that the area S enclosed by the velocity isocontour is equal to the rotor-swept area. This method, called CstArea herein, is introduced in [157]. Once the wake outline is defined, the wake centre is computed as the velocity deficit centroïd of S.

- Alternatively, the same principle can be used to define a method based on momentum conservation [157, 99] and will be called CstFlux. The wake outline is computed as a δU isoline enclosing a surface S such that the momentum deficit in the wake is equal to the mean rotor thrust. In other words, an optimisation algorithm is run to find the best value of S to fit the function $\mathcal{F}$ defined by Eq. 5.3 with the mean turbine thrust.

$$\mathcal{F}(S) = \rho \int\int_S U \cdot \delta U dy dz \tag{5.3}$$

This method has the advantage to be based on the physical arguments and does not assume *a priori* the shape of the wake but is more expensive because many isocontours must be tested. Similarly to the CstArea method, the wake centre is computed as the velocity deficit centroïd of S.

- Finally, the wake centre can be tracked by finding the minimum of a convolution product between the power density defined as $0.5U_xU^2$ and a Gaussian masking function [21]. It can be viewed as a modification of the MinPower algorithm with preprocessing using a spatial convolution averaging.

5.2 Pre-processing the instantaneous velocity field

As shown in Fig. 5.1, the turbulent velocity field downstream of the turbine can be very noisy and the wake may be mistaken for low-velocity eddies. All the tracking algorithms aforementioned may fail to find the wake centre for some frames or to mistake the wake with a low-velocity eddy, especially in the far wake. Consequently, some pre- and post-processing can be applied to improve the results, respectively to the dataset used by the tracking algorithm and to the output time series y_c, z_c.

For the SWiFT benchmark for instance [80], a post-processing approach is used. An *ad hoc* filtering of the failed frames is first applied (this is further detailed in Sect. 5.4.1), followed by median filtering of the time series of wake centre position. A prior study on the same turbine showed that a kernel size of 5 frames was optimal for this filter [157], hence removing outliers without changing too much the results.

With a post-processing approach, one can easily correct for some outliers, but the resulting time series might be changed by the post-processing. For instance, if a median filter with a too large kernel is used, the high-frequency component of the y_c, z_c time series might be damped, thus reducing σ_{fy}, σ_{fz}. Moreover, the frames modified by the median filter may not be realistic wake centre positions, leading to erroneous frames for the computation of the MFOR. Finally, if a consecutive number of frames larger than the filter's kernel is failing, the outliers will not be discarded. Such a situation can arise in the far wake as it will be shown herein. For all these reasons, the choice has been made to focus on pre-processing methods, i.e. modifications of U and δU used in the algorithms presented in Sect. 5.1.2 to help them find the 'true' wake centre.

5.2.1 Redefinition of the unperturbed velocity

The first method that we propose comes from the observation that the main source of tracking error is the inflow turbulence. It would thus be helpful to remove the atmospheric turbulence from the instantaneous velocity plane. This of course cannot be completely done since the atmospheric turbulence progressively merges with the wake, but we just need to remove enough atmospheric contribution to make the tracking algorithms find the right wake centre position.

Our approach is to redefine the unperturbed velocity U_0 that is used to compute δU and ΔU (see Eq. 2.7). In the literature, the unperturbed velocity is often defined as the temporally- and laterally-averaged velocity upstream of the turbine, i.e. $U_0(z) = U_\infty = \overline{U}(x = x_\infty, z)$ (Fig. 5.2a). Hereafter, this will be called the upstream definition and computed at $x_\infty = -2.5D$ as in the SWiFT benchmark.

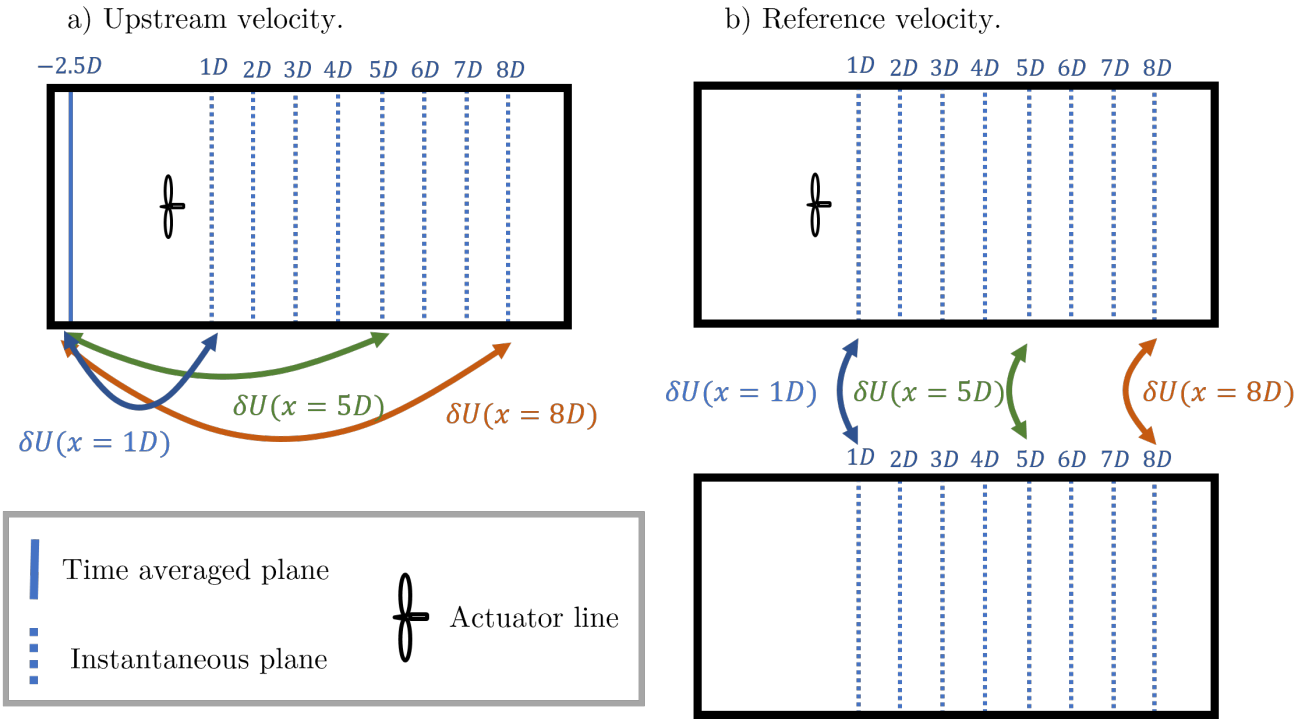

Figure 5.2: Two ways to define the unperturbed velocity: a) mean upstream velocity profile and b) instantaneous downstream profile in a reference simulation.

The upstream definition removes the mean shear (near-ground low velocities can be mistaken with the wake) but not the instantaneous eddies of the ABL.

Instead, it is here proposed to use instantaneous velocity planes from a reference simulation without wind turbine but with the same inflow. In practice, this is done by running the exact same simulation (same mesh, time step, inflow etc...) as the main run, but deactivating the ALM body forces. This will hereafter be called reference definition of the unperturbed velocity: $U_0 = U_{ref}(x, y, z, t)$ (Fig. 5.2b). The eddies of the ABL not affected by the wake are the same in both simulations and are expected to cancel each other when computing the mean velocity deficit $\delta U = U - U_{ref}$. This method, already introduced in [64] is computationally more expensive as it requires running another LES simulation. Note that this definition does not modify the MinPower results, where only U is used, and not δU. Moreover, this method is restrained to numerical simulations since measurements (full-scale or in a wind tunnel) cannot produce such a reference dataset.

Figure 5.3 reproduces Fig. 5.1, with δU computed with the reference definition of U_0. As expected, a lot of the ABL turbulence has been removed and far from the wake δU_x is close to 0 (e.g. for $z/D > 2$). Near the wake centre, this removal is not perfect because the wake interacts with the surrounding eddies, but ABL eddies lose their consistency and become spatially non-homogeneous. In particular the low-velocity eddy at $y/D = 2$ in Fig. 5.3b can no longer be mistaken with the wake. However, the velocity deficit planes are quite noisy. This is not surprising since the largest scales are not expected to be affected by the wake but the smallest are, and will thus differ between the main and the reference simulations. This spatial inhomogeneity is an issue for tracking algorithms based on velocity isolines because it creates many possible new contours.

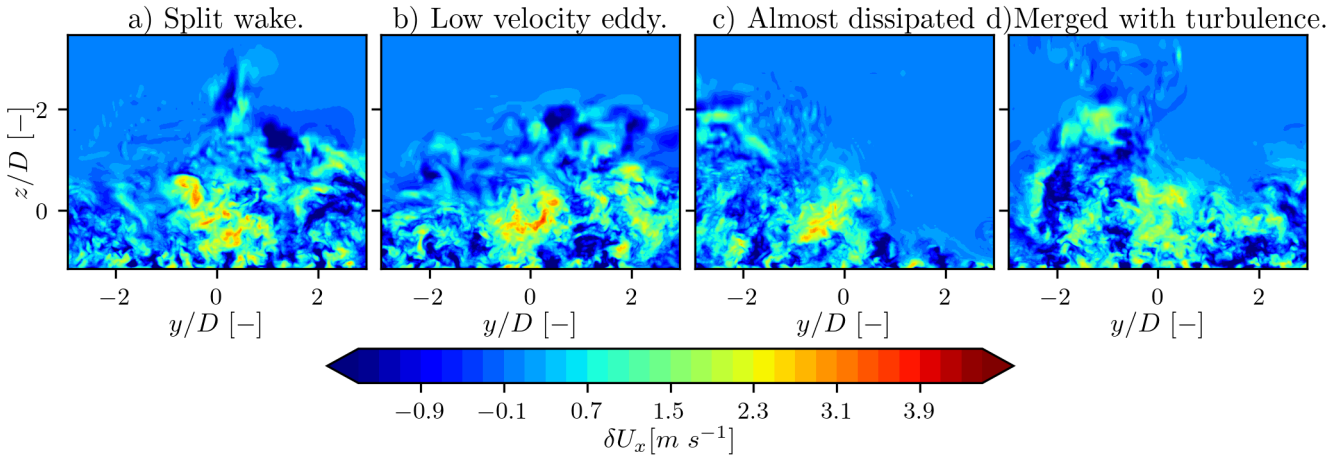

Figure 5.3: Same as Fig. 5.1 with $U_0 = U_{ref}$.

5.2.2 Moving average of the instantaneous velocity

The reference definition of the unperturbed velocity led to a velocity field with a lot of small-scale spatial variations. To smooth this data, we propose to apply a moving average operator $< . >$ on the velocity and reference velocity fields, as in [94]:

$$< U > (t) = \frac{1}{\delta T} \int_{t-\delta T/2}^{t+\delta T/2} U(\tau) d\tau \tag{5.4}$$

where δT is the window size. One must take care that the meandering motions are not filtered out by doing so: based on the hypothesis that the meandering length scale is equal to $D/2$, one can choose $\delta T = D/2U_h$ [94]. In our neutral case, this leads to $\Delta T = 1.7$ s, which is not usable since the data is sampled at 1 Hz.

To find an appropriate window, we here propose an approach based on a spectral analysis of the wake centre position. In Fig. 5.4, the PSD of the wake centre position is plotted in the horizontal and vertical directions. The positions y_c, z_c are computed with the CstFlux algorithm on the neutral case and without any pre- or post-processing. It is computed for three positions downstream: $1D$, $3D$ and $6D$. We restrained to $6D$ to keep a certain amount of confidence in the results, knowing that further downstream a large number of errors would degrade the results. Besides their amplitude, spectra are very similar from one position to another, indicating that meandering only increases in amplitude as it travels downstream but its spectral signature does not change. This is assumed to be true up to $8D$ downstream.

Most of the y_c; z_c variations happen at frequencies lower than 0.05 Hz. As a consequence, the filter window size must not be larger than 20 s or the amount of meandering may be significantly modified. According to the Nyquist–Shannon sampling theorem, we must thus not fall below a sampling of 10 s. To keep a margin, we set $\delta T = 7$ s i.e. 7 frames. The cut-off frequency could have been lowered in

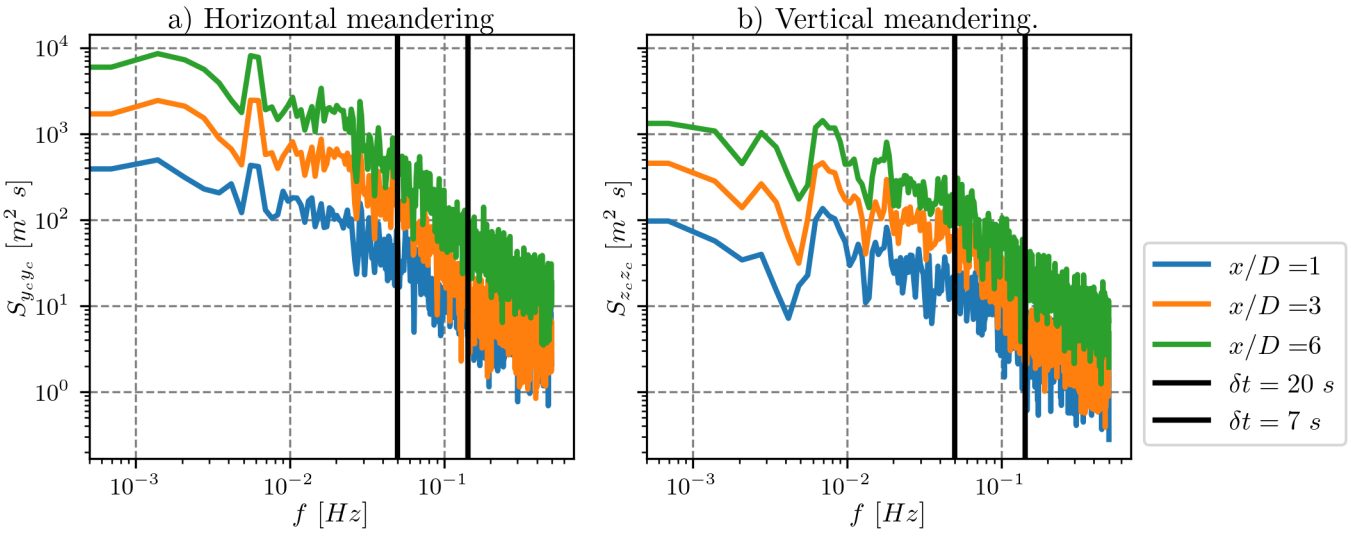

Figure 5.4: Spectra of the wake centre time series for the CstFlux with no pre-processing at different positions downstream. a) Horizontal coordinate; b) Vertical coordinate.

the stable and unstable cases proportionally to the incoming velocity. This choice was not retained and the same window size has been used for all cases. We may thus not expect to see meandering patterns of a larger time scale than 7 s, i.e. length scales smaller than 1.2 D. This value is dangerously close to the expected minimum length scale of wake meandering of $2D$, which is acknowledged to be an issue and prevents to analyse the actual length scale of meandering in the simulation. This choice has been maintained for its good results and because spectral analysis of wake meandering is not the main objective of this work.

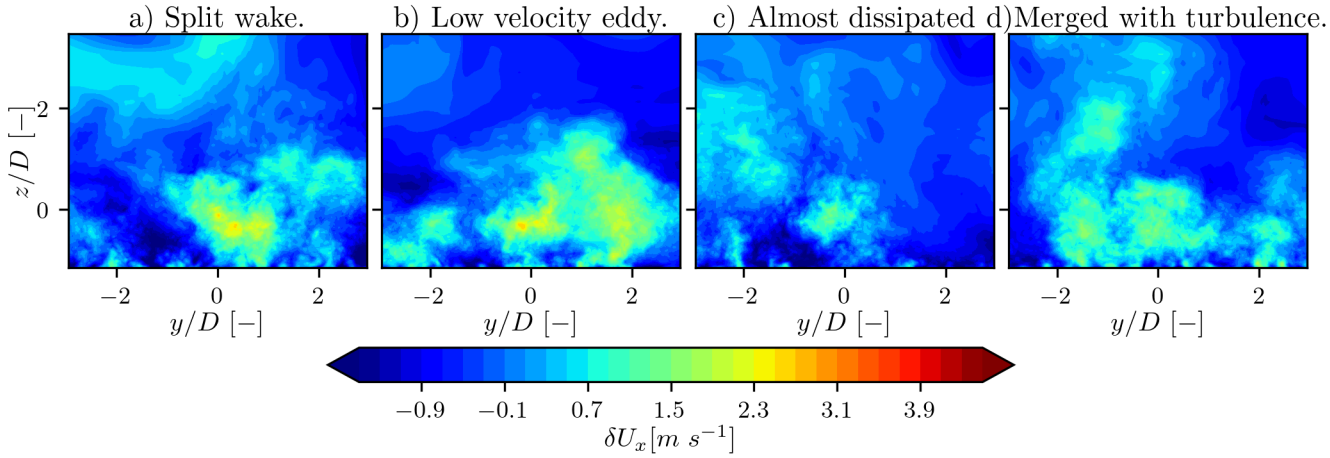

Figure 5.5: Same as Fig. 5.1 with $\delta T = 7$ s.

This filter applied to the velocity deficit with the upstream definition modifies the four planes plotted in Fig. 5.1 into Fig. 5.5. As expected, the velocity deficit is smoothed, and we can expect contour-

based algorithms to perform better on such data. In particular, the split case (Fig. 5.5a) is now merged and the wake is much more coherent. When applied to the reference definition of U_0 (Fig. 5.6), the resulting field are even more promising. The frame where the wake was almost dissipated (Fig. 5.6c) is now more clearly defined, due to the neighbouring frames increasing the amplitude of velocity deficit and to the removal of surrounding eddies that leads to a velocity of deficit close to 0 around the wake. Similarly, the wake that was indistinguishable from near-wall turbulence is now better defined because both the time average and the reference velocity contributed to removing the small-scale turbulence near the ground.

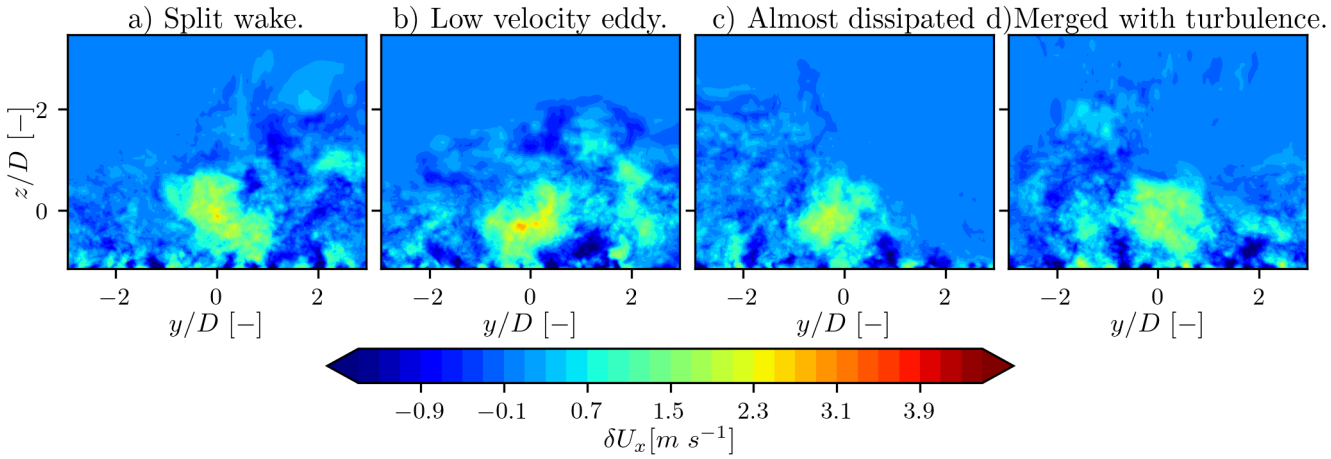

Figure 5.6: Same as Fig. 5.3 with $\delta T = 7$ s.

5.3 Modified simulations

In this chapter and the following ones, the three SWiFT cases are re-used, but with small modifications to be able to analyse the wake up to eight diameters downstream. The modified parameters are reported in Table 5.1, as well as the mean thrust coefficient and inflow parameters: mean velocity at hub height, turbulence intensities in each direction and stability parameter. Note that all the variables included in this stability parameter (see Eq. 1.23) have been computed at 10 m, in particular the friction velocity which is often taken at the ground.

As shown in Sect. A.1, the wake flowfield becomes non-physical near the outflow region when 1WAY nesting is used. However, using such mode is necessary when applying the reference definition of U_0 to have consistent flowfields between the main simulation and the reference simulation. We also showed that far from the boundary conditions, the differences between 1WAY and 2WAY nestings are negligible. For the following simulations, the 1WAY nesting is thus used between D_1 and D_2 instead of between D_{n-1} and D_n in the SWiFT benchmark and the sizes of the domain D_2 to D_n are increased, according to table 5.1. Note that for the stable case, the boundary conditions are not changed since only 2 domains are used.

	Neutral				Unstable				Stable	
Parameter	D_1	D_2	D_3	D_4	D_1	D_2	D_3	D_4	D_1	D_2
L_x [m]	-	3200	640	-	-	4000	1080	500	-	480
L_y [m]	-	1600	320	216	-	2000	540	250	-	180
U_g [m s^{-1}]	(u=11.42, v=-3.7)				-				-	
ΔT [s]	80				40				10	
$\overline{C}_T$ [-]	0.79				0.81				0.82	
U_h [m s^{-1}]	8.4				6.2				4.7	
I_x [%]	11.2				12.3				3.7	
I_y [%]	8.8				14.6				3.1	
I_z [%]	7.1				6.9				2.4	
ζ [-]	0.003				-0.16				0.60	

Table 5.1: Modified numerical parameters for the following chapters.

In the SWiFT benchmark, simulations were performed on 10-minute segments, and an ensemble average was computed over all the segments. This is very appropriate when studying the mean velocity, but as shown in Sect. 1.1.5, it neglects the inter-variance, i.e. large-scale variations, for second-order moments like turbulence or wake meandering. To avoid this, the velocity statistics are computed over the concatenated segments, without an ensemble average. This approach also has limitations: it leads to a spatially non-homogeneous turbulence field and it must be kept in mind that different periods are used for the three cases (80 min, 40 min and 10 min for the neutral, unstable and stable cases respectively). Note that the sampling frequency has been kept to 1 Hz.

In the following, the spatial coordinates are centred at the middle of the hub, i.e. the centre of the ALM is located at $(x, y, z) = (0, 0, 0)$ and the ground is located at $z = -z_h$. Moreover, in all the following work, only the streamwise component of the velocity is studied. The corresponding mean velocity and variance, $\overline{U}_x$ and k_x, will be the only variables studied in the wake.

5.4 Results

In this section, we compare the results given by four tracking algorithms implemented in the SAMWICH toolbox [154]: Gauss2D (blue), MinPower (red), CstArea (green) and CstFlux (orange). The two different definitions of the unperturbed velocity are also compared. The impact of the window size has not been investigated and it is fixed to $\delta T = 7$ s. In the following, 'tracking algorithm' refers to the algorithm itself (listed in Sect. 5.1.2) whereas 'tracking method' refers to the choice of the whole tracking chain i.e. algorithm as well as the pre- and post-processing.

5.4.1 Visual analysis

The four tracking techniques are tested on the velocity deficit field defined with the upstream (Figs. 5.7a and Figs. 5.8a) and the reference (Figs. 5.7b and Figs. 5.8b) definitions of the unperturbed velocity. To compare the tracking algorithms, results for the first 400 frames have been visually checked. For each algorithm, the number of time steps where the output wake position is wrong is

reported in Table 5.2. No criteria could be found to characterise automatically whether the algorithm failed or not so this visually-based method is the best that was found.

	Upstream			Reference			
total	Gauss2D	CstArea	CstFlux	Gauss2D	CstArea	CstFlux	Ambiguous
400	79	39	37	53	43	14	20
%	19,75	9,75	9,25	13,25	10,75	3,5	5
AutomDetec	40	0	0	31	0	0	
Remaining(%)	9,75	9,75	9,25	5,5	10,75	3,5	

Table 5.2: Number of errors for different wake tracking methods at $x/D = 8$ for the first 400 frames.

This qualitative analysis is based on whether the minimum velocity (excluding the small eddies close to the ground) is included in the detected wake, and on the coherence of the studied frame with the preceding and succeeding frames. For instance, Fig. 5.7a shows a frame where three different wake centres were found with the upstream velocity: near $y/D = 0$ for the CstArea and CstFlux algorithms and $y/D = 1.5$ for the Gauss2D and MinPower algorithms. This ambiguity is due to the presence of a low-velocity eddy near $y/D = 1.5$ (cf. Fig. 5.1b) that disappeared when using the reference velocity (Fig. 5.7b). For this time step, the CstArea and CstFlux are thus considered correct for both definitions, Gauss2D only for the reference velocity and MinPower for none. Note that the MinPower algorithm does not use U_0, and thus is not affected by the choice of reference or upstream definition.

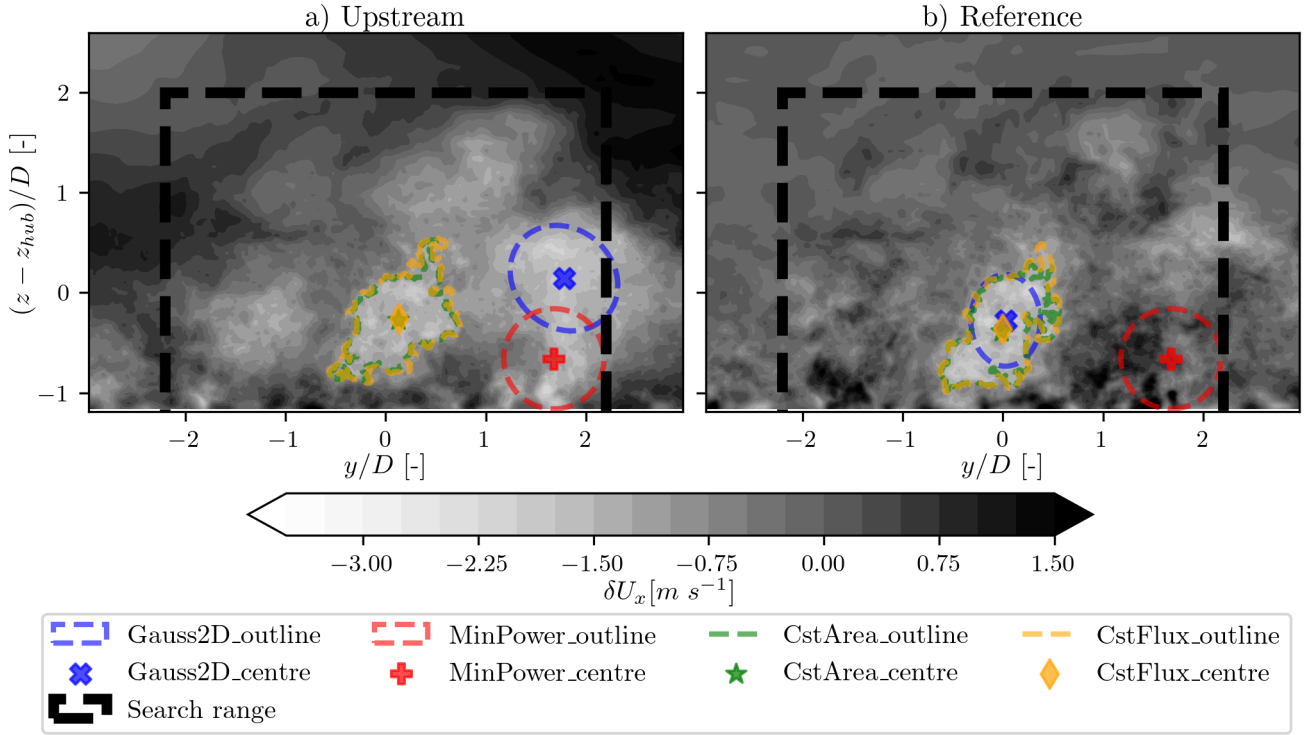

Figure 5.7: Results of different tracking algorithms and unperturbed velocity definitions.

For some frames, it is difficult to conclude which algorithm and U_0 definition gives the 'real' wake centre, either because the wake centre may not be unique or because the wake is strongly dissipated

and is hardly distinguishable from ABL turbulence. Figure 5.8 shows an example of the latter situation: with the upstream definition, the tracking algorithms clearly incorporate atmospheric turbulence and give slightly different results for y_c and z_c. When the reference velocity is used, most of the atmospheric eddies are removed, but the wake is also attenuated. Despite the CstArea and CstFlux predicting the same position for the wake centre, the tracked velocity deficit is too low to be confidently attributed to the wake and not a small eddy that was not present in the reference simulation. Consequently, the frame corresponding to Fig. 5.8 is labelled as 'Ambiguous' in Table. 5.2 for all algorithms (despite Gauss2D being 'more wrong' than the other algorithms in the reference case). In total, 20 ambiguous frames were found, i.e. 5% of the total.

The MinPower algorithm gives a very large number of outliers. Indeed, it is attracted by the low velocities near the ground and then systematically underpredicts the vertical position of the wake centre, as will be shown in Fig. 5.10. This algorithm may be efficient for one-dimensional tracking in the horizontal direction but is not suited for the present study in 2D. Moreover, it could not be improved by our pre-processing since it is not affected by the redefinition of the unperturbed velocity. Results from this algorithm are thus not reported in Table. 5.2.

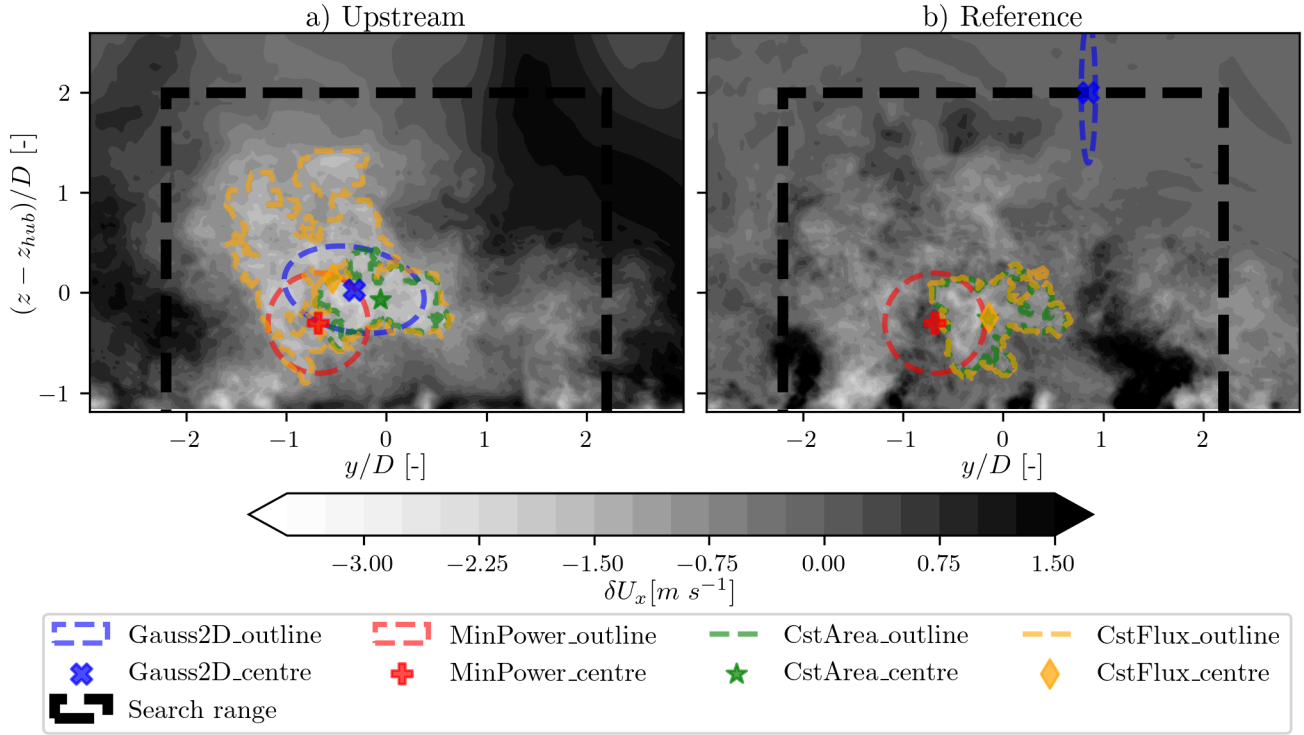

Figure 5.8: Time frame where the best-performing tracking method could not be determined.

For both U_0 definitions, the Gauss2D algorithm leads to the highest number of errors, followed by CstArea and then CstFlux. For the Gauss2D algorithm, many outliers can be automatically detected because the detected wake centre is at the edge of the search range, as in Fig. 5.8b. We thus use an *ad hoc* filter similarly to what was done in the SWiFT benchmark [80] where we discard a frame if the wake centre position fulfils at least one of these conditions:

- If the wake centre is too close to the ground (between ground level and the bottom tip level): $z_c < -D$

- If the wake centre is detected at the edge of the search range with a margin of ±10 %. In other words, if $|y_c| > 1.98D$ or if $z_c > 1.8D$.

At $x/D = 8$, this automatic filter removes about half of the errors of the Gauss2D algorithm. Even though it is applied to the other algorithm, it does only discard several frames over the total of 4800 and none among the 400 studied herein. This filter makes the Gauss2D equally or even more reliable than the CstArea one. However, recovering the wake centre at these time steps from interpolation is prone to errors because they tend to appear on several frames in a row. This interpolation is necessary to compute the spectra of the time series of y_c and z_c (Figs. 5.9, 5.10, and 5.11) but the time frames are simply discarded when computing the MFOR, leading to about 10% missing data. Such missing data can be problematic when computing velocity spectra in the MFOR as will be done in Ch. 6.

The reference definition of unperturbed velocity reduces the number of outliers for the Gauss2D and CstFlux methods but degrades the results for the CstArea algorithm. This is attributed to the fact that δU computed with the reference definition is spatially less homogeneous, leading to many more possible isolines that enclose an area equal to the rotor-swept area. Since the CstArea method has no criteria on velocity inside the isoline, it sometimes detects a wake where the velocity deficit is very low but where an isoline has been created by the use of the reference definition. This does not apply to the Gauss2D and CstFlux methods that check the velocity or momentum deficit inside the detected isoline. For these latter algorithms, the use of reference velocity mostly solves the cases where the ABL turbulence perturbs the tracking. Despite the number of outliers being lower in Table. 5.2, note that for some frames the algorithms with the reference velocity fail whereas for the upstream they do not. Overall though, the best results are achieved with the CstFlux algorithm with the reference definition of U_0, which led to only 3.5% outliers over the 400 studied frames.

5.4.2 Time series and spectral analysis

The precedent observations are completed by an analysis of the wake centre position given by the different methods. The time series (after the *ad hoc* filter has been applied) of the horizontal wake centre position is plotted in Fig. 5.9 over the first 1200 s. For both definitions of the unperturbed velocity, the algorithms find overall the same path for the wake centre.

For every method, some peaks can be observed, which correspond to outliers. Indeed, the wake cannot physically move so fast between two frames: even supposing that it can move laterally by $\overline{U}_h \approx 8$ m s^{-1}, it could at best be displaced of $0.3D$ in one frame.

These outliers can be removed by a post-processing method, for instance a median filter applied on y_c and z_c [157]. However this is not sufficient to solve all of them: for instance around $t = 350$ s, the wake position is detected around $y_c/D = 1$ with the upstream definition, whereas it is detected at $y_c/D = 0$ with the reference definition. A median filter would not change Fig. 5.9a into Fig. 5.9b and would thus not reveal the 'true' wake centre position. What has been observed on the first 400 frames is confirmed here: the reference definition improves the results for the Gauss2D and CstFlux algorithms but degrades it for the CstArea method. Note that the MinPower algorithm has very few outliers and behaves similarly to the Gauss2D and CstFlux. For y_c only it may be considered a robust method.

The evolution of the vertical coordinate has similarly been plotted in Fig. 5.10. As for the horizontal

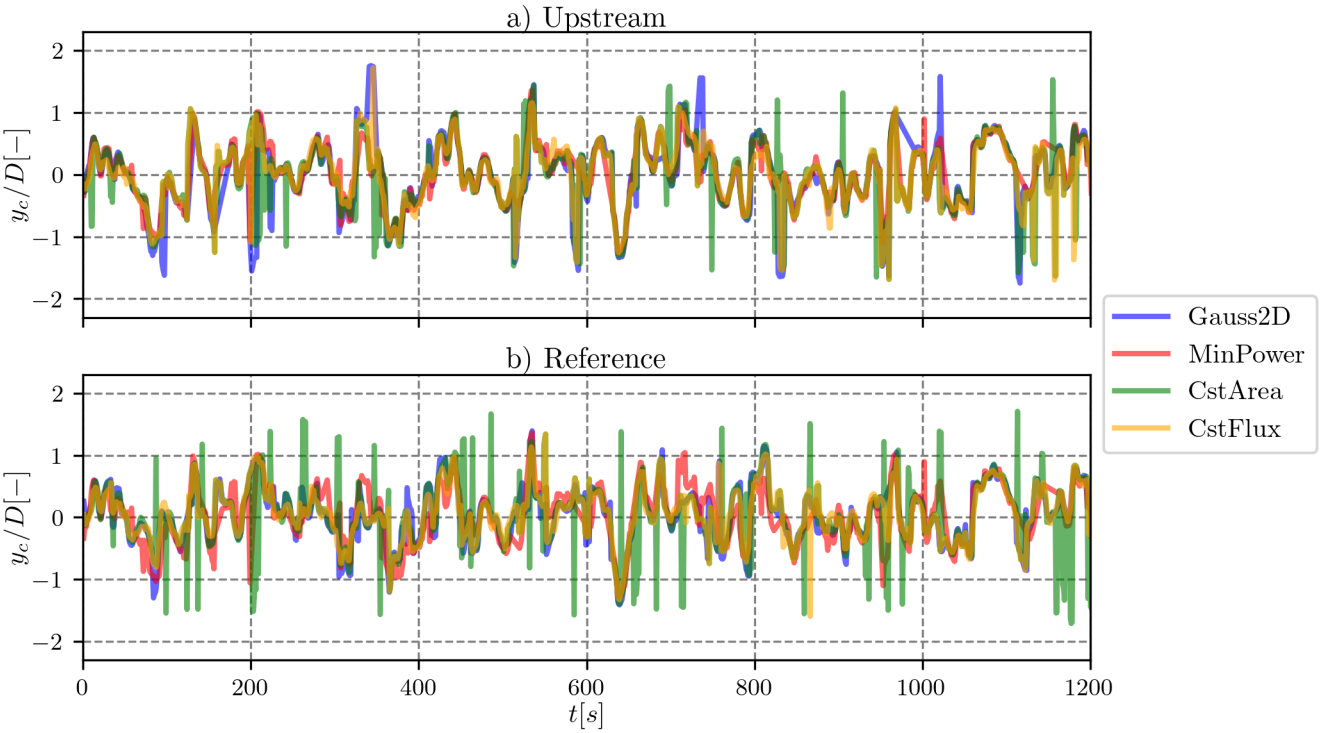

Figure 5.9: Time series of the wake centre's horizontal coordinate for different algorithms at $x/D = 8$ and a) $U_0 = U_\infty$ et b) $U_0 = U_{ref}$..

coordinate, the CstArea gives a lot more outliers with the reference definition compared to the upstream one. Whereas in the horizontal direction, the Gauss2D and CstFlux methods were giving approximately the same results, in the vertical direction the Gauss2D has many more outliers, leading to the results in Table. 5.2. These errors are almost always over-predictions, which we could not explain here. Conversely, the MinPower algorithm systematically predicts a wake centre closer to the ground than the other algorithms. As explained before, this is attributed to the low velocity at the ground that 'attracts' the minimum power to the low values of z_c. This is why it is not reported in Table. 5.2 nor studied in Sect. 5.4.3.

The PSDs of the wake centre coordinates are plotted in Fig. 5.11 for the upstream (a and c) and reference definitions of the unperturbed (b and c) velocity. It is computed on the whole 4800 second, with the built-in welch method of scipy where the segment length is set to 960 s (hence the minimum frequency being around 0.001 Hz). For both directions, the differences between algorithms or between U_0 definitions mostly arise at high frequency. It means that the large-scale movements of the wake centre position are mostly identical between all these methods, and the time series differ by high-frequency movements. This was already observed in the time series but is better confirmed in the present graph. One can note however that this is not true for the Gauss2D algorithm in the vertical direction: between $f = 0.005$ and $f = 0.1$ Hz it estimates significantly higher variations of the vertical wake variations. The errors observed in Fig. 5.10 thus degrade the low-frequency region of the wake meandering, which is the region of interest.

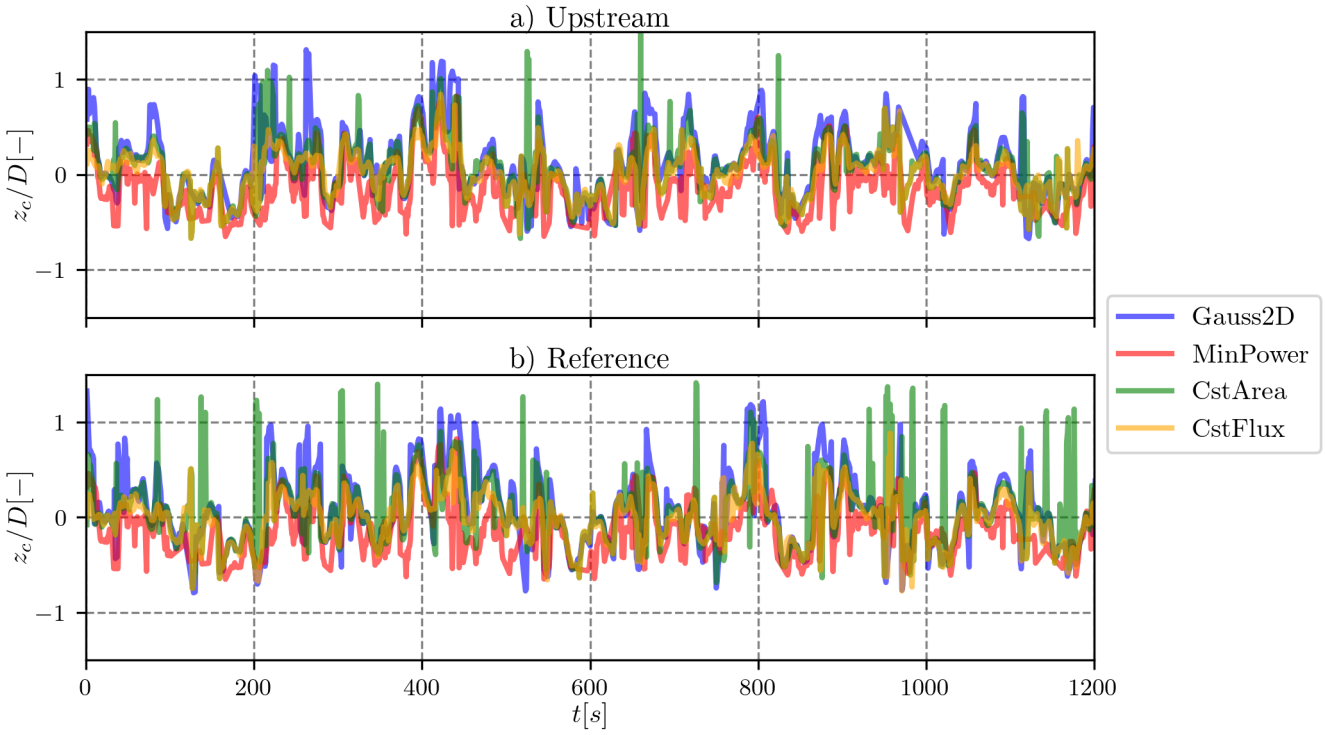

Figure 5.10: Time series of the wake centre's vertical coordinate for different algorithms at $x/D = 8$ and a) $U_0 = U_\infty$ et b) $U_0 = U_{ref}$.

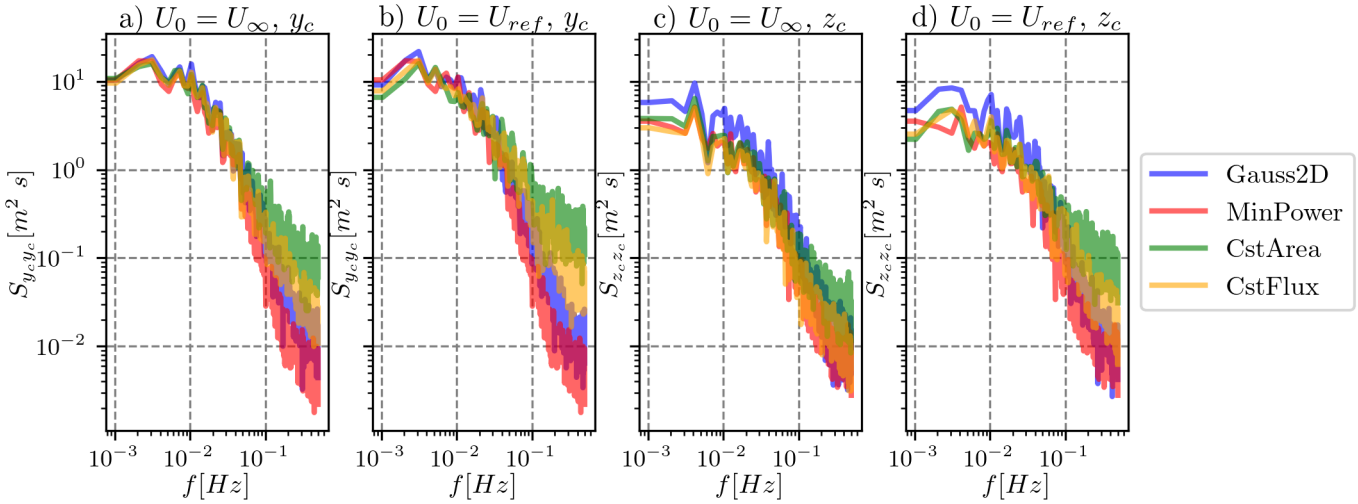

Figure 5.11: Spectra of the wake centre's vertical coordinate for different algorithms. Vertical and horizontal coordinates for the upstream and reference definitions of U_0.

5.4.3 Impact on the MFOR

From the preceding observations along with the visual analysis of the first 400 frames, it seems that the best wake tracking method is to use the CstFlux algorithm, with the reference definition of the unperturbed velocity. In this last step, we investigate the effect of different algorithms on the

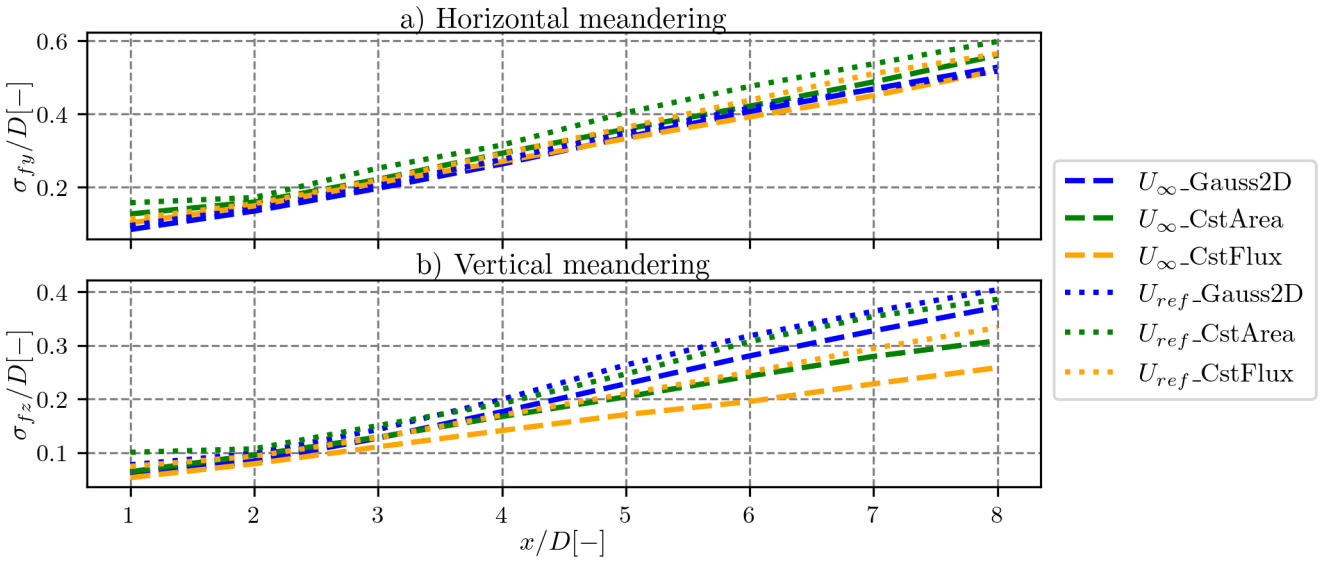

Figure 5.12: Impact of the wake tracking algorithm on the amount of meandering.

wake properties in the MFOR. Given that the ground is located around $z_{FF} \approx -1.2D$ and that the minimum value of z_{MF} is set to $-1D$, then for the frames where $z_c(t) < -0.2D$, the velocity field at $U_{MF}(z_{MF} < -1.2D - z_c(t))$ is located under the ground and is thus undefined. Since extrapolation led to erroneous results, these values are ignored when computing the mean velocity and TKE in the MFOR. The frames where the *ad hoc* filter detected outliers are also ignored to compute the MFOR.

The amount of meandering is plotted in Fig. 5.12a (horizontal direction) and 5.12b (vertical direction) for the Gauss2D, CstArea and CstFlux algorithms, with the upstream (dashed lines) and reference (dotted lines) definitions of U_0. First, one must note that a somewhat linear behaviour is predicted by every method, with different slopes and origins. At eight diameters downstream, the difference between the lowest and highest predicted values is about 20 % in the horizontal direction and 60 % in the vertical direction. These can be regarded as important discrepancies, given that such data will be used for model calibration.

The presence of outliers tends to increase the amount of meandering e.g. for the CstArea with U_{ref} case (dotted green line Fig. 5.12a). However, it does not allow us to conclude that the method leading to the lowest value of σ_f is systematically the best. For instance, the use of reference velocity shows an increase of σ_f for all methods despite reducing the number of outliers in the CstFlux and Gauss2D algorithms. Our interpretation is that using the reference allows better detection of the wake centre when it is positioned near the ground, thus increasing the amount of meandering, in particular in the vertical direction. Indeed, when the wake merges with the low-velocity eddies near the ground, it becomes hard for the algorithm to find a contour because isolines touch the ground and are not closed. Using the reference definition 'breaks' these low-velocity eddies and possibly facilitates the closing of isolines.

With the same plotting convention, the lateral profiles (taken at hub height) of $\Delta\overline{U_x}$ and k_x at $x/D = 8$ are plotted in Figs. 5.13a and 5.13b for the Gauss2D, CstArea and CstFlux algorithms, with the two definitions of U_0. The different tracking strategies result in up to 20 % difference for the maximum velocity deficit. In theory, a method predicting high values of σ_f should also predict high

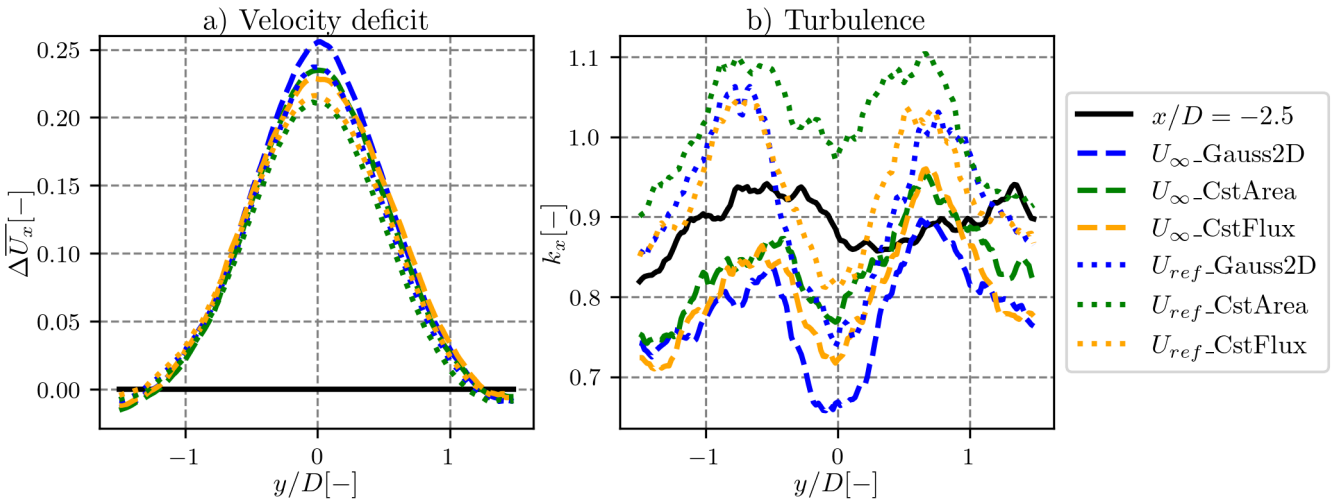

Figure 5.13: Impact of the wake tracking algorithm on the velocity deficit and turbulence horizontal profiles in the MFOR for the neutral case at $x/D = 8$.

values of $\Delta\overline{U_x}$ in the MFOR (since they all start from the same $\Delta\overline{U_x}$ in the FFOR). The opposite is here observed, indicating that the differences between various methods indeed come from errors and not different possible positions of the wake centre that would equally make sense.

One could argue that, at least for CstFlux and Gauss2D cases, if the algorithm mistakes the wake for a low-velocity region of the plane, it means that the detected region contains a larger velocity deficit than the actual wake. Thus, a larger number of outliers leads to a higher velocity deficit, and this reasoning would indicate that the lowest the velocity deficit in the MFOR, the better the method. This argument is however not considered strong enough for a final conclusion, especially since it contradicts the one we made for the meandering analysis.

The choice of the algorithm has only a weak impact on axial turbulence in the MFOR, but large differences arise between the two definitions of unperturbed velocities. The lateral profile of k_x is more symmetrical with the reference definition, and the values at the edges of the wake match more closely the upstream value (in black). It is hard to predict what would be the effect of mispredicting the wake centre on the resulting turbulence, but the Gauss2D and CstFlux algorithms with the reference definition of U_0 give a turbulence profile that is similar to what is expected in the far wake of a turbine. Moreover, it leads to turbulence values locally higher than the upstream values, whereas the upstream definition gives values almost systematically lower.

Conclusion and perspectives

In this chapter, we compared several wake tracking algorithms from the literature as well as pre-processing methods that improve the quality of the tracking. It appears that there is a strong sensitivity of the MFOR properties to the tracking method, in particular the definition of the unperturbed velocity. A visual analysis of the tracking algorithms and pre-processing methods, as well as the study of the time series and the resulting fields in the MFOR indicate that the best results are obtained with the CstFlux that uses the reference definition of the unperturbed velocity and where

a moving average operator is applied on the instantaneous velocity of 7 seconds.

This work is restrained to four tracking algorithms available in the SAMWICH toolbox. Other algorithms in the literature could be tried, in particular, the minimum power computed after convolution with a Gaussian mask [21]. The efficiency of tracking algorithms could be improved by using parallel computing or even tracking the wake in parallel with the simulation to avoid storing large quantities of data. More advanced pre-processing methods could be used, e.g. a two-dimensional empirical mode decomposition that separates spatial large-scale organized motion from random turbulent fluctuations [160]. The peaks in the position of the wake centre time series could be removed if the search range was reduced and re-centred on the previously found centre. However, this method would necessitate confidence in the initial point and one can imagine a case where the algorithm is stuck far from the wake centre. Finally, having a way to define a reference wake centre time series would be helpful to assess more quantitatively the performances of different wake tracking methods.

Chapter 6

Physical analysis of wake properties

The general purpose of this thesis is to develop an analytical model where the wake expansion and the meandering are taken independently into account. The present chapter aims at determining if such separation is possible, and how these two phenomena vary with the atmospheric conditions. To do so, we investigate the wake meandering and properties in the FFOR and MFOR for the three cases of stability defined in Sect. 5.3. The best practices deduced from Ch. 5 are re-used to compute the time series $y_c(t), z_c(t)$, necessary to this study: the CstFlux algorithm is chosen, with the reference definition of U_0 and a moving averaged operator with $\delta T = 7$ s is applied on the velocity field. Note that even though the reference velocity is used for the wake tracking, the upstream definition is used for the computation of ΔU and Δk in the wake, unless specified otherwise by a $._{ref}$ subscript. Most of the work presented herein has been published and presented at the TORQUE 2022 conference [156].

6.1 Wake meandering.

6.1.1 Amount of meandering.

We start here by analysing the amount of turbulence σ_f, defined as the variance of the wake centre coordinates. For the three cases of stability, the evolution of σ_{fy} and σ_{fz} are plotted in Figs 6.1a and 6.1b. In this chapter, the colours red, green and blue are used to represent the unstable, neutral and stable cases, respectively. Note that here, the linear trend of the wake centre signal has been removed before computing the standard deviation. Indeed, for the stable case, the wind direction is evolving somewhat linearly over time, leading to an increased value of σ_{fy} that we do not consider to be meandering. For the two other cases, this detrending has almost no effect. Similarly to other LES studies, horizontal meandering is found to be stronger than vertical meandering and the stronger the stability, the weaker the meandering.

Meandering is often attributed to the variations of wind direction and it has been proposed in the literature to estimate wake meandering as a linear function whose slope is equal to the variance of the inflow direction (see Eq. 2.51) [62]. Here, we approximate this variance by the lateral and vertical turbulence intensities, and propose for each direction and stability case two fitting laws:

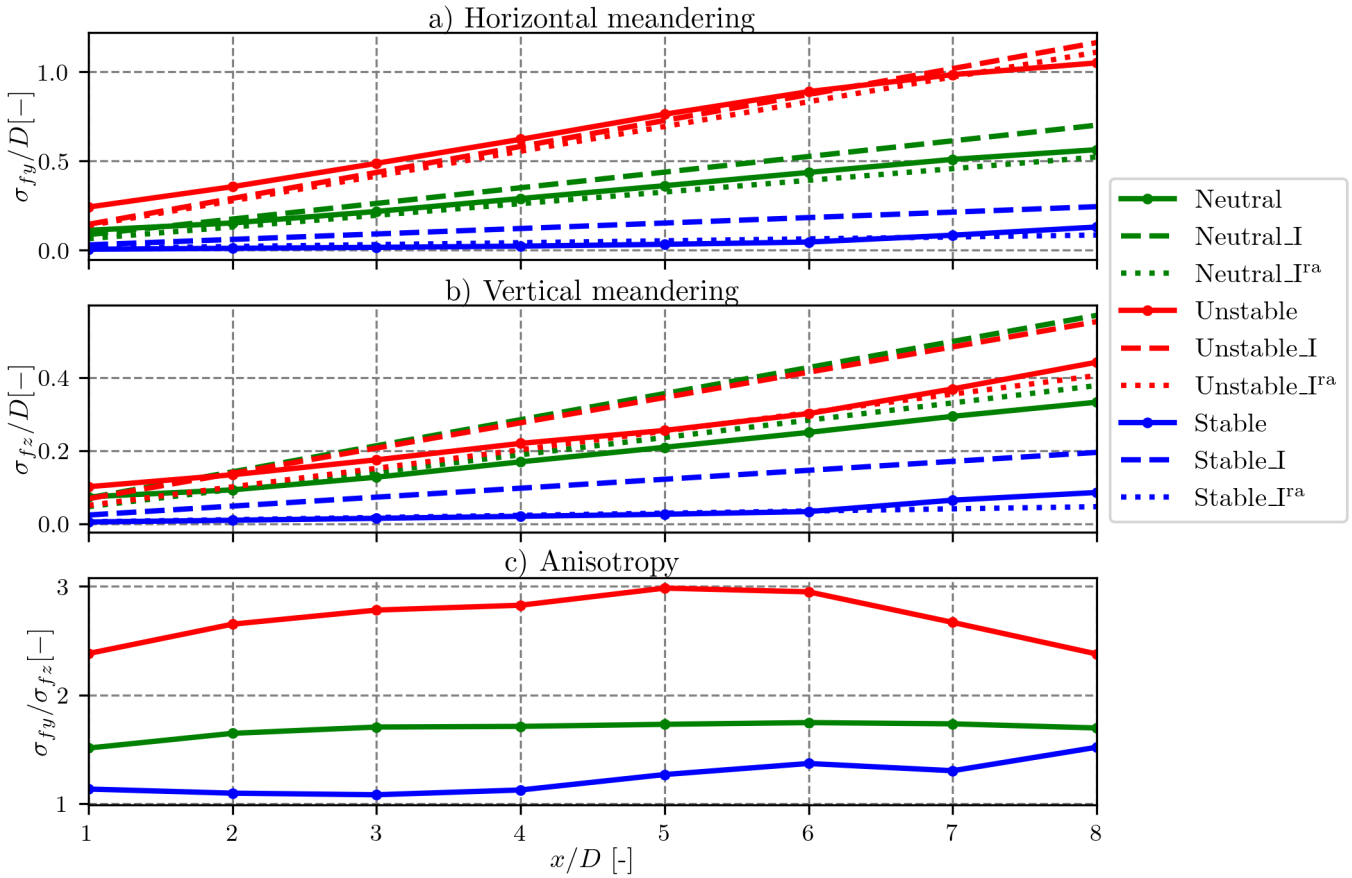

Figure 6.1: Amount of wake meandering: a) horizontal direction; b) vertical direction; c) anisotropy. Dashed lines indicate the fitting law of Eq. 6.1 and dotted lines of Eq. 6.2.

$$\frac{\sigma_{(fy,fz)}(x)}{D} = \frac{x}{D}\, I_{(y,z),\infty} \tag{6.1}$$

$$\frac{\sigma_{(fy,fz)}(x)}{D} = \frac{x}{D}\, I^{ra}_{(y,z),\infty} \tag{6.2}$$

where superscript $.^{ra}$ indicates that a spatial averaging over the rotor-swept area has been performed before computing the variance of the lateral or vertical velocities. In Figs. 6.1a and 6.1b, the linear functions corresponding to Eqs. 6.1 and 6.2 are plotted in dashed and dotted lines respectively. The differences between both functions are stronger in the stable case and in the vertical directions, where the small-scale variations take an important part in the total turbulence and are filtered by the spatial averaging. For most cases, the rotor-averaged turbulence intensities give a good estimation of the total wake meandering.

The anisotropy of the wake meandering, characterised by the ratio σ_{fy}/σ_{fz}, is plotted in Fig. 6.1c. It takes values between 2.5 and 3 for the unstable case, around 1.75 for the neutral case and around 1.25 for the stable case. Other LES studies have shown similar behaviour of decreasing anisotropy with increasing stability [11, 83], whereas the opposite trend has been observed in full-scale LiDAR measurements [85]. It must be noted that the turbine and atmospheric conditions vary from one

study to another and according to the fitting law that we proposed, wake meandering may be strongly sensitive to inflow conditions. Furthermore, all these studies from the literature use the Gauss2D algorithm of wake tracking which has been shown to overestimate the vertical meandering (see Sect. 5.4).

6.1.2 Self-similarity

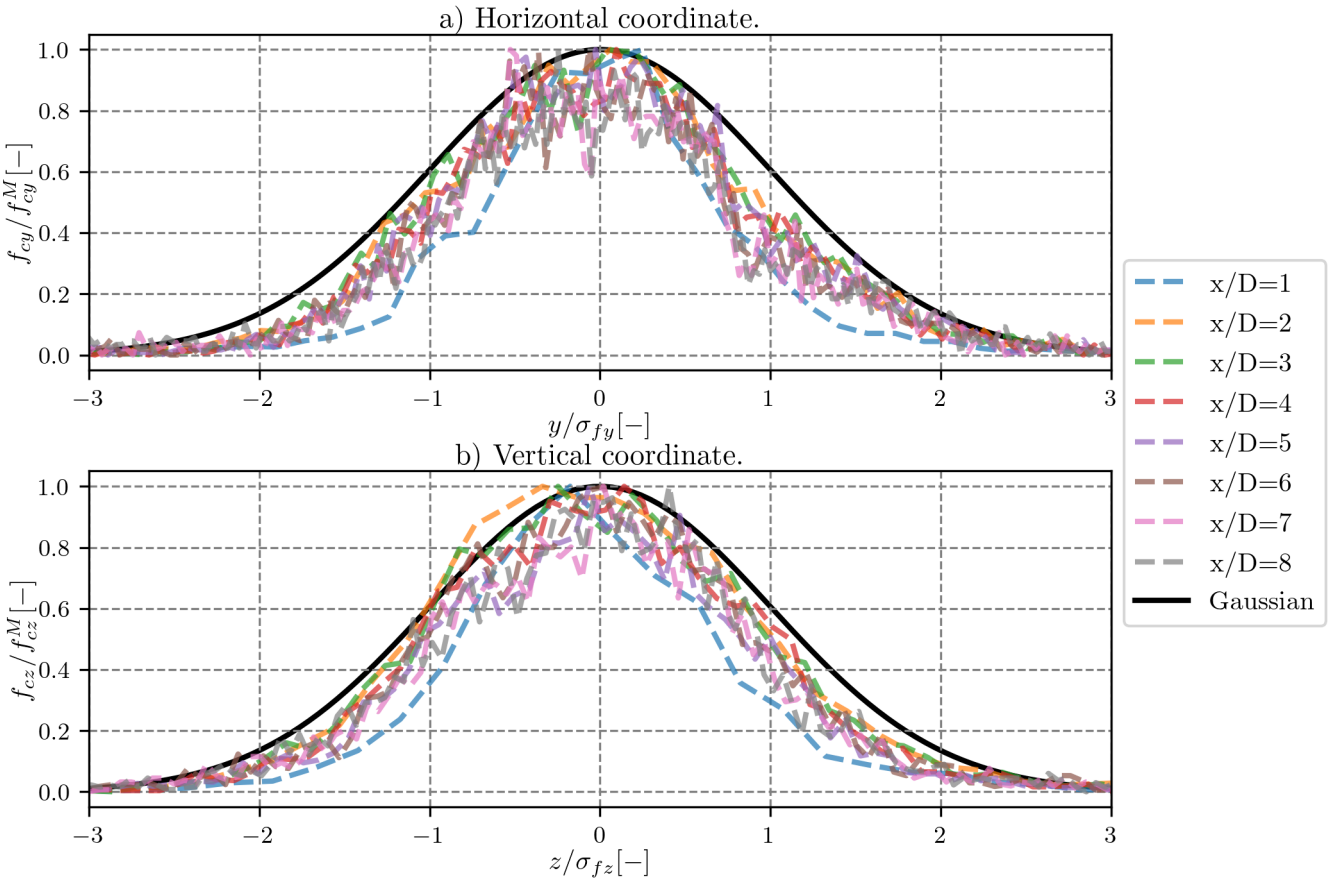

Figure 6.2: Self-similarity of the wake centre histogram for the neutral case.

In this section, we study the PDF of the wake centre position. For analytical models, it is convenient to assume it is a self-similar Gaussian function, i.e. that it can be written:

$$\frac{f_{cy}}{f_{cy}^{M}} = \exp\left(-\frac{1}{2}\frac{y^2}{\sigma_{fy}^2}\right) \tag{6.3}$$

where f_{cy} is the PDF of y_c that takes a maximum value of f_{cy}^{M}. The same expression can be written in the vertical direction (z). The normalised PDFs are plotted at each position downstream for the neutral case in Fig. 6.2, and in black is plotted a perfect self-similar Gaussian function (i.e. Eq. 6.3). Except at $x/D = 1$ where the data is noisy, the self-similarity is rather well reached, even in the vertical direction despite the ground presence that was expected to induce skewness in the

distribution. However, the width of the self-similar curve is slightly lower than that of the perfect Gaussian.

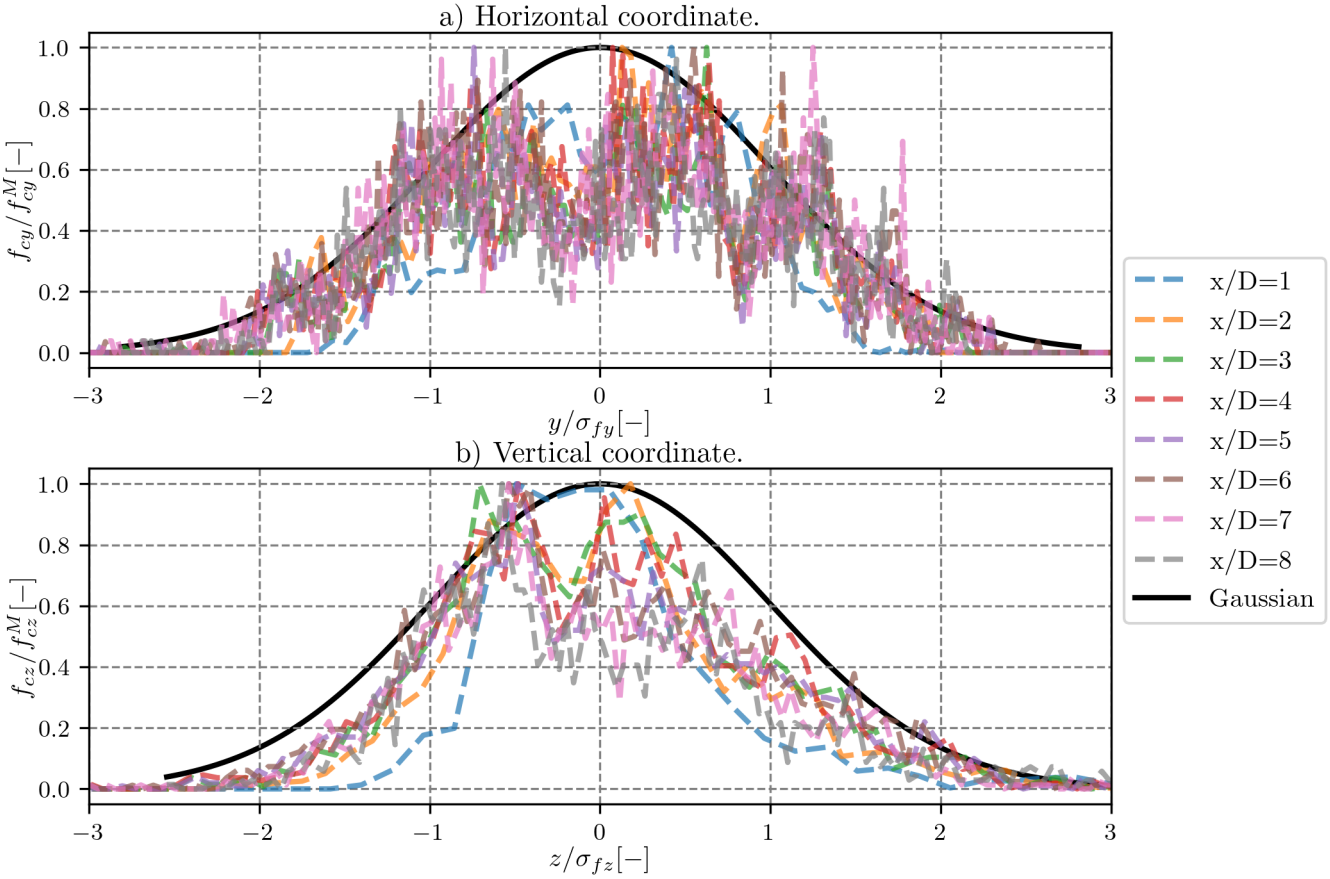

Figure 6.3: Self-similarity of the wake centre histogram for the unstable case.

For the unstable case (Fig. 6.3), data is very noisy but self-similarity is approximately reached in the horizontal direction, even though the given shape of the distributions is not at all Gaussian. This is attributed to non-converged statistics: the unstable simulation has been run for only forty minutes, twice less than the neutral case, whereas the integral time scale of turbulence is much larger (see Sect. 6.3.4). Hence, the wind direction differs by several degrees of azimuth between each segment of 10 minutes in the unstable simulations and much less in the neutral case, inducing different mean wake positions between each segment. Thus, our interpretation is that $\Delta T = 40$ mn in the unstable case did not lead to statistically converged data whereas $\Delta T = 80$ mn in the neutral case has been sufficient. More details on the statistical analysis can be found in [161].

In the stable case (Fig. 6.4), there seems to be some self-similarity up to 6 diameters downstream of the turbine. Further, the similarity is less good. One can note that this corresponds to a break of slope in Figs. 6.1a and 6.1b, indicating a change in the physics driving meandering. It could come from a linear-logarithmic (instead of linear) evolution of wake meandering, as suggested in [129] (see Eq. 2.54).

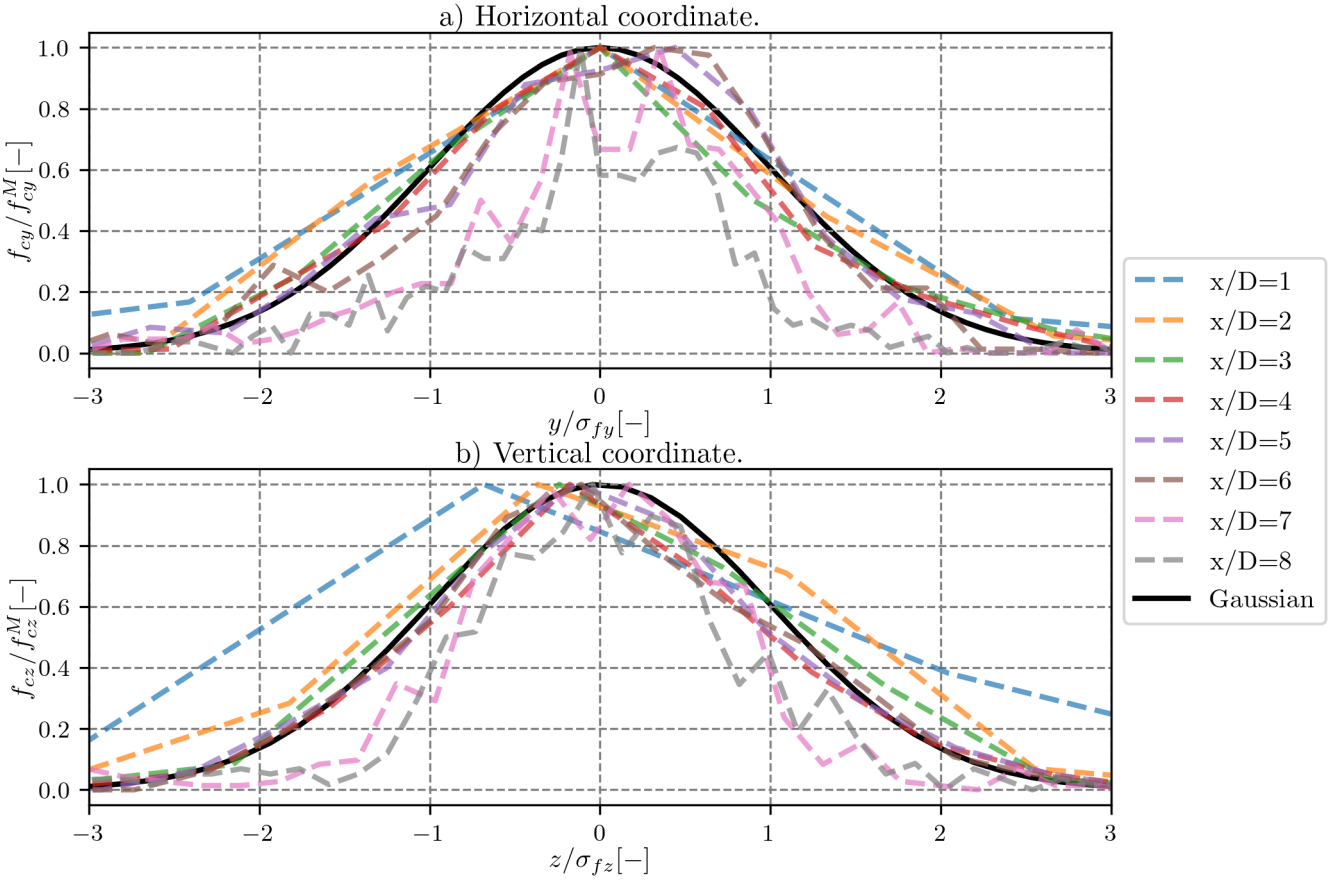

Figure 6.4: Self-similarity of the wake centre histogram for the stable case.

6.2 Velocity deficit

The evolution of the velocity deficit $\Delta\overline{U_x}$ as the wake travels downstream is studied in this section. For the sake of completeness, the reader can refer to Fig. B.1 where the Y-Z planes are plotted in the FFOR and MFOR for each case of stability and each position downstream. These plots can hardly be studied quantitatively so we propose herein other diagnostics.

6.2.1 Wake width

To quantify the wake expansion, which is crucial since we want to differentiate wake meandering and wake expansion, it is common to use the wake widths σ_y and σ_z. These quantities are defined for a Gaussian function as the standard deviation of the Gaussian distribution. However, the wake velocity deficit in LES is not perfectly Gaussian and thus σ can be computed by several different methods. We here use fitting with 2D-function, but many other techniques exist in the literature [162]. Similarly to the Gauss2D tracking algorithm presented in Ch.5, a function $\mathcal{F}$ is fitted on the mean velocity:

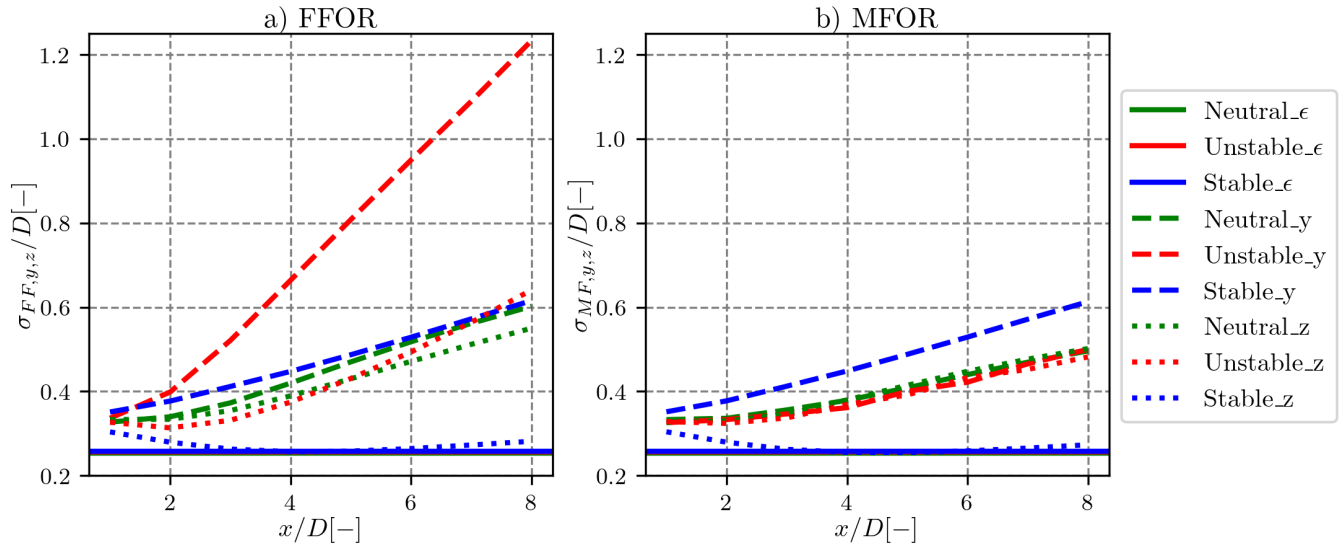

Figure 6.5: Wake widths computed with Eq. 6.4.

$$\mathcal{F}(y, z, \mathcal{A}_0, y_0, z_0, \sigma_y, \sigma_z, \omega_f) = \mathcal{A}_0 + C \exp\left[-c_1(y-y_0)^2 - 2c_2(y-y_0)(z-z_0) - c_3(z-z_0)^2\right] \tag{6.4}$$

where c_1, c_2 and c_3 are defined in Eq. 5.1. Parameter C is fixed as in the XA14 model (Eq. 2.28), and the optimisation is run on parameters $\{\mathcal{A}_0, y_0, z_0, \sigma_y, \sigma_z, \omega_f\}$ where ω_f is the angle of rotation of the wake. Contrarily to the Gauss2D tracking algorithm, the parameters of interest are σ_y and σ_z instead of y_0 and z_0, and the fit is done on the mean velocity deficit instead of the instantaneous one, hence removing all the surrounding turbulence and the risk of errors with it.

The isoline of this function at $\Delta\overline{U}_x/\Delta\overline{U}_x^M = 0.5$ is plotted in a white dashed-dotted line in Fig. B.1, and shows quite good results, in particular for the stable case where the wake is skewed. The resulting σ_y and σ_z are plotted in dashed and dotted lines respectively, in Fig. 6.5a for the FFOR and 6.5b for the MFOR. The value of ϵ defining the wake width at $x = 0$ [77] is also plotted in continuous lines as an additional check (see Sec. 2.4.1).

For all cases and both frames of reference, the wake widths depend linearly on x/D, according to [77] and unlike bluff bodies wakes where $\sigma \sim x^{1/3}$. This linear relation is valid from $x/D = 3$ in the MFOR and $x/D = 2$ in the FFOR. Similarly to other works on stable ABL [116, 86], the wake in the stable case is skewed by an angle of about $\omega \approx 45°$ due to the strong veer (see Fig. B.1). It is thus elongated in one transverse direction and narrow in the perpendicular direction. The rotation parameter ω introduced in Eq. 6.4, allows detecting this deformation, making σ_y and σ_z no longer aligned with y and z but rather with the elongated and thin directions, respectively. It leads to the results plotted in Fig. 6.5 where σ_y increases and σ_z is almost constant or even decreases.

Alternatively, the model developed in [116] can be used as a fitting function instead of Eq. 6.4. It writes:

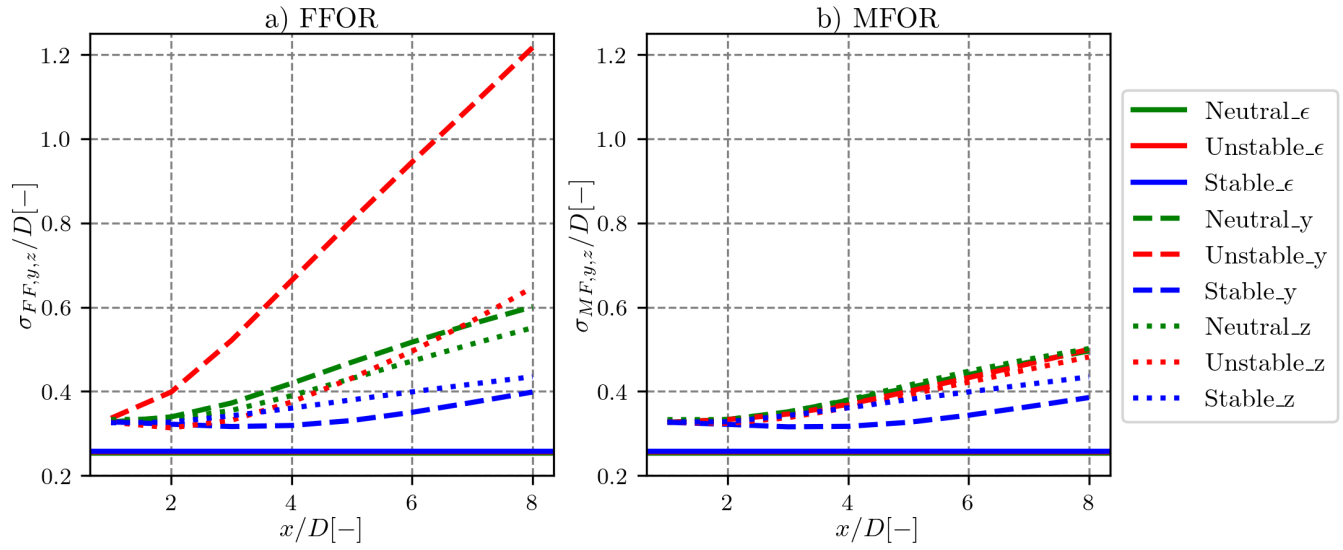

Figure 6.6: Wake widths computed with Eq. 6.5.

$$\mathcal{F}(y, z, \mathcal{A}_0, y_0, z_0, \sigma_y, \sigma_z, \omega_f) = \mathcal{A}_0 + C \exp\left[-\frac{1}{2}\frac{\left(y - y_0 + x\tan(\omega_f z/D)\right)^2}{\sigma_y^2} - \frac{1}{2}\frac{(z - z_0)^2}{\sigma_z^2}\right] \quad (6.5)$$

where ω_f is still the parameter accounting for the skewness of the wake, under a different form (see [116] for details). Similarly to Eq. 6.4, an optimisation algorithm is run on parameters $\{\mathcal{A}_0, y_0, z_0, \sigma_y, \sigma_z, \omega_f\}$ to fit this function on the 2D mean velocity deficit. The isoline of this function at to $\Delta\overline{U}_x/\Delta\overline{U}_x^M = 0.5$ is plotted in black dotted lines in Fig. B.1. One can see that it fits the velocity deficit similarly to Eq. 6.4. The resulting values of σ are plotted in Fig. 6.6: for the neutral and unstable cases, there are almost no changes, but the estimated wake widths in the stable case are much more coherent with what is observed in Fig. B.1: in particular, σ_z does not decrease. However, it leads to $\sigma_z > \sigma_y$, which is the opposite of what is often observed in the literature. This second method can be seen as the quantification of σ before the veer skews the wake whereas the first method quantifies σ after the effect of the veer. Using Eq. 6.5 makes more sense for us since σ is used to characterise the wake expansion, and little attention is attributed to skewed wakes herein. In all the following, values of σ from Fig. 6.6 will thus be used.

In the FFOR, the wake widths are a function of atmospheric stability: the more unstable the ABL, the higher the wake width. Moreover, the wake is strongly asymmetric: the horizontal width (in dashed lines) is much larger than the vertical one (in dotted lines). Conversely in the MFOR, the wake width is fairly axisymmetric (dotted and dashed red and green lines are similar in Fig. 6.6b), as it is assumed in the DWM [61] or the BP14 models. Moreover, the wake widths in the MFOR are equal in the neutral and unstable cases which could be due to similar values of C_T and $I_{x,\infty}$ (see Table 5.1). The differences in the FFOR, whether it is between vertical and horizontal directions or between neutral and unstable cases, can thus be interpreted as being mainly due to different values of meandering.

In some models dealing with meandering, it is assumed that the wake width in the FFOR can be

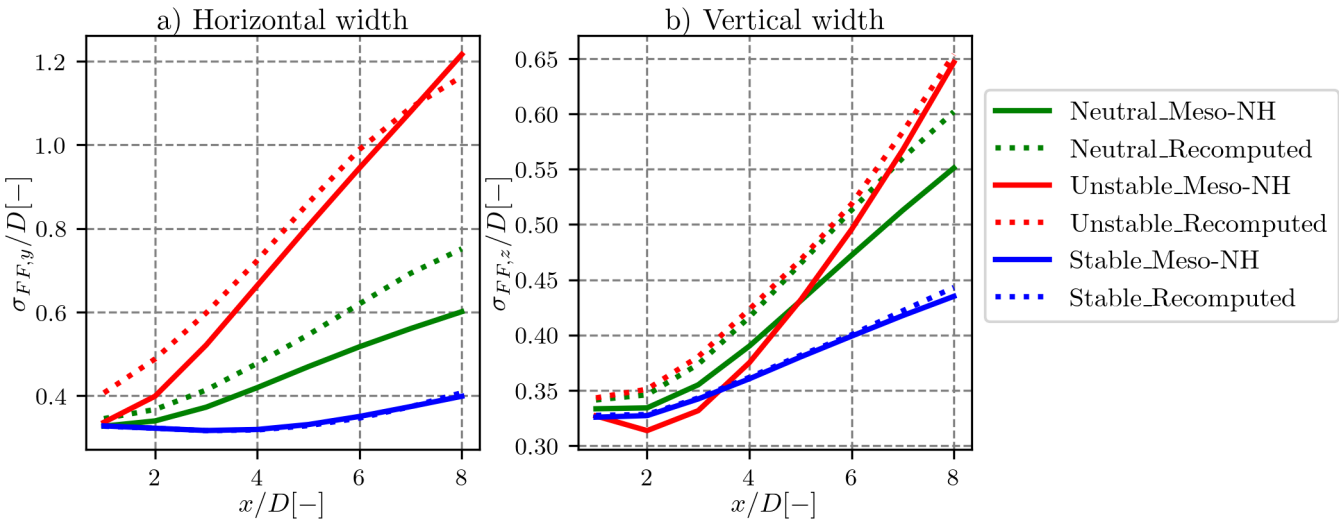

Figure 6.7: Wake widths in the FFOR: comparison between measured and predictions from MFOR and meandering.

found from its counterpart in the MFOR and the amount of meandering [129, 130] following:

$$\sigma_{y,FF}^2 = \sigma_{y,MF}^2 + \sigma_{fy}^2 \tag{6.6}$$

This relation, which will be further detailed in Ch. 8, has been verified on the three cases in the vertical and lateral directions and plotted in Fig. 6.7. The values of the wake widths in the FFOR computed from Eq. 6.6 (in dotted lines) fit correctly for the stable and unstable cases. Nevertheless, it leads to an overestimation of both the vertical and horizontal wake widths compared to what is computed directly in the FFOR (continuous lines). This was expected in the near wake because Eq. 6.6 has been developed with Gaussian shape hypotheses, but the discrepancies observed in the neutral case also arise in the far wake. It has been shown in Ch. 5 that the tracking method used herein (CstFlux with reference velocity) gives a relatively low wake width and a medium amount of meandering. Results of Fig. 6.7 could be improved only by using the upstream definition U_0 for the tracking, and the small differences observed in Fig. 5.12 would probably not be enough to fill the gap observed in Fig. 6.7.

6.2.2 Maximum deficit

The maximum velocity deficit is an indicator of the wake dissipation: the faster it decreases to 0, the faster the wake dissipates. The evolution of $\Delta\overline{U}_x^{\boldsymbol{M}}$ with x/D is plotted in Fig. 6.8a in the FFOR (dashed lines) and MFOR (dotted lines). The stronger the stability, the weaker the meandering (see Fig. 6.1) and thus the smaller the difference between FFOR and MFOR. Similarly to the wake width, the lower the stability, the faster the wake dissipation in the FFOR: at $x/D = 8$ the maximum velocity deficit in the unstable case is down to 4 % of the inflow turbulence, indicating that the wake is almost dissipated.

However, in the MFOR, the maximum velocity deficit in this case is still around 20 % of the inflow velocity, which cannot be considered negligible. The analysis in the MFOR contradicts the conclusion

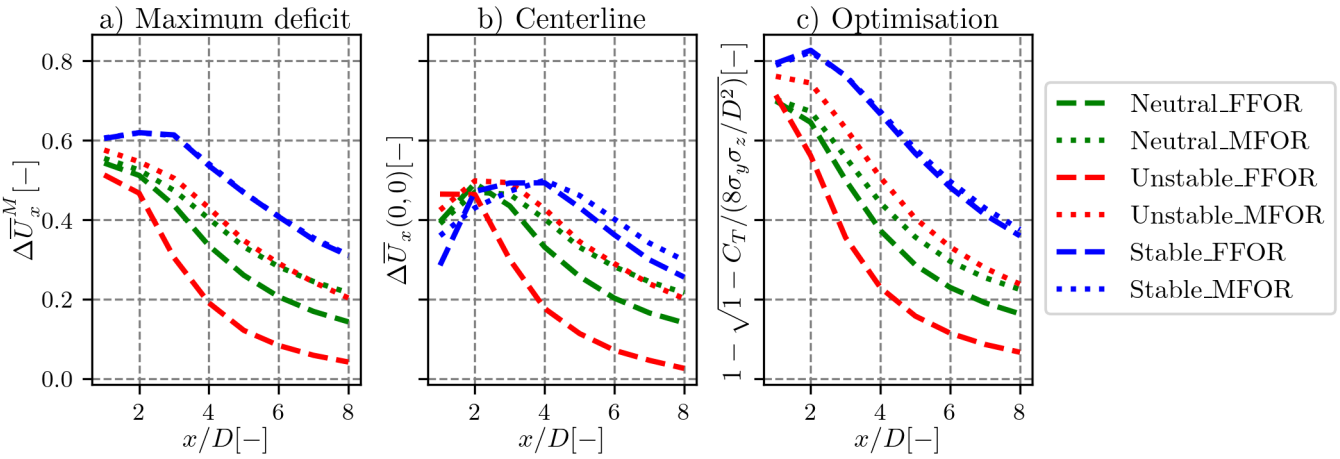

Figure 6.8: Maximum values of velocity deficit as a function of the downstream distance in both frames of reference, computed with different techniques.

made in the preceding paragraph: the wake is not dissipated in the unstable case at $x/D = 8$, but due to the large meandering motion, it is almost invisible when the time-averaged is done in the FFOR. Similarly to the wake widths, the maximum deficit in the MFOR is similar between the neutral and unstable cases.

The maximum deficit can be approximated by the deficit at the wake centreline, i.e. at $(y, z) = (0, 0)$. The evolution of $\Delta\overline{U}_x(0, 0)$ is plotted in Fig. 6.8b, and it shows that for the neutral and unstable cases, it captures rather well the maximum velocity deficit past a certain distance downstream. At $x/D < 3$, the maximum velocity deficit is located near the middle of the blades, due to the stronger lift and drag of the blade's airfoil. Yet, the underestimation due to this approximation is low, which can be attributed to the nacelle model.

Finally, the maximum deficit can be computed according to its value if one would use the XA14 (see Eq. 2.28) model with the values of σ_y and σ_z found in Fig. 6.6. Discrepancies were expected in the near wake due to the non-Gaussian shape in this region, but Fig. 6.8c shows that even in the far wake this latter method systematically overestimates the maximum wake deficit. It indicates that the wake widths found by optimisation are lower than what they should be, according to the maximum velocity deficit and the XA14 model.

6.2.3 Self-similarity

The self-similarity of the velocity deficit is also verified since many wake models are based on this assumption. As for the wake meandering distributions, the normalised Gaussian function is plotted in black. For the neutral case (Fig. 6.9), the self-similarity is reached in both directions from $x/D = 3$ in the FFOR and $x/D = 4$ in the MFOR. This difference is not surprising, since the meandering motions, which have been proven to also be distributed along with self-similar a Gaussian PDF, 'help' the FFOR function to reach self-similarity faster.

For the unstable case (Fig. 6.10), the Gaussian shape is reached even faster, around $x/D = 2$ in the horizontal direction for the FFOR. This is attributed to stronger meandering, however, in this case, the self-similarity is degraded starting from $x/D = 5$, in particular in the vertical direction.

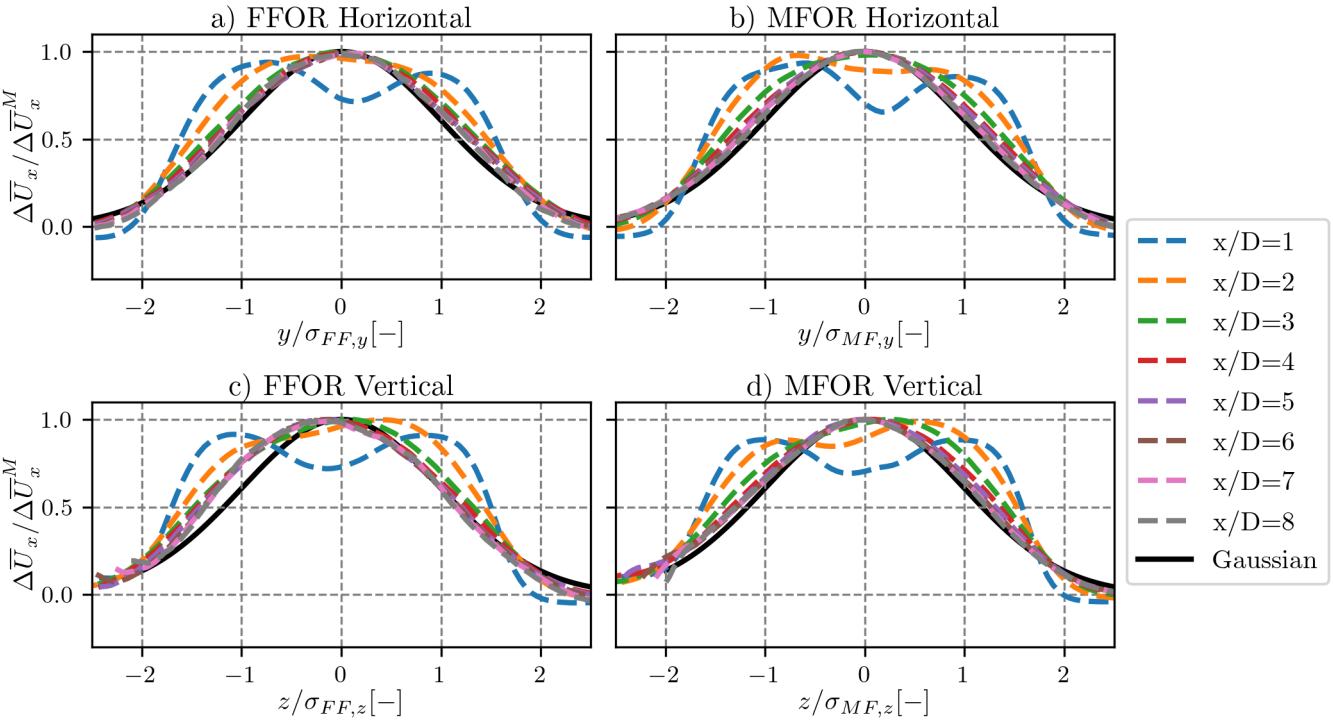

Figure 6.9: Self-similarity of the velocity deficit profiles for the neutral case.

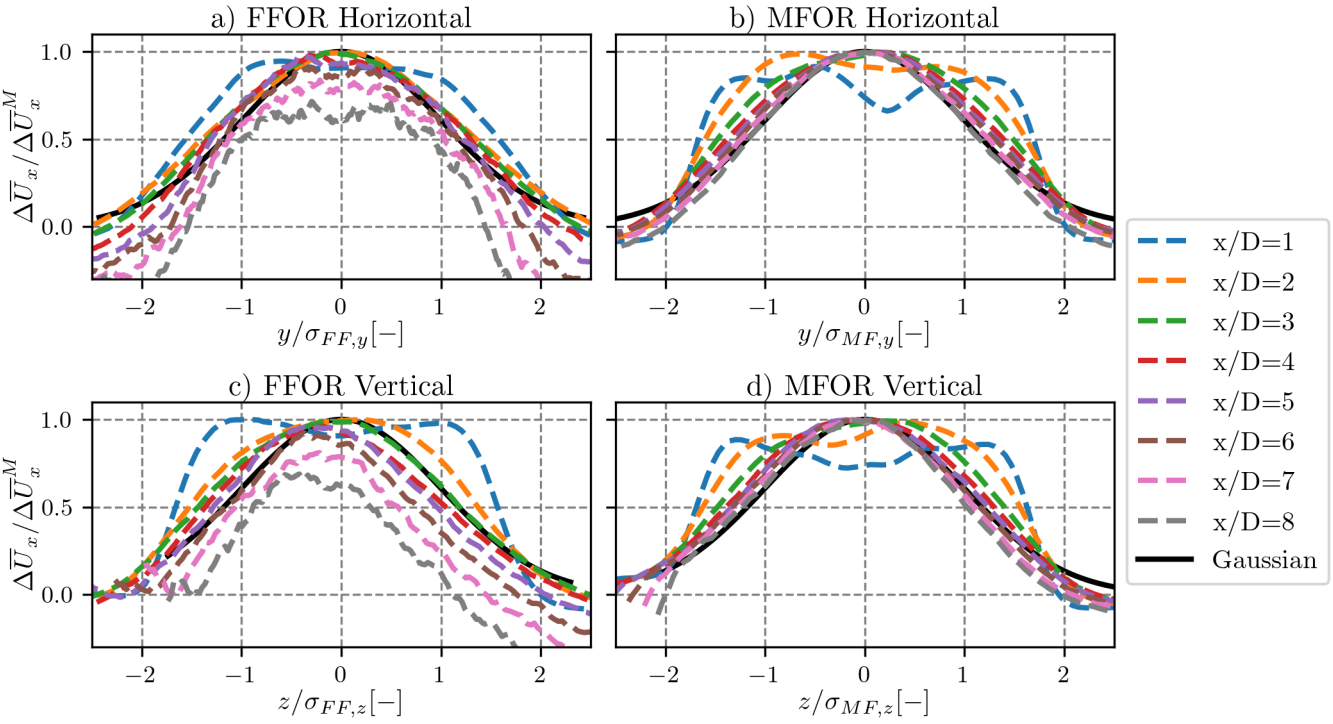

Figure 6.10: Self-similarity of the velocity deficit profiles for the unstable case.

Contrarily to the neutral case, the meandering process here has been shown to be not Gaussian (see Fig. 6.3), and thus it degrades the self-similarity in the FFOR. In the MFOR however, the velocity deficit profiles are similar to those of the neutral case. The velocity deficit in the MFOR is thus self-similar for both the downstream distance and the atmospheric stability (curves would superimpose if Figs. 6.9b and 6.10b or Figs. 6.9d and 6.10d were plotted on the same graph).

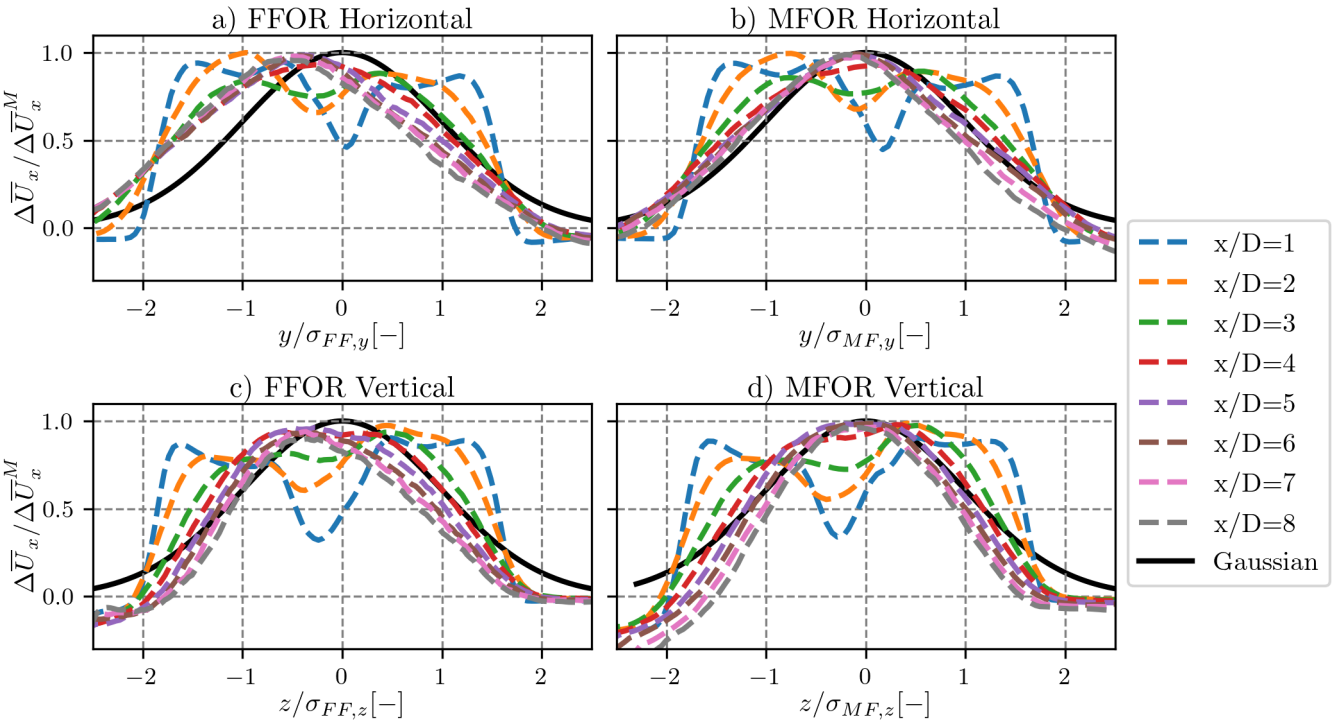

Figure 6.11: Self-similarity of the velocity deficit profiles for the stable case.

The stable case (Fig. 6.11) hardly reaches self-similarity at $x/D = 5$ in the MFOR, and even there, the fit with the Gaussian function is not as good as in the other cases. In the FFOR, self-similarity is reached, but not for a Gaussian shape. This is attributed to the skewness of the wake induced by veer. Due to this deformation, profiles plotted at constant y or z are no longer in the main direction of the wake and it is not surprising to see it failing to reach a Gaussian shape, even though results in the MFOR are improved compared to the FFOR.

6.3 Wake turbulence

The added turbulence is plotted for all cases, positions downstream and frames of reference in Figs. B.2, B.3 and B.4. The first plot is the added turbulence with a global normalisation, the second with a local normalisation and the third with a global normalisation, and with the unperturbed turbulence taken in the reference simulation. As for the velocity deficit, these maps cannot be analysed directly so we propose other tools to study the evolution of turbulence in the wake.

6.3.1 Added TI

The turbulence in the wake is here compared under its non-dimensional form, i.e. turbulence intensity, to compare the different cases. It is first computed as its global form ΔI_x, i.e. normalised by the velocity upstream of the turbine at hub height (see Eq. 2.9). The evolution of its maximum value with x/D in the FFOR and MFOR is plotted in Fig. 6.12a for the three cases of stability, with the same conventions as above. It is confirmed from this figure that in the MFOR, the flow fields of the unstable and neutral cases are very similar one to another but differ in the FFOR, in particular for the unstable case. In the MFOR like in the FFOR, the maximum TI decreases with x, starting from $x/D = 1$. In the stable case, however, this quantity is almost constant in the near wake and starts decreasing when $x/D = 5$ is reached, at a lower rate than in the neutral and unstable cases. Thus, even though it takes lower values at $x/D = 1$, the added TI in the stable case becomes higher than in the neutral and unstable cases, from $3D$ in the MFOR and $5D$ in the FFOR.

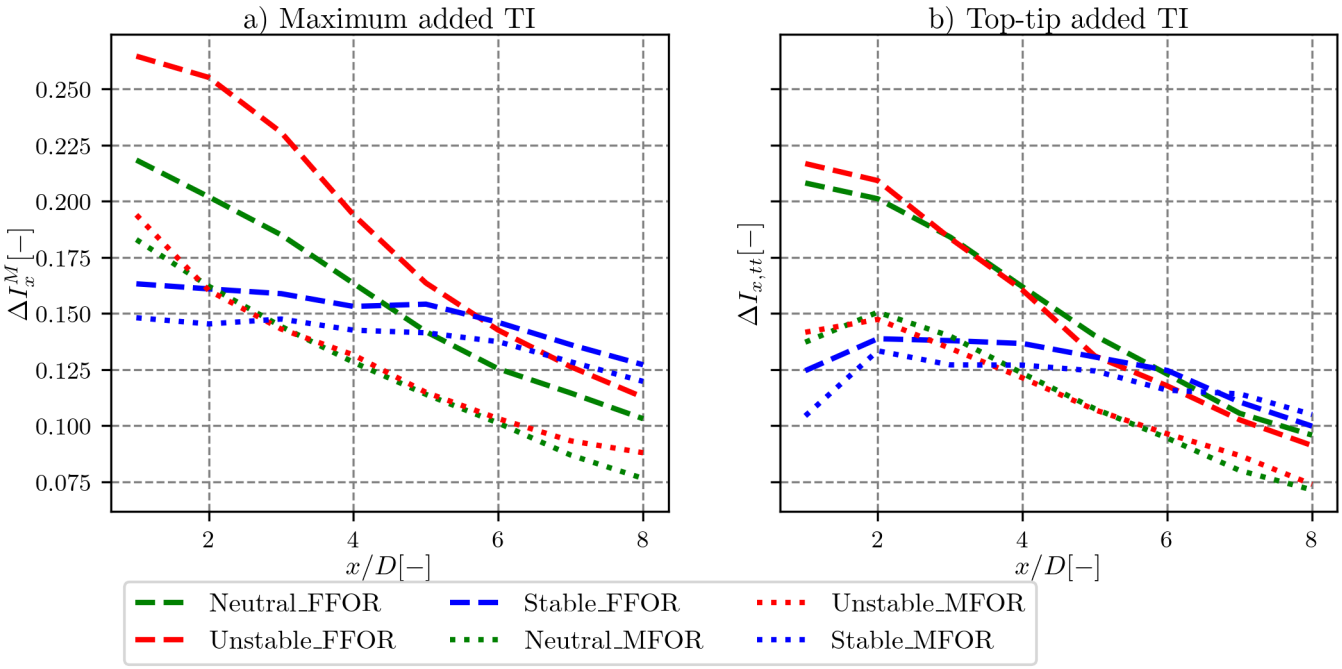

Figure 6.12: Global added turbulence intensity in the wake, computed with different conventions.

The maximum added turbulence may be approximated by its value at the top tip of the blade i.e. for $z = D/2$. This quantity is plotted in Fig. 6.12b as a function of x/D. For the neutral case in both frames, the top tip value is a good approximation of the maximum, except at $x/D = 1$. As shown in Fig. B.2, the maximum TI in the FFOR for the unstable case is not located at the top tip but rather around the hub-height blade tips i.e. $(y, z) \approx (\pm D/2, 0)$ and then moves toward the wake centre as x increases. This is due to meandering-induced turbulence and will be further discussed in Ch. 7. Consequently, the top-tip turbulence underestimates the maximum value. In the MFOR however, results are much better because the wake turbulence resembles that of the neutral case, with a slightly more axisymmetric shape. Similarly, the maximum added TI in the stable case is displaced towards the negative y due to veer and is thus not well captured by the value at the top tip.

With comparable thrust coefficients and inflow turbulence intensities (but without thermal effects), similar amplitudes and shapes of the added turbulence at the top tip than those in the MFOR were found in [111] (see Fig. 17, case 8 for a case equivalent to our neutral and unstable cases and case 6 for a case equivalent to our stable case).

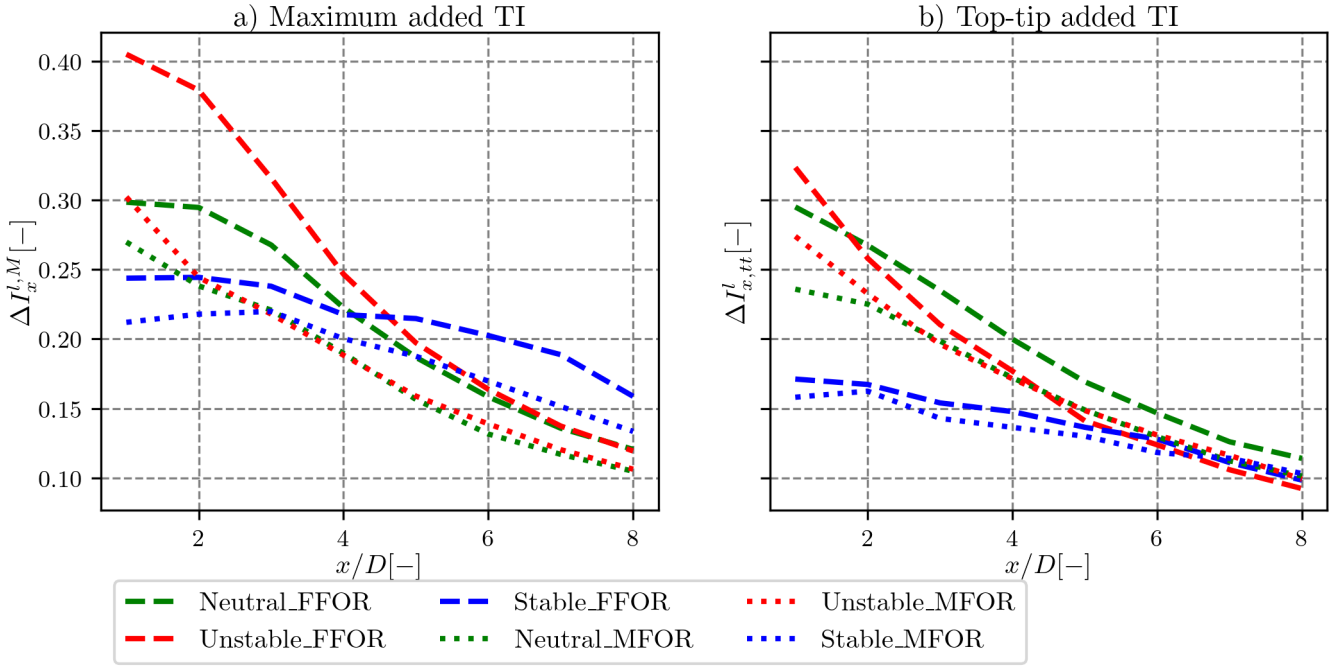

Figure 6.13: Same as Fig. 6.12 with the local turbulence intensity.

Alternatively, the added turbulence can be computed locally, i.e. the turbulence in the wake is normalised by the wake velocity and the unperturbed turbulence by the unperturbed velocity. Figure 6.13 reproduces Fig. 6.12 with this local added turbulence ΔI^l. First, one must note that due to wake velocity being lower than the upstream velocity, the local added TI is significantly higher than its global counterpart, up to about 50 % in the near wake. With ΔI^l as with ΔI the maximum and top-tip added TI in the MFOR is similar between the neutral and unstable cases, but here it is also in the FFOR from $x/D = 6$. As for the global added TI, the maximum value in the neutral case is well predicted by the top-tip value but underestimated in the stable and unstable cases. This is particularly true here for the unstable case in the FFOR that becomes lower than the MFOR value for $x/D > 4$, and thus does not reflect the actual local added TI field which is overall stronger in the FFOR (see Fig. B.3).

6.3.2 Self-similarity

As for the velocity deficit, assuming self-similarity for the turbulence can be useful to model it, e.g. in [92]. This assumption is herein verified for the three cases of stability and both frames of reference. The total turbulence in the wake is directly studied, thus avoiding the effects of normalisation. Turbulence is not expected to take a Gaussian shape so no reference function is plotted.

For the neutral case (Fig. 6.14), the turbulence approximately reaches a self-similar distribution in the FFOR at around $x/D = 6$, which is three diameters further than the velocity deficit. The maximum

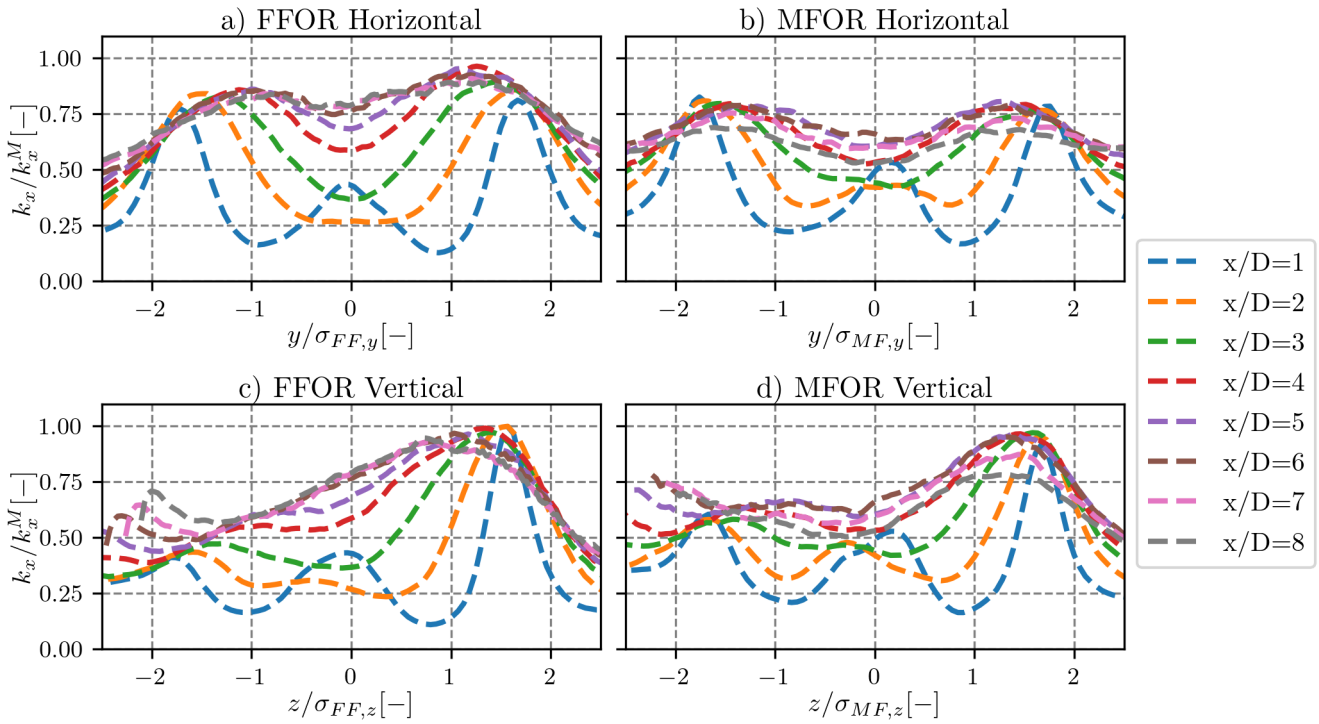

Figure 6.14: Self-similarity of the streamwise turbulence profiles for the neutral case.

turbulence intensity is displaced from $z/\sigma_z = 1.5$ in the vicinity of the rotor to around $z/\sigma_z = 1$ when self-similarity is reached. The same displacement of the maximum wake-added turbulence is also measured in the MFOR, but of lower magnitude, probably because σ_z in the MFOR is lower than in the FFOR. This indicates that the location of the maximum turbulence is not depending on the wake width. The self-similarity in the MFOR is less distinct for turbulence than for the other variables: this is attributed to atmospheric shear that leads to a non-symmetric distribution. Self-similarity in the FFOR might thus be the consequence of the self-similar meandering process rather than self-similarity of turbulence itself.

The assumption that it is shear that degrades self-similarity is confirmed by the unstable case (Fig. 6.15). This case has much less atmospheric shear and leads to much better self-similar turbulence profiles in the MFOR. In the FFOR, self-similarity is reached beyond $x/D = 4$. This could be attributed to higher meandering, which tends to spread the wake turbulence, but this would be in contradiction with the conclusions drawn for the FFOR velocity in the unstable case.

In the stable case (Fig. 6.16), the shear is even stronger than in the neutral case. Combined with the skewed wake shape, one cannot expect lateral and vertical profiles of turbulence to reach self-similarity. It is indeed not the case, neither the FFOR nor the MFOR, but one can note that despite very different values of σ_z, the maximum turbulence is reached at similar z/σ_z positions to the neutral case, thus suggesting here a universal behaviour.

For the sake of completeness, the global and local added turbulence profiles can be found in appendices (Figs. B.5 to B.10). Overall, these quantities reach a better self-similarity than k, in particular, the locally averaged added TI, which takes a top-hat shape in both FFOR and MFOR, hence avoiding maximum values near the top tip that taint the results. This latter quantity is however harder

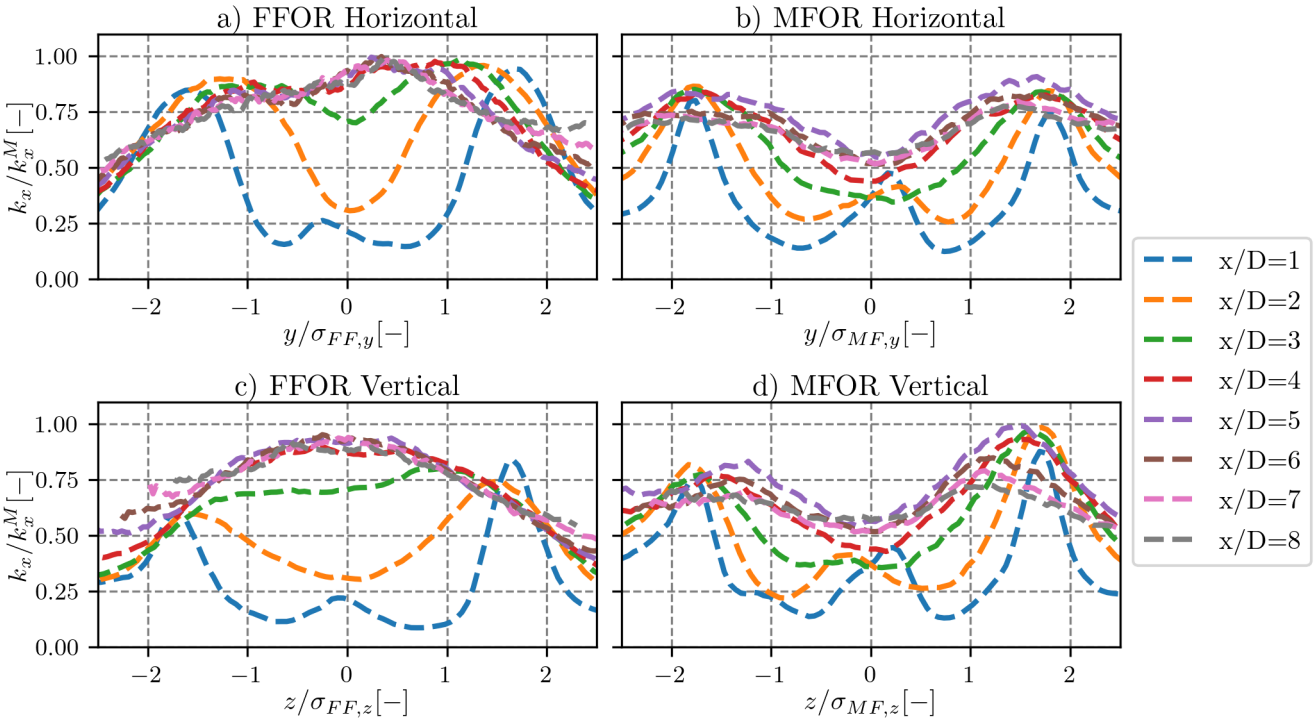

Figure 6.15: Self-similarity of the streamwise turbulence profiles for the unstable case.

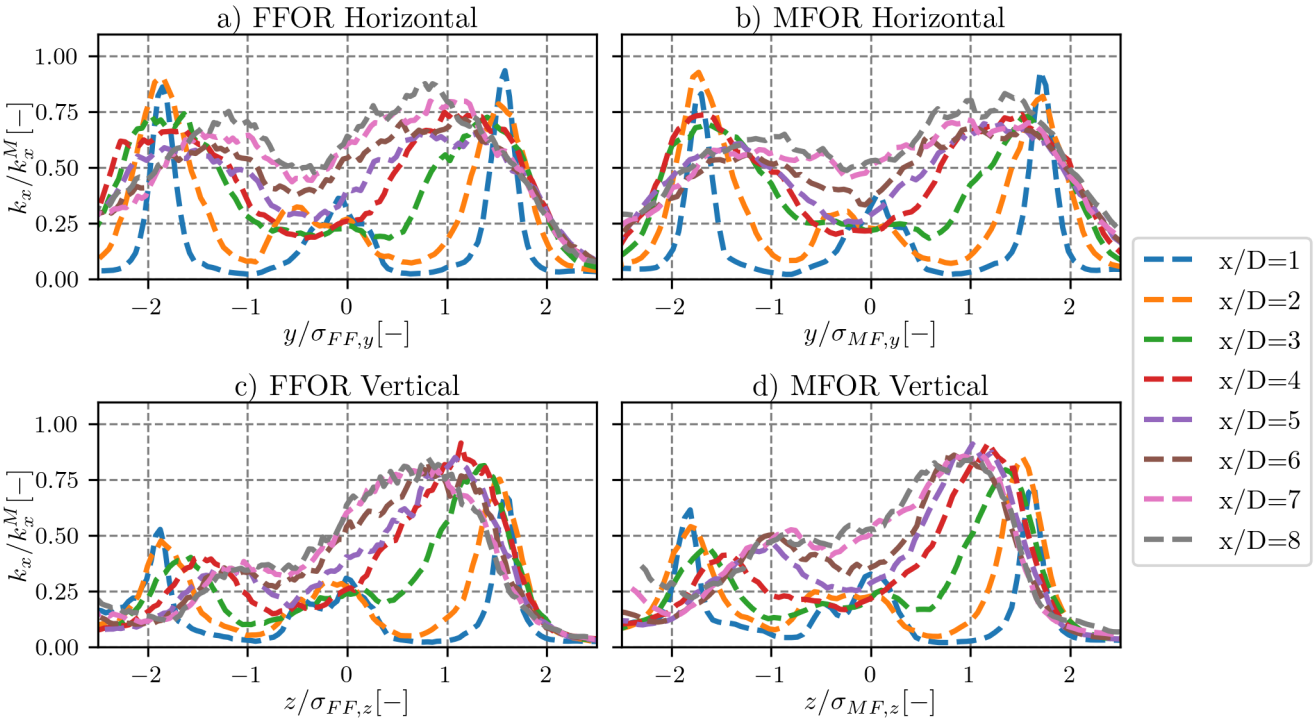

Figure 6.16: Self-similarity of the streamwise turbulence profiles for the stable case.

to interpret because one must distinguish the effect of turbulence from the effect of velocity, which is why it is not very much developed here. One can also note that these figures contain negative values, indicating smaller turbulence in the wake than upstream, in particular near the ground.

6.3.3 Spectral analysis

Even though it will not be used for analytical modelling, a spectral analysis of the wake turbulence can help understanding the physical phenomena at stake. In Figs 6.17 (FFOR) and 6.18 (MFOR) are compared the PSD of the streamwise velocity upstream of the turbine (in black) with the PSDs at three positions in the wake: 2, 5 and 8 diameters downstream. This is done for each case of stability and four vertical positions: bottom tip ($z = -D/2$), hub height ($z = 0$), mid-blade ($z = D/4$) and top tip ($z = D/2$). A welch algorithm is used with 2 segments for the low frequency and with 20 sub-segments for the high frequencies, leading to rather smooth PSDs over the whole frequency range but to some discontinuities at the limit between the two welch methods. The frequency axis is normalised as the Strouhal number i.e. $St = fD/U_h$.

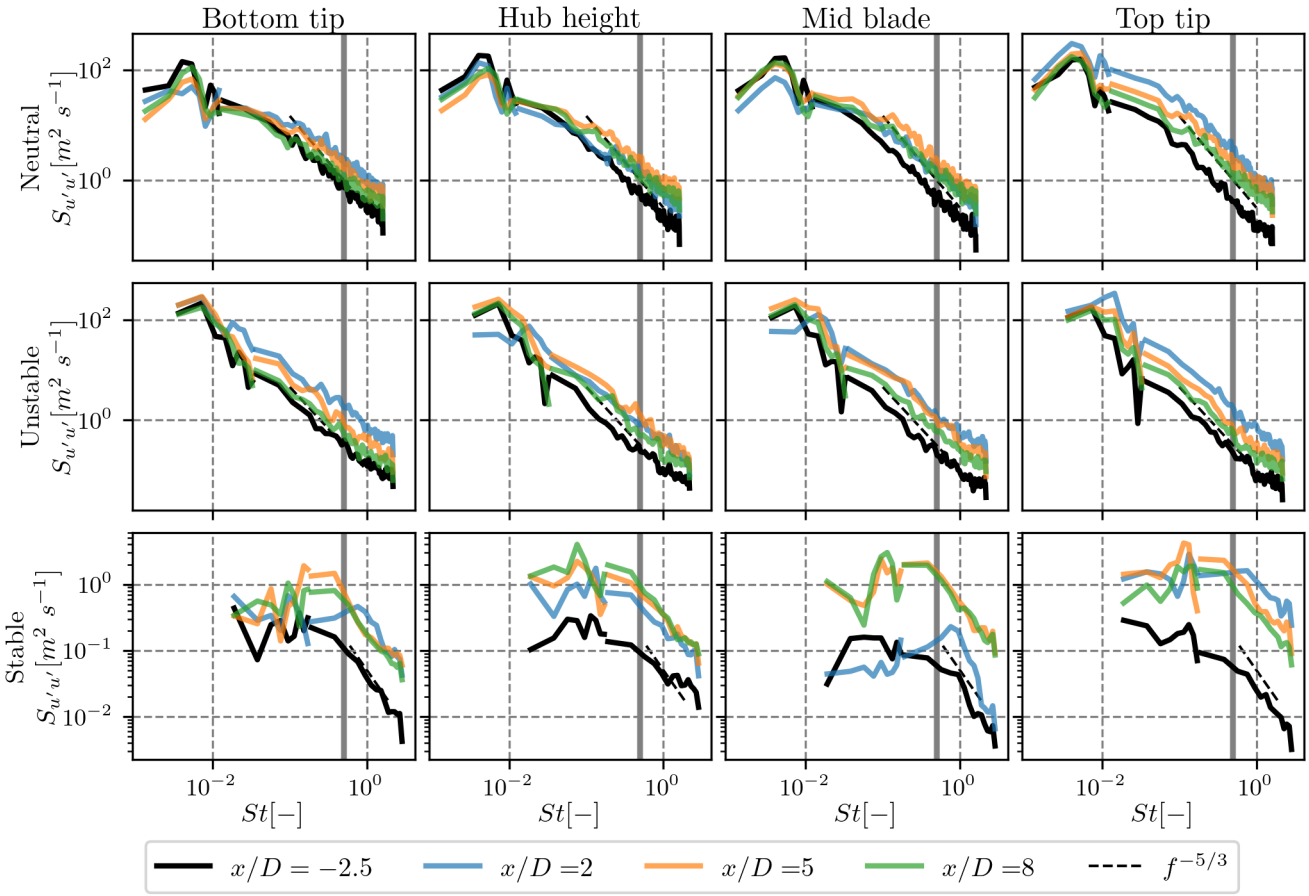

Figure 6.17: Evolution of the velocity spectra in the wake at different vertical positions, FFOR.

At the lowest frequencies, the PSDs in the FFOR (Fig. 6.17) are very similar between the upstream and downstream velocities. At high frequencies, the turbulence increases with height and decreases with downstream distance. Both upstream and downstream turbulence at high frequencies follow the

theoretical Richardson-Kolmogorov cascade plotted in a black dotted line, with different amplitudes. This indicates that the added turbulence in the wake is mostly small-scale, but this should be put into perspective: depending on the vertical position, the downstream turbulence overcomes the upstream one between $St \approx 0.1$ at the bottom tip to $St \approx 0.01$ at the top tip, corresponding respectively to wavelengths of 10 and 100 diameters. These 'small scales' are thus rather large compared to the wake dimensions.

In the FFOR, we expected to see the signature of wake meandering around $St = 0.5$ (i.e. wavelengths of $2D$). This Strouhal number, plotted as a grey vertical line, does not mark any change in the neutral and unstable case, but oddly marks a break of slope in the stable case, where the meandering is the weakest. Note that this could be because in the stable case, this limit is close to the frontier between the two welch algorithms, and could thus be only a numerical artefact.

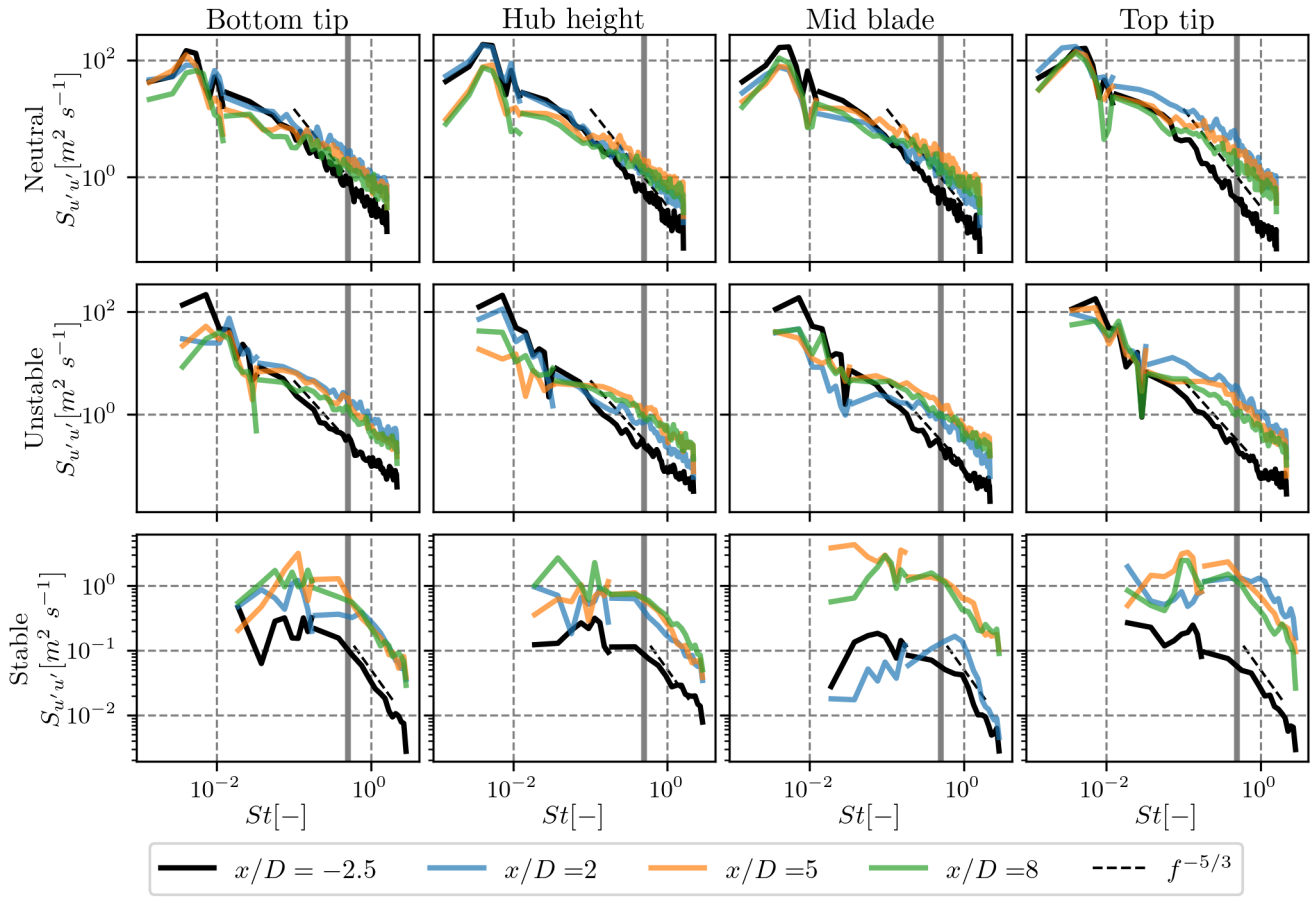

Figure 6.18: Evolution of the velocity spectra in the wake at different vertical positions, MFOR.

The same spectra are plotted in Fig. 6.18 in the MFOR. In this frame of reference, the low-frequency content of the neutral and unstable spectra is reduced compared to the FFOR, and is thus below the upstream value. As in the literature, [24, 91, 93], our results in the MFOR suggest that the wake acts as an active filter that damps the variations at low frequencies and increases those at high frequencies. These results could also be because the MFOR follows the largest eddies and thus does not take into account the variations induced by them. Moreover, the turbulence is displaced from the bottom of the wake to the top tip.

A clearer break of slope in the PSD around $St = 0.5$ can be observed in the MFOR compared to the FFOR for the three cases, in particular at the top tip. Above this frequency, the PSDs resemble the Richardson-Kolmogorov theoretical cascade, whereas, below that frequency, they are almost constant with f. This behaviour can be found in the three cases of stability. For all vertical and downstream positions, and across most of the frequency range, the magnitudes of the PSDs are similar between the neutral and unstable cases. They are also similar in amplitude to the stable cases at the highest frequencies.

An interesting case is the PSD at the mid-blade and $x/D = 2$ in the stable case (last line, third column, blue plot) in both the FFOR and MFOR. At this position downstream, the wake-added turbulence is mainly located at the tip of the blades and in the stable case it did not have the time yet to be diffused to the mid-blade position (see Fig. B.2). Turbulence at this location is thus shielded from large eddies by the turbine's blades and at the same time, it is not yet affected by the turbulence induced by the wake shear layer. As a consequence, the low frequencies are damped up to $St = 1$, which corresponds to wavelengths of the dimension of the rotor diameter.

6.3.4 Upstream length scale

Besides its different TI, the inflow of the stable case also differs from its spectral characteristics. The integral length scale $\Lambda_{u,x}$ of the incoming flowfield has been investigated for the three cases of stability and compared to the cutoff length scale ($2D = 54$ m) used in the DWM to differentiate the eddies affecting the MFOR and the eddies affecting the meandering. To do so, we first compute the auto-correlation of $\rho_{u'u'}$ (defined in Eq. 1.17) at hub height and for each lateral mesh point. It allows computing a laterally averaged auto-correlation of the velocity fluctuations, which is much smoother. This function is plotted in Fig. 6.19 up to the first zero crossing for the three cases of stability. The integral of $\rho_{u'u'}$ up to the first zero crossing gives the integral time scale $\mathcal{T}_u$, which can be related to the integral length scale thanks to the frozen turbulence hypothesis: $\Lambda_{u,x} = \mathcal{T}_u / U_h$.

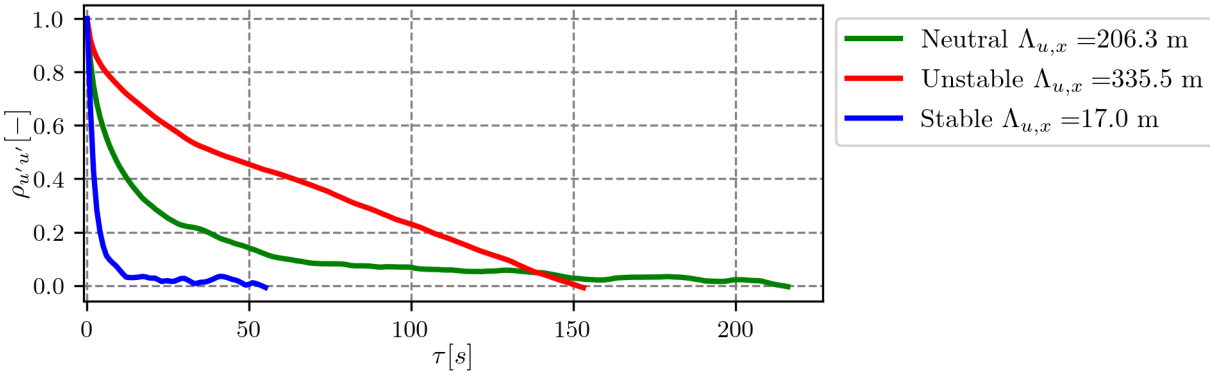

Figure 6.19: Auto-correlations of the velocity upstream the turbine.

This process led to $\Lambda_{u,x} = \{206.3, 335.5, 17\}$ m i.e. $\Lambda_{u,x}/D = \{7.6, 12.4, 0.6\}$ for the neutral, unstable and stable cases respectively. In this section, we assume that the largest length scale that can be found in MFOR is $2D$, even though it could not be verified in Fig. 6.18. Since $\Lambda_{u,x} < 2D$ in the stable case, there are almost no eddies energetic enough to move the whole wake in the stable case, explaining the very low values of σ_f in Fig. 6.1. Conversely, $\Lambda_{u,x}$ is larger in the unstable case than

in the neutral one, resulting in more meandering despite similar streamwise inflow TI, in accordance with the work of [83].

Furthermore, the MFOR turbulence field in the stable case misses the eddies of size ranging between $\Lambda_{u,x} = 17$ m and $2D$, because such length scales do not exist in the inflow. This can be a secondary explanation for the differences in the MFOR with the neutral and unstable cases (see Figs. 6.12 and 6.13) where all the length scales from the Kolmogorov scale to $2D$ are available in the inflow and will be found in the MFOR. According to this interpretation and if similar turbine operating conditions are met, a less-stable ABL would behave similarly to the neutral and unstable cases in the MFOR if $\Lambda_{u,x} > 2D$ is reached in its inflow, and a more-unstable ABL would simply result in more meandering but similar flow in the MFOR.

It could be argued that since meandering is caused by large-scale variations of v and w, it is the lateral and vertical length scales that are important to determine if the wake will meander or not. Applying the same method as above to the lateral and vertical velocities led to $\Lambda_{v,x} = \{57.8, 399.2, 38.3\}$ and $\Lambda_{w,x} = \{28.5, 60, 4.6\}$. The value of $\Lambda_{v,x}$ in the stable case is larger than expected, but it is attributed to the linear trend of the wind direction in our simulation. Removing this trend with a methodology similar to the Welch algorithm gets this value down to $\Lambda_{v,x} = 9$ m without affecting significantly the other values. Overall, the conclusion is similar than with $\Lambda_{u,x}$: the stable integral length scales are too small to move the wake as a whole and thus induce very little meandering. Moreover, we expect the turbulent length scales in the MFOR to be limited by both the rotor diameter and the available length scales upstream of the rotor. The first is the limiting factor for the neutral and unstable case and the second for the stable case.

This last interpretation could be validated by computing the largest turbulent eddy inside the wake. However, the auto-correlation of a single point is a very noisy function. Upstream the turbine, the flow is supposed to be spatially homogeneous and so the auto-correlation can be averaged laterally but this is not true inside the wake. Integral length scales in the wake could not be consistently computed and have thus not been studied herein, but would be interesting to compare them to the upstream values.

6.4 Conclusions

An analysis of the wind turbine wake in both frames of reference has been performed for three cases of atmospheric stability: unstable, neutral and stable. The rotor-averaged lateral and vertical turbulence intensities are shown to be good predictors of the amount of meandering. The hypothesis of axisymmetric wake in the MFOR is validated for the neutral and unstable cases but not for the stable case where the strong veer of the ABL leads to a skewed wake. It is shown that for two cases where C_T and $I_{x,\infty}$ are similar (neutral and unstable), and despite very different results in the FFOR, a robust wake tracking leads to case-independent turbulence and velocity fields in the MFOR. This has been confirmed with a spectral analysis where the neutral and unstable cases showed similar spectral behaviour in the MFOR. Self-similarities have also been assessed, showing good results for the meandering distribution and velocity deficit (in particular in the MFOR) but results are less conclusive for turbulence.

Even though three simulations are not enough to draw final conclusions, the present study confirms that the flow in the MFOR is mostly independent of atmospheric conditions, under the condition that

the integral length scale upstream of the rotor is sufficiently large. Since the threshold is expected to vary with the turbine's diameter, only strongly stable ABL fulfils this condition for small rotors like the Vestas V27, but for very large rotors it could happen in more common atmospheric conditions. To be comprehensive, this study should be completed with other simulations to study the sensibility of the results to the atmospheric and operating conditions.

Part III

Part C - Analytical modelling

Chapter 7

Breakdowns of the mean velocity and turbulence

The MFOR allows separating the effects of wake expansion from wake meandering. It has been concluded in the Ch. 6 that under certain conditions, the turbulence and the velocity in the wake are independent of atmospheric stability. It is thus an interesting tool, for both unsteady and steady-state wake models: one may account for the stability effects through the wake meandering and for operating and atmospheric conditions within a wake model in the MFOR.

Nevertheless, a wake model must in the end predict the wake velocity deficit and added turbulence in the FFOR. The present chapter aims at finding an expression of these quantities as a function of their counterparts in the MFOR. It will first be shown that it can be done by breaking down the expression into several terms, which are in a second part quantified based on the three LESs cases defined in the preceding chapters. Some terms are negligible but the nature of the predominant term depends on stability. Most of the work of this chapter will be published in the Wind Energy Science journal [161].

7.1 Analytical development

It is here recalled from Sect. 2.5.2 that the DWM can be used as a steady-state model where the mean velocity is computed as [63, 127]:

$$\overline{U_{FF,dwm}}(y,z) = \int\int U_{MF,dwm}(y-y_c, z-z_c) f_c(y_c,z_c) dy_c dz_c = U_{MF,dwm}(y,z) ** f_c(y,z) \quad (7.1)$$

where f_c is the two-dimensional wake centre's PDF and $**$ denotes a convolution product in two dimensions. Similarly, the added turbulence is assumed to be the sum of a 'rotor-added' k_a and a 'meandering' k_m terms, computed as:

$$k_{a,dwm}(y,z) = \int\int k_{MF,dwm}(y-y_c, z-z_c) f_c(y_c,z_c) dy_c dz_c = k_{MF,dwm}(y,z) ** f_c(y,z) \quad (7.2)$$

$$k_{m,dwm}(y,z) = \int\int \left(U_{MF,dwm}(y-y_c, z-z_c) - \overline{U_{FF,dwm}}(y,z)\right)^2 f_c(y_c,z_c) dy_c dz_c \quad (7.3)$$

$$= U^2_{MF,dwm}(y,z) ** f_c(y,z) - \overline{U_{FF,dwm}}^2(y,z) \quad (7.4)$$

where $k_{MF,dwm}$ is the modelled turbulence in the MFOR. Equation 7.4 is obtained by developing Eq. 7.3 and simplifying with Eq. 7.1. These formulas come from the fact that in the DWM, the wake is steady in the MFOR, which is not observed in real cases, and neither in our LES data. The present work aims at generalising them for an unsteady velocity field in the MFOR. To do so, we use the definition of the translation from one frame of reference to the other (see Eq. 2.15), which is abbreviated with a $\widehat{.}$ to clarify the mathematical formulations:

$$U_{FF}(y,z,t) = U_{MF}(y-y_c(t), z-z_c(t), t) = \widehat{U_{MF}(y,z,t)} \quad (7.5)$$

This operation can be interpreted as an unsteady translation of any field ϕ by meandering. It is illustrated in one dimension in Fig. 7.1 for an arbitrary unsteady field $\phi(y,t)$ defined at three time steps $\{t_0, t_1, t_2\}$ and where $y_c/D = \{1; 0; -1\}$. For instance, ϕ could be the velocity in the MFOR and $\widehat{\phi}$ the velocity in the FFOR. Before applying the operator, all the values of ϕ are centred at $y = 0$ (Fig. 7.1a), but due to the imposed meandering motion, the values of $\widehat{\phi}$ are centred at different positions (Fig. 7.1b). Note that even if ϕ is a steady field (i.e. the three curves in Fig. 7.1a are superimposed), $\widehat{\phi}$ would have been unsteady (curves in Fig. 7.1b would not be superimposed).

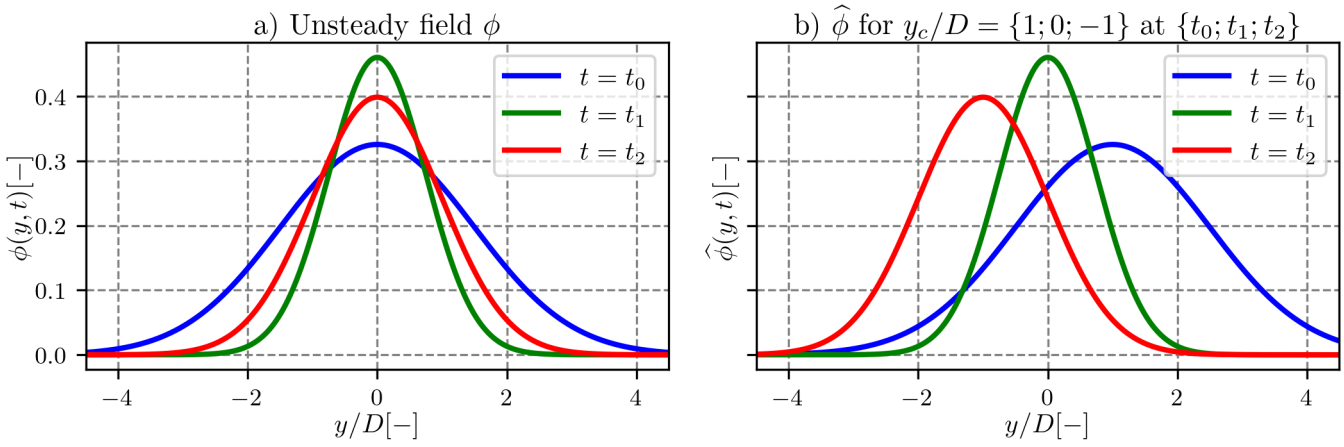

Figure 7.1: Illustration of the meandering operator for an arbitrary unsteady field ϕ.

For any variables ϕ and ψ, the following properties hold:

$$\widehat{\phi} + \widehat{\psi} = \widehat{\phi + \psi}. \tag{7.6}$$

$$\widehat{\phi} \cdot \widehat{\psi} = \widehat{\phi \cdot \psi}. \tag{7.7}$$

$$\widehat{\overline{\phi}} \neq \overline{\widehat{\phi}}. \tag{7.8}$$

$$\overline{\widehat{\phi}} = \overline{\phi} * * f_c. \tag{7.9}$$

Properties 7.6 and 7.7 are obtained from the linearity of the translation operator. Property 7.8 is trivial since $\widehat{\overline{\phi}}$ is time-dependent and $\overline{\widehat{\phi}}$ is not. Property 7.9 is an approximation, whose error is a $o(\Delta X + \Delta Y)$. It is demonstrated in Appendix C. Using the $\widehat{.}$ notation and applying the Reynolds decomposition to U_{MF} allows re-writing Eq. 7.5 as:

$$U_{FF} = \widehat{U_{MF}} = \widehat{\overline{U_{MF}}} + \widehat{U'_{MF}} \tag{7.10}$$

The mean velocity in the FFOR can be deduced by applying the averaging operator to this equation:

$$\overline{U_{FF}} = \underbrace{\overline{\widehat{\overline{U_{MF}}}}}_{(I)} + \underbrace{\overline{\widehat{U'_{MF}}}}_{(II)} \tag{7.11}$$

From Eq. 7.9, it appears that the term (I) is the convolution of $\overline{U_{MF}}$ with f_c, and can be viewed as a pure mean velocity term: it is null only if the mean velocity is null. Conversely, the term (II) is here viewed as a cross-term because it can be equal to 0 either if there is no meandering ($\widehat{\phi} = \phi$) or if there is no turbulence in the MFOR ($U'_{MF} = 0$). In the DWM model, $U_{MF,dwm}$ is steady so $U_{MF,dwm} = \overline{U_{MF,dwm}}$ and $U'_{MF,dwm} = 0$, thus Eqs. 7.1 and 7.11 are equivalent. The assumption of steady flow in the MFOR for analytical or DWM models is equivalent to the assumption that term (II) of Eq. 7.11 is negligible. Since $U'_{MF} = 0$ is not true in real cases nor in LESs, this hypothesis must be verified, which is one of the objectives of the present work.

For the turbulence equation, one can write from Eqs. 7.10 and 7.11:

$$\overline{U_{FF}^2} = \overline{\widehat{\overline{U_{MF}}}^2} + 2\overline{\widehat{\overline{U_{MF}}}\widehat{U'_{MF}}} + \overline{\widehat{U'_{MF}}^2} \tag{7.12}$$

$$\overline{U_{FF}}^2 = \overline{\widehat{\overline{U_{MF}}}}^2 + 2\overline{\widehat{\overline{U_{MF}}}}\,\overline{\widehat{U'_{MF}}} + \overline{\widehat{U'_{MF}}}^2 \tag{7.13}$$

The total turbulence in the FFOR can then be written as a function of the preceding quantities:

$$
\begin{aligned}
k_{FF} &= \overline{U_{FF}'^2} = \overline{U_{FF}^2} - \overline{U_{FF}}^2 \\
&= \overline{\widehat{U_{MF}}^2} - \overline{\widehat{U_{MF}}}^2 + 2\left(\overline{\widehat{U_{MF}}\widehat{U'_{MF}}} - \overline{\widehat{U_{MF}}}\,\overline{\widehat{U'_{MF}}}\right) + \overline{\widehat{U'_{MF}}^2} - \overline{\widehat{U'_{MF}}}^2 \\
&= \underbrace{\overline{\widehat{U_{MF}}^2} - \overline{\widehat{U_{MF}}}^2}_{(III)} + \underbrace{2\mathrm{cov}\left(\widehat{U_{MF}}, \widehat{U'_{MF}}\right)}_{(V)} + \underbrace{\overline{\widehat{U_{MF}'^2}}}_{(IV)} + \underbrace{\overline{\left(\widehat{U_{MF}'^2}\right)'}}_{(VI)} \underbrace{-\overline{\widehat{U'_{MF}}}^2}_{(VII)} \\
&= \underbrace{k_m}_{(III)} + \underbrace{k_a}_{(IV)} + \underbrace{2\mathrm{cov}\left(\widehat{U_{MF}}, \widehat{U'_{MF}}\right)}_{(V)} + \underbrace{\overline{\left(\widehat{U_{MF}'^2}\right)'}}_{(VI)} \underbrace{-\overline{\widehat{U'_{MF}}}^2}_{(VII)}
\end{aligned}
\tag{7.14}
$$

where $\mathrm{cov}(\phi, \psi)$ denotes the covariance between two variables ϕ and ψ. Equation 7.14 is broken down into five terms:

- Term (III) is the turbulence purely induced by meandering: in the case of a meandering steady wake i.e. $U'_{MF} = 0$, Eq. 7.14 reduces to this term only. The mathematical expression of the term (III) is identical to Eq. 7.4: it will thus be abbreviated k_m.
- Term (IV) of Eq. 7.14 is the turbulence purely induced by the rotor: in absence of meandering i.e. $\widehat{\phi} = \phi$, the equation reduces to this term only. Its expression is equivalent to Eq. 7.2 and it will thus be abbreviated k_a.
- Term (V) is the covariance of $\widehat{U_{MF}}$ and $\widehat{U'_{MF}}$.
- Term (VI) is the remaining of $\overline{\widehat{U'_{MF}}^2}$ when subtracting the rotor-added turbulence in the FFOR $k_a = \overline{\widehat{U_{MF}'^2}}$. It can be viewed as the varying part of the MFOR turbulence.
- Term (VII) is the square of the term (II). It is a dissipation term since it is always negative or null.

Like the term (II), terms (V), (VI) and (VII) are cross-terms because they are equal to zero if either the turbulence in the MFOR or the meandering is null. Contrarily to these cross-terms, terms (I), (III) and (IV) will hereafter be denoted as 'pure-terms'.

In the DWM model (see Sect. 2.5.1), $U'_{MF,dwm} = 0$ so Eq. 7.14 would reduce to k_m only, but a rotor-added turbulence term $k_{MF,dwm}$ is inserted to take the small-scale turbulence into account. It is thus assumed in this model that the wake turbulence is the sum of meandering-induced turbulence (term (III)) and small-scale, rotor-added turbulence (term (IV)). Equation 7.14 shows that three cross-terms are neglected under this assumption, i.e. that in a real case, there are interactions between small-scale turbulence and the meandering that modify the total turbulence. In other words, in the DWM formulation, terms (III) and (IV) are retained and terms (V), (VI) and (VII) are neglected. One of the objectives of this chapter is to quantify the error induced by this assumption.

Note that Eqs. 7.11 and 7.14 are derived mathematically, with no physical assumptions. They are thus expected to be correct, regardless of the y_c, z_c time series. Consequently, discrepancies between

the left- and right-hand sides of these equations cannot be attributed to the tracking algorithms but rather to numerical limitations (described in Sect. 7.2.2). Actually, one could use these equations with any values of y_c and z_c (and not necessarily the position of the wake centre): the equality should remain true but the different terms would just not have any physical meaning.

7.2 Error induced by neglecting the cross-terms.

7.2.1 Methodology

The datasets presented in Sect. 5.3 are used herein. $\overline{U}_x$ and k_x in the FFOR are directly computed as the mean and variance of the unsteady streamwise velocity field. We stick to the same tracking method, i.e. CstFlux algorithm with reference upstream velocity and a moving average of $\delta T = 7$ s to compute y_c, z_c and apply Eq. 7.5 at each time step to get the unsteady velocity in the MFOR. The Reynolds decomposition and meandering operator $\widehat{.}$ are then applied to get the values of terms (I) and (II) of Eq. 7.11 and terms (III), (IV), (V), (VI) and (VII) of Eq. 7.14.

The objective of this section is to quantify the importance of each term and to estimate the error induced by neglecting the cross-terms in the velocity and turbulence breakdowns, as for instance in the DWM model or in the model developed in Ch . 8. The normalised root-mean-square error (RMSE) indicator is used to quantify different levels of approximation with the actual results in the FFOR:

$$\text{RMSE} = \sqrt{\frac{\sum_{i=1}^{N}(\phi - \phi_p)^2}{N}} / (\phi^M - \phi^m) \tag{7.15}$$

where ϕ is the reference value (directly extracted from Meso-NH), ϕ_p is the value predicted by a given approximation, N is the number of samples, ϕ^M and ϕ^m are respectively the maximum and minimum values of ϕ, i.e. $\phi^M - \phi^m$ is the range of ϕ over these samples. When the RMSE is computed on a $Y - Z$ plane, only the truncated plane $\{y, z\} = \{[-2D, +2D], [-1D, 1D]\}$ is used to avoid edge effects and then N denotes the number of mesh points in this plane.

7.2.2 Numerical limitations of the approach

To compute terms (I) to (VII) of Eqs. 7.11 and 7.14, it is needed to start from the unsteady field U_{MF} and apply the Reynolds decomposition and operator $\widehat{.}$ (Eq. 7.5). To avoid losing any data, one should in theory compute the MFOR on a grid spanning from $y^m_{FF} + y^m_c$ to $y^M_{FF} + y^M_c$ and similarly in the vertical direction. For strong meandering cases, it would result in a very large grid that would be computationally costly to manipulate, especially for the $\widehat{.}$ operator where the 2D data must be interpolated at each time step. It has thus been decided to restrain the MFOR to $\{y, z\} = \{[-2.5D, +2.5D], [-2D, 2D]\}$. Consequently, some data is missing in the MFOR, leading to unavoidable small differences between the left and right hand-sides of Eqs. 7.11 and 7.14.

Moreover, the limitations detailed in Sect. 5.3 are recalled:

- The statistics (mean and variance) near the ground in the MFOR are computed with fewer samples than those at higher positions.
- Data is sampled at 1 Hz, over 80, 40 and 10 min for the neutral, unstable and stable cases respectively. Consequently, all the variations of the wind velocity at frequencies higher than 1 Hz are not taken into account in this work, nor is the subgrid turbulence. The latter is negligible in the unstable and neutral cases but can reach more than 10% of the total turbulence in the stable case.
- Only the streamwise component of the velocity is computed in the following, in both MFOR and FFOR.

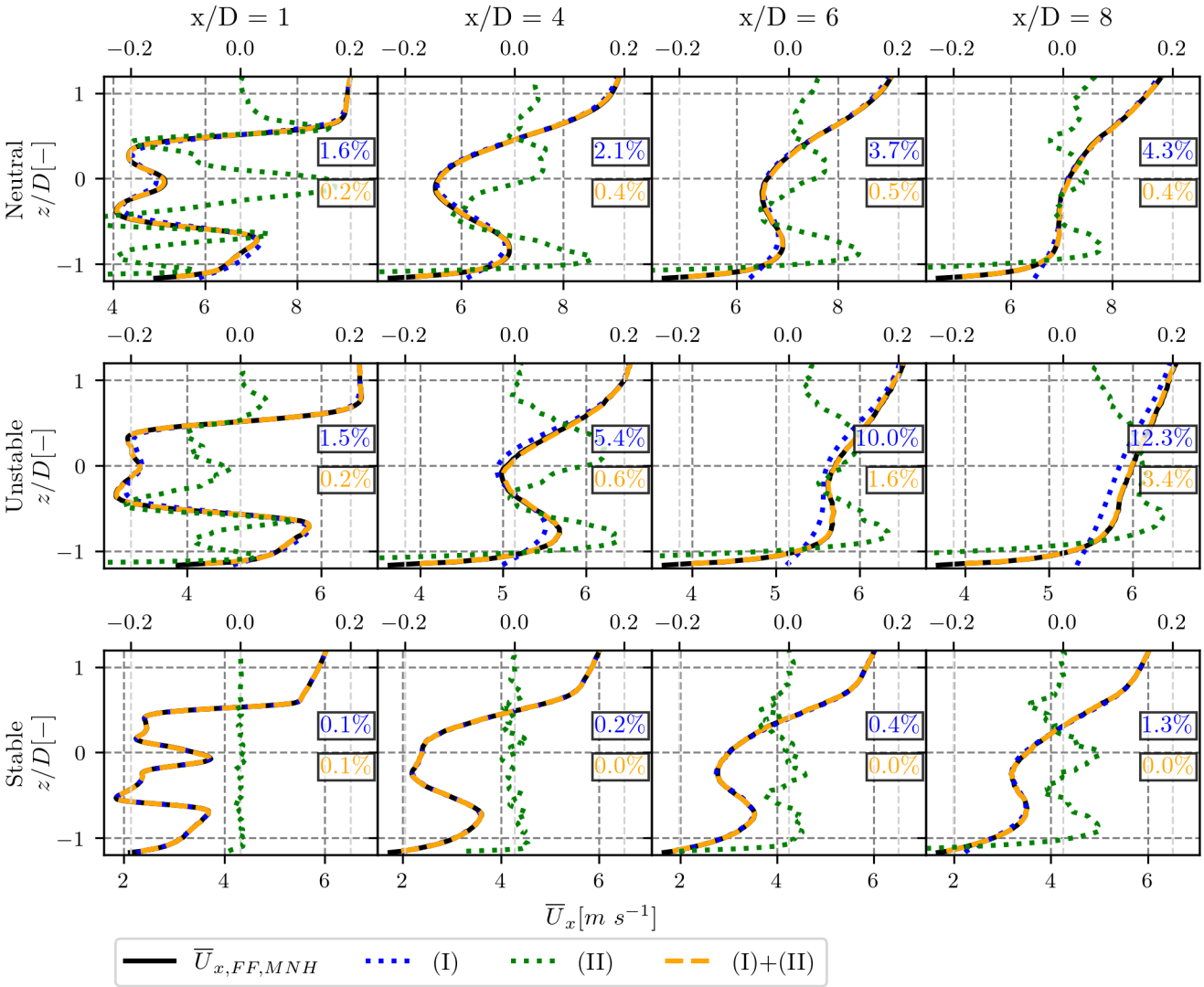

Figure 7.2: Contribution of terms (I) and (II) from Eq. 7.11 to the velocity in the wake, compared to the velocity in the FFOR. Term (II) is plotted on a different scale (top axis). The RMSEs corresponding to (I) and (I) + (II) are displayed in the corresponding colours.

7.2.3 Velocity field

In Eq. 7.11, the velocity is separated into two terms, (I) and (II). The vertical profiles of these terms are plotted in Fig. 7.2 for several downstream positions and for the three cases. The term (I), which is the convolution of the velocity in the MFOR with the distribution of wake centre position, fits very well with the velocity in the FFOR. Small differences only appear in the near wake. Term (II) is plotted on a secondary axis (displayed at the top of the figure) to show that it has a negligible value: less than 0.3 m/s in absolute value, i.e. less than 4 % for the neutral case. In the stable case, it is even more negligible but in the unstable case, it represents about 10 % at the wake centreline at $x/D = 8$. In this case, the relatively-large values of (II) are attributed to errors in the tracking algorithm. As it can be seen at the bottom of the profiles, the main role of the term (II) in the far wake is to reproduce the shear near the ground that is missing in the MFOR, and thus not present in term (I).

Even for (I)+(II), the RMSE tends to increase as the wake propagates downstream, which is attributed to an increase in the error close to the ground, due to undefined data. This number of errors increases with the amount of meandering because more and more data go outside of the computed MFOR (see Sect. 7.2.2) and thus the loss of data increases with x. Note that this RMSE is not computed only on the vertical profile but on the truncated 2D plane $\{y, z\} = \{[-2D, +2D], [-1D, 1D]\}$, i.e. it also accounts for discrepancies that are not visible on the profiles. According to the last remark in Sect. 7.1, the RMSE corresponding to the full breakdown equations (orange lines in Figs. 7.2, 7.3, 7.4 and 7.5) is the minimum RMSE achievable with our numerical dataset. When lower values are reached, it must be attributed to an error compensation.

This first observation indicates that neglecting term (II) is reasonable. Since the power output prediction of a farm is a direct application of analytical models, the error induced by this assumption is measured for the available power. The mass available power is here defined as:

$$P_a(x) = \int\int_S \overline{U}_x^3(x, y, z) dy dz \tag{7.16}$$

where S is the surface of a virtual wind turbine located at position x behind the wake-emitting turbine, with hub height at the same lateral and vertical position: $(y, z) = (0, 0)$. This quantity is computed for (I) and (I)+(II) at each available position downstream of the wind turbine, and compared to the same quantity directly computed on the Meso-NH field in the FFOR $P_{a,FF}$.

From Fig. 7.3, it appears that neglecting term (II) in the neutral case leads to a slight overestimation of the available power in the near wake of the wind turbine. The estimation is however fairly good, especially for a wind turbine located further than 3D downstream where the overestimation drops below 2 %. The relative error is larger in the unstable case but more importantly, it does not seem to converge and reaches -6 % at $x/D = 8$ due to the underestimation of the velocity already observed in Fig. 7.2 that was attributed to bad tracking results. In the stable case, the error is negligible, reaching at worse less than 0.4 %. If the velocity near the ground is not of interest, approximating the FFOR velocity as the term (I) alone can thus be acceptable given the low error on estimated power. This is especially relevant since the term (II) is chaotic (see Fig. 7.2) and thus hard to model.

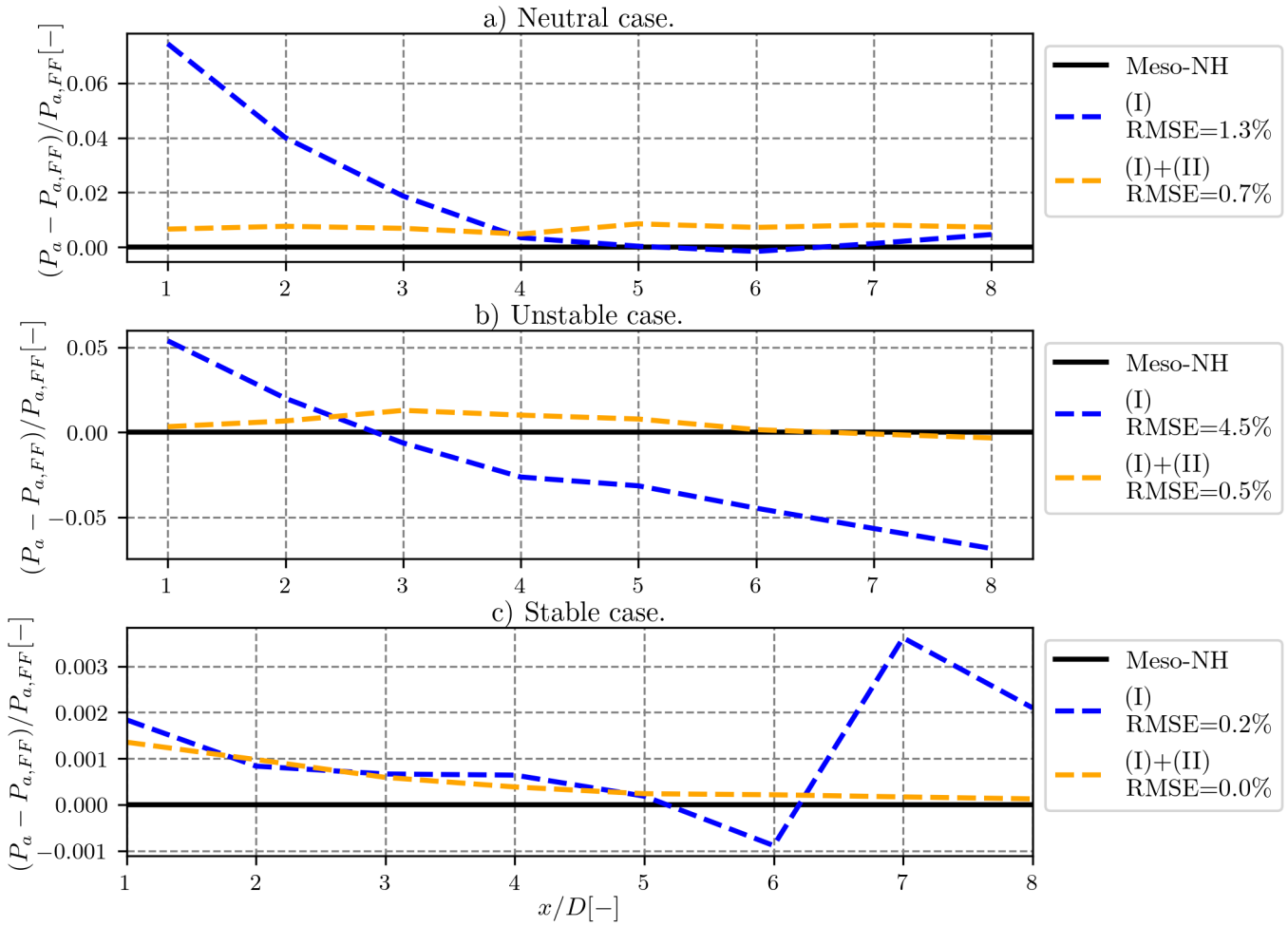

Figure 7.3: Available power predicted by (I) (blue line) and (I)+(II) (yellow line), normalised with the results in the FFOR (black line).

7.2.4 Turbulence field

The same study is performed for the turbulence breakdown. The vertical profiles of streamwise TKE are plotted for different levels of approximation, at different positions downstream in Fig. 7.4. In the DWM model, only the meandering (III) and rotor-added (IV) terms are retained. This corresponds to the blue curve: despite overall good orders of magnitude, the vertical asymmetry of the wake is not sufficiently pronounced, leading to an underestimated value of k_x at the top tip and overestimated value at the bottom tip. This issue, especially true in the near wake, has already been observed in another work that used an equation similar to Eq. 7.14 to compare the DWM results to *in situ* measurements [127]. If horizontal profiles at hub height are plotted instead (shown in Ch. 8), the results are much better and the (III)+(IV) approximation seems suitable, for the neutral but also the unstable and stable cases.

In the neutral and unstable cases, adding the covariance term (V) along with terms (III) and (IV) (green curve in Fig. 7.4) corrects for most of the vertical asymmetry of the turbulence profiles and leads to a rather good estimation of the maximum turbulence values at the top and bottom tips. In the stable case, even though the total RMSE in the truncated plane tends to be reduced, adding this

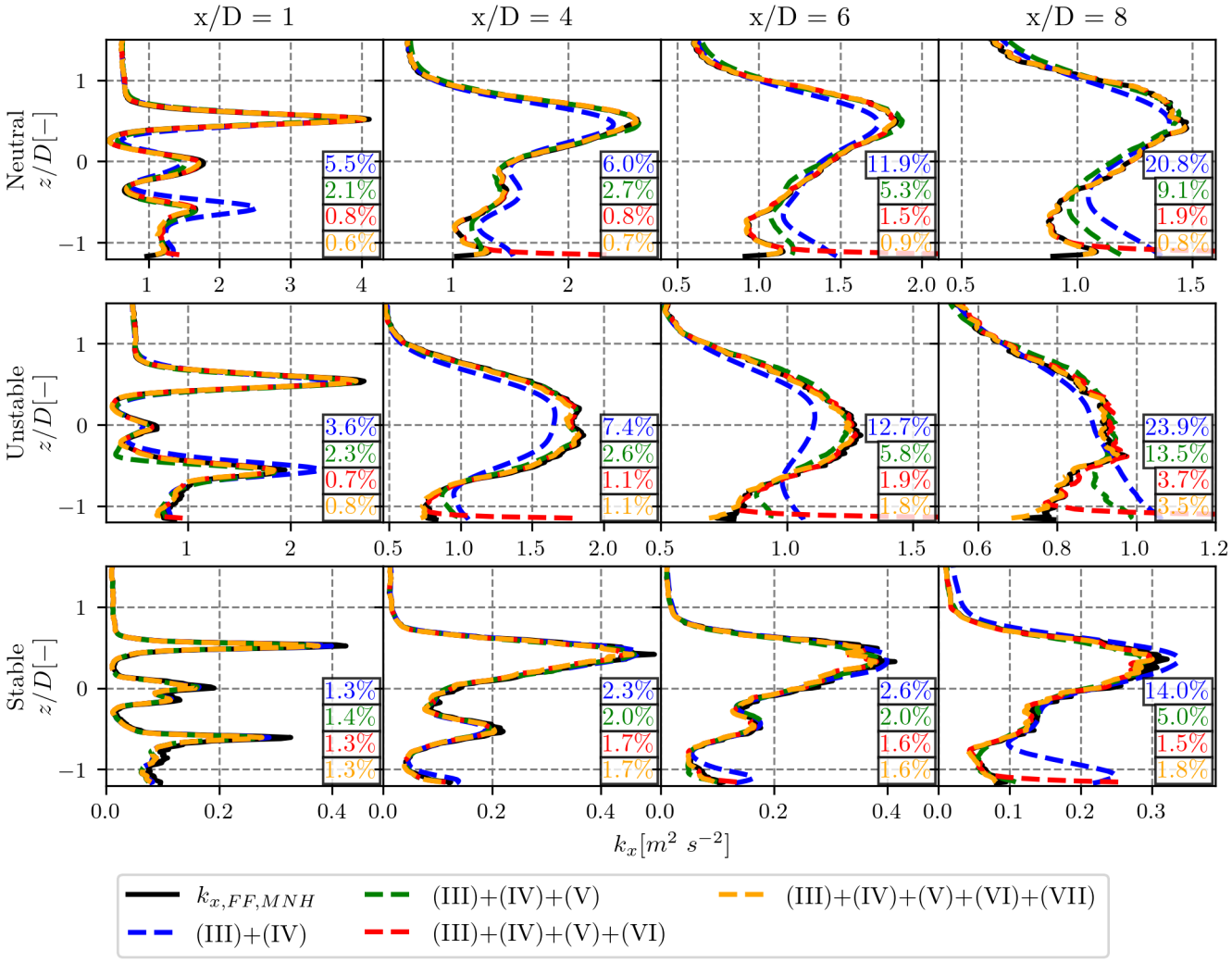

Figure 7.4: Streamwise turbulence in the wake of the wind turbine for different levels of approximation.

term leads to a decrease in streamwise turbulence at the peaks. The main effect of adding the term (VI) (red curve) is to take the spatial small-scale variations into account. It brings the total k_x even closer to its reference value but it does not change the overall shape of the wake except at the bottom of the wake where it corrects the overestimation of (III)+(IV)+(V). As pointed out previously, the term (VII) is the square of the term (II): like the latter, it mainly has an effect near the ground but is otherwise negligible.

To quantify more clearly these differences, the maximum streamwise turbulence $k_x^M(x)$ is studied. It is computed directly in the FFOR ($k_{x,LES}^M(x)$) and for different levels of approximation from Eq. 7.14. Their evolution with the downstream distance is plotted in Fig. 7.5, normalised by $k_{x,LES}^M(x)$ and the same colour convention as in Fig. 7.4 is used.

For the neutral case, neglecting the cross-terms leads to an underestimation of about 6 % to 12 % of the maximum turbulence in the wake. Adding the covariance term (V) brings this number down between 2 % and 6 %, and adding term (VI) to this total leads to a negligible underestimation

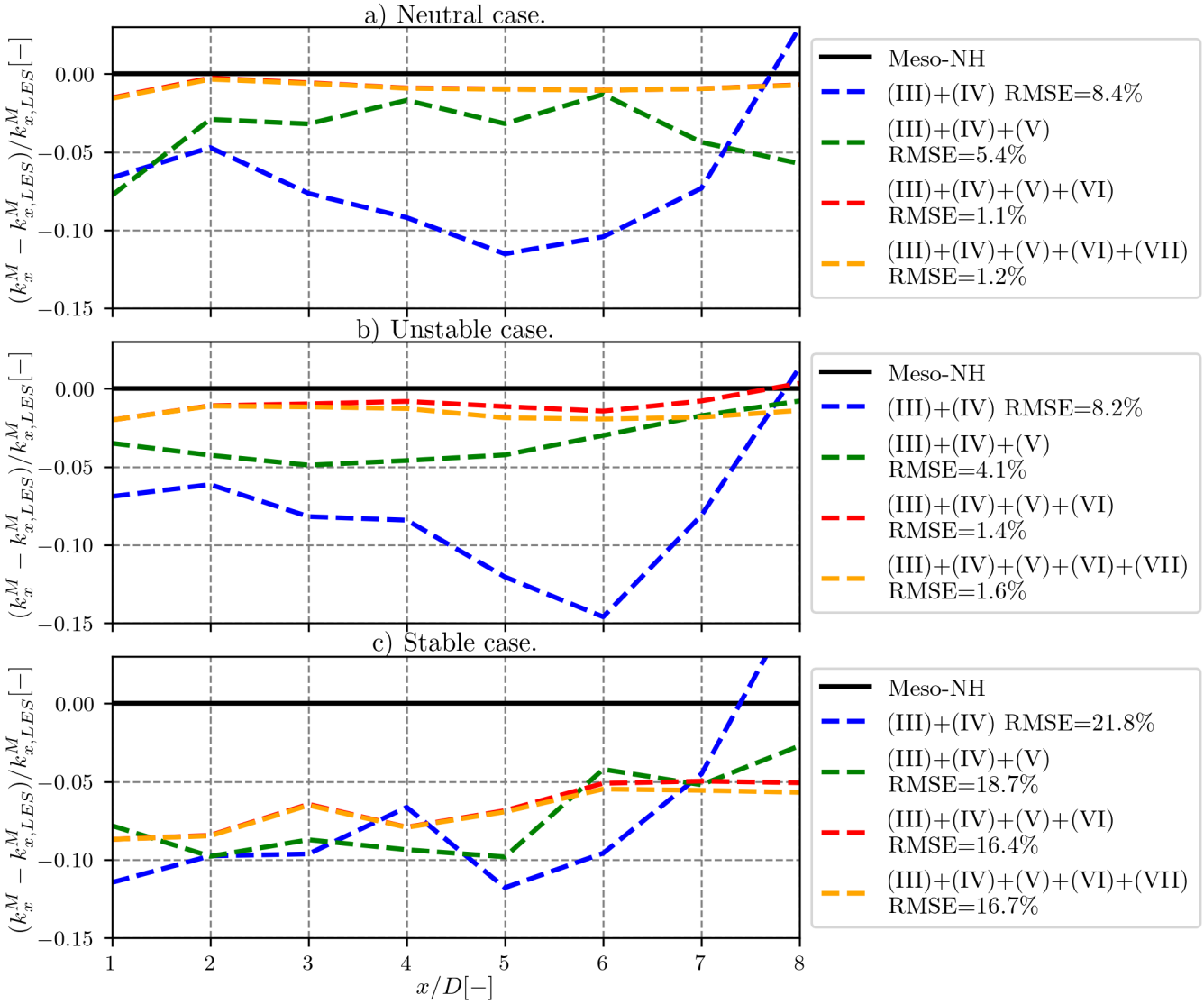

Figure 7.5: Normalised maximum turbulence in the wake for different levels of approximation. The RMSE of k_x^M over all the x positions is displayed.

(around 1 %). This term has a relatively large impact on the maximum turbulence because it relates to the spatial non-homogeneity, and thus can locally take a lot of importance for the maximum value at $x/D = 8$. According to this interpretation, if an ensemble average on the dataset was performed, or if a criterion with several points was used instead of the maximum value (for instance, a spatial average), the contribution of this term would be consequently smaller, except at the bottom of the wake (see Fig. 7.4). Term (VII) has a negligible effect on the maximum turbulence (orange and red curves are superimposed). The remaining gap is attributed to the error reconstruction due to the MFOR being computed on a too-small grid (see Sect. 7.2.2), but this may not be the only factor of error since errors are still observed in the stable case where the low meandering leads to very few loss of information.

For the unstable case, the same orders of magnitude are observed for the different k_x approximations: adding the convolution term (V) reduces the relative underestimation of k_x^M by at least half and using

(III)+(IV)+(V)+(VI) leads to a fairly good approximation. In the stable case, however, the error remains between 5 and 10 %, independently of the level of approximation. This can be observed in Fig. 7.4 where despite an improvement over the whole profile, the maximum is not well captured. The relatively high error percentage is attributed to low absolute values. Indeed, the error is of the order of magnitude of 0.04 $m^2\ s^{-2}$, which is in the end similar to the other cases. Term (VII) is almost negligible in every case.

It has been shown in this section that neglecting term (II) leads to a rather accurate velocity deficit in the wake and a reasonable estimation of the available power for a wind turbine inside the wake. For the turbulence breakdown, the term (VII) is also negligible, but the vertical turbulence profiles are prone to errors when terms (V) and (VI) are not taken into account, leading to an underestimation of the maximum turbulence in the wake. Term (VI) is erratic and is expected to disappear (except near the ground) if ensemble-averaged data is used, but term (V) seems to be consistently taking into account the asymmetry of the wake and should thus not be neglected. It is now needed to compare the shapes and the relative magnitudes of these terms before modelling them.

7.3 Analysis of the terms in the turbulence breakdown

In this section, the different terms of the turbulence breakdown equation are compared for the three cases of stability. The influence of atmospheric stability on each term of Eq. 7.14 is highlighted and the shape of these terms in the Y-Z plane is analysed.

7.3.1 Shape and values of the terms

The values of each term of Eq. 7.14 at different Y-Z planes downstream of the turbine in the FFOR are displayed in Figs. 7.6, 7.7 and 7.8 for the neutral, unstable and stable cases respectively. The terms are normalised by the maximum total turbulence in the FFOR $k^{M}_{x,LES}(x)$ in the 2D plane, so the scale is approximately the fraction of the total streamwise turbulence represented by each term. Term (IV) contains both the rotor-added turbulence and the inflow turbulence, which is removed by subtracting the reference turbulence field in the MFOR $k_{x,ref,MF} = \overline{U'^2_{x,ref,MF}}(x,y,z)$ taken from the reference simulation at the same location than the waked turbulence field (see Sect. 5.2.1). In the MFOR, the rotor-added streamwise turbulence is thus defined as the difference of streamwise turbulence between the simulation with and without the wind turbine:

$$\Delta k_{x,MF}(x,y,z) = \overline{U'^2_{x,MF}}(x,y,z) - \overline{U'^2_{x,ref,MF}}(x,y,z) \tag{7.17}$$

Note that the $y_c(t)$ and $z_c(t)$ computed in the simulation with a turbine are re-used to compute the reference MFOR field and to apply operator $\widehat{.}$ to the reference data. The rotor-added turbulence can then be defined in the FFOR as the convolution product of $\Delta k_{x,MF}(x,y,z)$:

$$\Delta(\mathrm{IV}) = \widehat{\overline{\Delta k_{x,MF}}} = \widehat{\overline{U'^2_{MF}}} - \widehat{\overline{U'^2_{ref,MF}}} = (\mathrm{IV}) - \widehat{\overline{k_{x,ref,MF}}} \tag{7.18}$$

If the upstream turbulence is used to define this term i.e. $\Delta(\mathrm{IV}) = (\mathrm{IV}) - k_\infty$, it leads to undistinguishable shapes, in particular for the unstable case. To be correct, one should first compute an

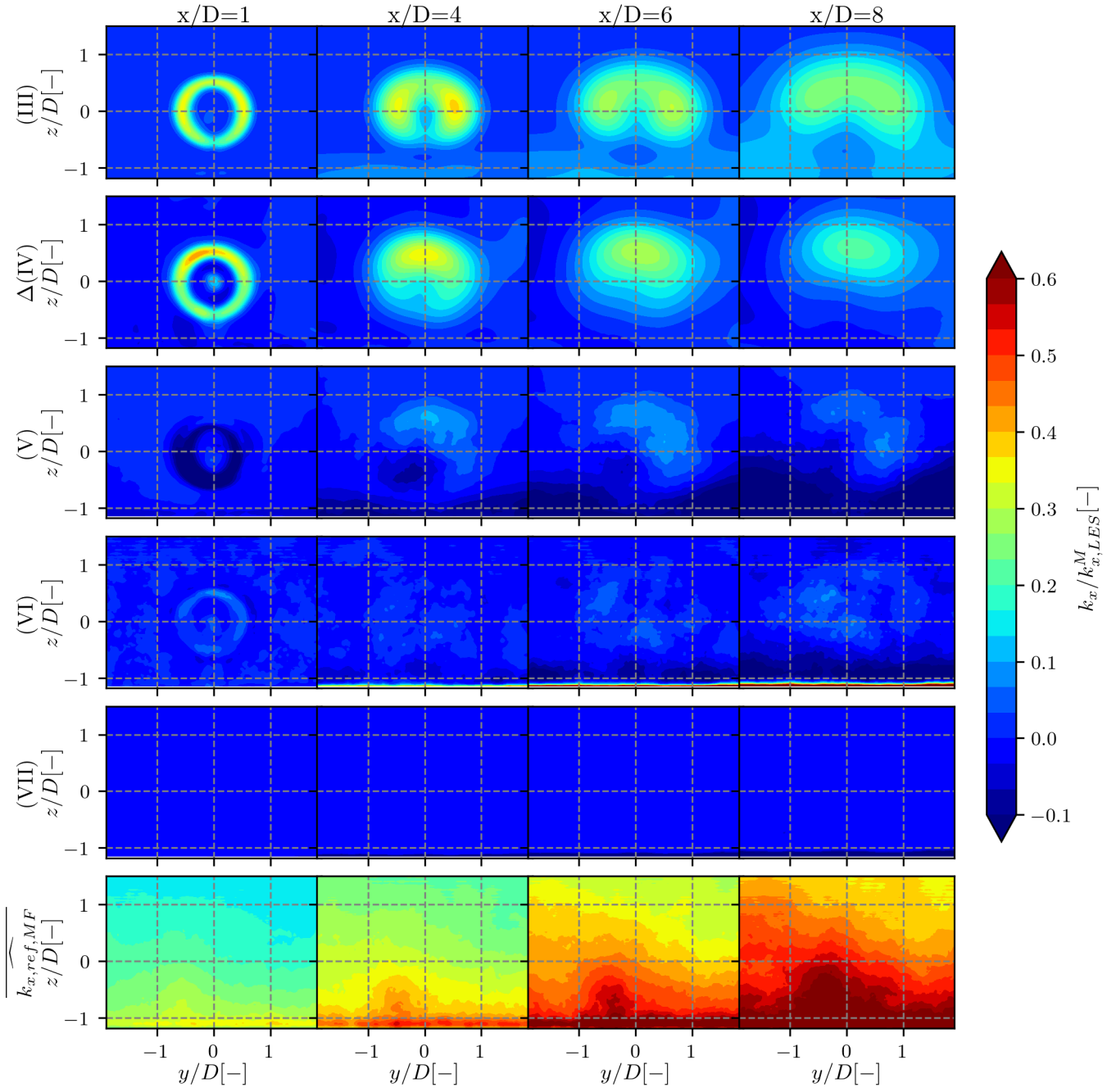

Figure 7.6: 2D maps of the different terms in Eq. 7.14 for the neutral case. Each row stand is a different term and each column is a different position downstream. The values are scaled by the maximum TKE in the FFOR at the given x position.

equivalent k_∞ in the MFOR and then compute:

$$\Delta(\text{IV}) = (\text{IV}) - \overline{\widehat{k_{x,\infty,MF}}} \tag{7.19}$$

which in the end requires a post-processing as computationally expensive as Eq. 7.18. Since both

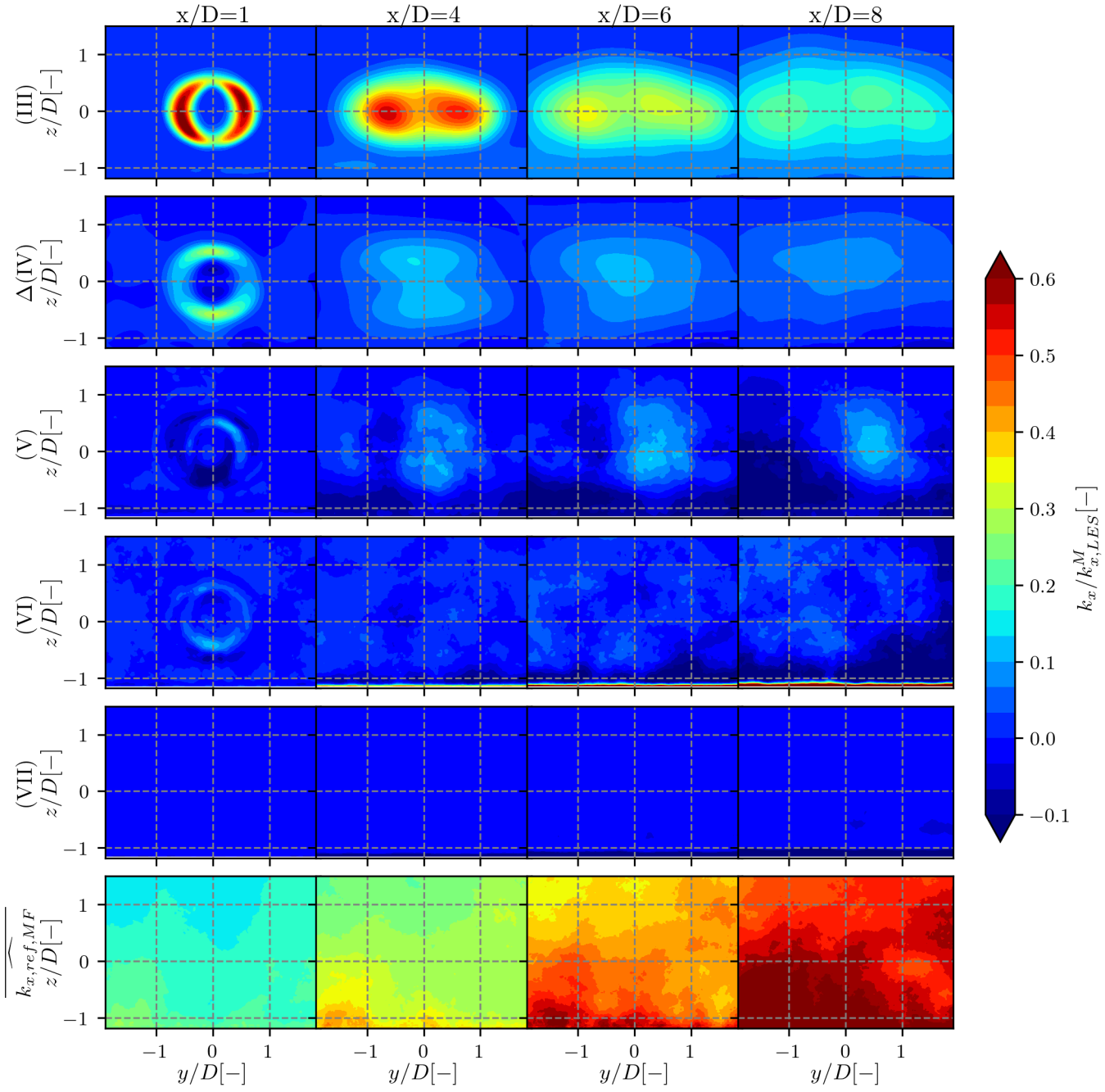

Figure 7.7: Same as 7.6 for the unstable case.

methods give similar results and since the computed TI in the MFOR is also similar (see Figs. B.2 and B.4), the definition with the reference simulation is chosen for this whole chapter and the following. It is plotted in the FFOR $\widehat{k_{x,ref,MF}}$ in the last line of Figs. 7.6, 7.7 and 7.8 to quantify how the wake turbulence is going back to its unperturbed value: the closest $\widehat{k_{x,ref,MF}}$ is to 1, the most dissipated is the wake.

For the neutral case of stability (Fig. 7.6), the meandering (III) and rotor-added Δ(IV) terms have

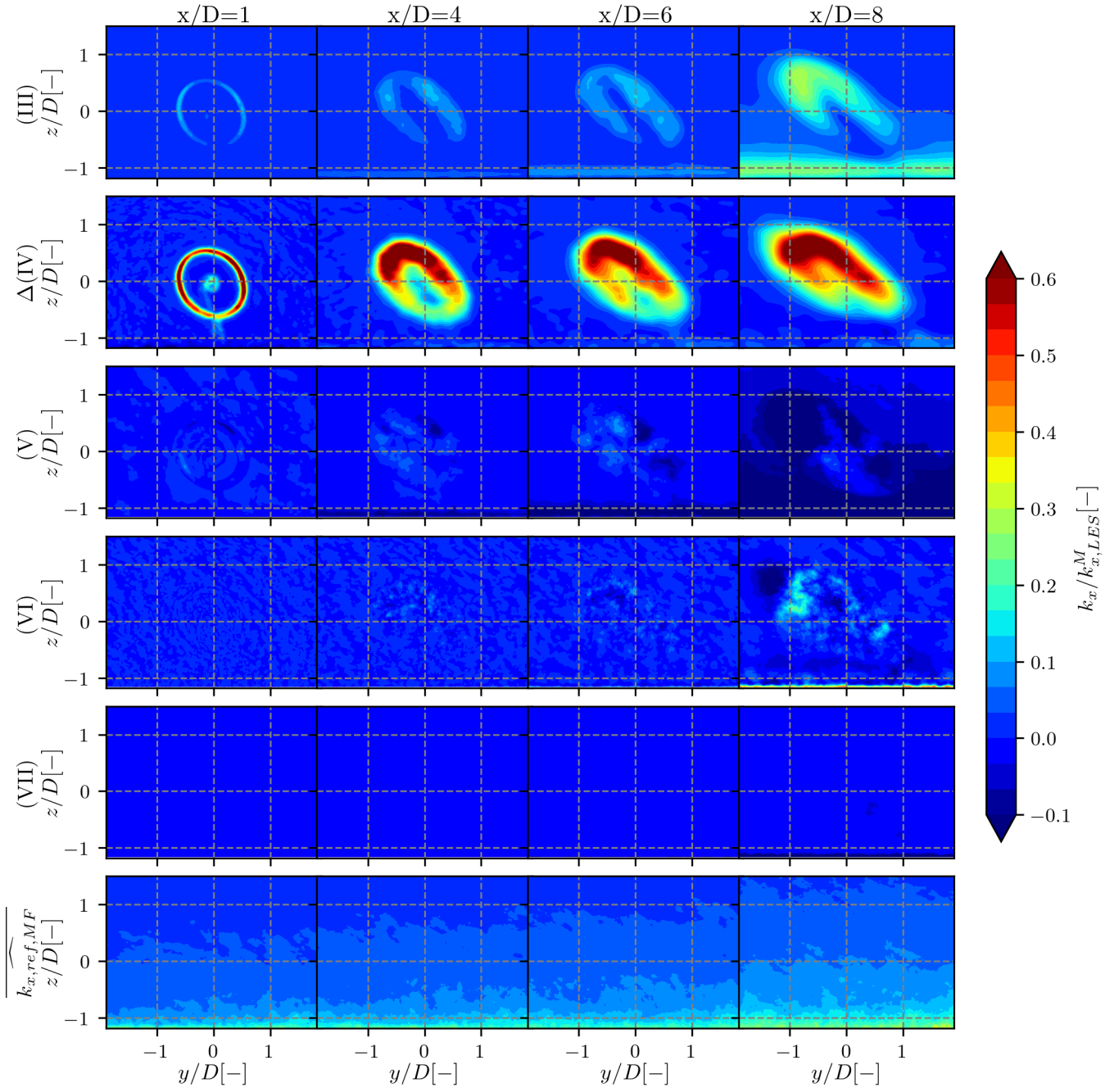

Figure 7.8: Same as 7.6 for the stable case.

similar orders of magnitude and contain most of the total wake added turbulence. However, the covariance term (V) cannot be ignored as it rebalances the total turbulence of about ±10% between the top and bottom regions of the wake, as shown in Fig. 7.4. Term (VI) also shows non-negligible values, in particular in the far wake where they approach those of the other terms, but the shape of this term seems to be randomly distributed (contrarily to term (V) which is located in the rotor-swept area). It confirms the analysis presented in the previous section where this term is attributed to small-scale non-homogeneity of the turbulence field and is expected to become negligible for a

smoother turbulence field, e.g. if an ensemble average over several segments is performed to compute the different terms. As stated in Sect. 7.2, the term (VII) is negligible, except near the ground.

Figure 7.7 has been plotted similarly to Fig. 7.6 with the results of the unstable case. The meandering term (III) is dominant over the others and the wake is quickly dissipating. The rotor-added turbulence has lower relative values and is more spread than in the neutral case. This is due to larger meandering in the unstable case i.e. a PDF f_c with larger values at the edge and thus more spreading caused by the operator $\widehat{.}$. The covariance term (V) is also not negligible: here it takes values between terms Δ(IV) and (III) in the far wake. Contrarily to the neutral case, it shows an approximate symmetry around the vertical axis instead of the horizontal one. Term (VI) has lower values, that seem to be randomly distributed as in the neutral case. Term (VII) is still negligible.

In the stable case (Fig. 7.8), it is the rotor-added turbulence that is largely predominant over the meandering and even the upstream terms. This can be explained by the fact that meandering is very weak, so the term (III) is low, the term Δ(IV) is almost not spread by the convolution with f_c, and the wake is barely dissipated, even at $x/D = 8$. The covariance term is here negligible except at $x/D = 8$ where it slightly reduces the peak of turbulence at the top-left end of the wake. Term (VI) and particularly term (VII) are negligible in front of term (IV). The shape of all these terms is skewed due to the strong veer present in the stable ABL.

7.3.2 Physical interpretation

Term (III) or k_m is the pure meandering term. For a fixed point downstream of the turbine, the meandering of the wake induces an alternation between low velocity (when the point is inside the wake) and high velocity (when it is outside the wake), i.e. variance in the unsteady velocity field, which is the definition of turbulence. k_m thus increases with the velocity deficit in the MFOR and with the amount of meandering. The former decreases with x as the wake dissipate whereas the latter increases with x, often linearly [100, 94, 163]. These two contradictory trends lead k_m to be strong and very localised at the tip of the blades in the near wake and to be progressively smeared as the wake travels downstream. Since the meandering is stronger in the horizontal direction than in the vertical direction and the velocity deficit is approximately axisymmetric (see Ch. 8 for more details), the highest values of k_m in the horizontal plane are stronger than in the vertical plane.

At a fixed x, the maximum values of k_m are localised near the tip of the blades in the near wake and are gradually spread as the wake travels downstream. The maximum added TI (i.e. square-root of the maximum value, normalised by the upstream velocity at hub height) induced by term (III) is plotted in dashed lines as a function of x/D in Fig. 7.9. As seen in Figs. 7.6, 7.7 and 7.8, the meandering-induced turbulence is inversely related to the atmospheric stability, but this term also decreases faster in the unstable case, likely because the stronger the meandering, the more spread the added turbulence. Consequently, at $x/D = 8$ the unstable and neutral added TI due to the meandering are almost identical, and the curves would probably switch positions at larger x. In the stable case, the velocity profile is barely dissipated up to $x/D = 8$ and the meandering starts to take consequent values at $x/D = 5$, which results in an increase of the added turbulence due to meandering starting from $x/D = 5$. One can predict that beyond $x/D = 8$, a maximum value is reached, followed by a shape similar to the unstable and neutral case.

Term Δ(IV) noted Δk_a for 'rotor-added turbulence' is the added turbulence that would be found in the wake of the turbine if there was no meandering. This turbulence is mainly due to the velocity

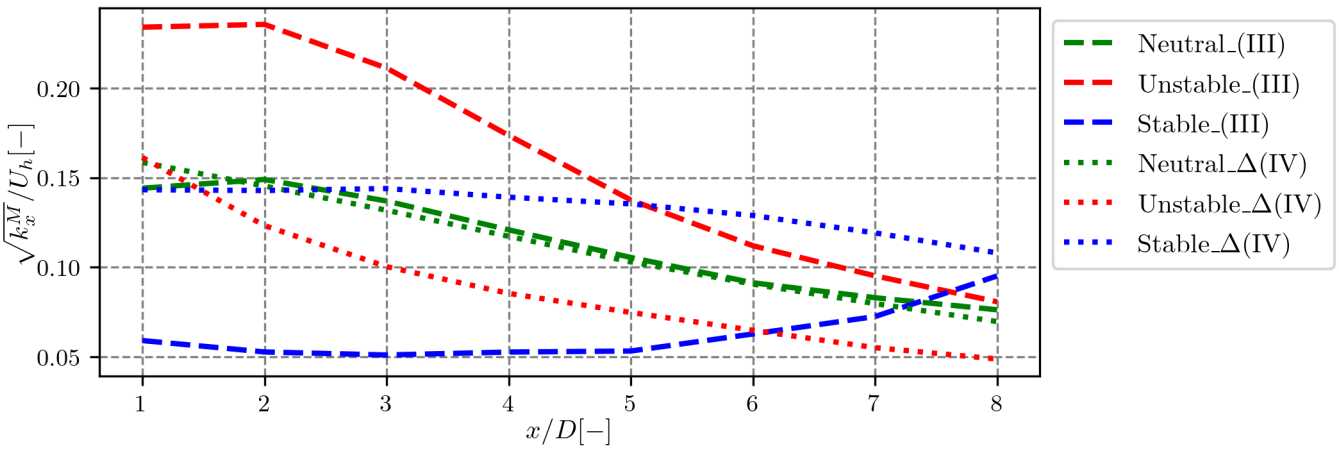

Figure 7.9: Evolution of the maximum value of terms (III) and Δ(IV) with x, normalized by the velocity at hub height.

gradient in the MFOR, localised at the edge of the wake. It is affected by the shear of the ABL, leading to a stronger gradient near the top tip and thus stronger rotor-added turbulence. This is particularly visible in the neutral and stable cases, where the atmospheric shear is significant. The MFOR turbulence, which is at the origins of k_a (i.e. term (IV)), shows a behaviour remarkably independent of the atmospheric stability, as it was shown in Ch. 6 (see Fig. B.4). Similarly to the velocity field, it is spread by meandering, more strongly in the lateral direction than in the vertical one, leading in the unstable case to lower values of k_a at the side tips than at the bottom tip despite the atmospheric shear being stronger at the side. This spreading due to meandering also induces lower values of maximum added turbulence for lower stability cases (dotted lines in Fig. 7.9).

The value of the cross-terms (V), (VI) and (VII) is 0 either if there is no meandering or if there is no turbulence in the MFOR. The latter is assumed in some models but none of these conditions is fulfilled in real cases nor LES. It has been chosen to regroup the two terms $\overline{\widehat{U_{MF}}\widehat{U'_{MF}}}$ and $-\overline{\widehat{U_{MF}}}\,\overline{\widehat{U'_{MF}}}$ into one single covariance term (V) since these two terms were very large in absolute value, but were compensating each other, and at the end were hard to interpret independently. Mathematically, this covariance term quantifies how the mean and varying parts of U_{MF} evolve together once displaced by the meandering operation $\widehat{.}$. In the near wake, the non-zero values are distributed at the tip of the blades and then gradually expand in the whole wake. Negative and positive values are symmetrically distributed (along the horizontal and vertical axis for the neutral and unstable cases respectively). From these results, no physical interpretation nor a relation between the values of U_x or k_x in the wake with the term (V) could be found yet. Modelling the covariance term has thus not been achieved in the Ch. 8, but we are confident that it is required for a good wake model based on the meandering, and that it is reachable given the shapes observed in Figs. 7.6 and 7.7.

Term (VI) can be viewed as the varying part of turbulence: before being moved by the meandering and averaged, this term is the varying part of the square of the deviation from the mean (in opposition to $k_{x,MF}$ which is the mean part of the square of the deviation from the mean). In the near wake, positive values are present at the tip of the blades in the neutral and unstable cases, but also outside of the wake. It then gradually expands in the whole wake and seems randomly distributed in the wake region with negative and positive values. From Figs 7.6, 7.7 and 7.8, it seems that excepted systematic negative values at the bottom of the wake ($z < D/2$), this term mainly reproduces the

spatial non-homogeneity of the wake and is thus not vital to be represented in an analytical model.

Term (VII) is always negative from its mathematical formulation: similarly to the viscous dissipation in the Navier-Stokes equations, it is a sink of energy. It has negligible values in all the stability cases. This last result should be taken with care: if the analogy with the viscous dissipation holds for this term, it means that it concerns small scales eddies, i.e. variations of the wind velocity at high frequency. Yet, as explained in Sect. 7.2.2, only the variations of time scale larger than 1 s are captured with the post-processing used in this work because of memory limitations. With a sampling frequency higher than 1 Hz, this term may have higher values.

It is important to note that all these results are sensitive to the wake tracking method: despite the method used here being among the most reliable available in the literature (see Ch. 5), there are always frames where the tracking failed, plus the limitations described in Sect. 7.2.2. For instance, the turbulence field in the MFOR (see Fig. B.4) is noisier and noisier as the wake travels downstream and in particular in the unstable case, which can be interpreted as a consequence of the tracking method being less and less reliable. This remark can be extended to all the terms of the turbulence equation presented in Figs. 7.6, 7.7 and 7.8. Moreover, the values and shapes of the different terms (in particular the cross-terms) might also change depending on the turbulence field, i.e. the eddies of the ABL, even for similar mean atmospheric conditions.

Conclusions

In this work, the turbulence and velocity in the FFOR have been developed into two categories: pure- and cross-terms. All these terms are evaluated for three cases of stability and a physical interpretation is proposed. Overall, the present work concluded that:

- Neglecting the cross-term of the mean velocity equation leads to small differences in the computation of the mean velocity profile in the FFOR.
- Neglecting cross-terms in the computation of turbulence in the FFOR leads to vertical profiles where the imbalance between the turbulence at the bottom tip and the top tip is underestimated. It is shown that most of the discrepancies by accounting for a 'covariance term'.
- In the unstable case, the meandering term is dominating the total streamwise turbulence whereas in the stable case, it is the rotor-added turbulence which is dominant. In the neutral case, those two terms are of similar magnitude and overall larger than the cross-terms. These cross-terms, especially the so-called covariance term however show local values sufficiently strong to correct significantly the maximum streamwise turbulence in the wake.

It must be noted that these conclusions are drawn based on the results of three particular cases of atmospheric stability and one model of turbine that can be regarded as rather small compared to modern rotors. The orders of magnitude given in this work should not be considered universal but are a good indication that for a meandering-based model, the cross-terms (or at least the covariance term) must be taken into account. In the next chapter, an analytical model for the dominant terms is developed on the neutral and unstable cases, based on the results presented herein.

Chapter 8

Proposition of a new analytical model

In this final chapter, we show how the results from Ch. 7 can be used to build a model for velocity and turbulence in the wake that independently takes into account wake expansion and wake meandering. Doing so, one can include a dependence on stability through wake meandering. This methodology is decomposed into two steps: first, an analytical formulation for rotor-added turbulence and rotor-induced velocity deficit in the MFOR is proposed. Then, given a function for the wake centre's PDF, an analytical model of the different terms from the breakdown equations (Eqs. 7.11 and 7.14) can be deduced. We here focus on a steady analytical model, but the second step can be replaced by a stochastic meandering model, and would thus be similar to the DWM model, with an analytical formulation instead of the Ainslie/Madsen model for the velocity and turbulence in the MFOR.

The present analytical model has not been calibrated because only three numerical cases were available, which is not considered sufficient for proper calibration given that the model depends on five parameters. Instead, this chapter proposes formulations that are directly verified with the wake parameters deduced in Ch. 6, and which are not linked to the inflow properties. Moreover, the model does not take veer into account yet, so only the neutral and unstable cases are studied herein. Most of the work of this chapter has been submitted for peer review to the Wind Energy Science journal [164].

8.1 Independent modelling of the wake in the MFOR and meandering

The first step of this analytical reasoning is to define the shape of the mean velocity deficit and added turbulence fields in the MFOR. This is done from the MFOR results of the LES found in Ch. 8: based on the computed shape, a model is proposed, whose parameters are deduced from LES. The RMSE between the model and the LES is then computed.

8.1.1 Velocity deficit

In the LESs datasets, the velocity deficit in the MFOR is computed as:

$$\Delta U_{MF}(x,y,z) = \frac{\overline{U}_{x,MF,ref}(x,y,z) - \overline{U}_{x,MF}(x,y,z)}{\overline{U}_{x,MF,ref}(x,y,z)} \tag{8.1}$$

whereas in the analytical model, it is defined as:

$$\Delta U_{MF,am}(x,y,z) = \frac{U_{x,\infty}(z) - U_{x,MF,am}(x,y,z)}{U_{x,\infty}(z)} \tag{8.2}$$

where $U_{x,\infty}(z)$ (hereafter abbreviated $U_\infty(z)$) is the time- and laterally-averaged streamwise velocity profile upstream of the turbine. Equation 8.1 is used because it allows computing a smooth and almost axisymmetric velocity deficit in the MFOR, which is very similar between the neutral and unstable cases. However, $\overline{U}_{x,MF,ref}$ is not modelled analytically, so Eq. 8.2 is used for the model. The maps of velocity deficit computed from Eq. 8.1 are not displayed here because they are similar to those computed from the upstream velocity, so the reader can refer directly to Fig. B.1.

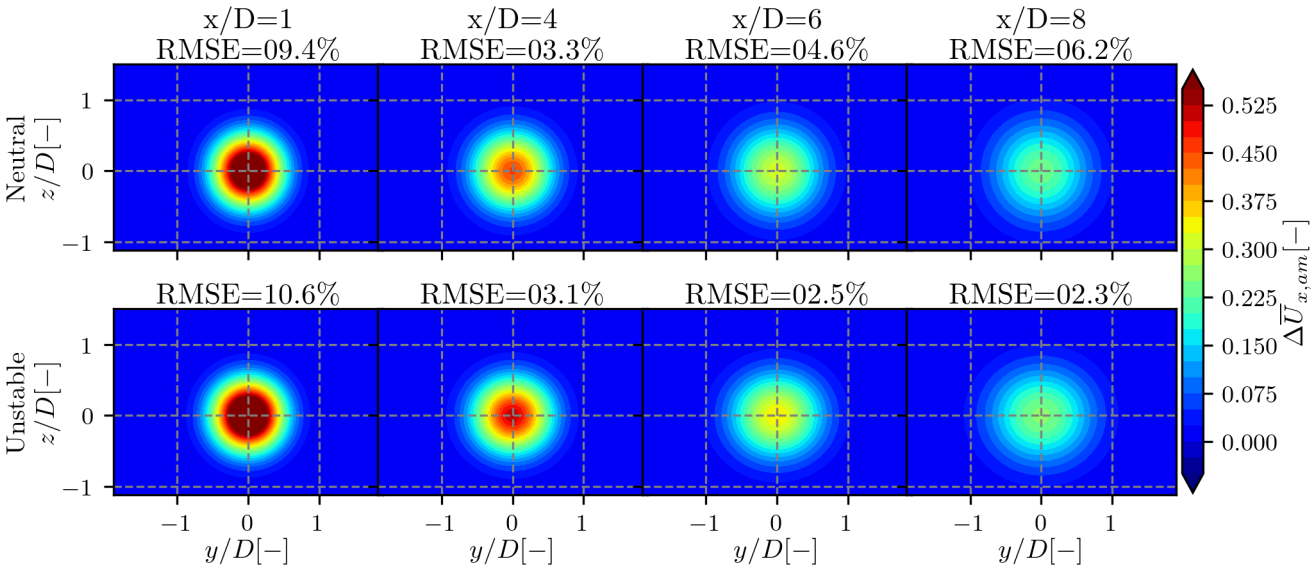

Figure 8.1: Modelled velocity deficit in the MFOR for the neutral (top) and unstable (bottom) cases. The RMSE is given with respect to the LES value (Fig. B.1).

In Ch. 6, we showed that the wake velocity deficit in the MFOR follows a self-similar Gaussian distribution for $x/D > 3$, in both horizontal and vertical directions. Based on this result, it is a natural choice to use the long-established Gaussian velocity deficit for our analytical model in the MFOR:

$$\Delta U_{MF,am}(x,y,z) = C(x)\exp\left(-\frac{y^2}{2\sigma_y^2(x)} - \frac{z^2}{2\sigma_z^2(x)}\right) \tag{8.3}$$

where subscript $_{.am}$ stands for 'analytical model', $C(x)$ is defined as in the XA14 model (Eq. 2.28) and σ_y, σ_z are the wake widths in the MFOR. Here we directly take the LESs values, computed in Ch. 6, but a complete model would require relating these parameters to the inflow conditions. Note that

this formulation corresponds to the XA14 model, but Ch. 6 showed that the wake is axisymmetric in the MFOR so it could be simplified using $\sigma_y = \sigma_z$, i.e. as in the BP14 model. However, it was chosen to stick to the non-axisymmetric formulation to be more generic.

For both cases, the resulting velocity deficit is plotted in Fig. 8.1. The RMSE is given with respect to the LES data (see Fig. B.1) in the truncated plane $\{y, z\} = \{[-2D, +2D], [-1D, 1D]\}$. It is higher in the near-wake because the shape of the velocity deficit is assumed to be Gaussian, whereas a 'top-hat' function is observed in the LESs datasets. As detailed in Sect. 2.4.1, a double-Gaussian [78] or super-Gaussian [114] shape would provide more accurate results in the near wake. Here the Gaussian shape is chosen because it simplifies the analytical resolution of the convolution products and few wind farms have inter-rotor spacings lower than $3D$.

8.1.2 Wake added turbulence in the MFOR

In order to model term (IV) or k_a, one needs an analytical form for the turbulence in the MFOR k_{MF}. It is proposed to separate the rotor-added turbulence Δ(IV) from the ambient turbulence. Similarly to the velocity deficit and to be consistent with Ch. 7, the ambient turbulence is chosen as the value from the reference simulation for the LES dataset:

$$k_{x,MF}(x, y, z) = \Delta k_{x,MF}(x, y, z) + k_{x,MF,ref}(x, y, z) \tag{8.4}$$

but as the upstream value for the analytical model:

$$k_{x,MF,am}(x, y, z) = \Delta k_{x,MF,am}(x, y, z) + k_{x,\infty}(z) \tag{8.5}$$

where $\Delta k_{x,MF}$ will be hereafter referred to as 'added turbulence' and $k_{x,\infty}$ (abbreviated k_∞) is the laterally averaged streamwise turbulence upstream of the turbine.

The derivation of a model for $\Delta k_{x,MF}$ is not as straightforward as for ΔU_{MF} because turbulence comes from the unsteadiness of the flow whereas an analytical model is by definition steady. Moreover, self-similarity of turbulence, as it is assumed in [92], has not been successfully proven for our datasets (see Ch. 6). Finally, since an analytical form of the model is needed in the FFOR, one must ensure that the convolution of $f_{c,am}$ with the chosen shape function for $\Delta k_{x,MF,am}$ has an analytical solution, which is not trivial for any function.

It is here proposed to assume that the turbulence in the MFOR is solely driven by wake-generated shear. To relate the turbulence in the MFOR to mean gradients, two models for the velocity scale u_0 are combined. In the first, it is assumed to be proportional to the square root of the TKE k [41]: $u_0 = C_\mu^{1/4} k^{1/2}$ where C_μ is a constant and l_m the mixing length. However in the present work, the three-dimensional TKE k is not computed, so it is replaced with the streamwise turbulence:

$$u_0 = C_\mu^{1/4} k_x^{1/2}. \tag{8.6}$$

The value $C_\mu = 0.09$ will be used in this work. Historically, this value has been fitted to yield correct behaviour in the log-law region of a wall and can be extended in regions where the turbulence production equals the dissipation [41]. It is a strong assumption that has not been verified, but since the mixing length is here fitted to make the MFOR model match the LES results, this choice has

no significant consequences. In the future, it would be interesting to compute this constant in the MFOR of a wind turbine wake. In the second method, the velocity scale is defined from the norm of the strain-rate tensor $|\overline{\overline{\mathcal{S}}}|$:

$$\begin{aligned} u_0 =& l_m|\overline{\overline{\mathcal{S}}}| \\ =& l_m \cdot \left[\left(\frac{\partial U_x}{\partial x}\right)^2 + \left(\frac{\partial U_y}{\partial y}\right)^2 + \left(\frac{\partial U_z}{\partial z}\right)^2 + \frac{1}{2}\left(\frac{\partial U_x}{\partial y} + \frac{\partial U_y}{\partial x}\right)^2 + \frac{1}{2}\left(\frac{\partial U_x}{\partial z} + \frac{\partial U_z}{\partial x}\right)^2 \right. \\ & \left. + \frac{1}{2}\left(\frac{\partial U_y}{\partial z} + \frac{\partial U_z}{\partial y}\right)^2 \right]^{-0.5} \end{aligned} \tag{8.7}$$

From the literature [165], it appears that in the wake of a wind turbine, the dominating term (in cylindrical coordinates) is $\partial U/\partial r$. It is here supposed that these results can be transposed in Cartesian coordinates and are still viable in the MFOR. The velocity scale can thus be written as a function of the derivatives of the streamwise velocity.

$$u_0 = l_m \cdot \sqrt{\frac{1}{2}\left(\frac{\partial U_x}{\partial y}\right)^2 + \frac{1}{2}\left(\frac{\partial U_x}{\partial z}\right)^2} \tag{8.8}$$

To simplify the equation of added turbulence in the MFOR and to analytically develop the convolution product, it is convenient to consider U_∞ as a constant with z when it comes to the vertical derivative, i.e. make the following approximation:

$$\frac{\partial U_x(y,z)}{\partial z} = U_\infty(z)\frac{\partial \Delta U_x(y,z)}{\partial z}. \tag{8.9}$$

Note that the model could be computed in the MFOR by developing the derivative with $U_x(y,z) = U_\infty(z)(1 + \Delta U(y,z))$ but then no analytical solution was found for the rotor-added turbulence in the FFOR $\Delta k_{x,a,am}$ (i.e. after the convolution), either with a power-law or a logarithmic profile for $U_\infty(z)$. Combining Eqs. 8.6 and 8.8, we obtain:

$$\begin{aligned} \Delta k_{x,MF,am} &= \left(\frac{u_0}{C_\mu^{1/4}}\right)^2 \\ &= \frac{l_m^2(x)}{2C_\mu^{1/2}} \cdot \left[\left(\frac{\partial U_{x,MF}}{\partial y}\right)^2 + \left(\frac{\partial U_{x,MF}}{\partial z}\right)^2 \right] \\ &= \frac{(C(x)U_\infty(z)l_m(x))^2}{2C_\mu^{1/2}} \left[\left(\frac{\partial \Delta U_{MF,am}}{\partial y}\right)^2 + \left(\frac{\partial \Delta U_{MF,am}}{\partial z}\right)^2 \right] \\ &= K_{MF}(x,z) \left[\left(\frac{y}{\sigma_y^2(x)}\right)^2 + \left(\frac{z}{\sigma_z^2(x)}\right)^2 \right] e^{-\frac{y^2}{\sigma_y^2(x)} - \frac{z^2}{\sigma_z^2(x)}} \end{aligned} \tag{8.10}$$

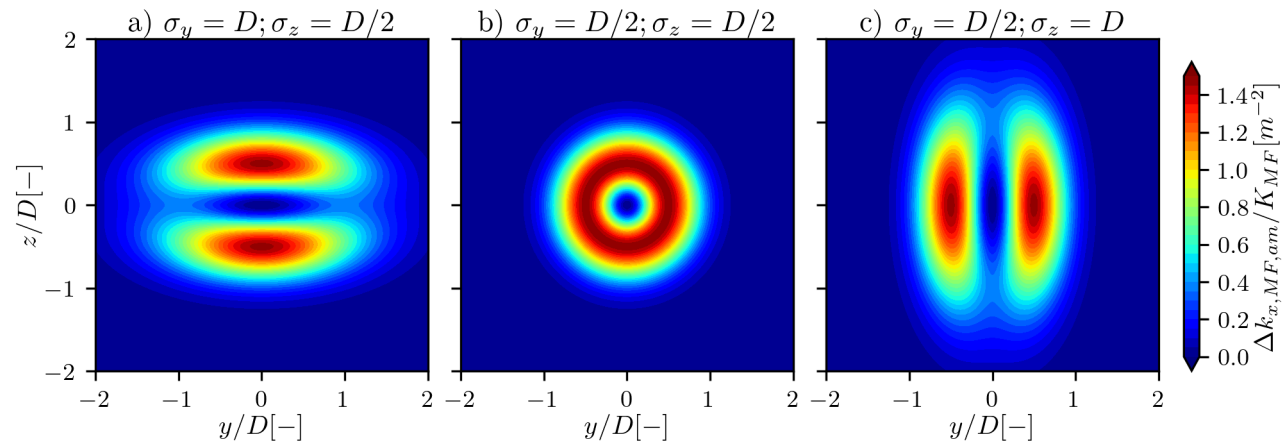

Figure 8.2: Chosen shape function for the turbulence in the MFOR, for different ratios of horizontal to vertical wake widths.

The shape function of the chosen model is plotted in Fig. 8.2 for different values of σ_y and σ_z. As for the velocity deficit model, if the wake widths are different, the wake will be elongated in the main direction. For the MFOR velocity model (Eq. 8.3), the isolines and the maximum point are unique. For the MFOR added turbulence, however, two isolines can be found for any value of added turbulence. If the wake is axisymmetric ($\sigma_y = \sigma_z = \sigma$), the maximum added turbulence is located on an isoline that describes a circle of radius σ. If $\sigma_y \neq \sigma_z$, two maxima are found at $(y, z) = (\pm\sigma_y, 0)$ if $\sigma_y > \sigma_z$ or $(y, z) = (0, \pm\sigma_z)$ if $\sigma_y < \sigma_z$.

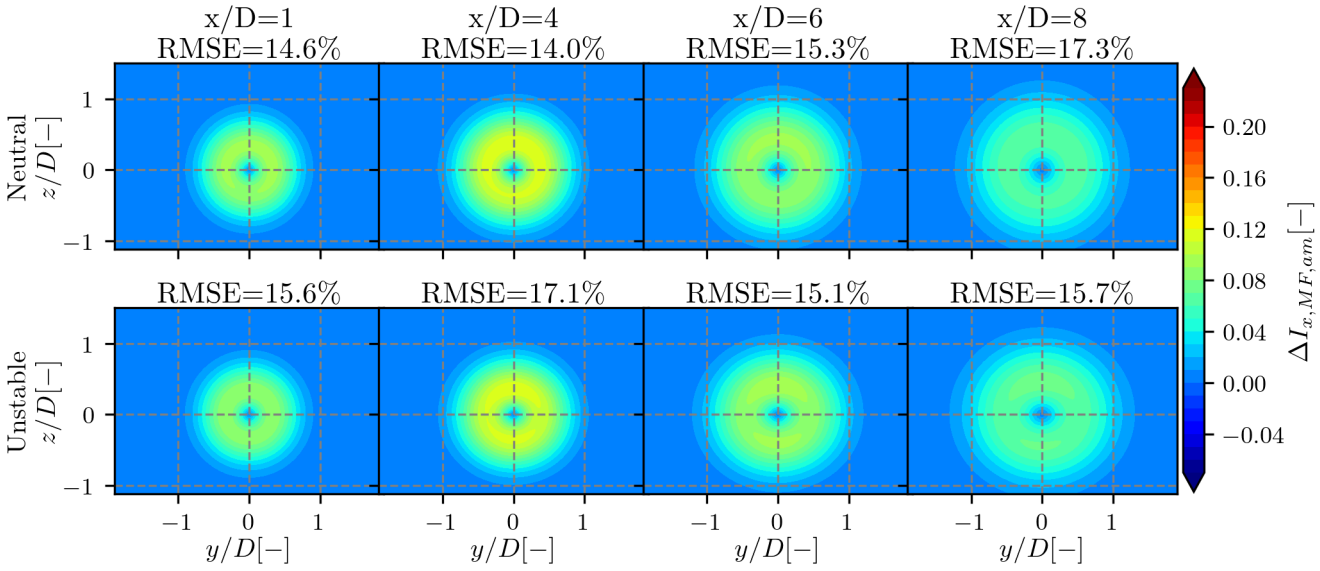

Figure 8.3: Modelled added turbulence in the MFOR. The RMSE is given with respect to the s values in Fig. B.4.

The maps of $\Delta k_{x,MF,am}$, computed with the LES parameters and normalised as the added TI (Eq. 2.11) are plotted in Fig. 8.3 and can be compared with the equivalent maps in Fig B.4. Strong assumptions were made to obtain Eq. 8.10, especially on shear, which led to an almost axisymmetric

turbulence field in the MFOR. Indeed, the only component inducing vertical asymmetry in Eq. 8.10 is $U_\infty(z)^2$. In the neutral case, the ratio between the squared velocity at the top and the bottom tip is $U_\infty^2(z=+D/2)/U_\infty^2(z=-D/2) \approx 1.2$, a fairly low value compared to the LES dataset where for instance, the ratio of added turbulence at $x/D=5$ between these two vertical positions is about 2.

In other words, if the TI was normalised with a vertical profile of $U_\infty(z)$ instead of the hub-height velocity U_h, our model's TI would be axisymmetric. It comes from the wake-generated shear, which is larger at the top tip than at the bottom tip due to the atmospheric shear. The asymmetry of the vertical profile of added turbulence is thus more complex than a simple scaling with the atmospheric shear as it is assumed in the presented model. This issue could be addressed in the future by computing the whole velocity derivative instead of using Eq. 8.9.

Moreover, the error in the near-wake due to the Gaussian shape assumption for velocity deficit in the MFOR propagates onto $\Delta k_{x,MF,am}$, leading to a much weaker but more spread streamwise turbulence. Finally, the model imposes that $\Delta k_{x,MF,am}=0$ at the centre of the wake, a condition that is not verified in the LES dataset (Fig. B.4). A possible improvement would be to add the streamwise gradient $\partial U_x/\partial x$ in Eq. 8.8. Despite these flaws, this expression has been chosen since there exists an analytical solution of its convolution with the wake centre position distribution $f_{c,am}$ and because it gives acceptable results. Note that an empirical correction can be used to correct for the overestimation near the ground [111], but this option has not been retained in the presented work since it aims to build a fully physically-built model.

8.1.3 Wake meandering

For the PDF of wake meandering, the central limit theorem leads to a Gaussian distribution [129]. This has been confirmed by the self-similarity of f_c in the neutral case in Ch. 6, and we assume that if a longer simulation had been run in the unstable case it would also be the case. Consequently, it is decided to model the PDF of the wake centre's distribution as:

$$f_{c,am}(x,y,z) = \frac{1}{2\pi\sigma_{fy}(x)\sigma_{fz}(x)}\exp\left(-\frac{y^2}{2\sigma_{fy}^2(x)}-\frac{z^2}{2\sigma_{fz}^2(x)}\right) \tag{8.11}$$

The distribution of the wake centre f_c is known to be non-axisymmetric ($\sigma_{fy}\neq\sigma_{fz}$) and thus its distribution σ_f is defined in two dimensions. In Fig. 8.4, the 1D PDFs $f_{cy}=1/(\sqrt{2\pi}\sigma_{fy})\exp(-y^2/(2\sigma_{fy}^2))$ and $f_{cz}=1/(\sqrt{2\pi}\sigma_{fz})\exp(-z^2/(2\sigma_{fz}^2))$ are plotted against the histograms of $y_c(t)$ and $z_c(t)$ found in the LESs datasets. The RMSE computed between the 2D histograms and Eq. 8.11 is indicated at each downstream position: the first value corresponds to the neutral case and the second to the unstable case. As expected from the observations of Ch. 6, the results are better converged for the neutral than for the unstable case. Simulations of more than 40 minutes should thus be performed to have a converged meandering distribution for such atmospheric stability and rotor size. For this particular case, we thus assume that the error between the model and LES data comes from the LES.

The RMSE associated to $\Delta U_{MF,am}$, $\Delta k_{x,MF,am}$ and $f_{c,am}$ (respectively Figs 8.1, 8.3 and 8.4) indicate the error induced from the different assumptions. In the FFOR velocity model, only $\Delta U_{MF,am}$ and $f_{c,am}$ will be used so the error will come from the Gaussian shape hypothesis of the velocity deficit in the near wake and the Gaussian distribution of the wake centre in the far wake. For the FFOR

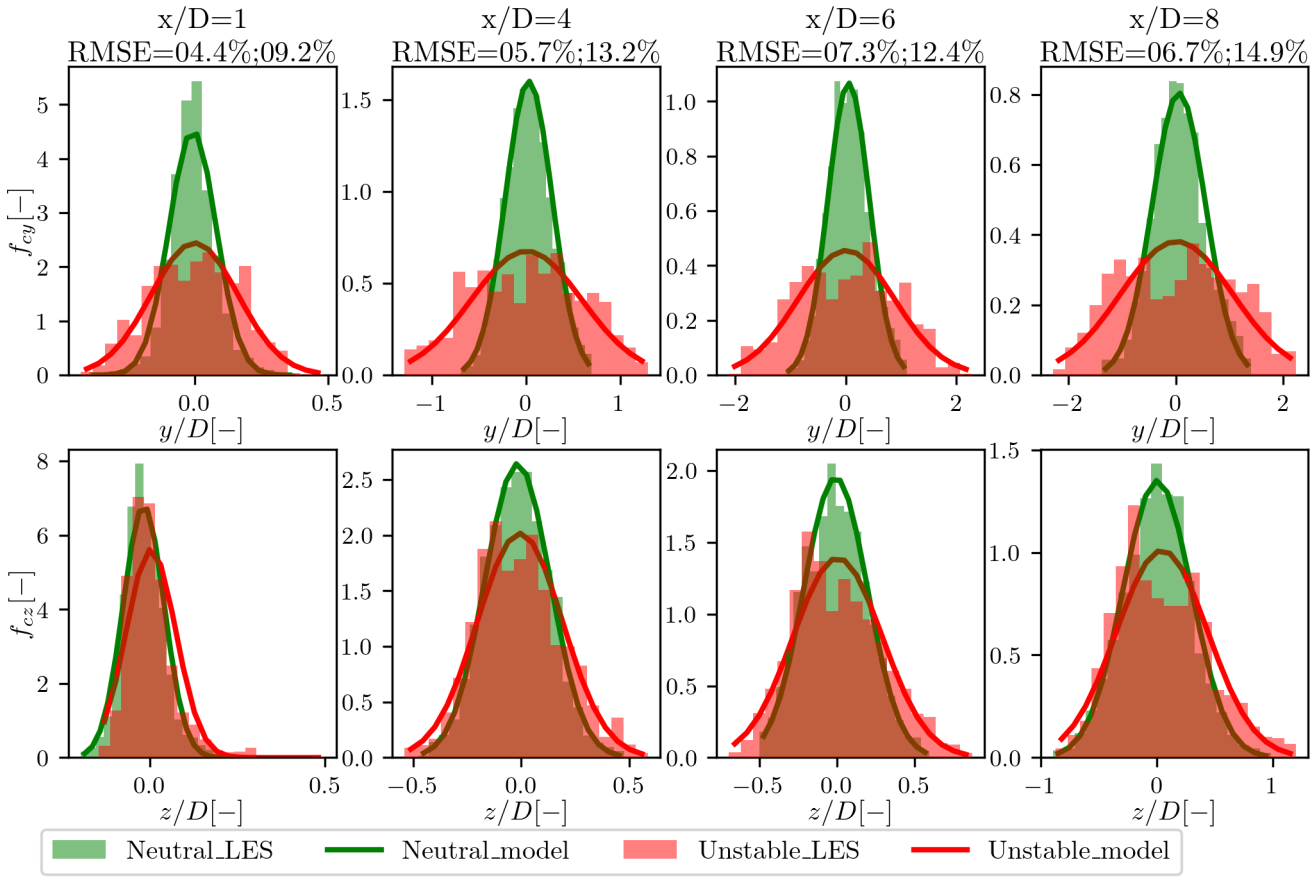

Figure 8.4: Histograms of the wake centre distribution in Meso-NH along with the modelled distributions (solid lines), in the horizontal (top) and vertical (bottom) directions. The RMSE is computed in the YZ plane.

turbulence model that uses the three functions, the error will mainly come from the chosen function of $\Delta k_{a,MF,am}$, in particular for the neutral case, due to the bad accounting of shear.

8.1.4 Parameters of the model

In our model, there are thus five parameters: wake width in the two directions, the standard deviation of wake meandering in the two directions and the mixing length. This number can be brought down to four if the wake in the MFOR is assumed to be axisymmetric ($\sigma_y = \sigma_z$), as it was shown in Ch. 6 for the neutral and unstable cases.

For the model to be operational, one would need to write these five parameters as a function of the relevant inflow and operating conditions, such as hub-height velocity, turbulence intensities, thrust coefficient etc... For instance, the lateral and vertical TI averaged over the rotor-swept area (Eq. 6.2) are a good estimator of σ_{fy} and σ_{fz} (see Sect. 6.1.1). However, in this work the values of the parameters deduced from the LES datasets in Ch. 6 are directly re-used because not enough simulations were available to deduce general relations between parameters and inflow conditions. To do so, a full sensitivity study should be carried on, with different values of ζ, C_T, U_h and I.

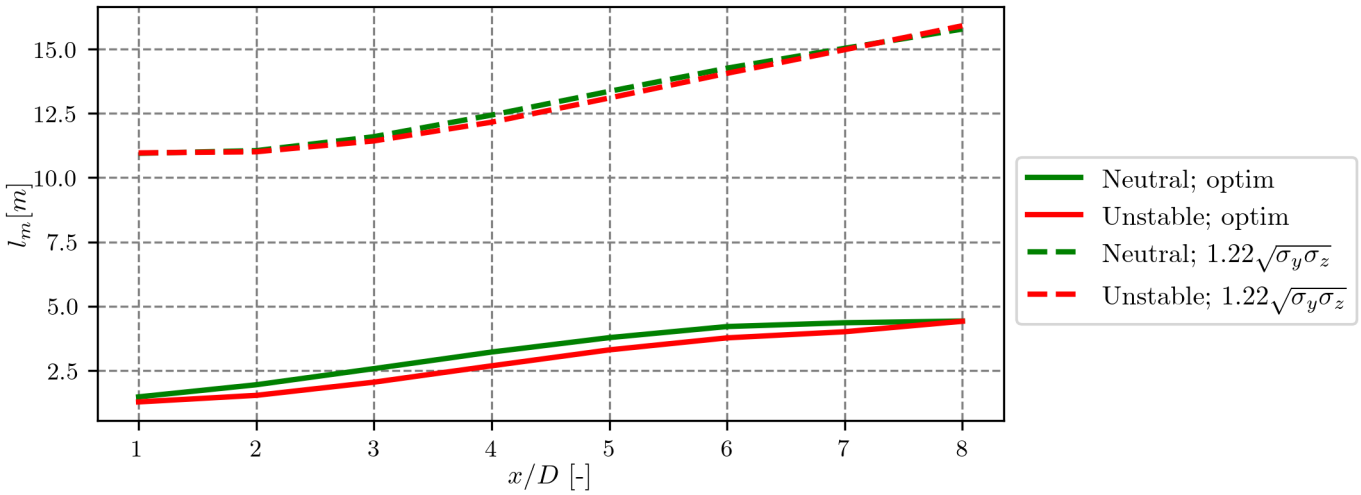

Figure 8.5: Mixing length in the wake.

The mixing length $l_m(x)$ has not been computed in the Ch. 6. In this work, it is imposed so that Eq. 8.10 fits the streamwise turbulence in the MFOR as good as possible. The resulting values are plotted in a continuous line in Fig. 8.5. It shows an approximately linear behaviour between $x/D = 2$ and $x/D = 6$, followed by a break of the slope. It is difficult to conclude for this relatively small range of x but it is reassuring that the shape is similar to [165].

In the DWM, the mixing length is set as half of the wake width, which is defined as the position where $\Delta U = 0.05$ [126]. This corresponds approximately to 2.448σ for a one-dimensional Gaussian function of width σ. By setting the total width of the wake as $\sigma = \sqrt{\sigma_y\sigma_z}$, it leads to:

$$l_m = 1.22\sqrt{\sigma_y\sigma_z} \tag{8.12}$$

The corresponding mixing length is plotted in Fig. 8.5. It leads to a very large overestimation of the optimal value that can be partially attributed to C_μ. Note that the order of magnitude would be similar to the optimised l_m if it was computed as a linear function of the wake growth instead of the wake width:

$$l_m = 1.22\left(\sqrt{\sigma_y\sigma_z} - \epsilon\right). \tag{8.13}$$

However, this would lead to $l_m(x = 0) = 0$ i.e. no turbulence directly behind the turbine, which cannot be considered an acceptable result. These mixing length formulations are thus not used in the present work but could be used in future developments in the model.

8.2 Model for the velocity in the FFOR

In Eq. 7.11, the velocity in the wake is written under its dimensional form whereas the model chosen in Eq. 8.3 is written under the velocity deficit form. To relate the velocity to the velocity deficit, it is needed to assume that despite its dependency on z (due to shear), the upstream velocity U_∞

can be considered as a constant when applying the 2D convolution product with the wake centre distribution. For any function $\phi(y,z)$, this simplification writes:

$$f_{c,am}(y,z) ** [U_\infty(z)\cdot\phi(y,z)] = U_\infty(z)\cdot[f_{c,am}(y,z) ** \phi(y,z)]\,. \tag{8.14}$$

An analytical form of the term (I) can then be deduced from the Eqs. 8.3 and 8.11:

$$\begin{aligned} U_{x,FF,am}(y,z) &= f_{c,am}(y,z) ** [U_\infty(z)\,(1+\Delta U_{FF,am}(y,z))] \\ &= U_\infty(z)\left(1+\int\int \Delta U_{MF,am}(y-y_c,z-z_c)\cdot f_{c,am}(y_c,z_c)dy_c dz_c\right) \\ &= U_\infty(z)\,(1+\Delta U_{FF,am}) \end{aligned} \tag{8.15}$$

The velocity deficit in the FFOR $\Delta U_{FF,am}$ is thus the convolution product of two Gaussian functions. It is known that the convolution product of two normalised Gaussian functions of variance σ_ϕ^2 and σ_ψ^2 is a normalised Gaussian function of variance $\sigma_\phi^2+\sigma_\psi^2$ [166]. Equation 8.15 can be written as the product of two convolution products, leading to:

$$\begin{aligned} \Delta U_{FF,am} &= 2C\pi\sigma_y\sigma_z\Bigg[\int \frac{1}{\sqrt{2\pi}\sigma_y}\exp\left(-\frac{(y-y_c)^2}{2\sigma_y^2}\right)\frac{1}{\sqrt{2\pi}\sigma_{fy}}\exp\left(-\frac{y_c^2}{2\sigma_{fy}^2}\right)dy_c \\ &\qquad \int \frac{1}{\sqrt{2\pi}\sigma_z}\exp\left(-\frac{(z-z_c)^2}{2\sigma_z^2}\right)\frac{1}{\sqrt{2\pi}\sigma_{fz}}\exp\left(-\frac{z_c^2}{2\sigma_{fz}^2}\right)dz_c\Bigg] \\ &= C\sqrt{\frac{\sigma_y^2}{\sigma_y^2+\sigma_{fy}^2}\frac{\sigma_z^2}{\sigma_z^2+\sigma_{fz}^2}}\exp\left(-\frac{y^2}{2\sigma_y^2+2\sigma_{fy}^2}-\frac{z^2}{2\sigma_z^2+2\sigma_{fz}^2}\right) \end{aligned} \tag{8.16}$$

Even though the reasoning of [129] is different, it is here shown that the BS19 (Eq. 2.5.2) can be found by neglecting term (II) and assuming Eq. 8.14 as well as Gaussian shapes for the velocity deficit in the MFOR and the wake centre's distribution. This is still a Gaussian form i.e. Eq. 2.27 with FFOR wake widths defined as $\sigma_{ty,tz}=\sqrt{\sigma_{y,z}^2+\sigma_{fy,fz}^2}$, and a maximum velocity deficit of

$$C_{FF} = C\sqrt{\frac{\sigma_y^2}{\sigma_y^2+\sigma_{fy}^2}\frac{\sigma_z^2}{\sigma_z^2+\sigma_{fz}^2}}. \tag{8.17}$$

To fulfil the conservation of momentum as in Eq. 2.28, one would need:

$$C_{FF} = 1-\sqrt{1-C_T/(8\sigma_{ty}\sigma_{tz}/D^2)} \tag{8.18}$$

and the model would then be equivalent to the XA14 model with wake widths σ_{ty} and σ_{ty}. Actually, with our methodology, the conservation of momentum can only be enforced in the MFOR or in the FFOR. This is the consequence of neglecting the term (II) in the velocity breakdown. The results

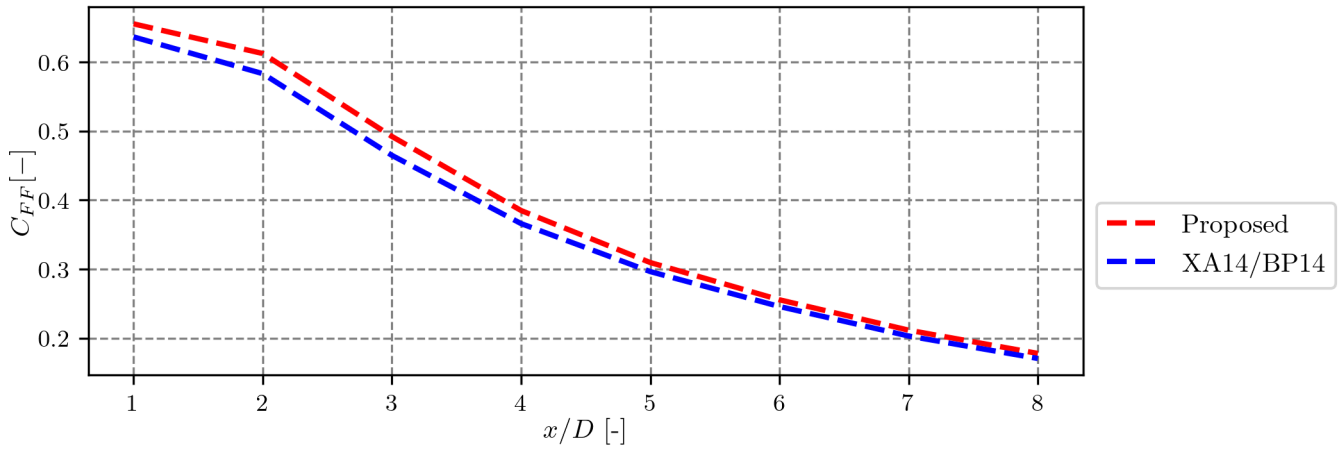

Figure 8.6: Maximum velocity deficit predicted with the model in red (Eq. 8.17) and fulfilling the momentum conservation in blue (Eq. 8.18).

of Eqs. 8.17 and 8.18 are plotted in Fig. 8.6 for the neutral case. The difference between both formulations is low, which is consistent with the fact that term (II) is overall negligible, so Eq. 8.17 is kept for this work.

Combining Eqs. 8.15 and 8.16 leads to our model for the velocity in the wake of a wind turbine:

$$U_{x,FF,am}(y,z) = U_\infty(z)\left(1 + C\sqrt{\frac{\sigma_y^2}{\sigma_y^2+\sigma_{fy}^2}\frac{\sigma_z^2}{\sigma_z^2+\sigma_{fz}^2}}\exp\left(-\frac{y^2}{2\sigma_y^2+2\sigma_{fy}^2}-\frac{z^2}{2\sigma_z^2+2\sigma_{fz}^2}\right)\right) \quad (8.19)$$

The resulting horizontal (top) and vertical (bottom) velocity profiles computed with the LESs parameters are plotted in Figs. 8.7 and 8.8 for the neutral and unstable cases, respectively. On the same figures are also plotted the velocity profiles in the FFOR in Meso-NH and the velocity profiles of the term (I) computed in Meso-NH, which is the only term modelled in the velocity breakdown equation. Despite the error in the near wake, the shapes are well-reproduced as soon as the wake takes an actual Gaussian shape. In the neutral case, the fit is good, except near the ground, where the assumption on shear (Eq. 8.14) might be too constraining. The overestimation of the velocity deficit in the FFOR, already observed in Fig. 6.7 is confirmed here. The results are however overall good and confirm that the hypotheses made in Sect. 8.1 for the velocity in the MFOR and the wake centre distribution are reasonable.

In the unstable case (Fig. 8.8), the results are still fine but some discrepancies are observed with the reference data. As pointed out in Sect. 8.1, the error on $f_{c,am}$ is larger in the unstable case than in the neutral case, supposedly because the unstable simulation has not run for long enough. Moreover, the tracking might not have been as good as in the neutral case: if all the meandering motions have not been detected by the tracking algorithm, the computed σ_{fz} is underestimated, explaining why the Gaussian shape is more pronounced in the model than in the reference data. Finally, the term (II) takes larger relative values in this case, explaining the larger gap between the blue and black curves in Fig. 8.8 compared to Fig. 8.7. Since the analytical model is a model of the term (I) i.e. the blue curve, it increases the potential error compared to the actual velocity field in the FFOR (black curve).

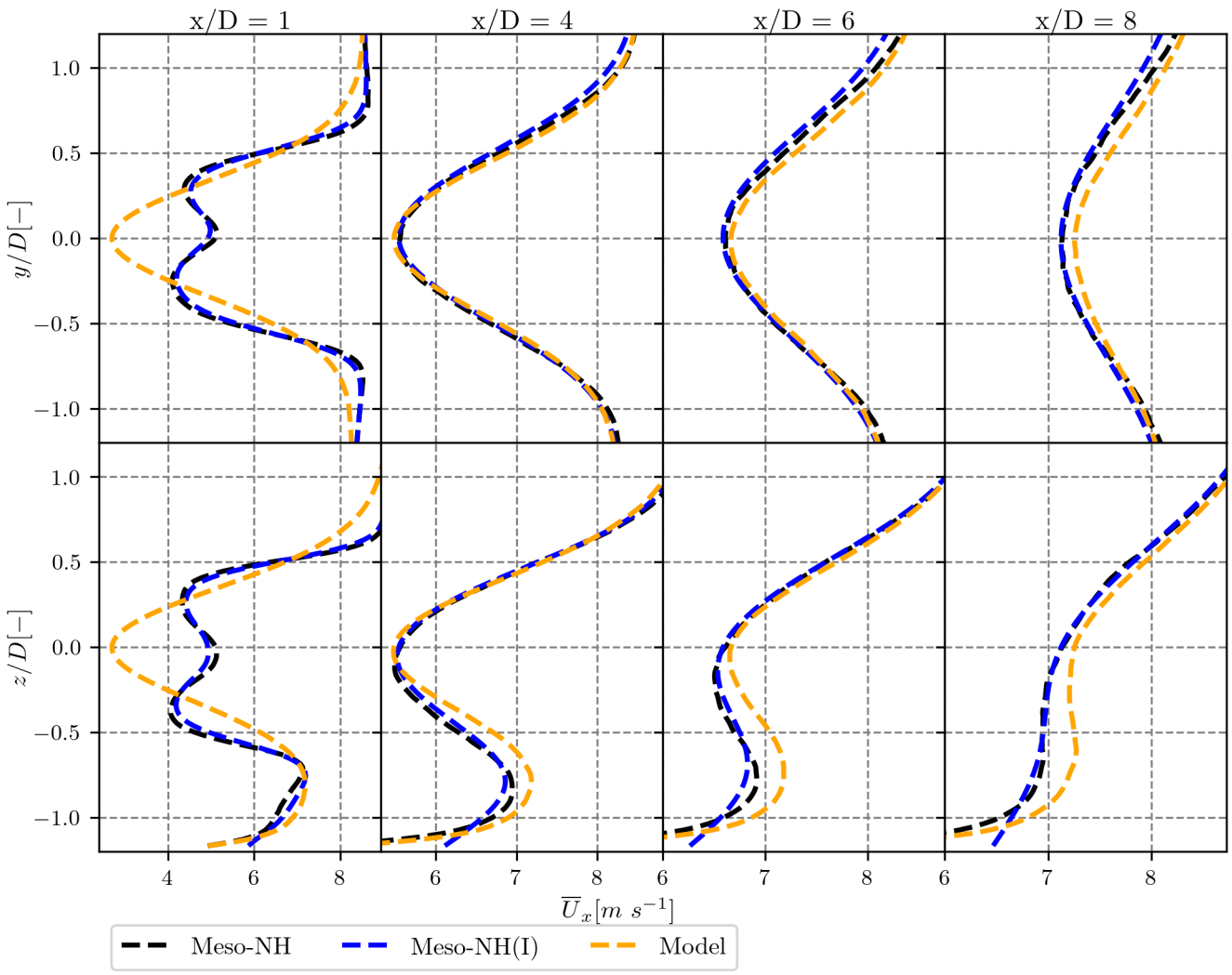

Figure 8.7: Results of the analytical velocity model (orange) in the neutral case, compared to the modelled term in Meso-NH (blue) and the total velocity in the FFOR (black) for the neutral case. Lateral (top) and vertical (bottom) profiles are plotted for different positions downstream.

8.3 Model for the turbulence in the FFOR

For the turbulence, a model is found only for terms (III) (Eq. 8.21) and Δ(IV) (Eq. 8.25). Even though the contribution of the three cross-terms of Eq. 7.14 is not negligible, the two modelled terms are the main contributions and the result of the model can be compared to the turbulence in the FFOR. The total modelled turbulence is here computed as:

$$k_{x,am} = k_\infty + k_{x,m,am} + \Delta k_{x,a,am}. \tag{8.20}$$

where k_∞ is taken directly 2.5 D upstream of the turbine in the LESs datasets.

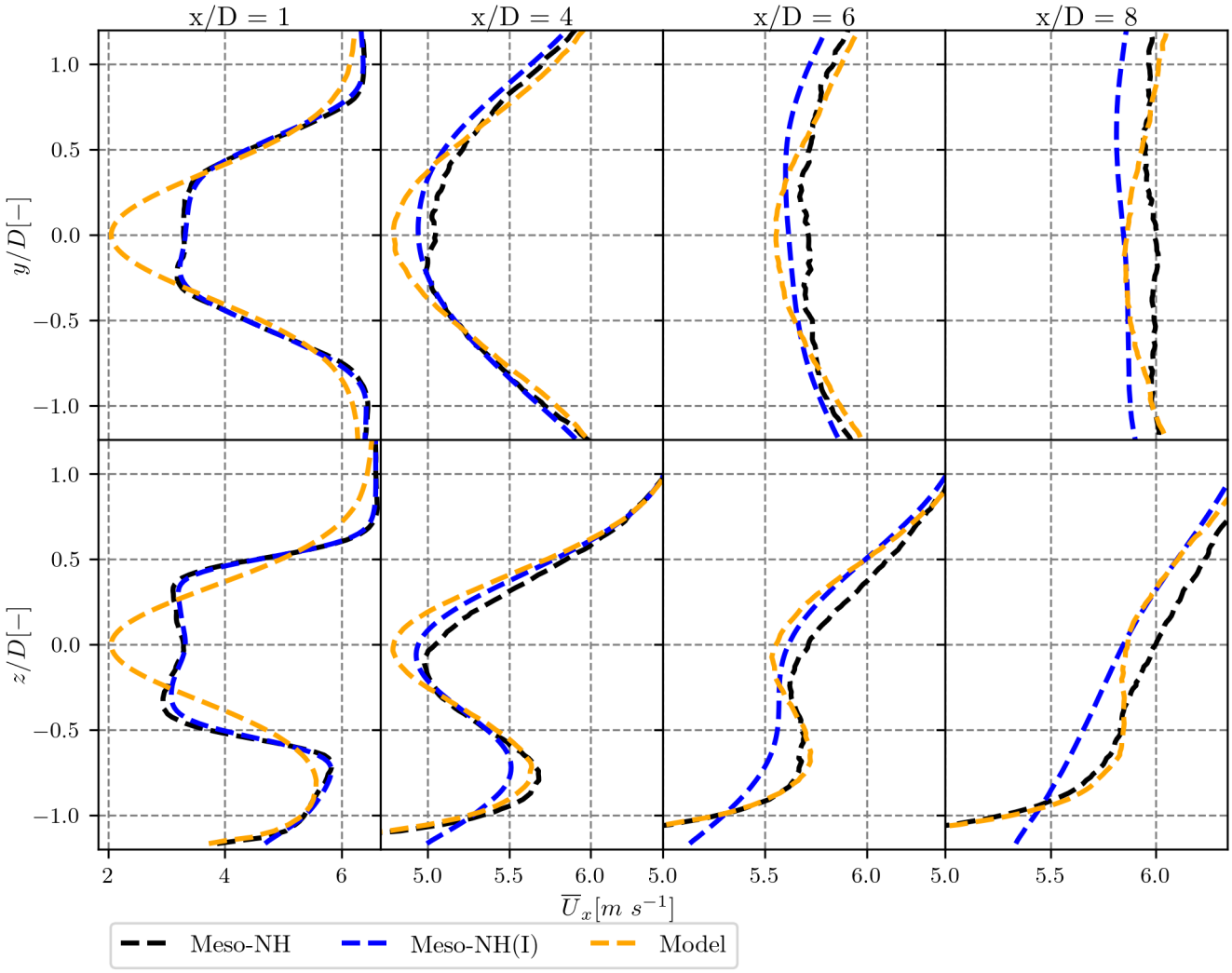

Figure 8.8: Results of the analytical velocity model (orange) in the unstable case, compared to the modelled term in Meso-NH (blue) and the total velocity in the FFOR (black) for the unstable case. Lateral (top) and vertical (bottom) profiles are plotted for different positions downstream.

8.3.1 Meandering term

With the same assumptions as for the term (I), it is possible to derive an analytical formulation for the term (III) of Eq. 7.14 i.e. the turbulence induced by meandering. For reference, this meandering turbulence field computed with the two LESs datasets is plotted in Fig. 8.9 under its turbulence intensity value (see Eq. 2.11).

To find an analytical form of the term (III), the assumption defined by Eq. 8.14 must again be used to get U_∞^2 out of the convolution product and Eq. 8.16 is re-used to compute the right-hand side of term (III): $\widehat{\overline{U_{MF}}}^2$. On the left-hand side, there is a convolution of the Gaussian function $f_{c,am}$ with $\Delta U^2_{MF,am}$, which is also a Gaussian function of widths $\sqrt{0.5}\sigma_y$ and $\sqrt{0.5}\sigma_z$. It is thus possible to use the property that the convolution of two Gaussian functions is a Gaussian function [166].

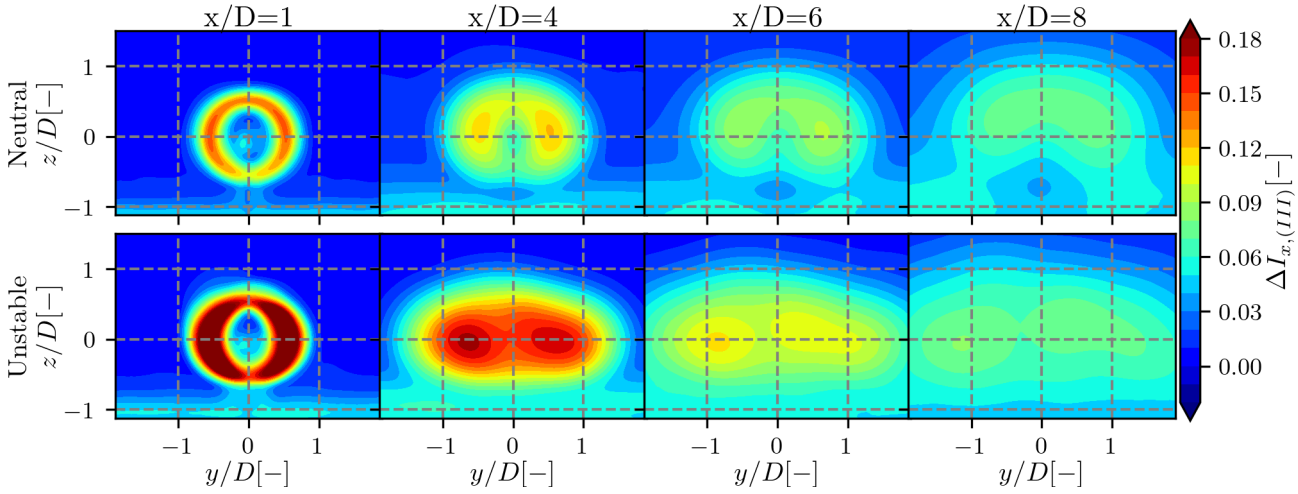

Figure 8.9: Meso-NH values of $k_{x,m}$ i.e. the term (III) for the neutral and unstable cases.

$$
\begin{aligned}
k_{x,m,am}(y,z) =& \left[f_{c,am} ** U^2_{x,MF,am}\right] - U^2_{x,FF,am} \\
=& U^2_\infty(z) \int\int \left(1 + \Delta U_{MF,am}(y - y_c, z - z_c)\right)^2 f_{c,am}(y_c, z_c) dy_c dz_c \\
& - U^2_\infty(z) \left(1 + \Delta U_{FF,am}\right)^2 \\
=& U^2_\infty(z) \int\int \Delta U^2_{MF,am}(y - y_c, z - z_c) f_{c,am}(y_c, z_c) dy_c dz_c - U^2_\infty(z) \Delta U^2_{FF,am} \\
=& (C U_\infty(z))^2 \left[\sqrt{\frac{\sigma_y^2}{\sigma_y^2 + 2\sigma_{fy}^2}} \sqrt{\frac{\sigma_z^2}{\sigma_z^2 + 2\sigma_{fz}^2}} \exp\left(-\frac{y^2}{\sigma_y^2 + 2\sigma_{fy}^2} - \frac{z^2}{\sigma_z^2 + 2\sigma_{fz}^2} \right) \right. \\
& \left. - \frac{\sigma_y^2}{\sigma_y^2 + \sigma_{fy}^2} \frac{\sigma_z^2}{\sigma_z^2 + \sigma_{fz}^2} \exp\left(-\frac{y^2}{\sigma_y^2 + \sigma_{fy}^2} - \frac{z^2}{\sigma_z^2 + \sigma_{fz}^2} \right) \right]
\end{aligned}
\tag{8.21}
$$

The shape of the term (III)$= k_{x,m,am}$ is thus not a double Gaussian, as one could interpret from Fig. 8.9, but rather a Gaussian function of width $\sqrt{0.5\sigma^2 + \sigma_f^2}$ minus a less pronounced Gaussian of thinner width $\sqrt{0.5\sigma^2 + 0.5\sigma_f^2}$. It can be verified that this expression is always larger than 0 i.e. the meandering only produces turbulence and does not dissipate it. The results of this model with the LESs values of the parameters are plotted in Fig. 8.10 at four positions downstream. To quantify the error induced by the model, the RMSE is computed between the model and the term (III) in the LESs datasets (Fig. 8.9). The results are overall promising: the shape and order of magnitude are respected for both cases. The increased error in the near and far wake is the direct consequence of the error made by the model on the term (I) and on the meandering estimation (see the two previous sections).

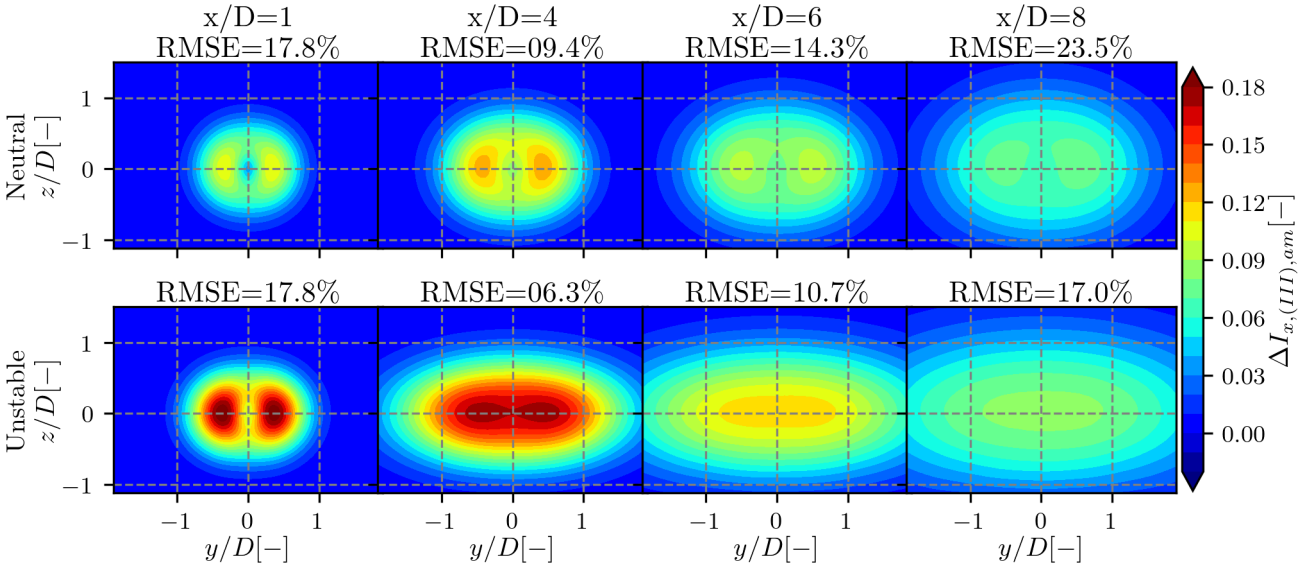

Figure 8.10: Results of $k_{x,m,am}$ i.e. the model for the term (III) for the neutral and unstable cases. The RMSE is given with respect to the term (III) computed from Meso-NH (Fig. 8.9).

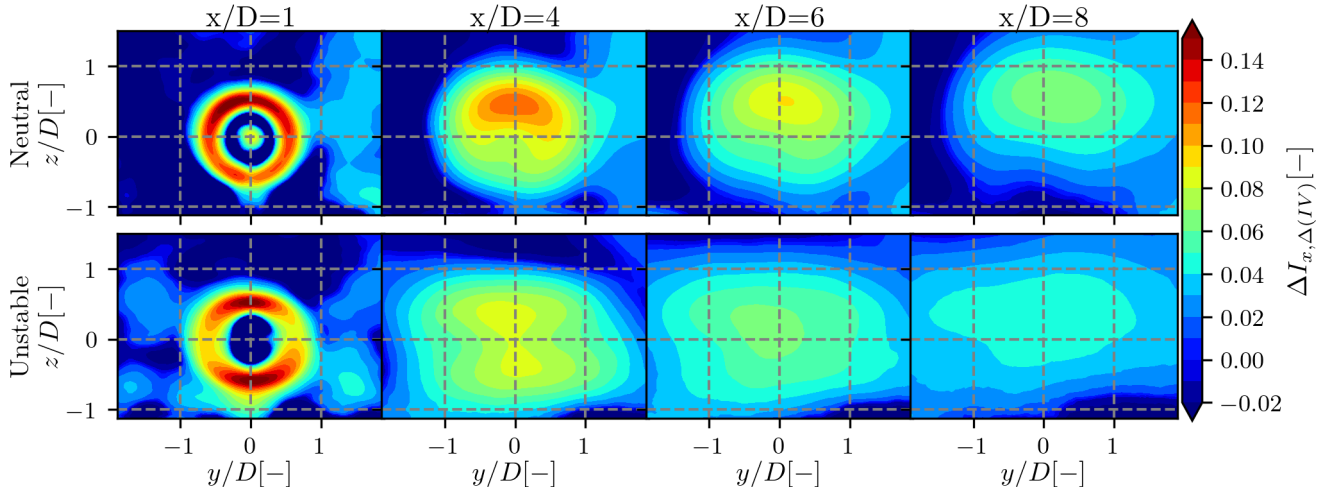

Figure 8.11: Results of the LESs datasets for term $\Delta k_{x,a}$ i.e. Δ(IV) for the neutral and unstable cases.

8.3.2 Rotor-added turbulence term

The term (IV) of Eq. 7.14, also written k_a for 'rotor-added turbulence', is simply the 2D convolution of k_{MF} with f_c. However, it has been chosen to model $\Delta k_{x,MF,am} = k_{x,MF,am} - k_{x,ref}$ instead of directly $k_{x,MF,am}$ because it is easier to interpret and model. Similarly to the unperturbed velocity, the reference turbulence is not modelled, so it is assumed that $\widehat{k_\infty(z)} = k_\infty(z)$ despite the dependency of k_∞ on z. In term of added turbulence, it thus writes :

$$\Delta(\mathrm{IV}) = \Delta k_{x,a,am} = \overline{\widehat{\Delta k_{x,MF,am}}} \tag{8.22}$$

The LES values of $\Delta(\mathrm{IV})$ are plotted in Fig. 8.11 under its turbulence intensity form. Applying the assumed shape for the added turbulence in the MFOR in Eq. 8.10 leads to an analytical form of the streamwise rotor-added turbulence:

$$\begin{aligned}
\Delta k_{x,a,am} &= \Delta k_{x,MF,am} * * f_{c,am} \\
&= \frac{K_{MF}}{2\pi\sigma_{fy}\sigma_{fz}} \int\int \left[\left(\frac{y_c}{\sigma_y^2}\right)^2 + \left(\frac{z_c}{\sigma_z^2}\right)^2 \right] \exp\left(-\frac{y_c^2}{\sigma_y^2} - \frac{z_c^2}{\sigma_z^2}\right) \exp\left(-\frac{(y-y_c)^2}{2\sigma_{fy}^2} - \frac{(z-z_c)^2}{2\sigma_{fz}^2}\right) dy_c dz_c \\
&= \frac{K_{MF}}{2\pi\sigma_{fy}\sigma_{fz}} \left[\int \left(\frac{y_c}{\sigma_y^2}\right)^2 \exp\left(-\frac{y_c^2}{\sigma_y^2} - \frac{(y-y_c)^2}{2\sigma_{fy}^2}\right) dy_c \int \exp\left(-\frac{z_c^2}{\sigma_z^2} - \frac{(z-z_c)^2}{2\sigma_{fz}^2}\right) dz_c \right. \\
&\qquad \left. + \int \left(\frac{z_c}{\sigma_z^2}\right)^2 \exp\left(-\frac{z_c^2}{\sigma_z^2} - \frac{(z-z_c)^2}{2\sigma_{fz}^2}\right) dz_c \int \exp\left(-\frac{y_c^2}{\sigma_y^2} - \frac{(y-y_c)^2}{2\sigma_{fy}^2}\right) dy_c \right]
\end{aligned} \tag{8.23}$$

At this point, the added turbulence in the FFOR is the sum of two terms, that are identical if the coordinates y and z are swapped: solving one of these terms makes the solution for the other trivial. It is the product of two convolutions: the first of $f : y \to y^2 \exp(-y^2/\sigma_y^2)$ with a Gaussian function and the second of two Gaussian functions. The first convolution product has been solved with a computer algebra tool [167] and the other has already been solved in Eq. 8.21. It gives:

$$\begin{aligned}
&\int \left(\frac{y_c}{\sigma_y^2}\right)^2 \exp\left(-\frac{y_c^2}{\sigma_y^2} - \frac{(y-y_c)^2}{2\sigma_{fy}^2}\right) dy_c \int \exp\left(-\frac{z_c^2}{\sigma_z^2} - \frac{(z-z_c)^2}{2\sigma_{fz}^2}\right) dz_c \\
=&\frac{\sqrt{2\pi}\sigma_{fy}(\sigma_y^2 y^2 + \sigma_{fy}^2\sigma_y^2 + 2\sigma_{fy}^4)}{\sigma_y(\sigma_y^2 + 2\sigma_{fy}^2)^{5/2}} \exp\left(-\frac{y^2}{\sigma_y^2 + \sigma_{fy}^2}\right) \frac{\sqrt{2\pi}\sigma_{fz}\sigma_z}{\sqrt{\sigma_z^2 + 2\sigma_{fz}^2}} \exp\left(-\frac{z^2}{\sigma_z^2 + 2\sigma_{fz}^2}\right) \\
=&2\pi\sigma_{fy}\sigma_{fz} \frac{\sigma_y\sigma_z}{\sqrt{\sigma_y^2 + 2\sigma_{fy}^2}\sqrt{\sigma_z^2 + 2\sigma_{fz}^2}} \frac{(\sigma_y^2 y^2 + \sigma_{fy}^2\sigma_y^2 + 2\sigma_{fy}^4)}{\sigma_y^2(\sigma_y^2 + 2\sigma_{fy}^2)^2} \exp\left(-\frac{y^2}{\sigma_y^2 + \sigma_{fy}^2} - \frac{z^2}{\sigma_z^2 + 2\sigma_{fz}^2}\right)
\end{aligned} \tag{8.24}$$

From Eq. 8.24, it remains to add the same quantity with $y \leftarrow z$ and $z \leftarrow y$, factorise and simplify to deduce the model for $\Delta k_{x,a}$:

$$\Delta k_{x,a,am} = K_{FF} \left(\frac{y^2\sigma_y^2 + \sigma_y^2\sigma_{fy}^2 + 2\sigma_{fy}^4}{\sigma_y^2(\sigma_y^2 + 2\sigma_{fy}^2)^2} + \frac{z^2\sigma_z^2 + \sigma_z^2\sigma_{fz}^2 + 2\sigma_{fz}^4}{\sigma_z^2(\sigma_z^2 + 2\sigma_{fz}^2)^2} \right) \exp\left(-\frac{y^2}{\sigma_y^2 + 2\sigma_{fy}^2} - \frac{z^2}{\sigma_z^2 + 2\sigma_{fz}^2}\right) \tag{8.25}$$

with:

$$K_{FF} = \frac{K_{MF}}{\sqrt{1+2(\sigma_{fy}/\sigma_y)^2}\sqrt{1+2(\sigma_{fz}/\sigma_z)^2}}. \tag{8.26}$$

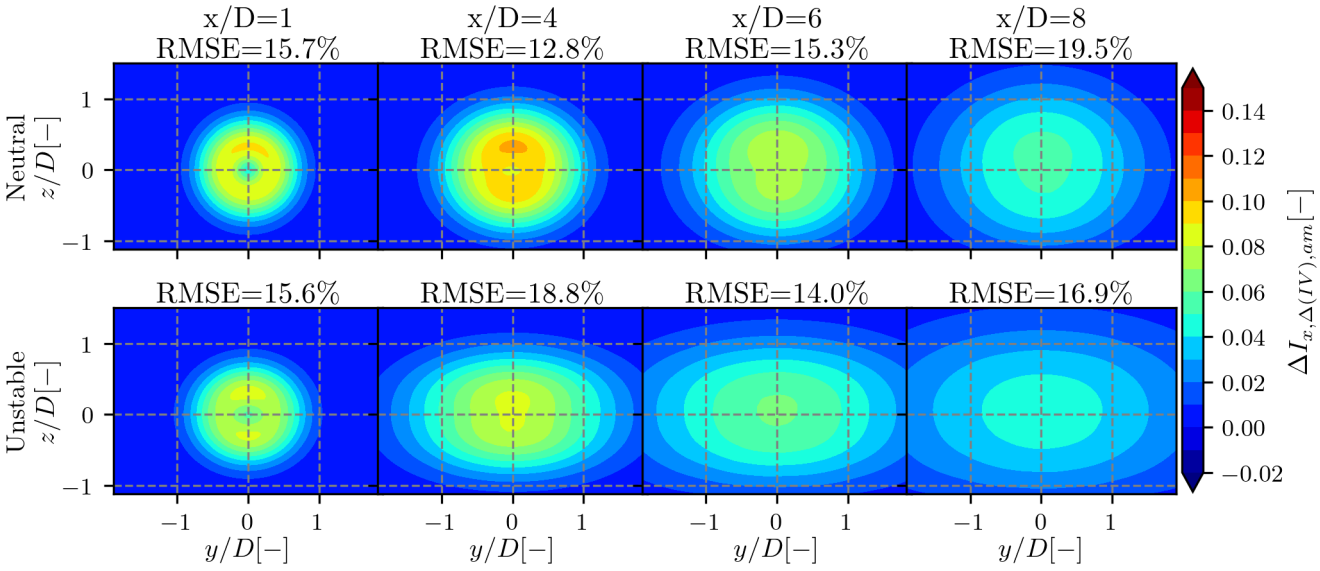

Figure 8.12: Results of $\Delta k_{x,a,am}$ i.e. the model for term Δ(IV) for the neutral and unstable cases. The RMSE is given with respect to the term $\Delta k_{x,a}$ computed from Meso-NH (Fig. 8.11).

It can be noted that in absence of meandering, i.e. for $\sigma_f = 0$, the model retrieves its MFOR form (Eq. 8.10). The result of Eq. 8.25 is plotted in Fig. 8.12 at four positions downstream in the neutral and unstable cases, and the RMSE is given with respect to the LESs results for term Δk_a (Fig. 8.11). As for the term (I) and (III), the expression of $k_{a,am}$ is based on a Gaussian velocity deficit hypothesis, even in the near wake where the LES wake is closer to a top-hat function. The velocity gradient that is the source of the rotor-added turbulence is thus lower and more spread in the model compared to the actual values. Another issue of the model is that it poorly takes into account shear, due to the assumptions of Eqs. 8.9 and 8.14. Indeed, the only source of vertical asymmetry in Eq. 8.25 is U_∞^2, i.e. the velocity shear upstream of the turbine. In the neutral case, it leads to a model that is less asymmetric than what is observed in the MFOR in Meso-NH (Fig. B.4), and this error propagates in the FFOR. In the unstable case, this issue is less marked due to weaker atmospheric shear.

8.3.3 Functional analysis

The two equations used to model the meandering and rotor-added turbulence terms do not have a trivial form as the Gaussian shape of the velocity deficit. The corresponding shape functions for an axisymmetric wake ($\sigma_y = \sigma_z$ and $\sigma_{fy} = \sigma_{fz}$) are plotted at hub height in Fig. 8.13 for different values of σ_{fy}/σ_y.

When the meandering is negligible, the meandering-induced turbulence is negligible and the added turbulence takes a bimodal shape. As the amount of meandering increases, the meandering turbulence increases, the maximum rotor-added turbulence decreases, and both phenomena are modified from a bimodal to a unimodal shape. For $\sigma_{fy} >> \sigma_y$, both terms are spread, reaching an almost constant shape over the studied range. Note that the vertical axes of both figures are not in the same unit and consequently cannot be compared in absence of a value for the mixing length l_m.

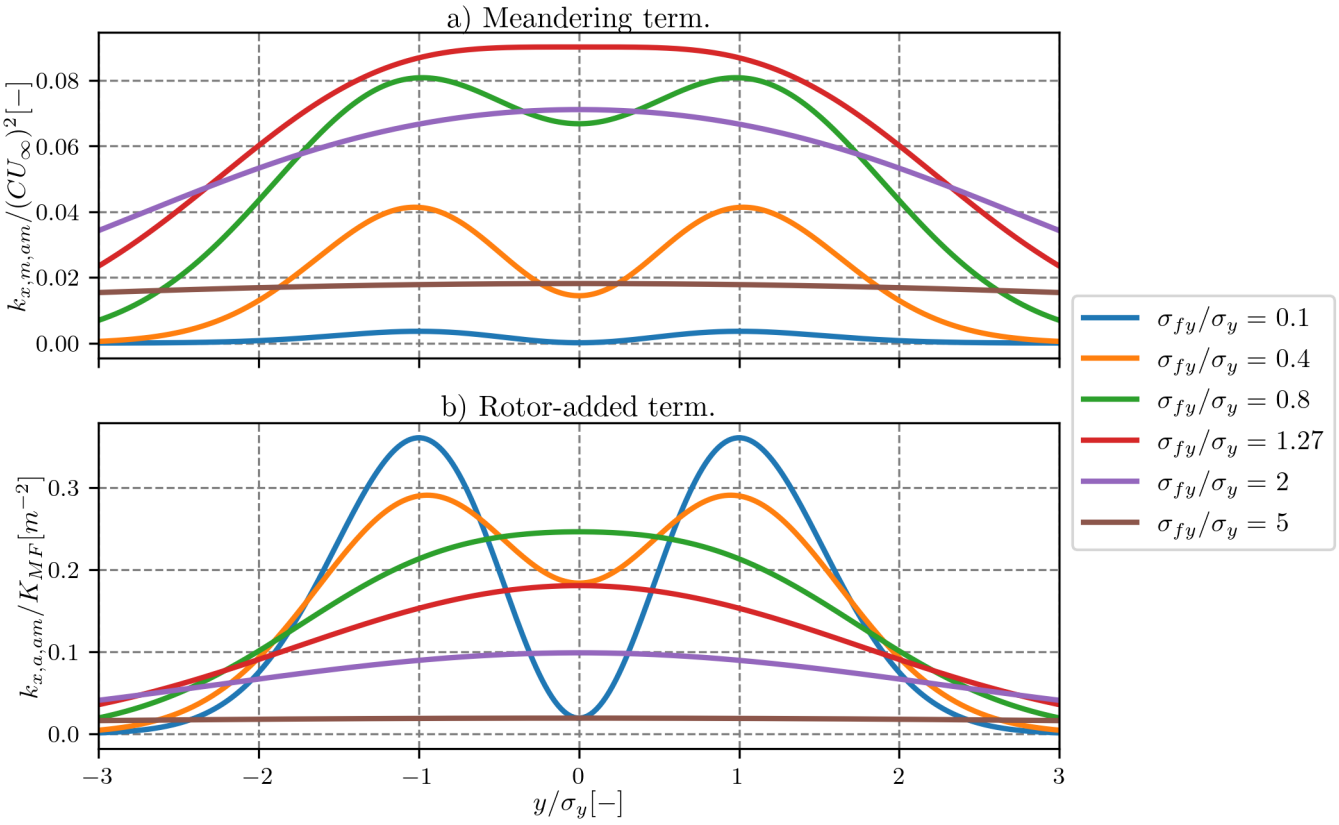

Figure 8.13: Shape functions of the meandering and rotor-added turbulence terms depending on the ratio σ_{fy}/σ_y.

The maximum value (across all σ_{fy}/σ_y) of the meandering-induced turbulence is located at the centre of the wake. Computing Eq. 8.21 at $(y, z) = (0, 0)$ for $\sigma_y = \sigma_z$ and $\sigma_{fy} = \sigma_{fz}$ leads to the following function:

$$\frac{\sigma_{fy}}{\sigma_y} \rightarrow \frac{1}{1 + 2\left(\frac{\sigma_{fy}}{\sigma_y}\right)^2} - \left(\frac{1}{1 + \left(\frac{\sigma_{fy}}{\sigma_y}\right)^2}\right)^2 \tag{8.27}$$

This function takes its maximum for $\sigma_{fy}/\sigma_y = \sqrt{0.5\left(1 + \sqrt{5}\right)} \approx 1.27$. It corresponds to the point where this term takes a unimodal shape and is plotted in a red curve in Fig. 8.13. For this position, it takes the value:

$$\max\left(\Delta k_{x,m,am}/(CU_\infty)^2\right) \approx 0.09 \tag{8.28}$$

The maximum value of the rotor-added turbulence is reached if $\sigma_f = 0$, i.e. if there is no meandering. In such a case, it takes the same value as the MFOR model (Eq. 8.10). As explained in Sect. 8.1.2, if the wake is axisymmetric, the maximum value is located on an isoline that describes a circle of radius $\sigma = \sigma_y = \sigma_z$ around the wake centre. If the wake is not axisymmetric, it takes its maximum value at $(\pm\sigma_y, 0)$ if $\sigma_y > \sigma_z$ or $(0, \pm\sigma_z)$ if $\sigma_y < \sigma_z$. In any case, the maximum value reached at this position is:

$$\max(\Delta k_{x,a,am}/K_{MF}) = \frac{1}{\max(\sigma_y;\sigma_z)^2} e^{-1} \text{ m}^{-2}. \tag{8.29}$$

8.3.4 Results of the model for turbulence

With the same plotting convention as in Figs. 8.7 and 8.8, the profiles of turbulence in the horizontal and vertical directions are plotted in Figs. 8.14 and 8.15 for the neutral and unstable cases, respectively.

As it was noted in Sects. 8.3.1 and 8.3.2, the error on the near-wake velocity model due to the Gaussian shape assumption propagates on the turbulence model. More realistic shapes (double or super-Gaussian) that show larger wake-generated shear in the near wake would result in higher and more localised meandering and rotor-added turbulence, as in the Meso-NH profiles. After $x/D = 4$ i.e. when the Gaussian velocity shape is reached, the results of the model in both cases are much better, in particular in the horizontal direction: the order of magnitude is respected and the positions of maxima are correct. In the neutral case, where a double peak shape is still distinguishable at these positions, the minimum turbulence located at $y = 0$ is slightly overestimated.

The vertical profiles (bottom lines of Figs. 8.14 and 8.15) show less good results. In the neutral case in particular, the maxima of the double Gaussian shape are located near $z/D \pm 0.3$ instead of the tip positions $z/D \pm 0.5$ as seen in the LESs data. Moreover, the turbulence is overestimated in the bottom part of the wake and underestimated in the top part. This is the combination of two different issues. On one hand, the terms (V) and (VI) from Eq. 7.14 are not modelled yet and it has been shown in Ch. 7 that these terms (in particular the term (V)) redistribute the TKE from the bottom to the top of the wake. The error due to this first approximation is represented by the difference between the blue and black curves. On the other hand, the shear in the model is only accounted for through U_∞^2 in factor of $k_{m,am}$ and $k_{a,am}$. This small contribution is compensated by the upstream turbulence k_∞ that is larger at the bottom than at the top, leading to almost symmetric vertical profiles for the model profiles whereas the LES profiles, even when neglecting the cross-terms, have much stronger asymmetry. The error due to this second approximation is represented by the difference between the orange and blue curves.

In the unstable case, the results of the model are surprisingly better than the Meso-NH approximation of (III)+(IV) near the ground. One can note that this was already the case for the velocity model (Figs. 8.7 and 8.8). A possible explanation would be that in the unstable case, the meandering standard deviation σ_f becomes larger than the wake width in the MFOR σ (see Fig. 8.5), and that both $k_{m,am}$ and $k_{a,am}$ tends toward a Gaussian shape in these conditions. Consequently, and despite

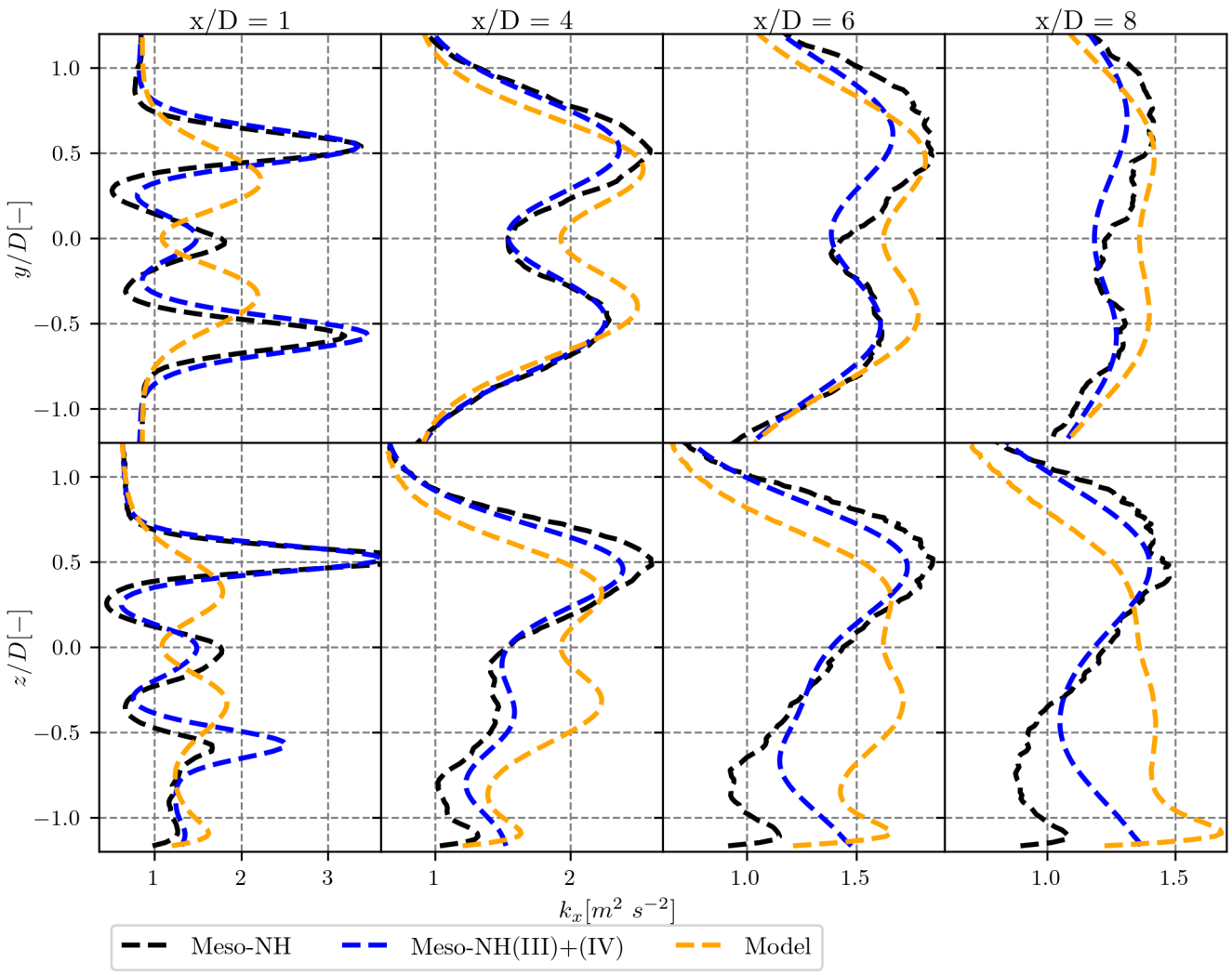

Figure 8.14: Results of the streamwise turbulence analytical velocity model (orange) in the neutral case, compared to the modelled terms in Meso-NH (blue) and the total turbulence in the FFOR (black). Lateral (top) and vertical (bottom) profiles are plotted for different positions downstream.

the error induced by neglecting terms (V) and (VI), it is not surprising to find a vaguely Gaussian function in the modelled unstable case, which happens to be the actual shape of the turbulence field. Moreover, the models for velocity deficit as for turbulence, impose that the flowfield goes back to the unperturbed value far from the wake, which is observed in the reference data (in black) but not necessarily in the computed terms (III)+(IV) which are subject to numerical limitations (see Sect. 7.2.2).

Conclusions

This work aimed at modelling the velocity and turbulence in the wake of a wind turbine based on the meandering phenomenon. The originality is that it allows calibrating independently the effects of meandering and the wake expansion and that it provides an analytical solution for the whole

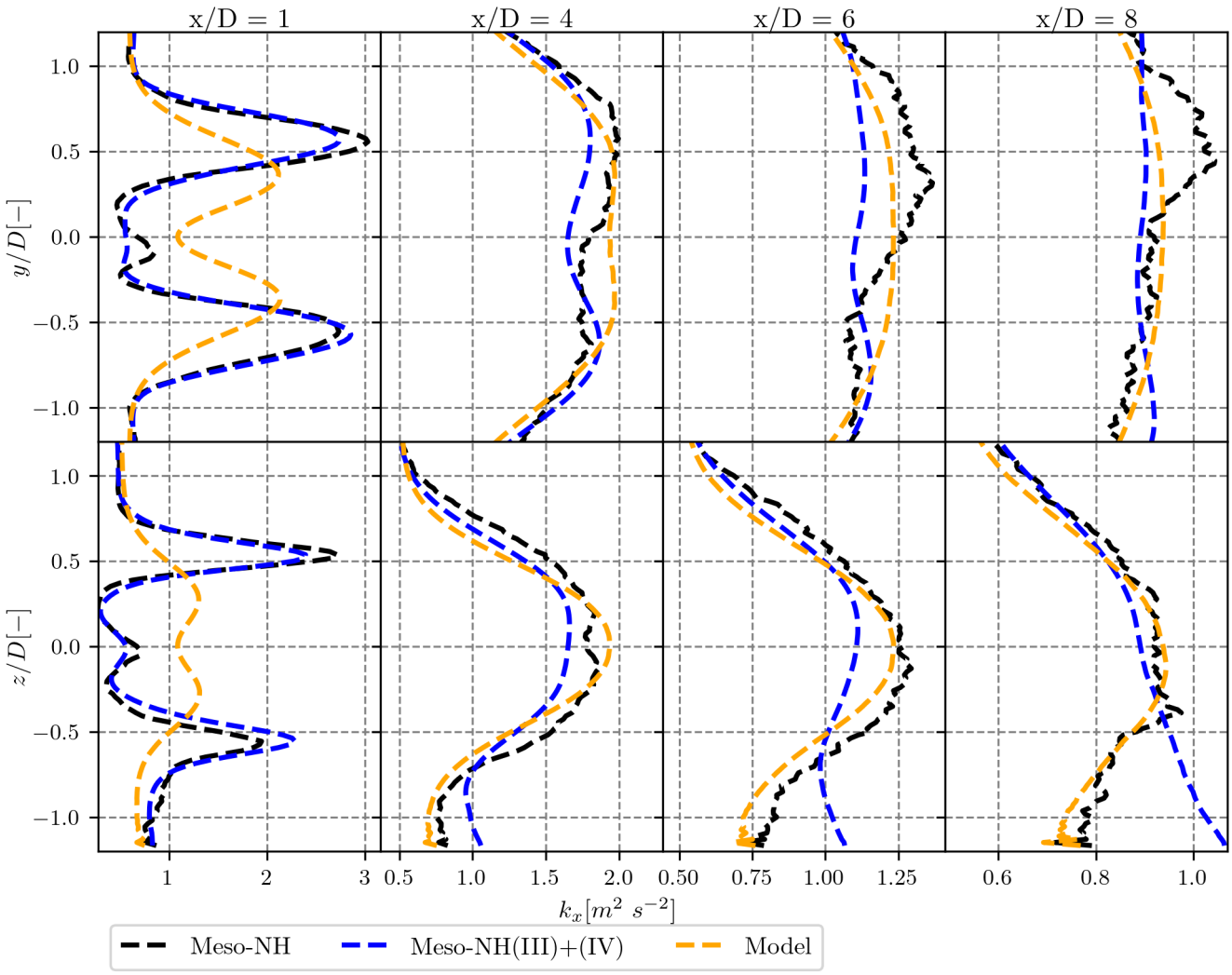

Figure 8.15: Results of the streamwise turbulence analytical velocity model (orange) in the unstable case, compared to the modelled terms in Meso-NH (blue) and the total turbulence in the FFOR (black). Lateral (top) and vertical (bottom) profiles are plotted for different positions downstream.

turbulence profile rather than only the maximum value. The model has been tested on two LESs datasets that simulated a single wind turbine wake under a neutral and an unstable atmosphere. For the velocity, the results are good, either in the vertical or lateral direction. The horizontal turbulence profiles are also satisfying but in the vertical direction, due to the neglected terms and simplistic treatment of shear, the model overestimates turbulence at the bottom of the wake and underestimates it at the top.

This is the first step toward a fully analytical and physically-based model for turbulence and velocity in the wake of a wind turbine that takes into account meandering independently of wake expansion. For future works, it would be interesting to derive an analytical model for the other terms of turbulence breakdown. The treatment of shear must be improved to model more realistic vertical turbulence profiles. The added turbulence in the MFOR could also be improved by taking into account the velocity gradient in the streamwise direction $\partial U_x/\partial x$. For the model to be complete, an expression for every term of the Reynolds-stress tensor (or at least the diagonal terms to get the

total TKE) would be needed, which implies a model for the lateral and vertical velocities U_y and U_z. Better near-wake modelling could be achieved by using a non-Gaussian velocity assumption in the vicinity of the rotor (such as super-Gaussian or double-Gaussian functions). Taking into account veer such as in [116] is necessary to apply the model to cases where the wake is skewed, typically in cases of a stably stratified ABL. Finally, a calibration (i.e. relating different parameters σ, σ_f and l_m to the inflow conditions) under different atmospheric conditions will be needed to have an operational method.

The expressions of velocity and added turbulence in the MFOR that are used to build the present steady-state model can also be used as inputs to a DWM-like model: combined with a synthetic turbulence generation, the unsteady effects of meandering can be modelled.

Conclusion and perspectives

This work aimed at better understanding and modelling the interactions between wind turbine wakes and the ABL. We started by demonstrating that the ALM in Meso-NH can predict accurately the behaviour of wind turbine wakes in realistic atmospheric conditions. This validation was performed against the SWiFT benchmark where wakes under neutral, unstable and stable atmospheric conditions were measured on a utility-scale turbine and reproduced with several high-fidelity numerical codes of the community. This study also showed that the time-splitting, introduced to improve the computational cost of the simulations, leads to an overestimation of the turbine's efforts and of the turbulence in the wake.

Wake tracking, i.e. defining the position of the wake centre at each time step, is essential to compute the amount of meandering and the velocity in the moving frame of reference (MFOR). The MFOR follows the wake centre at each time step (in opposition to the FFOR which is bound to the ground) and is largely reused in this work. Doing so for a wake evolving in the ABL is particularly difficult because the instantaneous wake is modified as it travels downstream, to the point that it becomes nearly indistinguishable from atmospheric turbulence. In the present work, we compared several algorithms of the literature for wake tracking and proposed pre-processing methods to improve the results. Based on this study, best practices are defined and followed for the rest of our work. We also showed that the results in the MFOR strongly depend on the tracking method, indicating that it should be chosen carefully.

The Meso-NH simulations of the SWiFT benchmark were then re-used for a deeper analysis, in particular wake meandering and wake properties (wake width, mean velocity deficit, added turbulence and self-similarity) in the MFOR. The results indicate that if the integral length scale upstream of the turbine is sufficiently large, the velocity and turbulence in the MFOR become independent of atmospheric stability. Moreover, the wake is symmetric in the MFOR and the asymmetry observed in the FFOR is shown to entirely come from meandering.

The next step of this work was to break down the mean velocity and turbulence in the FFOR into different terms that are functions of the mean velocity and turbulence in the MFOR. These terms fall into two categories. The firsts are pure-terms, that are solely driven by small-scale turbulence or wake meandering. The remaining terms are called cross-terms since they depend on both phenomena. From the SWiFT simulations, we showed that cross-terms are negligible in the velocity breakdown but not in the turbulence breakdown. Cross-terms are usually neglected in models dealing with meandering, which could explain some discrepancies observed with measurements. We also quantified each term for the three stability cases simulated with Meso-NH and showed that the meandering turbulence is predominant in the unstable case whereas it is the wake turbulence that is predominant in the stable case.

Finally, we proposed an analytical model based on these breakdowns. An analytical form was found for the pure-terms but not yet for the cross-terms. For the wake velocity, this model is equivalent to an already existing model in the literature but the turbulence model is new. It is less empiric than most models of the literature and is built to predict the spatial distribution of turbulence in the wake. Moreover, the effect of wake expansion and of wake meandering are naturally separated and can be independently calibrated. According to the findings of Ch. 6, it allows separating turbine-induced phenomena from ABL-induced phenomena.

To wrap up, a new tool for high-resolution simulations has been validated for different atmospheric stabilities, and post-processing methods for wake tracking have been compared and improved. This Ph. D. thesis provided new insights on the behaviour of wind turbine wakes in non-neutral ABL, showing in particular that atmospheric stability mainly impacts wake meandering and not wake expansion. We finally proposed a new analytical method to compute independently wake expansion and wake meandering.

Technical perspectives

Improvements of ALM simulations with Meso-NH. Despite relatively good predictions of the wake properties in the SWiFT benchmark, the torque and thrust show rather high values compared to measurements and other LESs. Several ideas are currently investigated to resolve this issue, one of the most promising being a better interpolation of the wind used as an input of the blade element, as in [168].

Even though it serves its main purpose of reducing the acceleration where there are no body forces from the ALM, the implementation of the nacelle and tower in Meso-NH is very basic and could be improved and validated.

In the current version of Meso-NH, the blade pitch and rotational speed of the rotor are set at the beginning of the simulation to a fixed value. It is not an issue for a single turbine as it is the case here, but having a controller that modifies these parameters during the simulation will be needed for realistic wind farm cases.

Finally, precursor simulations in Meso-NH would be useful to generate the unsteady ABL conditions upstream of the turbine, in particular for sensitivity studies.

Finalising and improving the analytical model. In addition to neglecting the cross-term, the proposed model only deals with streamwise turbulence. For a complete knowledge of the wake flow, all the terms and the two other components of turbulence should also be taken into account.

Other phenomena such as veer or ground effects should also be taken into account to better model the wake properties in realistic cases.

Before using it, the model must also be calibrated, i.e. its parameters (σ_{fy}, σ_{fz}, σ_y, σ_z and l_m) must be related to atmospheric and operating conditions. The model can then be compared to other existing models in the literature, in particular for different atmospheric conditions.

The originality of this work is also that it proposes a new methodology where wake expansion and meandering are independently taken into account. If the results of inter-comparisons are not

satisfying, the chosen shape functions (in particular for turbulence in the MFOR) can always be modified without changing the methodology.

A need for further physical interpretation

In what conditions does the MFOR/FFOR framework still makes sense? We showed that the framework of MFOR and FFOR is very useful to study wake meandering. In this work, consistent MFOR profiles were found for different ABL stabilities, up to 8 diameters downstream. However, there are concerns that this methodology does no longer make sense as the wake reaches very far distances such as 20 diameters downstream, where it might be mixed with the inflow turbulence and the assumption that it keeps its integrity does no longer make sense.

Answering this question requires running different tracking methods on a reference case where the wake centre's position is known *a priori*. This reference case should however be realistically reproducing the velocity deficit planes observed in LES.

Under its current form, this framework is also limited to single wind turbine wakes. In the case of two wakes interacting with each other, it is not clear if one or two wake centres should be defined, and how could it be.

Extending the results on the impact of stability on the wake to more ABL conditions. Our LES results in Ch. 6 indicate that as long as the integral length scale is sufficiently large and operating conditions are similar, the wind turbine wake in the MFOR becomes independent of atmospheric stability. This study however only contains three simulations, and more data are needed to strengthen these findings. For instance, it could take the form of a sensitivity study on different parameters, in particular velocity and turbulence at hub height, static stability and thrust coefficient, to validate or not the aforementioned observations.

What is the physical interpretation of the cross-terms in the velocity and turbulence breakdowns? In Ch. 7, a physical interpretation has been given for the pure-terms but not for the cross-terms. Doing so would lead to a better understanding of the interaction between small-scale turbulence and wake meandering and its role in the production and dissipation of turbulence. This is a crucial step toward the modelling of such terms, which, we believe, must be taken into account when dealing with meandering wakes.

Long term perspectives

A new high-fidelity tool for wake analysis in atmospheric conditions. The first achievement of the present work has been to validate the full chain of simulation needed to study a meandering wake inside a realistic ABL. It includes the set-up of the ABL corresponding to given inflow conditions, the LES simulations of the wake and the post-processings among which the wake tracking plays an essential role. Even though each step can be improved, all are operational and can now be used to simulate plenty of new cases, whether it is for the calibration of models or other applications. Such studies are planned for the near future in our team at IFPEN. Since both Meso-NH and

the post-processing tools are open-source, any research team that wants to investigate wind turbine wakes inside ABL can also use this chain of simulations.

An application to engineering tools. Once calibrated, and if it compares well against those existing in the literature, the analytical model that we proposed here will be implemented in the engineering tools FarmShadow^{TM} developed at IFPEN. This code can either work in steady-state or in dynamic mode. In the first mode, the full model developed herein can be directly implemented, and will allow optimising wind farm layouts for the output power, but also with constraints on the loading thanks to the model for turbulence. Since the model will be, by nature, calibrated in both MFOR and FFOR, the results in the MFOR can be directly used as inputs of the dynamic mode, similarly to the Ainslie model in the DWM. Such dynamic models can be used on their own, but might also be used to generate modified turbulent inflow conditions for the DeepLinesWind^{TM} multi-physic code. This could be used, for instance, to perform unsteady aero-hydro-servo-elastic simulations on large floating offshore wind turbines. Indeed, offshore wind is expected to increase in the next years, but the depth of the Atlantic coast is often too deep for fixed offshore, so the floating option is seriously considered. But this industry is still at an early stage and such multi-physic studies are necessary for manufacturers before they deploy their floating wind farms. Of course, this model can be used for more standard cases like an onshore turbine where the orography is negligible.

Better accuracy of the wake models. Our work confirmed previous literature findings [94]: the meandering, and thus the wake dissipation, is a function of atmospheric stability even for a fixed turbulence intensity. In many analytical models, however, it is assumed that the atmospheric conditions can be entirely accounted for with the turbulence intensity and the mean wind speed. When averaged over a year, this assumption holds because one can suppose that the stable and unstable atmospheric conditions will compensate each other. For estimations of profitability, this approximation is thus acceptable because it will be run on large time scales. Nevertheless, to maintain the equilibrium of the electric network, the electricity transmission operators need to estimate the power produced by wind over a season, a day, and even an hour. On such reduced time scales, the atmospheric stability must be taken into account, and thus appropriate wake models as the one we here propose here will be needed. For instance in France, the model could be used in the IPES (Insertion des Productions d'Énergies renouvelables intermittentes dans le Système électrique) code of RTE, the electricity transmission operator, to estimate the hourly wind production and adapt the grid in consequences.

Conclusion et perspectives (français)

Ce travail visait à mieux comprendre et modéliser les interactions entre les sillages d'éoliennes et la CLA. Nous avons commencé par démontrer que l'ALM dans Meso-NH permet de prédire avec précision le comportement des sillages d'éoliennes dans des conditions atmosphériques réalistes. Cette validation a été menée sur le benchmark SWiFT où des sillages en conditions atmosphériques neutre, stable et instable ont été mesurés pour une éolienne de petite taille et reproduits avec plusieurs codes haute-fidélité de la communauté. Cette étude a également montré que la méthode de time-splitting, introduite pour améliorer le temps de calcul des simulations, mène à une surestimation des efforts de la turbine et de la turbulence dans le sillage.

Le suivi de sillage, c.-à-d. la définition de la position du centre de sillage à chaque pas de temps, est essentiel pour calculer la quantité de méandrement et les caractéristiques du vent dans le repère mobile (MFOR). Le MFOR suit le centre de sillage à chaque pas de temps (contrairement au FFOR qui est lié au sol) et est beaucoup utilisé dans ce travail. Le suivi de sillage dans la CLA est particulièrement difficile car le sillage instantané est modifié au fur et à mesure qu'il se déplace en aval de l'éolienne, jusqu'à ce qu'il soit presque impossible de le distinguer de la turbulence atmosphérique. Dans ce travail, nous avons comparé plusieurs algorithmes de suivi de la littérature et avons proposé des méthodes de pré-traitement pouvant améliorer leurs résultats. En se basant sur cette étude, une procédure de post-traitement est définie et suivie pour le reste de ce travail. Nous avons aussi montré que les résultats dans le MFOR dépendent fortement de la méthode de suivi de sillage utilisé, ce qui indique que ces dernières doivent être choisies avec précautions.

Les simulations Meso-NH du benchmark SWiFT ont été réutilisées pour une analyse approfondie, en particulier du méandrement, et des propriétés du sillage (largeur, maximum de déficit de vitesse, turbulence ajoutée, auto-similarité) dans le MFOR. Les résultats indiquent que si la longueur intégrale de la turbulence est suffisamment grande, la vitesse de vent et la turbulence dans le MFOR deviennent indépendantes de la stabilité atmosphérique. De plus, le sillage est symétrique dans le MFOR et l'asymétrie observée dans le FFOR peut donc être entièrement attribuée au méandrement.

L'étape suivante du travail a été de décomposer la vitesse moyenne et la turbulence dans le FFOR en plusieurs autres termes qui sont des fonctions de la vitesse moyenne et de la turbulence dans le MFOR. Ces termes sont séparés en deux catégories. Les premiers sont les termes dits 'purs', qui sont liés soit au méandrement, soit à la turbulence de petite échelle. Les seconds sont appelés termes 'croisés' car ils dépendent des deux phénomènes à la fois. À l'aide des simulations SWiFT, nous avons montré que les termes croisés sont négligeables dans la décomposition de la vitesse, mais pas dans la décomposition de la turbulence. Ces termes croisés sont en général négligés dans les modèles de la littérature traitant du méandrement, ce qui pourrait expliquer certaines différences observées avec les mesures. Nous avons également quantifié chaque terme pour les trois cas de stabilité simulés

avec Meso-NH et montré que la turbulence de méandrement est dominante dans le cas instable tandis que c'est la turbulence du sillage qui domine la turbulence totale dans le cas stable.

Finalement, nous avons proposé un modèle analytique basé sur ces décompositions. Une forme analytique a été trouvée pour les termes purs mais pas pour les termes croisés. Concernant le déficit de vitesse dans le sillage, ce modèle est équivalent à un autre de la littérature, mais le modèle pour la turbulence est totalement nouveau. Il est moins empirique que la plupart des modèles existants et permet de prédire la distribution spatiale de la turbulence dans le sillage. De plus, les effets de l'expansion du sillage et du méandrement sont pris en compte indépendamment. D'après les résultats du Ch. 6, cela va permettre de séparer les phénomènes liés au fonctionnement de la turbine de ceux liés à la CLA.

Pour résumer, un nouvel outil de simulation à haute-fidélité a été validé pour différentes conditions de stabilité atmosphérique, et des méthodes de post-traitement pour le suivi de sillage ont été comparées et améliorées. Cette thèse de doctorat apporte de nouvelles connaissances sur le comportement des sillages d'éoliennes dans une CLA non-neutre, montrant en particulier que la stabilité atmosphérique influe surtout sur le méandrement et peu sur l'expansion du sillage. Pour finir, nous proposons un nouveau modèle analytique permettant de calculer indépendamment le méandrement et l'expansion du sillage.

Perspectives techniques

Améliorations des simulations ALM avec Meso-NH. Malgré de plutôt bonnes prédictions des propriétés du sillage dans le benchmark SWiFT, la poussée et le couple montrent des valeurs relativement élevées par rapport aux mesures et aux autres LES. Plusieurs pistes sont à l'heure actuelle explorées pour résoudre ce problème, l'une des plus prometteuses étant une meilleure interpolation du vent utilisé pour calculer les efforts des éléments de pales, comme dans [168].

Bien qu'elle serve sa principale fonction de réduire l'accélération là où il n'y a pas de termes sources de l'ALM, l'implémentation de la nacelle et de la tour dans Meso-NH est très basique et gagnerait à être améliorée et validée de manière plus approfondie.

Dans la version actuelle de Meso-NH, le pitch des pales et la vitesse de rotation du rotor sont fixés au début de la simulation. Ce n'est pas un problème pour une simulation avec une éolienne seule comme cela a été fait ici, mais implémenter un contrôleur qui modifierait ces paramètres pendant la simulation est nécessaire pour une simulation réaliste de ferme d'éolienne.

Finalement, une simulation précurseur dans Meso-NH serait utile pour générer des conditions d'entrée turbulentes en amont de l'éolienne, en particulier pour des études de sensibilité.

Finaliser et améliorer le modèle analytique. En plus de négliger certains termes, le modèle proposé se limite à la turbulence axiale. Pour compléter le modèle, les termes croisés et les autres composantes de la turbulence pourraient être pris en compte.

D'autres phénomènes tels que le cisaillement horizontal (veer) ou les effets du sol devraient également être pris en compte pour une meilleure représentation du sillage dans des conditions réalistes.

Pour être opérationnel, il faut que le modèle soit calibré, c.-à-d. que ses paramètres (σ_{fy}, σ_{fz}, σ_y,

σ_z et l_m) soient exprimés en fonction des conditions atmosphériques et du point de fonctionnement de l'éolienne. Il pourra alors être comparé à d'autres modèles de la littérature, en particulier pour différentes conditions atmosphériques.

L'originalité de ce travail réside avant tout dans la proposition d'une nouvelle méthodologie où l'expansion et le méandrement du sillage sont indépendamment pris en compte. Si les résultats des inter-comparaisons ne sont pas satisfaisants, rien n'empêche de changer les fonctions de forme choisies (en particulier pour la turbulence dans le MFOR) en gardant la méthodologie générale proposée ici.

Un besoin d'une meilleure compréhension physique

Quelles sont les limites de l'approche MFOR/FFOR ? Nous avons montré que la méthodologie du MFOR et FFOR est très utile pour étudier le méandrement de sillage. Dans ce travail, des profils cohérents ont été trouvés dans le MFOR pour différentes stabilités atmosphériques, jusque 8 diamètres en aval. Toutefois, on peut douter que cette méthodologie a toujours un sens quand le sillage atteint des distances très lointaines, par exemple 20 diamètres en aval, où le sillage instantané sera mélangé avec la turbulence environnante et où l'hypothèse qu'il garde sa cohérence en se déplaçant ne tient plus.

Pour répondre à cette question, il y aurait besoin d'utiliser différentes méthodes de suivi de sillage sur un cas de référence où le centre de sillage serait connu *a priori*. Mais il faudrait que ce cas de référence reproduise de manière réaliste la position des plans de déficit de vitesse observés en LES.

Dans sa forme actuelle, ce cadre du MFOR/FFOR est aussi limité à un sillage unique, donc à une éolienne isolée. Dans le cas de deux sillages ou plus qui interagissent, il n'est pas clair qu'il faille définir un ou plusieurs centres de sillages, et comment cela pourrait se faire.

Étendre les résultats sur l'impact de la stabilité sur les sillages à plus de conditions atmosphériques. Nos résultats LES du Ch. 6 indiquent que tant que la longueur intégrale de la turbulence est suffisamment grande et que les conditions de fonctionnement sont similaires, les sillages d'éoliennes dans le MFOR deviennent indépendants de la stabilité atmosphérique. Cette étude est cependant limitée à trois simulations, et plus de données sont nécessaires pour consolider ces résultats. Par exemple, cela peut prendre la forme d'une étude de sensibilité sur différents paramètres, en particulier la vitesse et la turbulence à hauteur de hub, la stabilité statique et le coefficient de poussée, permettant ainsi de valider ou non les observations susmentionnées.

Comment interpréter physiquement les termes croisés de la décomposition de la turbulence ? Dans le Ch. 7, une interprétation physique a été proposée pour les termes purs, mais pas pour les termes croisés. Compléter ce manque permettrait une meilleure compréhension de l'interaction entre les petites échelles de la turbulence et le méandrement du sillage, et son rôle dans la production et la dissipation de la turbulence. C'est une étape cruciale pour modéliser ces termes qui sont, d'après notre interprétation, essentiels à prendre en compte quand il s'agit de modéliser les sillages qui méandrent.

Perspectives à long terme

Un nouvel outil haute-fidélité pour l'analyse des sillages. Le premier objectif de cette thèse a été de valider la chaîne entière de simulation nécessaire à l'étude du méandrement des sillages au sein d'une CLA réaliste. Cela inclut l'initialisation de la CLA en fonction de conditions de vent données, la simulation LES du sillage et les post-traitements parmi lesquels le suivi de sillage prend une place centrale. Bien que chaque étape soit encore améliorable, elles sont toutes opérationnelles et peuvent être utilisées pour simuler de nombreux nouveaux cas, que ce soit pour la calibration de modèles ou d'autres applications. De telles études sont prévues dans un futur proche au sein de notre équipe à l'IFPEN, mais sont aussi accessibles à toute équipe de recherche voulant étudier les sillages d'éoliennes dans la CLA car cette chaîne de calcul est entièrement open-source.

Une application aux modèles d'ingénierie. Une fois calibré, et si il se compare bien aux autres modèles de la littérature, le modèle analytique que nous proposons ici sera implémenté dans le modèle d'ingénierie FarmShadow^{TM} développé au sein de l'IFPEN. Ce code peut à la fois fonctionner en mode statique ou dynamique. Dans le premier mode, il serait implémenté tel quel, et permettrait d'optimiser les configurations de parcs éoliens pour la puissance produite, avec également des contraintes sur le chargement des pales grâce au modèle de turbulence. Comme le modèle sera, par nature, calibré à la fois dans le MFOR et le FFOR, les résultats dans le MFOR pourront directement être utilisés pour le mode dynamique, de manière similaire au modèle d'Ainslie dans le DWM. Un tel modèle dynamique peut être utilisé seul, ou pourra être utilisé pour générer des champs de vents turbulents modifiés pouvant être utilisés par le code multiphysique DeepLinesWind^{TM}. Il pourrait alors servir, par exemple, à mettre en place des simulation aero-hydro-servo-elastique instationnaires pour de grandes éoliennes flottantes. En effet, il est attendu que l'éolien en mer, en particulier les éoliennes flottantes, prenne une part plus importante dans les prochaines années. Toutefois, c'est encore une technologie naissante, et de telles études sont donc importantes pour les turbiniers avant de déployer leurs parcs flottants. Bien sur, ce modèle peut s'appliquer à d'autres cas plus classiques comme une éolienne onshore, tant que le l'orographie n'est pas trop prononcée.

Une précision plus fine des modèles de sillage. Notre travail confirme de précédentes observations de la littérature [94]: le méandrement, et donc la dissipation du sillage, dépend de la stabilité atmosphérique, et ce même pour un niveau d'intensité de turbulence donné. Dans de nombreux modèles analytiques, cependant, on suppose que les conditions atmosphériques peuvent être entièrement décrites par l'intensité de turbulence et la vitesse de vent moyenne. Pour une estimation annuelle ou pluri-annuelle du rendement, cette supposition peut être considérée correcte car les conditions stables et instables vont se compenser au cours de l'année. Toutefois, les opérateurs de réseaux électriques ont besoin d'équilibrer le réseau à tout instant. Une estimation du productible éolien à des échelles de temps saisonnières, journalières voir plus faibles est donc requise pour équilibrer le réseau en fonction. Sur de telles échelles réduites, la stabilité atmosphérique doit être prise en compte, et donc un modèle approprié tel que celui développé ici doit être utilisé. Par exemple en France, notre modèle pourrait être utilisé dans le logiciel IPES (Insertion des Productions d'Énergies renouvelables intermittentes dans le Système électrique) utilisé par RTE (le Réseau de Transport de l'Électricité) pour estimer à l'échelle de l'heure la production éolienne en fonction des données météorologiques et d'adapter le réseau électrique en conséquence.

Part IV

Appendices

Appendix A

Numerical parametrisation of the SWiFT simulations

A.1 One way and two way nesting

In the grid nesting of Meso-NH, the exchange of informations between the father D_i and son D_{i+1} domains can either be 1WAY or 2WAY. In the first case, the boundary conditions of the son domain for a given variable is imposed to be equal to the value of the variable in the father domain. In the second case, an additional step is added where the flowfield of the son domain is interpolated on the father domain. In other words, in 1WAY nesting, the father domain is blind to the phenomena arising in the son domain (such as a wind turbine wake) but not in 2WAY nesting.

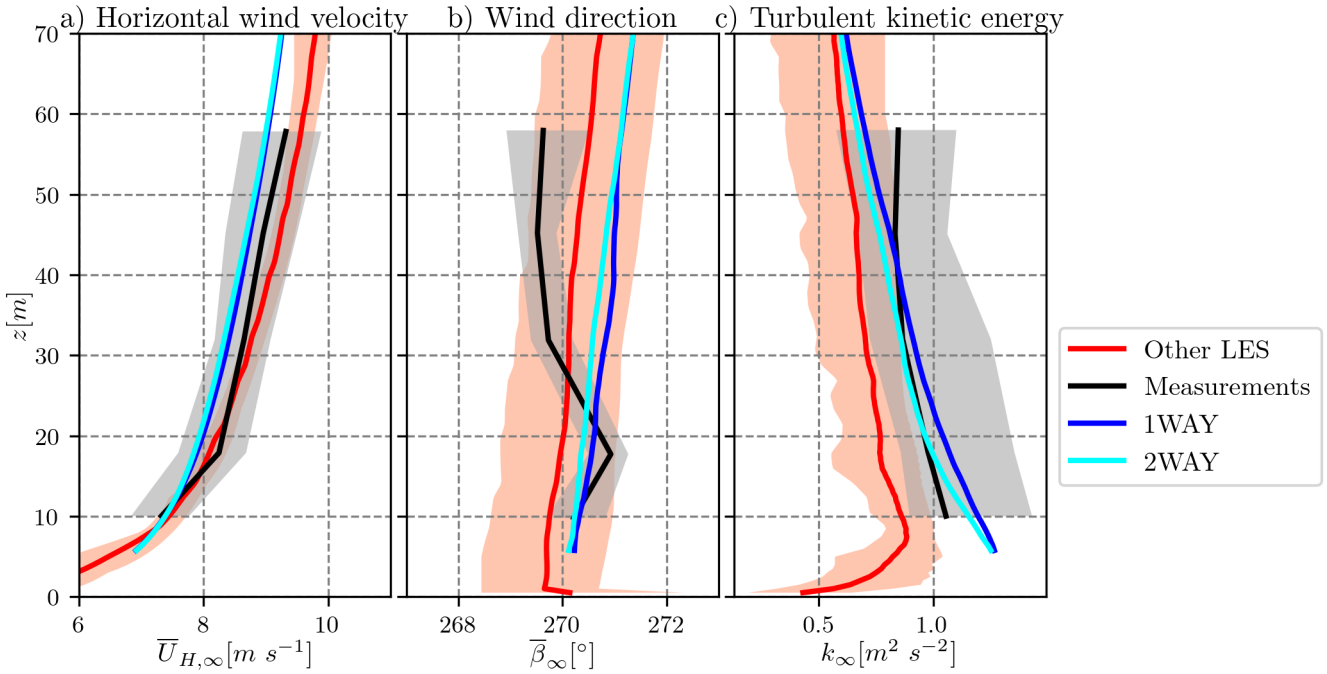

Figure A.1: Inflow conditions for 1WAY and 2WAY nestings.

To be sure that the wake is not recycled in the SWiFT simulations, a 2WAY nesting is used, excepted between the most refined domain where the ALM is activated and its father domain. Hence, the father domains are blind to the wake and act like a precursor simulation, with no risk of recycling the wake in the D_1 cyclic boundary conditions. However one could argue that in the neutral and unstable cases, the D_1 domain is sufficiently large to have a the wake fully dissipated before reaching the cyclic boundary condition. This is verified by running a similar simulation as the one presented in Sect. 4.2 but with a 2WAY nesting, even between D_3 and D_4. This case is plotted in cyan in the following figures. The inflow conditions (Fig. A.1) are indeed very similar, and the small differences are hardly imputable to a possible recycling of the wake. The given interpretation is that the informations of D_4 is transmitted to D_3, D_2 and then D_1, is recycled and thus changes the boundary conditions. Similarly, the efforts of the turbine are not shown here because they are very similar from one simulation to the other and the very thin discrepancies can be attributed to the inflow conditions.

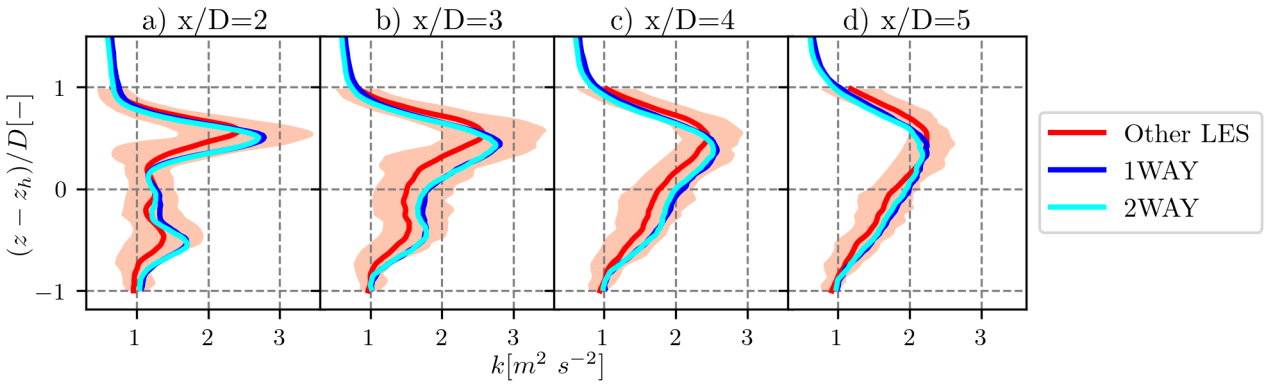

Figure A.2: Effect of using 1WAY or 2WAY nesting on the wake turbulence.

The vertical TKE profiles in the wake are investigated in Fig. A.2 in the four planes of the SWiFT benchmark. The TKE is chosen because it is more sensitive than mean variables such as $\Delta\overline{U}_H$ (see Sect. 4.3). However, the change of boundary conditions leads to only very small discrepancies that can be attributed to the inflow conditions. Likewise, the wake meandering is not shown here because it is almost identical between the two cases.

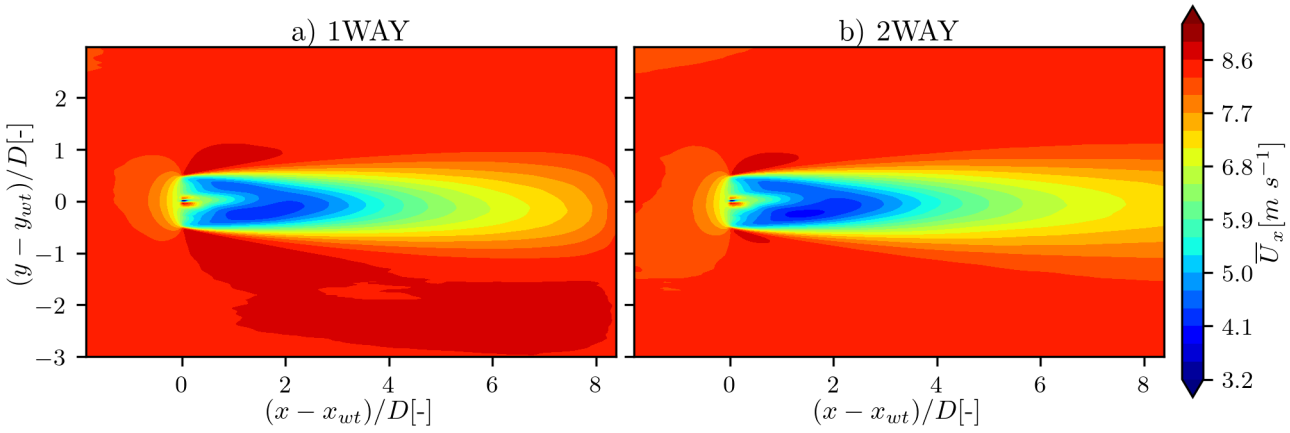

Figure A.3: Mean axial velocity in the wake for 1WAY and 2WAY nestings at $z = z_h$.

For the SWiFT benchmark, using the 1WAY nesting is thus appropriate since it leads to the same results as the 2WAY but ensures that the wake does not impact the inflow conditions. However, differences appear when the wake approaches to the outflow boundary of domain D_4. In Fig. A.3, the mean axial velocity is plotted in the wake for the 1WAY and 2WAY nestings. As shown in Fig. A.3, the velocity near the edge of the domain in the 1WAY simulation is going back to the inflow value. This is because domain D_3 does no see the wake and drives the boundary conditions at the outflow of D_4, forcing it to come back to the inflow conditions. Conversely, in the 2WAY simulation, the wake is propagating downstream in a much more realistic shape and the velocity at the outflow boundary of D_4 exhibits a velocity deficit. Using simulations with 1WAY nesting is thus not appropriate when investigating the wake behaviour near the outflow, which is why simulations are modified for Chs. 5, 6, 7 and 8.

To initialise the ABL in Meso-NH, a large domain with cyclic boundaries is run until a realistic ABL turbulence is obtained. With such method, it must be avoided that the wake reaches the cyclic boundary condition, otherwise it will modify the inflow. To do so, the 1WAY nesting can be used to prevent the wake from going out of the nested domain as in the present work. However we here showed that using the 1WAY nesting leads to erroneous wakes near the outflow of the main domain. Alternatively, the computational domain can be increased to have a dissipated the wake before it reaches the outflow [147]. It implies to run a large domain, and thus needs needlessly large computational resources. Even with a very large domain, the inflow conditions will be slightly changed whereas the improvement of tracking methods that will be proposed in Ch. 5 necessitates knowing *a priori* the exact unsteady inflow. Ideally, all these issues could be solved if a precursor simulation could be performed in Meso-NH as in other LES codes or if the boundary conditions of the 1WAY nesting could be improved.

A.2 Effect of the tower and nacelle in Meso-NH

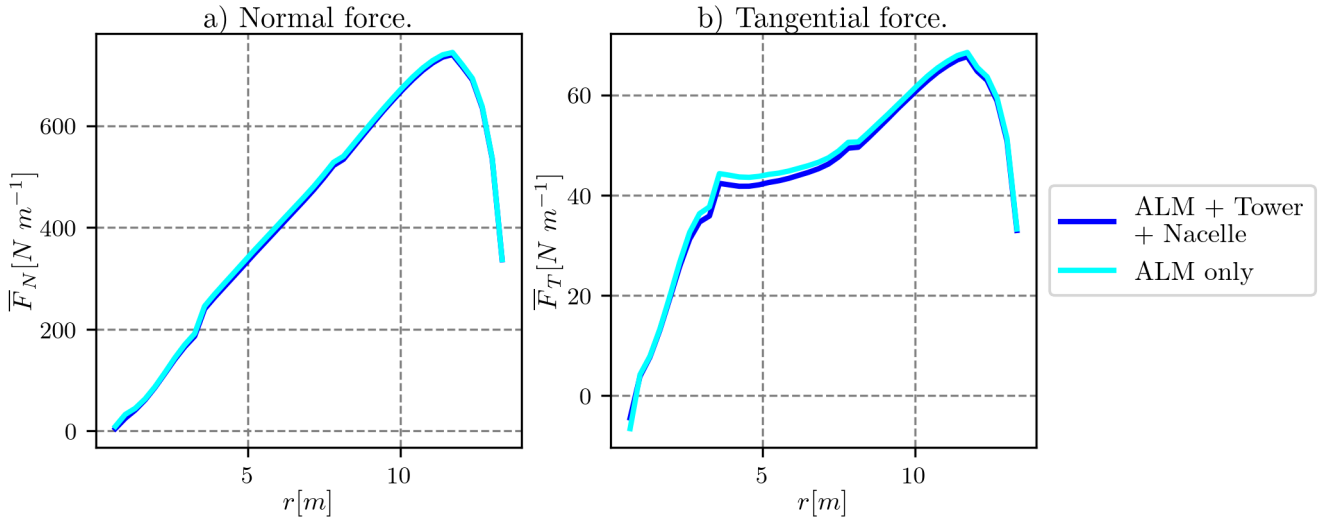

Figure A.4: Evolution of the normal and tangential forces along the blade for the simulation with and without the nacelle and tower implementation. Neutral case.

In this section we describe the impact of our simple implementation of the hub and tower on the turbine behaviour and wake. Indeed, in order to improve the accuracy of the flowfield, especially in the near wake, one needs to account for these elements, and not only for the effect of the blades. The implementation is described in Sect. 3.3.3. Basically the drag forces of the hub and tower are applied at only one point per level, and then smeared as it is the case for the blade body forces.

The neutral case of the SWiFT benchmark has been reproduced without this implementation. In the following figures, it is denoted 'ALM only' and is plotted in cyan. The reference simulation is the one presented in Sect. 4.2, plotted in blue and denoted 'ALM + Tower + Nacelle'. The 1WAY nesting is used because it allows to have exactly the same inflow between both simulations and since we expect the turbine and nacelle to mostly affect the near wake, the comparison is restricted to the four planes of the SWiFT benchmark. The normal and tangential efforts are plotted in Fig. A.4. It was expected that the presence of the nacelle would modify the effort of the blades, in particular near the blade's root but it appears that no significant difference is observed between both simulations.

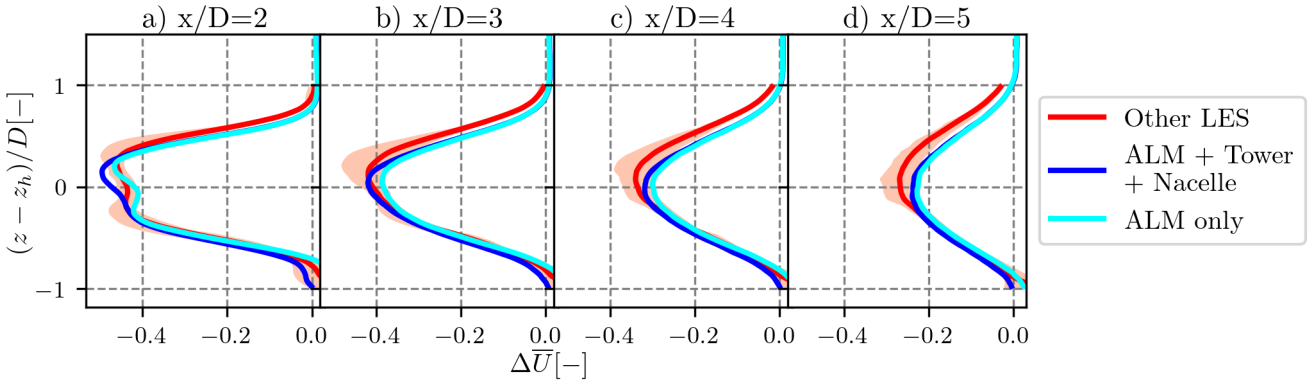

Figure A.5: Effect of the tower and nacelle implementation on the wake mean velocity deficit.

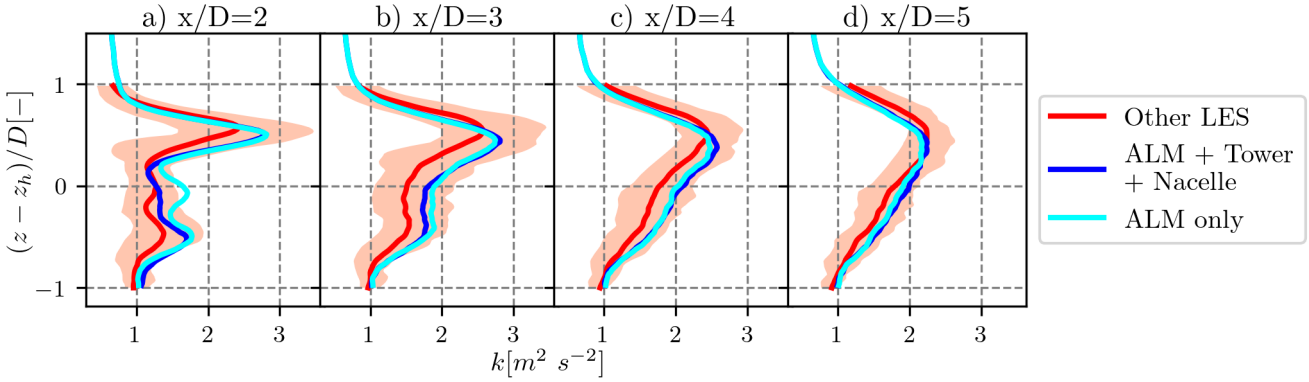

Figure A.6: Effect of the tower and nacelle implementation on the TKE in the wake.

The impact of the nacelle and tower on the wake is highlighted in Figs. A.5 and A.6 for the mean velocity deficit and TKE, respectively. In the near wake, the simulation without tower or nacelle shows a high-velocity region at hub height, leading to a 'W-shaped' velocity profile around the nacelle. This effect comes from a speed-up between the root of the blades and is representing realistically the actual near wake where the nacelle blocks this acceleration. These additional gradients of velocity around the hub position have consequences on the turbulence profiles: at hub height, the simulation

without tower and nacelle predicts a higher turbulence in the near wake. However these differences gradually decrease and both simulation are hardly distinguishable in the far wake.

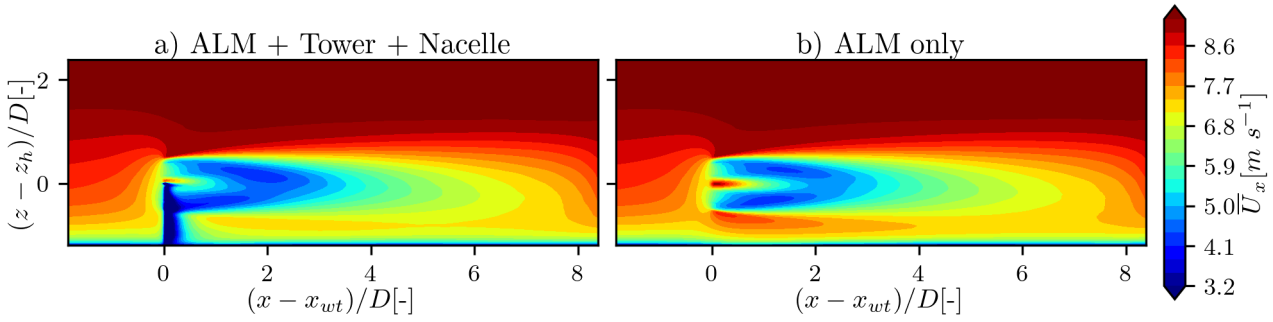

Figure A.7: Mean axial velocity in the wake the simulations with and without the tower and nacelle implementations at $y = y_{wt}$.

The tower mostly affects the very-near wake, before $x/D = 2$ where the first measurements of SWiFT are performed. In Fig. A.7, the velocity in the wake is plotted in a vertical plane at $y = y_{wt}$. One can observe two main differences, mostly arising between the rotor and $x/D = 2$. As shown in Fig. A.5, the absence of nacelle leads to an acceleration region in the middle of the rotor, where there are no body forces. However, the implementation of the nacelle is improvable since there is still a small region of flow acceleration, but more reference data would be needed for a proper validation of the nacelle effects. Moreover, a second difference arises at the bottom of the wake, where the velocity accelerates up to velocities higher than the upstream velocity. In the simulation with all the turbine's elements, this is prevented by the tower model.

This simple implementation of the nacelle and tower has although shown some limits, in particular it does not create unsteady effects such as vortex shedding [95]. However, it allows correcting for the accelerations arising in the near wake due to the absence of body forces at the nacelle and tower locations. Further implementation and validation are required for a more realistic behaviour, but it is not in the scope of this Ph. D. and we will stick to the presented implementation for this work.

Appendix B

Additional figures for the wake analysis

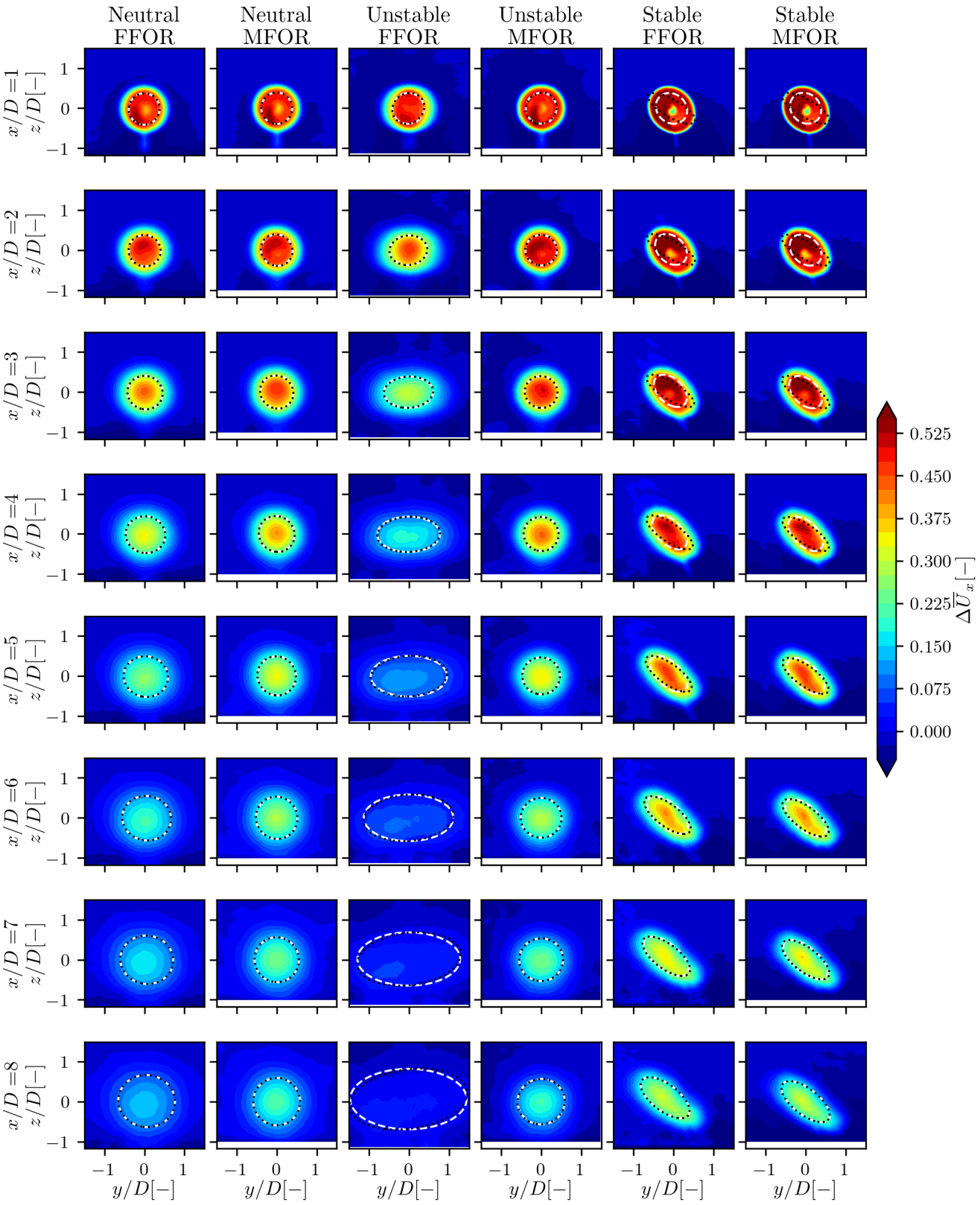

Figure B.1: Velocity deficit in the wake of the wind turbine at different positions downstream for the three cases in the FFOR and MFOR. Isolines corresponding to $\Delta\overline{U}_x/\Delta\overline{U}_x^{M} = 0.5$ for the fits using Eqs. 6.4 and 6.5 are plotted in dashed white and dotted black lines, respectively.

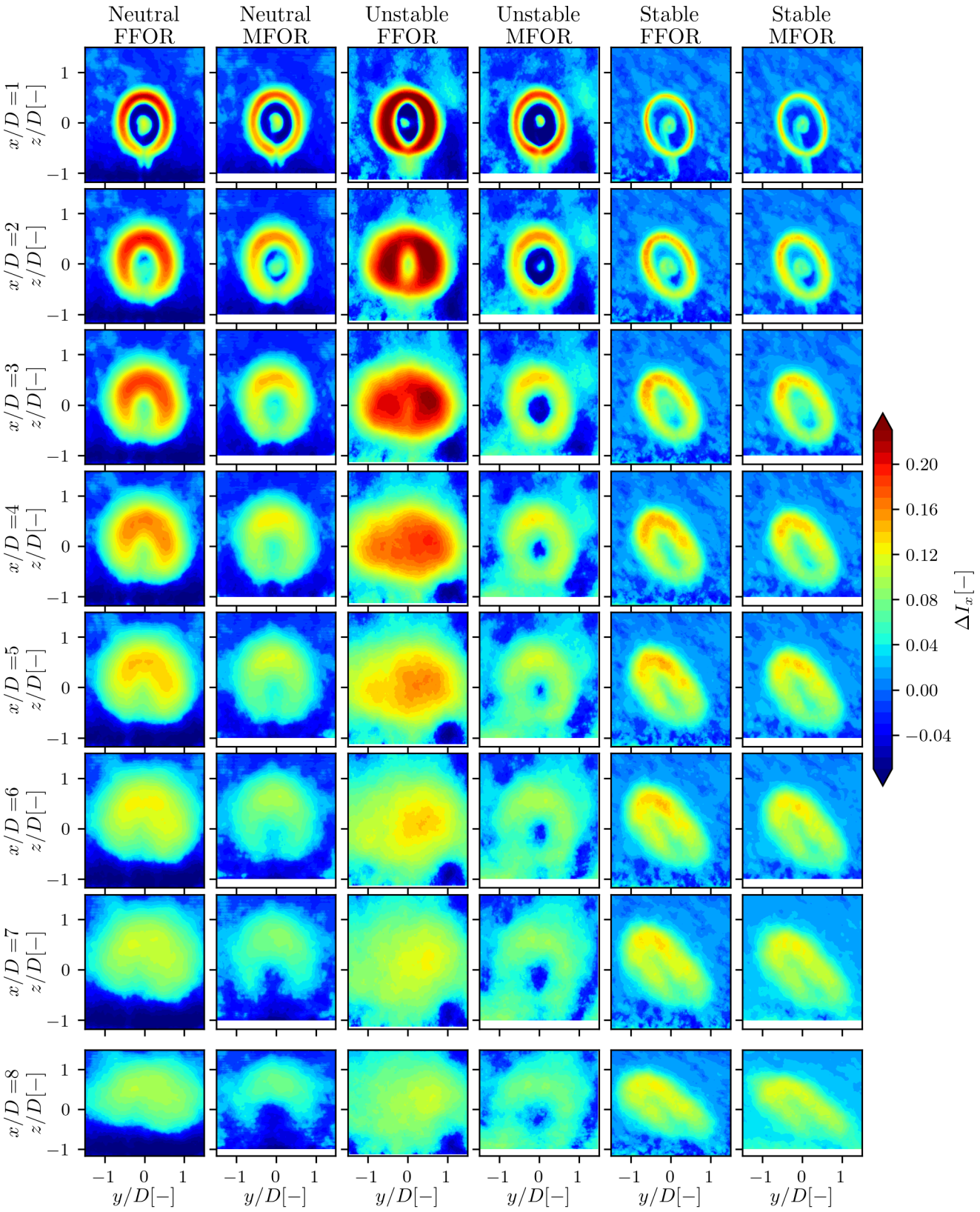

Figure B.2: TI in the wake of the wind turbine at different positions downstream for the three cases in the FFOR and MFOR.

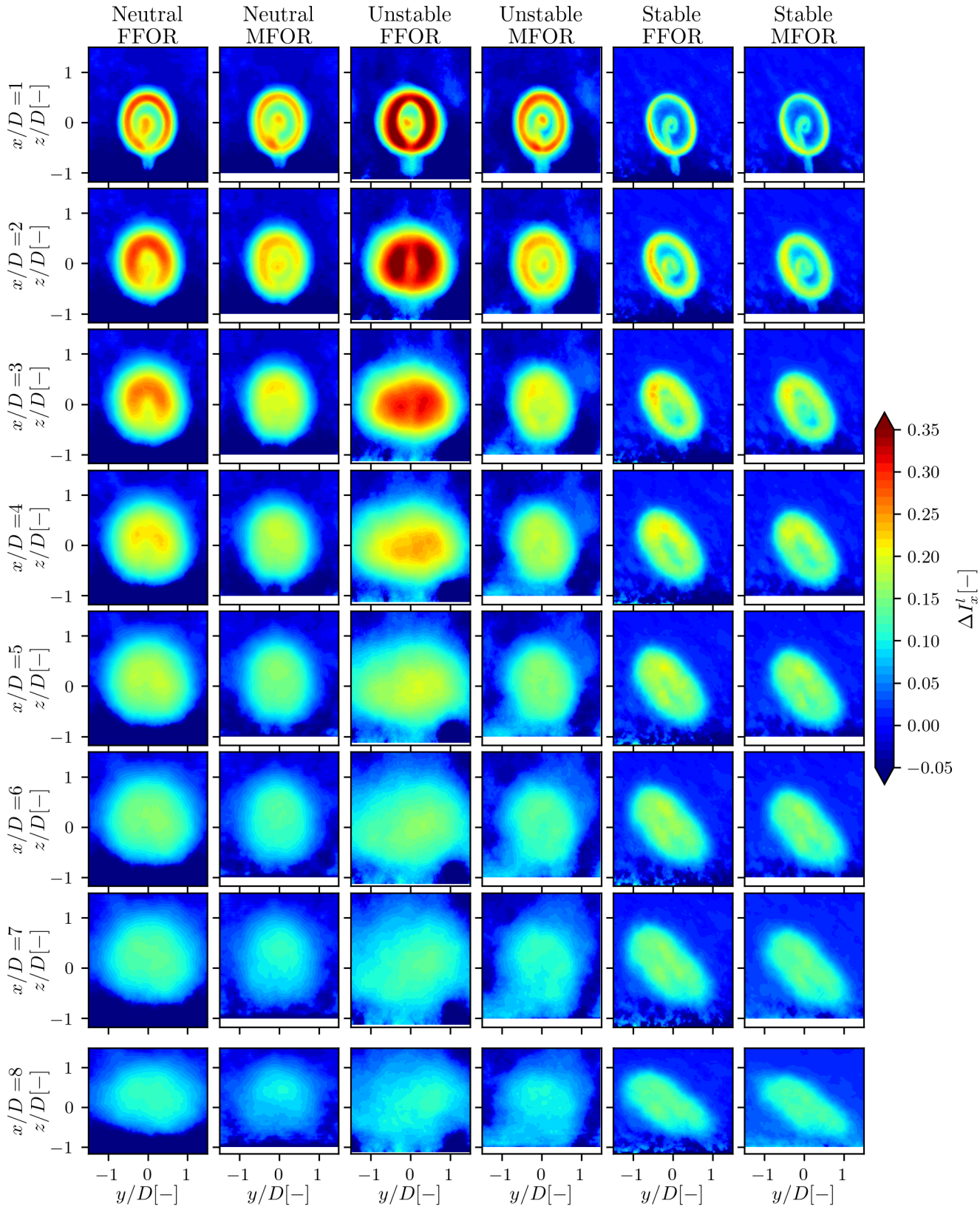

Figure B.3: Same as Fig. B.2, with the local added TI.

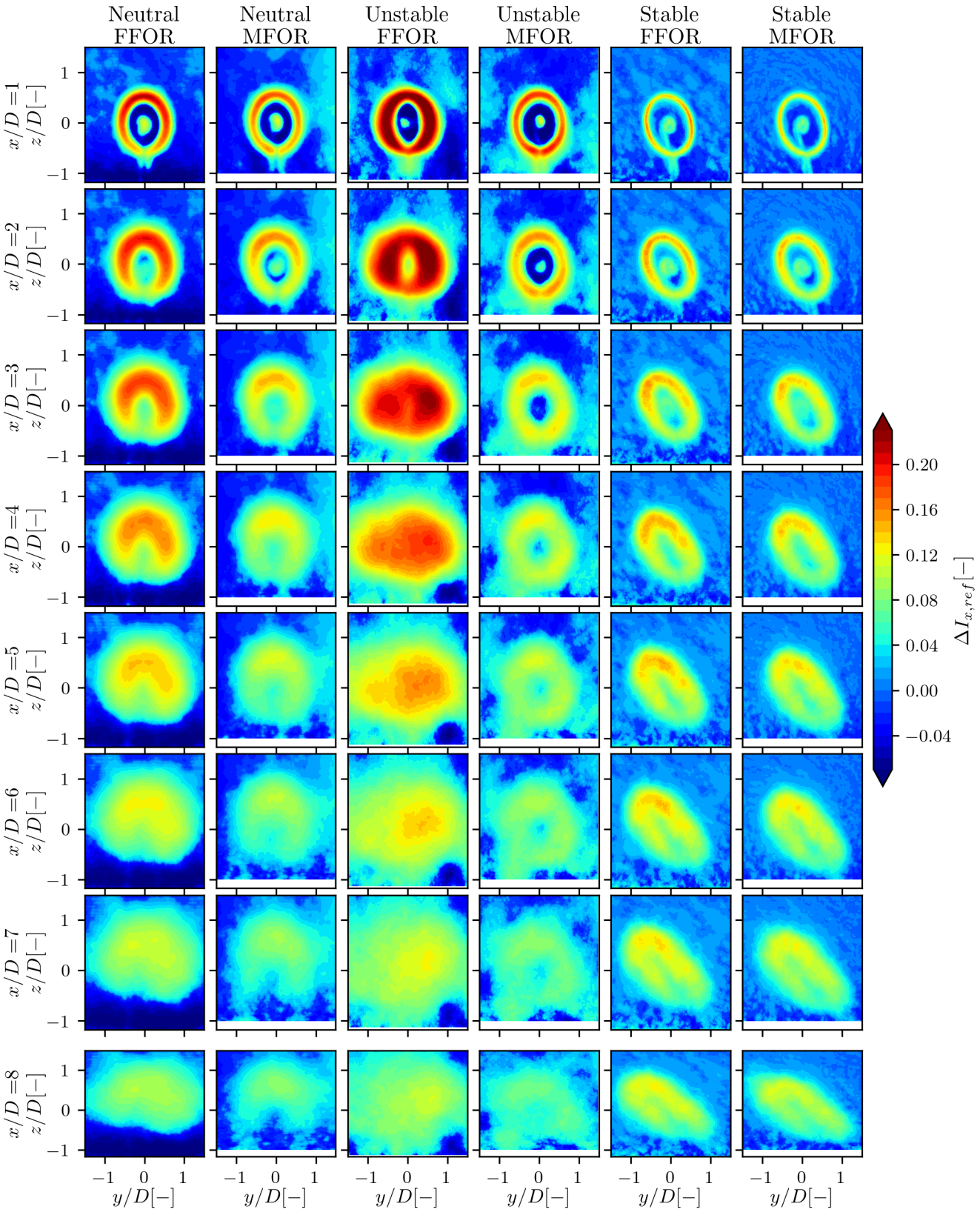

Figure B.4: Same as Fig. B.2, with the reference axial TKE as k_∞.

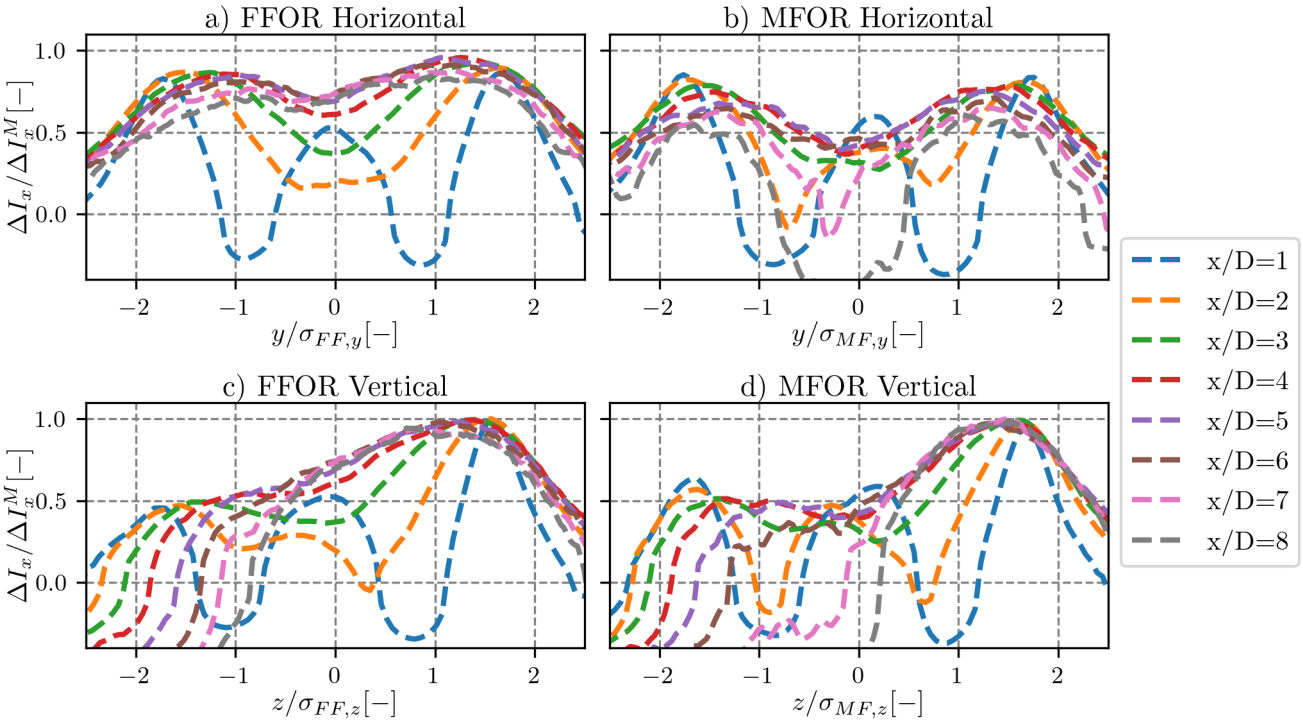

Figure B.5: Self similarity of the added TI profiles for the neutral case.

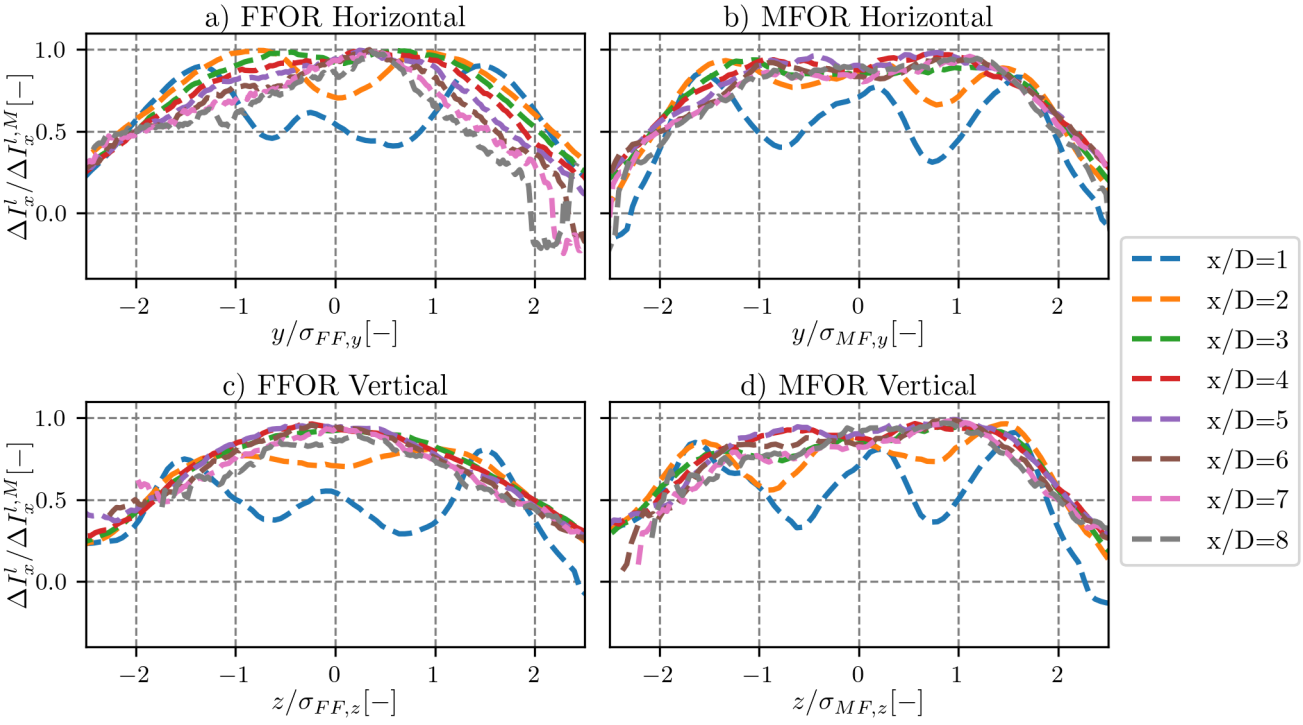

Figure B.6: Self similarity of the added TI profiles for the unstable case.

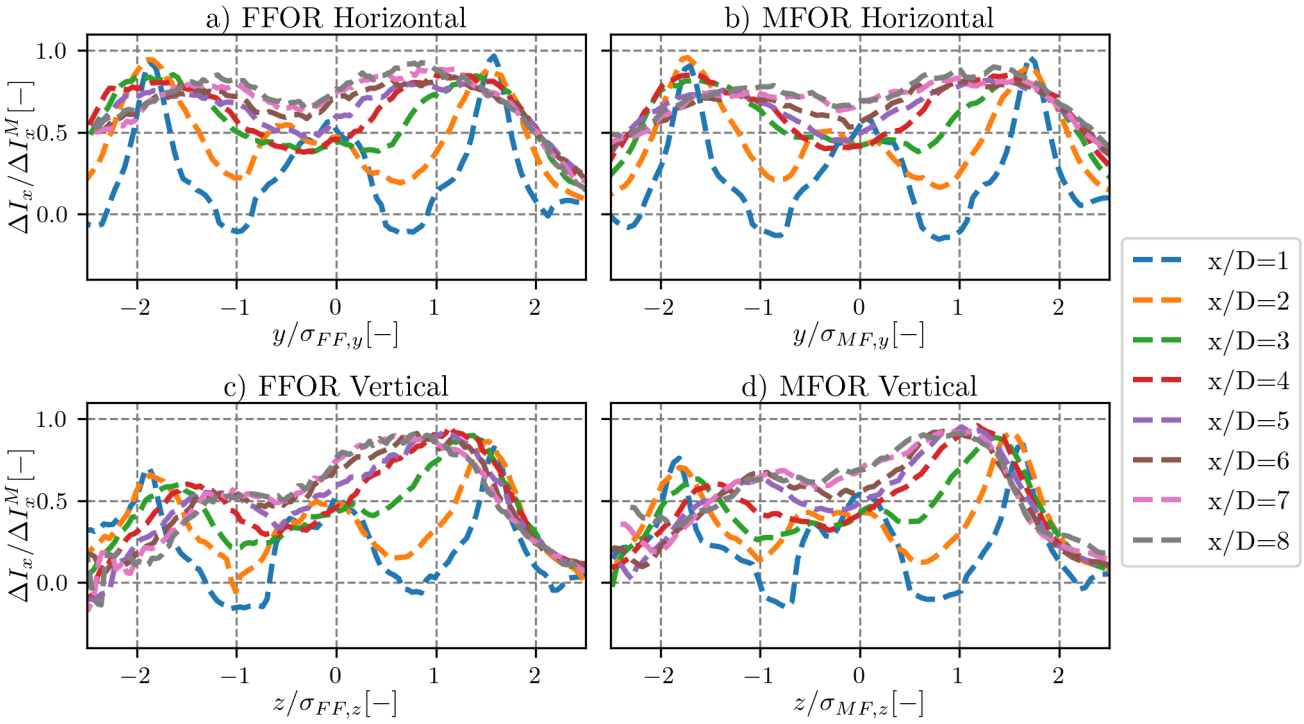

Figure B.7: Self similarity of the added TI profiles for the stable case.

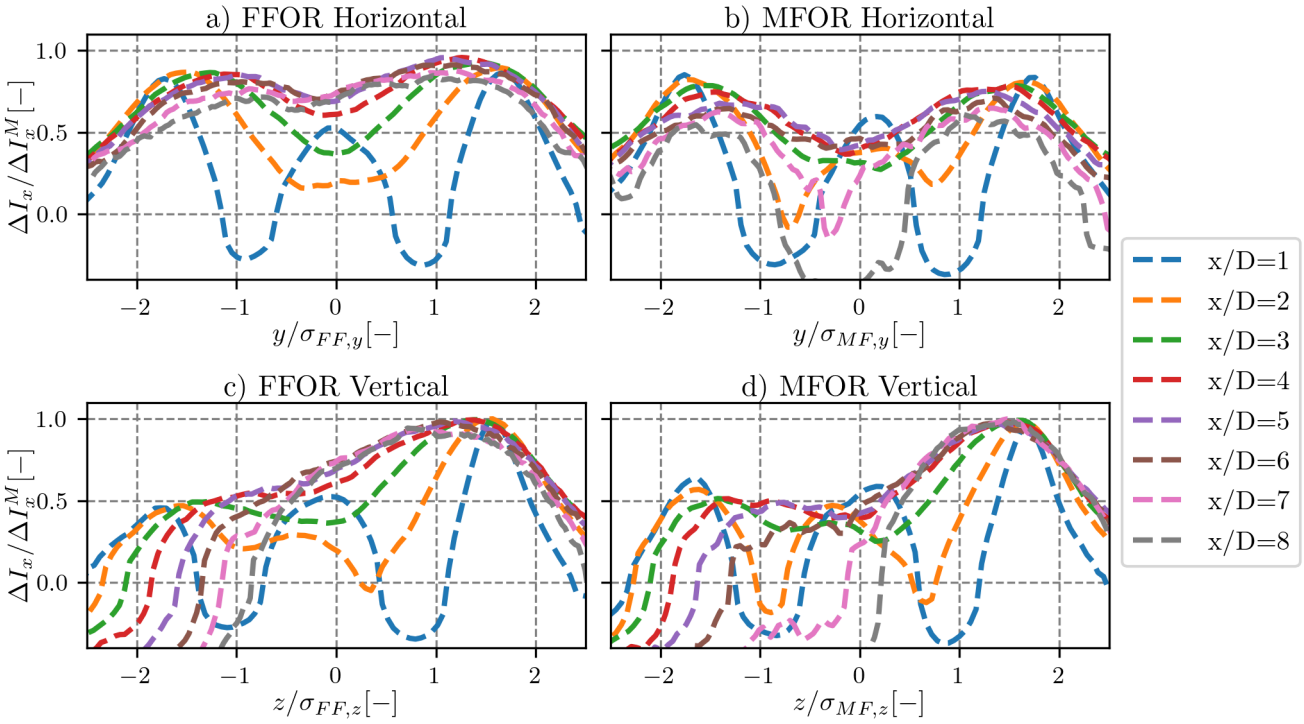

Figure B.8: Self similarity of the local added TI profiles for the neutral case.

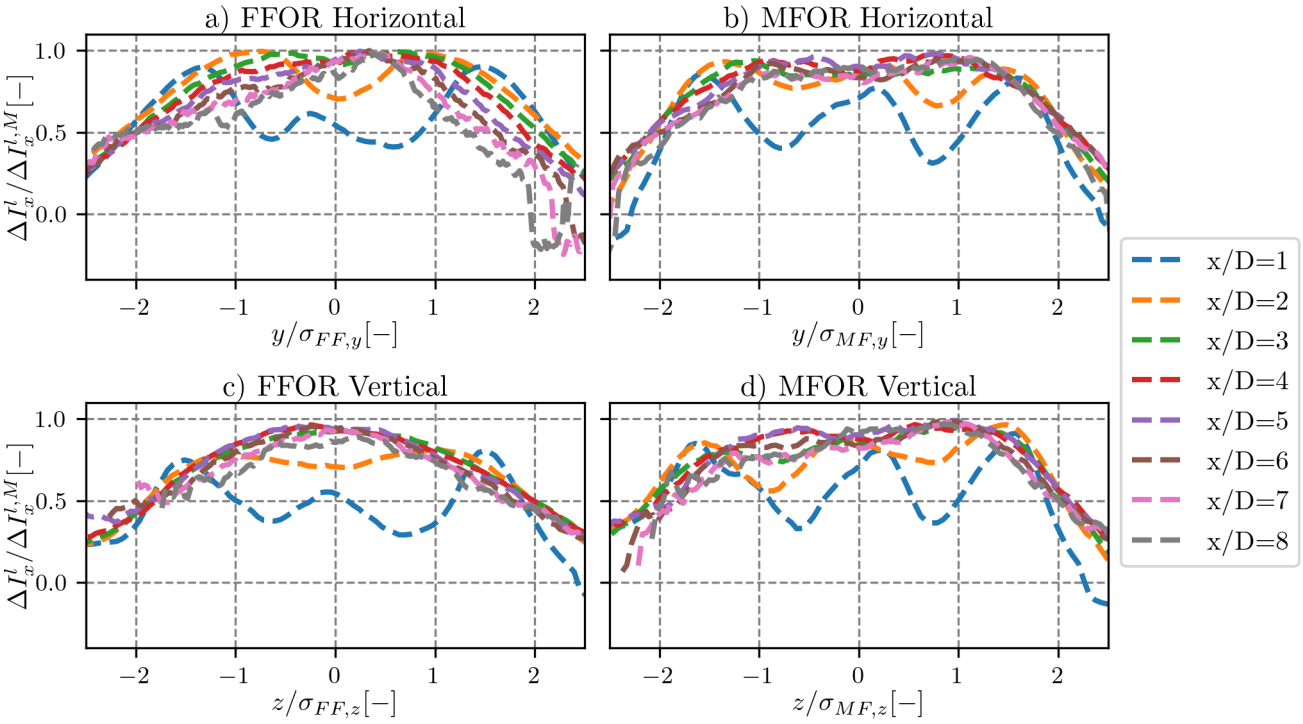

Figure B.9: Self similarity of the local added TI profiles for the unstable case.

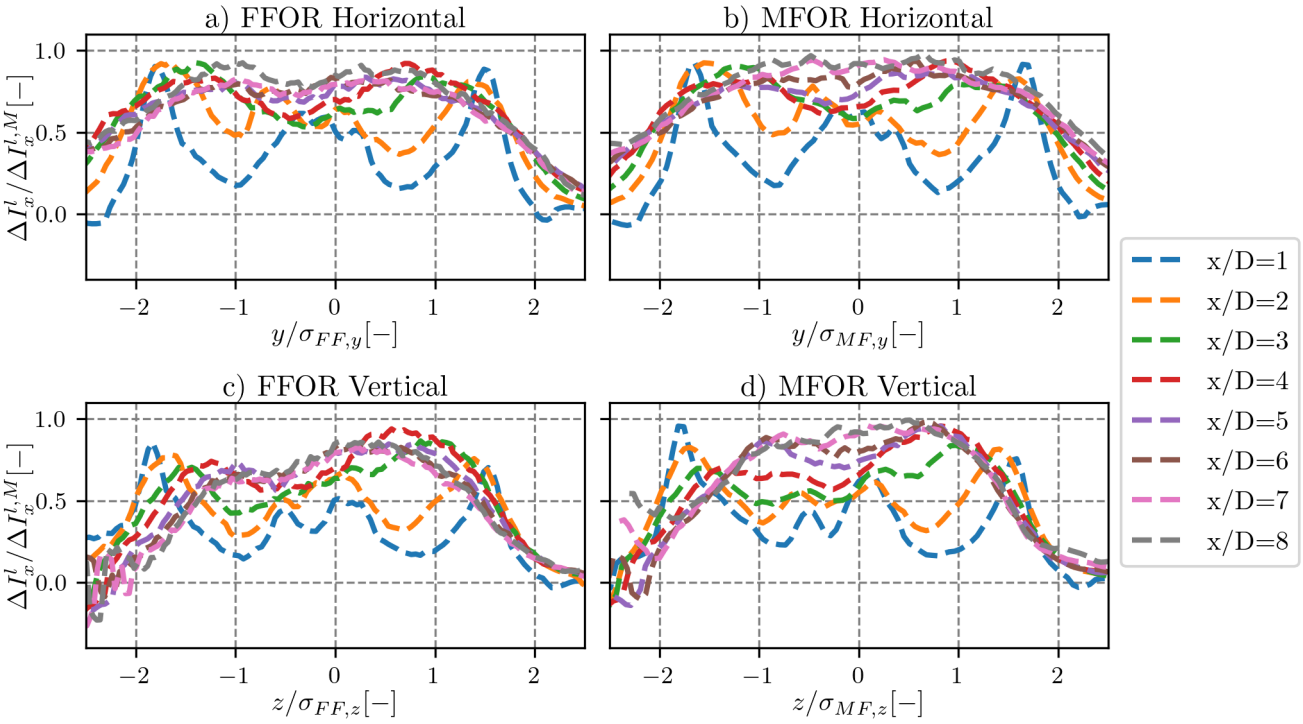

Figure B.10: Self similarity of the local added TI profiles for the stable case.

Appendix C

Demonstration of Eq. 7.9

This appendix is dedicated to the demonstration of the following relation:

$$\overline{\overline{\phi}} = \overline{\phi} * * f_c. \tag{C.1}$$

where $\overline{\phi}$ is a steady variable, f_c is the two-dimensional PDF of the time series $y_c(t), z_c(t)$ and $**$ denotes a 2D convolution. Equation C.1 can be re-written more explicitly:

$$\overline{\overline{\phi}(y - y_c(t), z - z_c(t))} = \int_{y_m \in \mathbb{R}} \int_{z_m \in \mathbb{R}} \overline{\phi}(y_m, z_m) f_c(y - y_m, z - z_m) dy_m dz_m \tag{C.2}$$

The 2D PDF is formally defined as:

$$f_c(y, z) = \frac{1}{n_t \Delta Y \Delta Z} \sum_{i=1}^{n_t} \chi_{[y_c(t_i)-\Delta Y/2, y_c(t_i)+\Delta Y/2]}(y) \chi_{[z_c(t_i)-\Delta Z/2, z_c(t_i)+\Delta Z/2]}(z) \tag{C.3}$$

where n_t is the number of samples, ΔY and ΔZ are the sizes of the mesh in the vertical and horizontal directions and $\chi_{[\phi_1,\phi_2]}$ is the indicator function on the interval $[\phi_1, \phi_2]$, defined as:

$$\chi_{[\phi_1,\phi_2]}(t) = \begin{cases} 1 & \text{if } t \in [\phi_1, \phi_2] \\ 0 & \text{else.} \end{cases} \tag{C.4}$$

Inserting Eq. C.3 into the right-hand side of Eq. C.2 leads to:

$$\frac{1}{n_t \Delta Y \Delta Z} \sum_{i=1}^{n_t} \int_{y_c(t_i)-\Delta Y/2}^{y_c(t_i)+\Delta Y/2} \int_{z_c(t_i)-\Delta Z/2}^{z_c(t_i)+\Delta Z/2} \overline{\phi}(y - y_m, z - z_m) dy_m dz_m. \tag{C.5}$$

We can then take the limit as $\Delta Y \to 0$ and $\Delta Z \to 0$ and apply a Taylor development up to the second order. It is defined for a function g at position (y_0, z_0) and with $h \to 0$ and $k \to 0$ as:

$$g(y_0 + h, z_0 + k) = g(y_0, z_0) + h \frac{\partial g}{\partial y} + k \frac{\partial g}{\partial z} + o(h + k) \tag{C.6}$$

where $o(h+k)$ means that the error induced by this approximation is negligible compared to $h+k$ as $h \to 0$ and $k \to 0$. Using this Taylor development requires the function $\overline{\phi}$ is continuous up to its second derivative. For the LES data, this is debatable but could be circumvented by estimating the residual $o(h+k)$. For the analytical model however, this is not an issue, since we only use Gaussian or products of polynomial and Gaussian functions. Applying the Taylor development with $g = \overline{\phi}$, $y_0 = y - y_c(t_i)$, $z_0 = z - z_c(t_i)$, $h = y_c(t_i) - y_m$ and $k = z_c(t_i) - z_m$ leads to:

$$\begin{aligned}\overline{\phi}(y-y_m, z-z_m) =& \overline{\phi}(y-y_c(t_i), z-z_c(t_i)) + (y_c(t_i)-y_m)\frac{\partial \overline{a}}{\partial y}(y-y_c(t_i), z-z_c(t_i)) \\ &+ (z_c(t_i)-z_m)\frac{\partial \overline{\phi}}{\partial z}(y-y_c(t_i), z-z_c(t_i)) + o(y_c(t_i)-y_m, z_c(t_i)-z_m) \quad \text{(C.7)}\end{aligned}$$

Note that this decomposition can be used since we suppose that $\Delta Y \to 0$ and $\Delta Z \to 0$, and since $y_c(t_i) - y_m < \Delta Y$ and $z_c(t_i) - z_m < \Delta Z$, it leads to $y_c(t_i) - y_m \to 0$ and $z_c(t_i) - z_m \to 0$. Moreover, if a quantity is negligible compared to $o(y_c(t_i) - y_m, z_c(t_i) - z_m)$, it is also negligible compared to $o(\Delta Y + \Delta Z)$. We thus can re-write Eq. C.5 as:

$$\begin{aligned}(C.5) =& \frac{1}{n_t \Delta Y \Delta Z}\sum_{i=1}^{n_t} \overline{\phi}(y-y_c(t_i), z-z_c(t_i)) \int_{y_c(t_i)-\Delta Y/2}^{y_c(t_i)+\Delta Y/2} \int_{z_c(t_i)-\Delta Z/2}^{z_c(t_i)+\Delta Z/2} dy_m dz_m \\ &+ \frac{1}{n_t \Delta Y \Delta Z}\sum_{i=1}^{n_t} \frac{\partial \overline{\phi}}{\partial y}(y-y_c(t_i), z-z_c(t_i)) \int_{y_c(t_i)-\Delta Y/2}^{y_c(t_i)+\Delta Y/2} \int_{z_c(t_i)-\Delta Z/2}^{z_c(t_i)+\Delta Z/2} (y_c(t_i)-y_m) dy_m dz_m \\ &+ \frac{1}{n_t \Delta Y \Delta Z}\sum_{i=1}^{n_t} \frac{\partial \overline{\phi}}{\partial z}(y-y_c(t_i), z-z_c(t_i)) \int_{y_c(t_i)-\Delta Y/2}^{y_c(t_i)+\Delta Y/2} \int_{z_c(t_i)-\Delta Z/2}^{z_c(t_i)+\Delta Z/2} (z_c(t_i)-z_m) dy_m dz_m \\ &+ \frac{1}{n_t \Delta Y \Delta Z}\sum_{i=1}^{n_t} \int_{y_c(t_i)-\Delta Y/2}^{y_c(t_i)+\Delta Y/2} \int_{z_c(t_i)-\Delta Z/2}^{z_c(t_i)+\Delta Z/2} o(\Delta Y + \Delta Z) dy_m dz_m \quad \text{(C.8)}\end{aligned}$$

The second and third lines of Eq. C.8 are equal to 0 because it is the integral of a linear function centred at the middle of the integration range. Consequently, we can write:

$$(C.5) = \frac{1}{n_t}\sum_{i=1}^{n_t} \overline{\phi}(y-y_c(t_i), z-z_c(t_i)) + o(\Delta Y + \Delta Z) \quad \text{(C.9)}$$

Finally leading to our result, up to an error negligible compared to the mesh size:

$$\overline{\phi} * * f_c = \overline{\overline{\phi}(y-y_c(t_i), z-z_c(t_i))} + o(\Delta Y + \Delta Z) \quad \text{(C.10)}$$

References

[1] Parth Bhatia, Sarah Burch, et al. Climate change 2022: Mitigation of climate change. Technical report, Intergovernmental Panel on Climate Change, 2022. https://www.ipcc.ch/report/ar6/wg3/.

[2] Kelly Trout, Greg Muttitt, et al. Existing fossil fuel extraction would warm the world beyond 1.5 c. *Environmental Research Letters*, 17(6):064010, may 2022.

[3] IEA. Net zero by 2050. Technical report, 2021. https://www.iea.org/reports/net-zero-by-2050.

[4] Ivan Komusanac, Guy Brindley, et al. Wind energy in europe: Statistics and the outlook for 2022-2026. Technical report, WindEurope, 2022. https://windeurope.org/intelligence-platform/product/wind-energy-in-europe-2021-statistics-and-the-outlook-for-2022-2026/#findings.

[5] Thomas Telsnig, Ivan Komusanac, and Carlos Eduardo Lima Da Chunha. Eu annual report. Technical report, IEA wind, 2020. https://iea-wind.org/iea-publications/.

[6] J. K. Lundquist, K. K. DuVivier, et al. Costs and consequences of wind turbine wake effects arising from uncoordinated wind energy development. *Nature Energy*, 4(1):26–34, nov 2018.

[7] F. Porté-Agel, M. Bastankhah, and S. Shamsoddin. Wind-Turbine and Wind-Farm Flows: A Review. *Boundary Layer Meteorol*, September 2019.

[8] R. J. Barthelmie and L. E. Jensen. Evaluation of wind farm efficiency and wind turbine wakes at the Nysted offshore wind farm. *Wind Energy*, 13(6):573–586, May 2010.

[9] Haiying Sun, Xiaoxia Gao, and Hongxing Yang. A review of full-scale wind-field measurements of the wind-turbine wake effect and a measurement of the wake-interaction effect. *Renewable and Sustainable Energy Reviews*, 132:110042, 2020.

[10] Pierre-Antoine Joulin. *Modélisation à fine échelle des interactions entre parcs éoliens et météorologie locale*. PhD thesis, SDU2E, 2019. Thèse de doctorat dirigée par Masson, Valéry Océan, atmosphère, climat Toulouse, INPT 2019.

[11] Mahdi Abkar and Fernando Porté-Agel. Influence of atmospheric stability on wind-turbine wakes: A large-eddy simulation study. *Physics of Fluids*, 27(3):035104, March 2015.

[12] Patrick Murphy, Julie K. Lundquist, and Paul Fleming. How wind speed shear and directional veer affect the power production of a megawatt-scale operational wind turbine. *Wind Energy Science*, 5(3):1169–1190, sep 2020.

[13] William Corrêa Radünz, Yoshiaki Sakagami, et al. Influence of atmospheric stability on wind farm performance in complex terrain. *Applied Energy*, 282:116149, jan 2021.

[14] Gunner C. Larsen, Helge Aa Madsen, et al. Wake meandering: a pragmatic approach. *Wind Energy*, 11(4):377–395, July 2008.

[15] Fernando Carbajo Fuertes, Corey Markfort, and Fernando Porté-Agel. Wind Turbine Wake Characterization with Nacelle-Mounted Wind Lidars for Analytical Wake Model Validation. *Remote Sensing*, 10(5):668, April 2018.

[16] Yvonne Käsler, Stephan Rahm, et al. Wake measurements of a multi-mw wind turbine with coherent long-range pulsed doppler wind lidar. *Journal of Atmospheric and Oceanic Technology*, 27(9):1529 – 1532, 2010.

[17] R.J. Barthelmie, S.C. Pryor, et al. Wind turbine wake characterization in complex terrain via integrated doppler lidar data from the perdigão experiment. *Journal of Physics: Conference Series*, 1037:052022, jun 2018.

[18] G.C. Larsen, A.T. Pedersen, et al. Full-scale 3d remote sensing of wake turbulence - a taster. *J Phys : Conf Ser*, 1256:012001, jul 2019.

[19] P Doubrawa, M Debnath, et al. Benchmarks for model validation based on LiDAR wake measurements. *J Phys : Conf Ser*, 1256:012024, jul 2019.

[20] Leonardo P. Chamorro and Fernando Porté-Agel. A Wind-Tunnel Investigation of Wind-Turbine Wakes: Boundary-Layer Turbulence Effects. *Boundary Layer Meteorol*, 132(1):129–149, April 2009.

[21] N Coudou, M Moens, et al. Development of wake meandering detection algorithms and their application to large eddy simulations of an isolated wind turbine and a wind farm. *J Phys : Conf Ser*, 1037:072024, jun 2018.

[22] G. España, S. Aubrun, et al. Wind tunnel study of the wake meandering downstream of a modelled wind turbine as an effect of large scale turbulent eddies. *Journal of Wind Engineering and Industrial Aerodynamics*, 101:24–33, feb 2012.

[23] G. España, S. Aubrun, et al. Spatial study of the wake meandering using modelled wind turbines in a wind tunnel. *Wind Energy*, 14(7):923–937, oct 2011.

[24] E. Barlas, S. Buckingham, and J. van Beeck. Roughness effects on wind-turbine wake dynamics in a boundary-layer wind tunnel. *Boundary Layer Meteorol*, 158(1):27–42, sep 2015.

[25] Hui Hu, Wei Tian, et al. *An Experimental Study on the Performances of Wind Turbines over Complex Terrains*.

[26] P E Hancock, S Zhang, et al. Wind tunnel simulation of a wind turbine wake in neutral, stable and unstable wind flow. *J Phys : Conf Ser*, 555:012047, dec 2014.

[27] Leonardo P. Chamorro and Fernando Porté-Agel. Effects of thermal stability and incoming boundary-layer flow characteristics on wind-turbine wakes: A wind-tunnel study. *Boundary Layer Meteorol*, 136(3):515–533, jun 2010.

[28] D. Medici and P. H. Alfredsson. Measurements behind model wind turbines: further evidence of wake meandering. *Wind Energy*, 11(2):211–217, March 2008.

[29] M. Bastankhah and F. Porté-Agel. Wind tunnel study of the wind turbine interaction with a boundary-layer flow: Upwind region, turbine performance, and wake region. *Physics of Fluids*, 29(6):065105, jun 2017.

[30] Chengyu Wang, Filippo Campagnolo, et al. How realistic are the wakes of scaled wind turbine models? *Wind Energy Science*, 6(3):961–981, jun 2021.

[31] B. Maronga, M. Gryschka, et al. The parallelized large-eddy simulation model (PALM) version 4.0 for atmospheric and oceanic flows: model formulation, recent developments, and future perspectives. *Geoscientific Model Development*, 8(8):2515–2551, aug 2015.

[32] Martin Dörenkämper, Björn Witha, et al. The impact of stable atmospheric boundary layers on wind-turbine wakes within offshore wind farms. *Journal of Wind Engineering and Industrial Aerodynamics*, 144:146–153, sep 2015.

[33] Christine Lac, Jean-Pierre Chaboureau, et al. Overview of the meso-NH model version 5.4 and its applications. *Geoscientific Model Development*, 11(5):1929–1969, may 2018.

[34] Daniel Nugent and Benjamin K. Sovacool. Assessing the lifecycle greenhouse gas emissions from solar PV and wind energy: A critical meta-survey. *Energy Policy*, 65:229–244, feb 2014.

[35] Cédric Le Cunff, Jean-Michel Heurtier, et al. Fully coupled floating wind turbine simulator based on nonlinear finite element method: Part i — methodology. In *Volume 8: Ocean Renewable Energy*. American Society of Mechanical Engineers, jun 2013.

[36] Jason M. Jonkman, Jennifer Annoni, et al. Development of FAST.farm: A new multi-physics engineering tool for wind-farm design and analysis. In *35th Wind Energy Symposium*. American Institute of Aeronautics and Astronautics, jan 2017.

[37] Charles Meneveau. Big wind power: seven questions for turbulence research. *Journal of Turbulence*, 20(1):2–20, jan 2019.

[38] Lilla Koloszár. Lecture notes in computational methods for incompressible fluids, 2018.

[39] Paul Valery University. Une variable numérique : dispersion et variance. `https://www.univ-montp3.fr/miap/ens/site/uploads/Main.StatL2S4/Cours11E46XP3.pdf`. Accessed: 2022-06-07.

[40] Ulf Högström, J. C. R. Hunt, and Ann-Sofi Smedman. Theory and measurements for turbulence spectra and variances in the atmospheric neutral surface layer. *Boundary Layer Meteorol*, 103(1):101–124, apr 2002.

[41] Stephen B. Pope. *Turbulent Flows*. Cambridge University Press, August 2000.

[42] Xiaoli G. Larsén, Søren E. Larsen, and Erik L. Petersen. Full-scale spectrum of boundary-layer winds. *Boundary Layer Meteorol*, 159(2):349–371, feb 2016.

[43] Leonardo Alcayaga, Gunner Chr. Larsen, et al. Large-scale coherent structures in the atmosphere over a flat terrain. *J Phys : Conf Ser*, 1618:062030, sep 2020.

[44] Météo-France. La structure de l'atmosphère. `http://education.meteofrance.fr/dossiers-thematiques/le-fonctionnement-de-l-atmosphere/la-composition-de-l-atmosphere/la-structure-de-latmosphere`. Accessed: 2022-06-07.

[45] Roland B. Stull, editor. *An Introduction to Boundary Layer Meteorology*. Springer Netherlands, 1988.

[46] J. A. Businger, J. C. Wyngaard, et al. Flux-profile relationships in the atmospheric surface layer. *J Atmospheric Sci*, 28(2):181–189, mar 1971.

[47] Yu Cheng, Qi Li, et al. A model for turbulence spectra in the equilibrium range of the stable atmospheric boundary layer. *Journal of Geophysical Research: Atmospheres*, 125(5), mar 2020.

[48] Francesco Tampieri. *Turbulence and Dispersion in the Planetary Boundary Layer*. Springer-Verlag GmbH, 2016.

[49] Isaac Van der Hoven. POWER SPECTRUM OF HORIZONTAL WIND SPEED IN THE FREQUENCY RANGE FROM 0.0007 TO 900 CYCLES PER HOUR. *Journal of Meteorology*, 14(2):160–164, apr 1957.

[50] J. C. Kaimal, J. C. Wyngaard, et al. Spectral characteristics of surface-layer turbulence. *Q J R Meteorolog Soc*, 98(417):563–589, jul 1972.

[51] R. Bolgiano. Turbulent spectra in a stably stratified atmosphere. *Journal of Geophysical Research*, 64(12):2226–2229, dec 1959.

[52] IEC. Iec61400-1 : Wind turbine generator systems. Technical report, CENELEC, 2004.

[53] Delphine De Tavernier and Dominic von Terzi. The emergence of supersonic flow on wind turbines. *Journal of Physics: Conference Series*, 2265(4):042068, may 2022.

[54] Quentin Rodier. *Paramétrisation de la turbulence atmosphérique dans la couche limite stable*. PhD thesis, Université Toulouse Sabatier, 2017.

[55] Kyoungboo Yang. Geometry design optimization of a wind turbine blade considering effects on aerodynamic performance by linearization. *Energies*, 13(9), 2020.

[56] M.O.L. Hansen. *Aerodynamics of Wind Turbines*. Earthscan, 2013.

[57] Jens Nørkær Sørensen. Aerodynamic aspects of wind energy conversion. *Annual Review of Fluid Mechanics*, 43(1):427–448, jan 2011.

[58] L. P. Chamorro, C. Hill, et al. On the interaction between a turbulent open channel flow and an axial-flow turbine. *Journal of Fluid Mechanics*, 716:658–670, jan 2013.

[59] Matthew J. Churchfield, Sang Lee, et al. A numerical study of the effects of atmospheric and wake turbulence on wind turbine dynamics. *Journal of Turbulence*, 13:N14, jan 2012.

[60] Ewan Machefaux, Gunner C. Larsen, et al. An experimental and numerical study of the atmospheric stability impact on wind turbine wakes. *Wind Energy*, 19(10):1785–1805, dec 2015.

[61] Gunner Chr. Larsen, Helge Madsen Aagaard, et al. *Dynamic wake meandering modeling*. Risø National Laboratory, 2007.

[62] J. F. Ainslie. Calculating the flowfield in the wake of wind turbines. *Journal of Wind Engineering and Industrial Aerodynamics*, 27(1-3):213–224, January 1988.

[63] Rolf-Erik Keck, Martin de Maré, et al. Two improvements to the dynamic wake meandering model: including the effects of atmospheric shear on wake turbulence and incorporating turbulence build-up in a row of wind turbines. *Wind Energy*, pages n/a–n/a, November 2013.

[64] Xiaolei Yang and Fotis Sotiropoulos. Wake characteristics of a utility-scale wind turbine under coherent inflow structures and different operating conditions. *Phys Rev Fluids*, 4(2), feb 2019.

[65] S.-P. Breton, J. Sumner, et al. A survey of modelling methods for high-fidelity wind farm simulations using large eddy simulation. *Philos Trans R Soc Math Phys Eng Sci*, 375(2091):20160097, March 2017.

[66] Shengbai Xie and Cristina Archer. Self-similarity and turbulence characteristics of wind turbine wakes via large-eddy simulation. *Wind Energy*, 18(10):1815–1838, August 2014.

[67] A. Crespo, J. Hernández, and S. Frandsen. Survey of modelling methods for wind turbine wakes and wind farms. *Wind Energy*, 2(1):1–24, January 1999.

[68] Ingrid Neunaber, Michael Hölling, et al. Distinct turbulent regions in the wake of a wind turbine and their inflow-dependent locations: The creation of a wake map. *Energies*, 13(20):5392, oct 2020.

[69] Giovanni De Cillis, Stefania Cherubini, et al. POD-based analysis of a wind turbine wake under the influence of tower and nacelle. *Wind Energy*, nov 2020.

[70] Wei Zhang, Corey D. Markfort, and Fernando Porté-Agel. Near-wake flow structure downwind of a wind turbine in a turbulent boundary layer. *Experiments in Fluids*, 52(5):1219–1235, December 2011.

[71] Antonia Englberger and Andreas Dörnbrack. Impact of Neutral Boundary-Layer Turbulence on Wind-Turbine Wakes: A Numerical Modelling Study. *Boundary Layer Meteorol*, 162(3):427–449, October 2016.

[72] Alexander Pique, Mark A. Miller, and Marcus Hultmark. Characterization of the wake behind a horizontal-axis wind turbine (HAWT) at very high reynolds numbers. *J Phys : Conf Ser*, 1618:062039, sep 2020.

[73] X. Mao and J. N. Sørensen. Far-wake meandering induced by atmospheric eddies in flow past a wind turbine. *Journal of Fluid Mechanics*, 846:190–209, may 2018.

[74] Tuhfe Göçmen, Paul van der Laan, et al. Wind turbine wake models developed at the technical university of Denmark: A review. *Renewable Sustainable Energy Rev*, 60:752–769, July 2016.

[75] NO Jensen. A note on wind turbine interaction. techreport, Risoe National Laboratory, 1983.

[76] Sten Frandsen, Rebecca Barthelmie, et al. Analytical modelling of wind speed deficit in large offshore wind farms. *Wind Energy*, 9(1-2):39–53, January 2006.

[77] Majid Bastankhah and Fernando Porté-Agel. A new analytical model for wind-turbine wakes. *Renewable Energy*, 70:116–123, October 2014.

[78] Aidan Keane, Pablo E. Olmos Aguirre, et al. An analytical model for a full wind turbine wake. *J Phys : Conf Ser*, 753:032039, September 2016.

[79] Niranjan S. Ghaisas and Cristina L. Archer. Geometry-Based Models for Studying the Effects of Wind Farm Layout. *Journal of Atmospheric and Oceanic Technology*, 33(3):481–501, March 2016.

[80] Paula Doubrawa, Eliot W. Quon, et al. Multimodel validation of single wakes in neutral and stratified atmospheric conditions. *Wind Energy*, jul 2020.

[81] Yu-Ting Wu and Fernando Porté-Agel. Atmospheric Turbulence Effects on Wind-Turbine Wakes: An LES Study. *Energies*, 5(12):5340–5362, December 2012.

[82] Philippe Chatelain, Stéphane Backaert, et al. Large Eddy Simulation of Wind Turbine Wakes. *Flow Turbulence and Combustion*, 91(3):587–605, June 2013.

[83] Bowen Du, Mingwei Ge, et al. Influence of atmospheric stability on wind turbine wakes with a certain hub-height turbulence intensity. *Physics of Fluids*, 2021.

[84] Fernando Porté-Agel, Yu-Ting Wu, et al. Large-eddy simulation of atmospheric boundary layer flow through wind turbines and wind farms. *Journal of Wind Engineering and Industrial Aerodynamics*, 99(4):154–168, April 2011.

[85] Davide Conti, Nikolay Dimitrov, et al. Wind turbine wake characterization using the Spinner-Lidar measurements. *J Phys : Conf Ser*, 1618:062040, sep 2020.

[86] Antonia Englberger, Andreas Dörnbrack, and Julie K. Lundquist. Does the rotational direction of a wind turbine impact the wake in a stably stratified atmospheric boundary layer? *Wind Energy Science*, 5(4):1359–1374, oct 2020.

[87] Hao Lu and Fernando Porté-Agel. Large-eddy simulation of a very large wind farm in a stable atmospheric boundary layer. *Physics of Fluids*, 23(6):065101, June 2011.

[88] H M Johlas, L A Martínez-Tossas, et al. Large eddy simulations of offshore wind turbine wakes for two floating platform types. *J Phys : Conf Ser*, 1452(1):012034, jan 2020.

[89] Dries Allaerts and Johan Meyers. Boundary-layer development and gravity waves in conventionally neutral wind farms. *Journal of Fluid Mechanics*, 814:95–130, feb 2017.

[90] Tanmoy Chatterjee, Jing Li, et al. Wind farm response to mesoscale-driven coastal low level jets: a multiscale large eddy simulation study. *Journal of Physics: Conference Series*, 2265(2):022004, may 2022.

[91] L. P. Chamorro, M. Guala, et al. On the evolution of turbulent scales in the wake of a wind turbine model. *Journal of Turbulence*, 13:N27, jan 2012.

[92] Victor P. Stein and Hans-Jakob Kaltenbach. Non-equilibrium scaling applied to the wake evolution of a model scale wind turbine. *Energies*, 12(14):2763, jul 2019.

[93] Nicolas Coudou, Sophia Buckingham, et al. Experimental study on the wake meandering within a scale model wind farm subject to a wind-tunnel flow simulating an atmospheric boundary layer. *Boundary Layer Meteorol*, 167(1):77–98, dec 2017.

[94] Xu Ning and Decheng Wan. LES study of wake meandering in different atmospheric stabilities and its effects on wind turbine aerodynamics. *Sustainability*, 11(24):6939, dec 2019.

[95] M. J. Churchfield, P. J. Moriarty, et al. Comparison of the Dynamic Wake Meandering Model, Large-Eddy Simulation, and Field Data at the Egmond aan Zee Offshore Wind Plant: Preprint. 2014.

[96] Aliza Abraham, Teja Dasari, and Jiarong Hong. Effect of turbine nacelle and tower on the near wake of a utility-scale wind turbine. *Journal of Wind Engineering and Industrial Aerodynamics*, 193:103981, oct 2019.

[97] Juan José Trujillo. *Large scale dynamics ofwind turbine wakes - Measurement and modelling in the full field*. PhD thesis, Carl von Ossietzky Universität Oldenburg, 2017.

[98] Valery L. Okulov, Igor V. Naumov, et al. A regular strouhal number for large-scale instability in the far wake of a rotor. *Journal of Fluid Mechanics*, 747:369–380, apr 2014.

[99] P. Doubrawa, L. A. Martínez-Tossas, et al. Comparison of mean and dynamic wake characteristics between research-scale and full-scale wind turbines. *J Phys : Conf Ser*, 1037:072053, jun 2018.

[100] Rolf-Erik Keck, Martin de Maré, et al. On atmospheric stability in the dynamic wake meandering model. *Wind Energy*, 17(11):1689–1710, September 2013.

[101] Juan-José Trujillo, Ferhat Bingöl, et al. Light detection and ranging measurements of wake dynamics. part II: two-dimensional scanning. *Wind Energy*, 14(1):61–75, jan 2011.

[102] Yann-Aël Muller, Sandrine Aubrun, and Christian Masson. Determination of real-time predictors of the wind turbine wake meandering. *Experiments in Fluids*, 56(3), mar 2015.

[103] John K. Kaldellis, Panagiotis Triantafyllou, and Panagiotis Stinis. Critical evaluation of wind turbines' analytical wake models. *Renewable and Sustainable Energy Reviews*, 144:110991, jul 2021.

[104] Cristina L. Archer, Ahmadreza Vasel-Be-Hagh, et al. Review and evaluation of wake loss models for wind energy applications. *Applied Energy*, 226:1187–1207, September 2018.

[105] Jens N. Sørensen, Robert F. Mikkelsen, et al. Simulation of wind turbine wakes using the actuator line technique. *Philos Trans R Soc Math Phys Eng Sci*, 373(2035):20140071, February 2015.

[106] I. Katic, J. Højstrup, and N. O. Jensen. A Simple Model for Cluster Efficiency. In W. Palz and E. Sesto, editors, *EWEC'86. Proceedings. Vol. 1*, pages 407–410. A. Raguzzi, 1987.

[107] Alfredo Peña, Pierre-Elouan Réthoré, and Ole Rathmann. Modeling large offshore wind farms under different atmospheric stability regimes with the Park wake model. *Renewable Energy*, 70:164–171, October 2014.

[108] Alfredo Peña, Pierre-Elouan Réthoré, and M. Paul van der Laan. On the application of the Jensen wake model using a turbulence-dependent wake decay coefficient: the Sexbierum case. *Wind Energy*, 19(4):763–776, May 2015.

[109] Amin Niayifar and Fernando Porté-Agel. Analytical modeling of wind farms:a new approach for power prediction. *Energies*, 2016.

[110] Wai-Chi Cheng and Fernando Porté-Agel. A Simple Physically-Based Model for Wind-Turbine Wake Growth in a Turbulent Boundary Layer. *Boundary Layer Meteorol*, 169(1):1–10, June 2018.

[111] Takeshi Ishihara and Guo-Wei Qian. A new Gaussian-based analytical wake model for wind turbines considering ambient turbulence intensities and thrust coefficient effects. *Journal of Wind Engineering and Industrial Aerodynamics*, 177:275–292, June 2018.

[112] Johannes Schreiber, Amr Balbaa, and Carlo L. Bottasso. Brief communication: A double-gaussian wake model. *Wind Energy Science*, 5(1):237–244, feb 2020.

[113] Carl R. Shapiro, Genevieve M. Starke, et al. A wake modeling paradigm for wind farm design and control. *Energies*, 12(15):2956, aug 2019.

[114] Frédéric Blondel and Marie Cathelain. An alternative form of the super-gaussian wind turbine wake model. jan 2020.

[115] Yu Cheng, Mingming Zhang, et al. A new analytical model for wind turbine wakes based on Monin-Obukhov similarity theory. *Applied Energy*, 239:96–106, April 2019.

[116] Mahdi Abkar, Jens Sørensen, and Fernando Porté-Agel. An Analytical Model for the Effect of Vertical Wind Veer on Wind Turbine Wakes. *Energies*, 11(7):1838, July 2018.

[117] Sten Tronæs Frandsen. *Turbulence and turbulence-generated structural loading in wind turbine clusters*. PhD thesis, DTU, 2007. Risø-R-1188(EN).

[118] A. Crespo and J. Hernandez. Turbulence characteristics in wind-turbine wakes. *Journal of Wind Engineering and Industrial Aerodynamics*, 61(1):71–85, June 1996.

[119] Unsal Hassan. *A wind tunnel investigation of the wake structure within small wind turbine farms*. Harwell Laboratory, Energy Technology Support Unit, 1993.

[120] J. Jonkman, P. Doubrawa, et al. Validation of FAST.Farm Against Large-Eddy Simulations. *J Phys : Conf Ser*, 1037:062005, June 2018.

[121] I. Reinwardt, N. Gerke, et al. Validation of wind turbine wake models with focus on the dynamic wake meandering model. *J Phys : Conf Ser*, 1037:072028, June 2018.

[122] Jakob Mann. Wind field simulation. *Probabilistic Engineering Mechanics*, 13(4):269–282, oct 1998.

[123] Rolf-Erik Keck, Dick Veldkamp, et al. *A consistent turbulence formulation for the dynamic wake meandering model in the atmospheric boundary layer*. PhD thesis, DTU, Denmark, 2013.

[124] J. F. Ainslie. Development of an eddy viscosity model for wind turbine wakes. In *7th BWEA Wind Energy Conf.*, 1985.

[125] H. Aa. Madsen, G. C. Larsen, et al. Calibration and validation of the dynamic wake meandering model for implementation in an aeroelastic code. *Journal of Solar Energy Engineering*, 132(4), oct 2010.

[126] Rolf-Erik Keck, Dick Veldkamp, et al. Implementation of a Mixing Length Turbulence Formulation Into the Dynamic Wake Meandering Model. *Journal of Solar Energy Engineering*, 134(2), March 2012.

[127] Davide Conti, Nikolay Dimitrov, et al. Probabilistic estimation of the dynamic wake meandering model parameters using SpinnerLidar-derived wake characteristics. *Wind Energy Science*, 6(5):1117–1142, sep 2021.

[128] Wai Hou Lio, Gunner Chr. Larsen, and Gunhild R. Thorsen. Dynamic wake tracking using a cost-effective LiDAR and kalman filtering: Design, simulation and full-scale validation. *Renewable Energy*, 172:1073–1086, jul 2021.

[129] Robert Braunbehrens and Antonio Segalini. A statistical model for wake meandering behind wind turbines. *Journal of Wind Engineering and Industrial Aerodynamics*, 193:103954, October 2019.

[130] J. F. Ainslie. Wake modelling and the prediction of turbulence properties. In *8th BWEA Wind Energy Conf.*, 1986.

[131] Frederic Blondel and Marie Cathelain. Extension of the farmshadow library to large wind farm simulation using added-turbulence models: the farmshadow v2.0 library. Technical report, IFP Energies nouvelles, 2019.

[132] A. Leonard. Energy cascade in large-eddy simulations of turbulent fluid flows. In *Turbulent Diffusion in Environmental Pollution, Proceedings of a Symposium held at Charlottesville*, pages 237–248. Elsevier, 1975.

[133] J. Smagorinsky. General circulation experiment with the primitive equations. *Monthly Weather Review*, 91(3):99–164, mar 1963.

[134] M. Germano. A proposal for a redefinition of the turbulent stresses in the filtered navier–stokes equations. *Physics of Fluids*, 29(7):2323, 1986.

[135] J P Boris, F F Grinstein, et al. New insights into large eddy simulation. *Fluid Dynamics Research*, 10(4-6):199–228, dec 1992.

[136] J. P. Lafore, J. Stein, et al. The meso-NH atmospheric simulation system. part i: adiabatic formulation and control simulations. *Annales De Geophysique*, 16(1):90–109, 1998.

[137] J. Cuxart, P. Bougeault, and J.-L. Redelsperger. A turbulence scheme allowing for mesoscale and large-eddy simulations. *Q J R Meteorolog Soc*, 126(562):1–30, jan 2000.

[138] James W. Deardorff. Stratocumulus-capped mixed layers derived from a three-dimensional model. *Boundary Layer Meteorol*, 18(4):495–527, jun 1980.

[139] Quentin Rodier, Valéry Masson, et al. Evaluation of a buoyancy and shear based mixing length for a turbulence scheme. *Subduction Zone Geodynamics*, 5, aug 2017.

[140] Rachel Honnert, Valery Masson, et al. A theoretical analysis of mixing length for atmospheric models from micro to large scales. *Subduction Zone Geodynamics*, 2021.

[141] J. L. Redelsperger, F. Mahé, and P. Carlotti. A simple and general subgrid model suitable both for surface layer and free-stream turbulence. *Boundary Layer Meteorol*, 101(3):375–408, dec 2001.

[142] J. Stein, E. Richard, et al. High-resolution non-hydrostatic simulations of flash-flood episodes with grid-nesting and ice-phase parameterization. *Meteorology and Atmospheric Physics*, 72(2-4):203–221, feb 2000.

[143] H. Glauert. Airplane Propellers. In *Aerodynamic Theory*, pages 169–360. Springer Berlin Heidelberg, 1935.

[144] Jens N. Sørensen and Wen Zhong Shen. Numerical modeling of wind turbine wakes. *J Fluids Eng*, 124(2):393–399, may 2002.

[145] Niels Troldborg. *Actuator Line Modeling of Wind Turbine Wakes*. PhD Thesis, 2009.

[146] Pankaj K. Jha, Matthew J. Churchfield, et al. Guidelines for volume force distributions within actuator line modeling of wind turbines on large-eddy simulation-type grids. *Journal of Solar Energy Engineering*, 136(3):031003, jan 2014.

[147] Pierre-Antoine Joulin, Maria Laura Mayol, et al. The actuator line method in the meteorological LES model meso-NH to analyze the horns rev 1 wind farm photo case. *Subduction Zone Geodynamics*, 7, jan 2020.

[148] Richard J.A.M. Stevens, Luis A. Martínez-Tossas, and Charles Meneveau. Comparison of wind farm large eddy simulations using actuator disk and actuator line models with wind tunnel experiments. *Renewable Energy*, 116:470–478, feb 2018.

[149] Niels Troldborg, Jens N. Sorensen, and Robert Mikkelsen. Numerical simulations of wake characteristics of a wind turbine in uniform inflow. *Wind Energy*, 13(1):86–99, jan 2010.

[150] R. C. Storey, S. E. Norris, and J. E. Cater. An actuator sector method for efficient transient wind turbine simulation. *Wind Energy*, 18(4):699–711, mar 2014.

[151] PA Joulin, ML Mayol, et al. Coupling the actuator line method to the high order meteorological LES model meso-NH to study wind farm wakes impacts on local meteorology. *J Phys : Conf Ser*, 1256:012019, jul 2019.

[152] E Jézéquel, M Cathelain, et al. Validation of wind turbine wakes modelled by the meso-NH LES solver under different cases of stability. *J Phys : Conf Ser*, 1934(1):012003, may 2021.

[153] Christopher Lee Kelley and Brandon Lee Ennis. SWiFT site atmospheric characterization. Technical report, jan 2016.

[154] Eliot Quon. Samwich box: Simulated and measured wake identification and characterization toolbox¶. `https://ewquon.github.io/waketracking/`.

[155] M. P. van der Laan, M. Baungaard, and M. Kelly. Inflow modeling for wind farm flows in RANS. *J Phys : Conf Ser*, 1934(1):012012, may 2021.

[156] Erwan Jézéquel, Frédéric Blondel, and Valéry Masson. Breakdown of the velocity and turbulence in the wake of a wind turbine – part 1: large eddy simulations study. may 2022.

[157] E. W. Quon, P. Doubrawa, and M. Debnath. Comparison of rotor wake identification and characterization methods for the analysis of wake dynamics and evolution. *J Phys : Conf Ser*, 1452:012070, jan 2020.

[158] Henry Korb, Henrik Asmuth, et al. Exploring the application of reinforcement learning to wind farm control. *J Phys : Conf Ser*, 1934(1):012022, may 2021.

[159] Lukas Vollmer, Gerald Steinfeld, et al. Estimating the wake deflection downstream of a wind turbine in different atmospheric stabilities: an LES study. *Wind Energy Science*, 1(2):129–141, sep 2016.

[160] Mehdi Sadeghi, Karine Truffin, et al. Development and application of bivariate 2d-EMD for the analysis of instantaneous flow structures and cycle-to-cycle variations of in-cylinder flow. *Flow, Turbulence and Combustion*, 106(1):231–259, aug 2020.

[161] Erwan Jézéquel, Frédéric Blondel, and Valéry Masson. Breakdown of the velocity and turbulence in the wake of a wind turbine – part 2: Analytical modeling. may 2022.

[162] Daniel Duda, Václav Uruba, and Vitalii Yanovych. Wake width: Discussion of several methods how to estimate it by using measured experimental data. *Energies*, 14(15), 2021.

[163] Peter Brugger, Corey Markfort, and Fernando Porté-Agel. Field measurements of wake meandering at a utility-scale wind turbine with nacelle-mounted doppler lidars. *Wind Energy Science*, 7(1):185–199, feb 2022.

[164] Erwan Jézéquel, Frédéric Blondel, and Valéry Masson. Analysis of wake properties and meandering under different cases of atmospheric stability: a large eddy simulation study. *Journal of Physics: Conference Series*, 2265(2):022067, may 2022.

[165] Giacomo Valerio Iungo, Vignesh Santhanagopalan, et al. Parabolic RANS solver for low-computational-cost simulations of wind turbine wakes. *Wind Energy*, 21(3):184–197, dec 2017.

[166] Jeremy Teitelbaum. Convolution of gaussians is gaussian. https://jeremy9959.net/Math-5800-Spring-2020/notebooks/convolution_of_gaussians.html. Accessed: 2022-04-29.

[167] David Scherfgen. Integral calculator. https://www.integral-calculator.com/. Accessed: 2022-04-29.

[168] Matthew J. Churchfield, Scott J. Schreck, et al. An advanced actuator line method for wind energy applications and beyond. In *35th Wind Energy Symposium*. American Institute of Aeronautics and Astronautics, jan 2017.

List of Figures

1 Performances of the Horns Rev 1 wind farm 2
2 Degree of modelling and cost of different methods to assess wake effects. 3
3 Performances du parc de Horns Rev 1 8
4 Degré de modélisation et coût des différentes méthodes existants pour estimer les effets de sillage. 10

1.1 The Reynolds' experiment. 18
1.2 Reynolds decomposition applied to a time-dependent velocity signal. 20
1.3 A cumulus highlighting the different structures of turbulence. 23
1.4 The different layers of the terrestrial atmosphere. 26
1.5 Visualisations of different ABL states 28
1.6 Typical profiles of mean virtual potential temperature θ_v and mean velocity magnitude. 29
1.7 The impact of the different parameters on the theoretical velocity profile in the SL. . 31

2.1 Composition of a wind turbine. 40
2.2 Schematic of the lift and drag forces acting on an airfoil. 41
2.3 Schematic of the mean wake structure. 43
2.4 Isocontours of turbulence intensity simulated with LES under unstable, neutral and stable conditions. 46
2.5 Isocontours of wind velocity in the wake with and without veer. 47
2.6 Schematic of the moving and fixed frames of reference 49
2.7 The effect of averaging on the wake's velocity deficit in the FFOR and the MFOR. . . 50
2.8 Working principle of analytical wake modelling. 52
2.9 Near wake velocity deficit modelling. 56
2.10 The dynamic wake meandering model. 59

3.1 Separation of the turbulence spectrum in resolved and subgrid parts. 66
3.2 Grid nesting principle in Meso-NH 73
3.3 Schematic of the time splitting principle. Courtesy of [10] 76

3.4 Comparison of the efforts evaluated in Meso-NH and from the Mexico experiments. . 77

4.1 Schematic of the SWiFT facility used for this benchmark. 82
4.2 Flowchart of the methodology of the presented work. 84
4.3 Spectral analysis of the turbulence build-up region. 85
4.4 Illustration of the successive nestings in the neutral simulation. 86
4.5 Neutral benchmark: mean inflow (65 m upstream the wind turbine), Y-averaged. . . . 88
4.6 Neutral benchmark: velocity spectra (65 m upstream the wind turbine). 88
4.7 Neutral benchmark: mean turbine response. 89
4.8 Neutral benchmark: mean velocity deficit in the wake at hub height. 90
4.9 Neutral benchmark: wake meandering in the y and z directions. 90
4.10 Neutral benchmark: mean velocity deficit in the MFOR. 91
4.11 Time step sensitivity: mean tangential and normal forces on the blades. 92
4.12 Time step sensitivity: vertical profiles of mean velocity deficit in the wake at $y = y_{wt}$. 92
4.13 Time step sensitivity: vertical profiles of mean TKE in the wake at $y = y_{wt}$. 93
4.14 Unstable benchmark: mean inflow (65 m upstream the wind turbine), Y-averaged. . . 94
4.15 Inflow u and v spectra for the unstable benchmark 95
4.16 Unstable benchmark: mean turbine response. 95
4.17 Unstable benchmark: mean velocity in the FFOR deficit in the wake at hub height. . 96
4.18 Unstable benchmark: wake meandering in the y and z directions. 96
4.19 Unstable benchmark: mean velocity deficit in the MFOR in the wake at hub height. . 97
4.20 Stable benchmark: mean inflow (65 m upstream the wind turbine), Y-averaged. . . . 98
4.21 Stable benchmark: mean turbine response. 99
4.22 Stable benchmark: mean velocity deficit in the wake at hub height. 99

5.1 Instantaneous velocity in the wake with U_∞. 102
5.2 Two ways to define the unperturbed velocity. 105
5.3 Instantaneous velocity in the wake with U_{ref}. 106
5.4 Spectra of the wake centre time series. 107
5.5 Instantaneous velocity in the wake with $< U_\infty >$. 107
5.6 Instantaneous velocity in the wake with $< U_{ref} >$. 108
5.7 Tracking results. 110
5.8 Ambiguous tracking results. 111
5.9 Time series of the wake centre's horizontal coordinate. 113
5.10 Time series of the wake centre's vertical coordinate. 114

5.11 Spectra of the wake centre's vertical coordinate. 114
5.12 Impact of the wake tracking algorithm on the amount of meandering. 115
5.13 Impact of the wake tracking algorithm on the MFOR 116

6.1 Amount of wake meandering in the horizontal and vertical directions. 120
6.2 Self-similarity of the wake centre histogram for the neutral case. 121
6.3 Self-similarity of the wake centre histogram for the unstable case. 122
6.4 Self-similarity of the wake centre histogram for the stable case. 123
6.5 Wake widths computed with Eq. 6.4. 124
6.6 Wake widths computed with Eq. 6.5. 125
6.7 Wake widths in the FFOR: comparison between measured and predictions from MFOR and meandering. 126
6.8 Maximum values of velocity deficit in both frames of reference. 127
6.9 Self-similarity of the velocity deficit profiles for the neutral case. 128
6.10 Self-similarity of the velocity deficit profiles for the unstable case. 128
6.11 Self-similarity of the velocity deficit profiles for the stable case. 129
6.12 Global added turbulence intensity in the wake 130
6.13 Local added turbulence intensity in the wake 131
6.14 Self-similarity of the streamwise turbulence profiles for the neutral case. 132
6.15 Self-similarity of the streamwise turbulence profiles for the unstable case. 133
6.16 Self-similarity of the streamwise turbulence profiles for the stable case. 133
6.17 Evolution of the velocity spectra in the wake at different vertical positions, FFOR. . . 134
6.18 Evolution of the velocity spectra in the wake at different vertical positions, MFOR. . 135
6.19 Auto-correlations of the velocity upstream the turbine. 136

7.1 Illustration of the meandering operator. 142
7.2 Contribution of terms (I) and (II) to the velocity in the wake 146
7.3 Available power predicted by (I) and (I)+(II) 148
7.4 Streamwise turbulence in the wake of the wind turbine. 149
7.5 Normalised maximum turbulence in the wake for different levels of approximation. . . 150
7.6 2D maps of the turbulence's breakdown terms for the neutral case. 152
7.7 Same as 7.6 for the unstable case. 153
7.8 Same as 7.6 for the stable case. 154
7.9 Evolution of the maximum value of terms (III) and Δ(IV). 156

8.1 Modelled velocity deficit in the MFOR for the neutral and unstable cases 160

8.2 Chosen shape function for the turbulence in the MFOR. . . . 163
8.3 Modelled added turbulence in the MFOR. . . . 163
8.4 Histograms of the Meso-NH and modelled wake centre PDF. . . . 165
8.5 Mixing length in the wake. . . . 166
8.6 Error induced by the absence of momentum conservation in the model. . . . 168
8.7 Results of the analytical velocity model in the neutral case. . . . 169
8.8 Results of the analytical velocity model in the unstable case. . . . 170
8.9 Meandering-induced turbulence term in Meso-NH. . . . 171
8.10 Meandering-induced turbulence term in the model. . . . 172
8.11 Rotor-added turbulence term in Meso-NH. . . . 172
8.12 Rotor-added turbulence term in the model. . . . 174
8.13 Shape functions of the meandering and rotor-added turbulence terms. . . . 175
8.14 Vertical and horizontal profiles of total modelled turbulence in the neutral case. . . . 177
8.15 Vertical and horizontal profiles of total modelled turbulence in the unstable case. . . . 178

A.1 Inflow conditions for 1WAY and 2WAY nestings. . . . 191
A.2 Effect of using 1WAY or 2WAY nesting on the wake turbulence. . . . 192
A.3 Mean axial velocity in the wake for 1WAY and 2WAY nestings at $z = z_h$. . . . 192
A.4 Effect of the tower and nacelle implementation on the blade's efforts 193
A.5 Effect of the tower and nacelle implementation on the wake mean velocity deficit. . . . 194
A.6 Effect of the tower and nacelle implementation on the TKE in the wake. . . . 194
A.7 Mean axial velocity in the wake the simulations with and without the tower and nacelle. 195

B.1 Velocity deficit planes 198
B.2 Turbulence intensity planes 199
B.3 Local turbulence intensity planes 200
B.4 Turbulence intensity planes, with the reference value 201
B.5 Self similarity of the added TI profiles for the neutral case. . . . 202
B.6 Self similarity of the added TI profiles for the unstable case. . . . 202
B.7 Self similarity of the added TI profiles for the stable case. . . . 203
B.8 Self similarity of the local added TI profiles for the neutral case. . . . 203
B.9 Self similarity of the local added TI profiles for the unstable case. . . . 204
B.10 Self similarity of the local added TI profiles for the stable case. . . . 204

List of Tables

3.1 Values of the constants of the MNH subgrid parametrisation. 72

4.1 Inflow conditions measured with the meteorological mast. 82
4.2 Numerical parameters of the different domains in the neutral case. 87
4.3 Numerical parameters of the different domains in the unstable case. 93
4.4 Numerical parameters of the different domains in the stable case. 97

5.1 Modified numerical parameters for the following chapters. 109
5.2 Number of errors for different wake tracking methods at $x/D = 8$ for the first 400 frames. 110

List of Symbols

Capital letters

$\mathcal{A}$	Max velocity deficit in the optimisation function.	[-]
A_r	Rotor-swept area.	[m^2]
$C(x)$	Velocity deficit at the centreline of the wake.	[-]
C_D	Drag coefficient.	[-]
C_L	Lift coefficient.	[-]
C_T	Thrust coefficient.	[-]
$C_{\mathcal{P}}$	Power coefficient.	[-]
C_{pd}	Specific heat of the dry air.	[-]
C_ϕ	Constants of the models.	[-]
C_μ	Turbulence model constant.	[-]
D	Diameter of the wind turbine.	[m]
D_i	i-th computational domain.	[-]
D_w	Diameter of the wake.	[m]
$\mathcal{F}$	Optimisation function	[-]
F	Self similarity function	[-]
F_{2D}	2D force of an airfoil	[m s^{-2}]
F_c	Coriolis force coefficient	[s^{-1}]
F_N	Force normal to the blade	[N]=[kg m s^{-2}]
F_T	Force tangential to the blade	[N]=[kg m s^{-2}]
G	LES low-pass filter	[-]
I	Turbulence intensity (TI).	[-]
I^l	Local TI.	[-]
I_x, I_y, I_z	Components of the TI.	[-]
K_{MF}	Amplitude of the modelled turbulence in the MFOR.	[-]
K_{FF}	Amplitude of the modelled term (IV).	[-]
K_ϕ	Dummy constant.	[-]
L_{MO}	Monin-Obukhov length.	[m]
L_X, L_Y	Computational domain's dimensions.	[m]
$M_{R_1 \to R_1}$	Transfer matrix between coordinate systems R_1 and R_2.	[-]
N_B	Number of blades.	[-]
$N_{seg-main}$	Number of 10-minutes segments in the main simulation.	[-]
P	Pressure.	[Pa]=[kg m^{-1} s^{-2}]
P_{1b}	Pressure of 1 bar.	[Pa]=[kg m^{-1} s^{-2}]
$\mathcal{P}$	Rotor power.	[W]=[kg m^2 s^{-3}]

$\mathcal{P}_{gen}$	Generator power.	[W]=[kg m^2 s^{-3}]
R_d	Gas constant for dry air.	[-]
Re	Reynolds number.	[-]
$R_{\phi\psi}$	Cross-correlation of ϕ and ψ.	[?]
S	Surface of integration.	[m^2]
$S_{\phi\psi}$	Cross-power spectral density of ϕ and ψ.	[?]
$\mathcal{S}_{ij}$	Strain-rate tensor.	[s^{-2}]
St	Strouhal number.	[-]
S_m	Source term in the momentum equation	[kg m^{-2} s^{-2}]
S_q	Source term of moisture.	[kg m^{-3} s^{-1}]
S_θ	Source term of heat.	[kg K m^{-3} s^{-1}]
T	Absolute temperature.	[K]
$\mathcal{T}$	Integral time scale.	[s]
U	Norm of the velocity vector.	[m s^{-1}]
U_g	Geostrophic wind.	[m s^{-1}]
U_h	Velocity at hub height.	[m s^{-1}]
U_H	Horizontal velocity.	[m s^{-1}]
U_{rel}	Relative velocity.	[m s^{-1}]
U_T	Thrust-based velocity in the wake.	[m s^{-1}]
U_w	Velocity in the wake.	[m s^{-1}]
U_∞	Free-stream velocity.	[m s^{-1}]
U_0	Unperturbed velocity, i.e. either as U_∞ or U_{ref}.	[m s^{-1}]

Lower-case letters

a	Induction factor.	[-]
b	Dummy variable.	[?]
c_a	Chord of an airfoil.	[m]
c_-	Constant of the double gaussian model.	[-]
c_1, c_2, c_3	Skewed Gaussian function coefficients.	[-]
f	Frequency.	[Hz]=[s^{-1}]
f_c	Normalised 2D PDF of the wake centre position.	[-]
f_{cy}, f_{cz}	Normalised 1D PDFs of the wake centre position.	[-]
f_M	Cut-off frequency for the DWM.	[Hz]=[s^{-1}]
f_T	Characteristic turbine's frequency.	[Hz]=[s^{-1}]
g	Gravity constant.	[m s^{-2}]
k	Turbulent kinetic energy (TKE).	[m^2 s^{-2}]
k_a	Rotor-added turbulence.	[m^2 s^{-2}]
k_m	Meandering turbulence.	[m^2 s^{-2}]
k_{sgs}	Subgrid TKE.	[m^2 s^{-2}]
k_x, k_y, k_z	Components of the TKE.	[m^2 s^{-2}]
k_y^*,k_z^*	Lateral and vertical wake expansion coefficients.	[-]
l_m	Mixing length.	[m]
n_s	Super Gaussian order .	[-]
q_T	Specific humidity of the air.	[kg. kg $^{-1}$]
r	Radial component in the rotor frame of reference.	[m]
s	Dummy variable.	[?]
$u = U_x$	Streamwise velocity component.	[m s^{-1}]
u_{n1}	Velocity of 1 m s^{-1}.	[m s^{-1}]
u_*	Friction velocity.	[m s^{-1}]
u_0	Velocity scale.	[m s^{-1}]
$v = U_y$	Lateral velocity component.	[m s^{-1}]
$w = U_z$	Vertical velocity component.	[m s^{-1}]
x	Streamwise distance.	[m]
x_∞	Position upstream the turbine.	[m]
y	Lateral distance.	[m]
x_N	Length of the near wake.	[m]
z	Altitude (vertical distance).	[m]
x_c, y_c, z_c	Coordinates of the wake centre's position.	[m]
z_h	Hub height.	[m]
z_i	Depth of the ABL.	[m]
z_0	Roughness length.	[m]

Lower-case greek letters

α	Angle of attack.	[rad]
α_F	Frandsen wake growth rate.	[-]
α_J	Jensen wake growth rate.	[-]
β	Wind direction.	[°]
β_w	Wake width parameter.	[-]
γ	Pitch angle.	[rad]
γ_l	Local pitch angle.	[rad]
δT	Time period of the moving average operator.	[s]
δ_{ij}	Kronecker symbol.	[-]
δU	Velocity deficit.	[m s^{-1}]
δD	Infinitesimal drag force.	[N m^{-1}]=[kg s^{-2}]
δL	Infinitesimal lift force.	[N m^{-1}]=[kg s^{-2}]
ϵ	Initial wake width.	[m]
ϵ_D	Dissipation term in the TKE equation.	[m^2 s^{-3}]
ϵ_{ijk}	Levi-Civita symbol for vectorial product.	[-]
ζ	Stability parameter.	[-]
η	Kolmogorov length scale.	[m]
θ	Dry potential temperature.	[K]
θ_v	Virtual potential temperature.	[K]
κ	Von Kármán constant.	[-]
λ	Wavelength	[m]
λ_T	Tip-speed ratio	[-]
λ_M	Cut-off length scale for the DWM.	[m]
ν	Kinematic viscosity.	[m^2 s^{-1}]
ν_θ	Thermal diffusivity of air.	[m^2 s^{-1}]
ν_q	Molecular diffusivity for water vapor in air.	[m^2 s^{-1}]
ν_t	Eddy viscosity.	[m^2 s^{-1}]
ρ	Density of the air.	[kg m^{-3}]
$\rho_{\phi\psi}$	Correlation function	[?]
σ	Wake width.	[m]
σ_f	Amount of meandering.	[m]
τ	Time or spatial lag for auto-correlation.	[?]
τ_{ij}	Turbulent tensors in LES.	[?]
φ	Tangential component in the rotor frame of reference.	[rad]
ϕ	Dummy variable.	[?]
ϕ_l	Latitude.	[rad]
ψ	Dummy variable.	[?]
ψ_M	Stability function of the log profile.	[-]
ω_f	Skew angle of the Gaussian function.	[rad]

Capital greek letters

Γ	Gamma function.	[-]
Δ	Mesh size.	[m]
Δ_G	LES filter size.	[m]
ΔI	Added turbulence intensity, global normalisation.	[-]
ΔI^l	Added turbulence intensity, local normalisation.	[-]
ΔU	Normalised velocity deficit.	[-]
Δt	Meso-NH time step.	[s]
ΔT	Sampling period.	[s]
$\Delta X,\ \Delta Y,\ \Delta Z,$	Grid resolution.	[s]
Λ	Integral length scale.	[m]
Π	Exner function.	[-]
Φ	Wavenumber	[m^{-1}]
Ψ	Angle between relative velocity and rotor plane.	[rad]
Ω	Wind turbine's rotational speed.	[rad s^{-1}]
Ω_E	Earth's rotational speed.	[rad s^{-1}]

Sub- and Superscripts

X^a	Anisotropic tensor.
X^m	Minimum value.
X^M	Maximum value.
X^{ra}	Averaged value over the rotor swept area.
X^v	Variation from the reference state.
$\overline{X}$	Reynolds averaged variable.
X'	Fluctuating part of the Reynolds averaging.
$\widetilde{X}$	Resolved part of a variable.
X"	Subgrid part of a variable.
$\widehat{X}$	Meandering operator.
X_{am}	Analytical model.
X_d	Dry quantity.
X_{dwm}	DWM results.
X_{FF}	Value in the FFOR.
X_{ij}	Einstein notation.
X_{MF}	Value in the MFOR.
X_r	Reference state value.
X_{ref}	Value in the reference simulation.
X_{sgs}	Sub-grid scale.
X_{TB}	Value in the synthetic turbulent box.
X_{tt}	Value at the top tip.
X_{wt}	Value at the wind turbine location.
X_∞	Freestream or undisturbed value.
$X\|_s$	Value at the ground surface.

Acronyms

1WAY	One-way grid nesting.	Page 73
2WAY	Two-way grid nesting.	Page 73
ABL	Atmospheric Boundary Layer.	Page 21
AEP	Annual Energy Production.	Page 63
ALM	Actuator Line Method.	Page 65
BP14	Model of Bastankhah and Porte-Agel	Page 54
BS19	Model of Braunbehrens and Segalini	Page 62
CBL	Convective Boundary Layer.	Page 27
CFL	Courant-Friedrich-Levy (criterion).	Page 66
CM	Coarse mesh.	Page 73
DEAR	Deardorff mixing length.	Page 72
DNS	Direct Numerical Simulations.	Page 65
DTU	Danmarks Tekniske Universitet.	Page 81
DWM	Dynamic Wake Meandering.	Page 58
FFOR	Fixed Frame Of Reference.	Page 50
FM	Fine mesh.	Page 73
FOWT	Floating Offshore Wind Turbine.	Page 39
HAWT	Horizontal Axis Wind Turbine.	Page 39
HM21	Honnert and Masson mixing length.	Page 72
HPC	High Performance Computing.	Page 4
IEA	International Energy Agency.	Page 1
LES	Large Eddy Simulation.	Page 66
LiDAR	Light Detection And Ranging.	Page 3
Meso-NH	MESOscale Non-Hydrostatic.	Page 69
MEXICO	Model Experiments in Controlled Conditions.	Page 81
MFOR	Moving Frame Of Reference.	Page 50
NREL	National Renewable Energy Laboratory.	Page 81
PDF	Probability density function.	Page 62
PSD	Power Spectral Density.	Page 24
RANS	Reynolds Averages Navier-Stokes Simulations.	Page 66
RMSE	Root-mean-square error.	Page 145
SAMWICH	Simulated And Measured Wake Identification and CHaracterization.	Page 90
S(A)BL	Stable (Atmospheric) Boundary Layer.	Page 28
SCADA	Supervisory Control And Data Acquisition.	Page 3
SGS	Subgrid scale.	Page 66
SL	Surface Layer.	Page 28
SWiFT	Scaled Wind Farm Technology.	Page 81
TI	Turbulence Intensity.	Page 21
TKE	Turbulent Kinetic Energy.	Page 21
TSR	Tip Speed Ratio.	Page 41
XA14	Model of Xie and Archer	Page 55